Revealing Deformation Mechanisms of Advanced Face-centred Cubic Alloys at Cryogenic Environment via In Situ Neutron Diffraction

By

LEI TANG

A thesis submitted to
the University of Birmingham
for the degree of
DOCTOR OF PHILOSOPHY

School of Metallurgy and Materials
College of Engineering and Physical Sciences
The University of Birmingham (UK)
November 2021

Table of Contents

Acknowledgements

Pursuing a Ph.D. has been a challenging but unforgettable experience for me, and I would like to give my gratitude and thanks to those who supported me throughout this journey over the last 3 years.

First and foremost, I would like to thank heartily my supervisor Dr. Biao Cai. I feel exceptionally lucky to have your guidance, positivity, and unique approach to academia. Thank you for all your insightful comments, valuable advice, and extensive support in experiments and shaping my manuscripts. Your drive, ambition, and enthusiasm for research have inspired my research path and future. I would also like to give my appreciation to my second supervisor Prof. Moataz M. Attallah for his help in experiments and stimulating advice which helped shape and direct the project.

In addition to my supervisors, I sincerely thank the staff and friends from the University of Birmingham, Diamond Light Source, and Central South University, in particular to Prof. Guofu Xu, Dr. Oxana Magdysyuk, Dr. Kun Yan, Dr. Yu-Lung Chiu, Dr. Minshi Wang, Dr. Stano Imbrogno, Dr. Sheng Li, Dr. Fuqing Jiang, Dr. Li Wang, Mr. Zihan Song, Miss Wanxuan Teng, Mr. Tay Sparks, Theresa Morris, Jaswinder Singh, Amy Jade Newell, and Jag Sangha for their constant help and support in experiments.

I also want to thank the beamline of ENGIN-X, ISIS Neutron and Muon Source (the Rutherford Appleton Laboratory, UK) for providing the beamtime (RB1820630, RB1920111, and RB2010324). The beamline scientist, Dr. Saurabh Kabra, is greatly acknowledged for his excellent support in experiments and data analysis.

I acknowledge the financial supports for my Ph.D. project, provided by the University of Birmingham and China Scholarship Council.

A heartfelt thanks also go to all my friends who have supported me every single day and for always believing in me. Special thanks to dear Miss Qian Jiang, Dr. Runcheng He, Dr. Jibo Tang, Dr. Ping Liu, and Mr. Hongjing Guo.

Finally, to my whole family, thanks for your love and support, and my heartfelt gratitude to my dear mom and dad, you have provided unfaltering support and a love I never question.

List of Publications

Published Papers

1. **Lei Tang ,** Li Wang, Minshi Wang, Huibin Liu, Saurabh Kabra, Yulung Chiu, Biao Cai, ***Synergistic deformation pathways in a TWIP steel at cryogenic temperatures: In situ neutron diffraction***, Acta Materialia 200 (2020) 943–958.

https://doi.org/10.1016/j.actamat.2020.09.075.

2. **Lei Tang**, Kun Yan, Biao Cai, Yiqiang Wang, Bin Liu, Saurabh Kabra, Moataz M. Attallah, Yong Liu, ***Deformation mechanisms of FeCoCrNiMo0.2 high entropy alloy at 77 and 15 K***, Scripta Materialia 178 (2020) 166–170.

https://doi.org/10.1016/j.scriptamat.2019.11.026.

3. **Lei Tang**, Fuqing Jiang, Jan S. Wróbel, Bin Liu, Saurabh Kabra, Ranxi Duan, Junhua Luan, Zengbao Jiao, Moataz M. Attallah, Duc Nguyen-Manh, Biao Cai, ***In Situ Neutron Diffraction Unravels Deformation Mechanisms of a Strong and Ductile FeCrNi Medium Entropy Alloy***, Journal of Materials Science and Technology, 116 (2022) 103–120.

https://doi.org/10.1016/j.jmst.2021.10.034.

4. Zihan Song, Oxana V. Magdysyuk, **Lei Tang**, Tay Sparks, Biao Cai, ***Growth dynamics of faceted Al13Fe4 intermetallic revealed by high-speed synchrotron X-ray quantification***, Journal of Alloys and Compounds 861 (2021).

https://doi.org/10.1016/j.jallcom.2021.158604.

5. Sheng Li, Biao Cai, Ranxi Duan, **Lei Tang**, Zihan Song, D. White, Oxana V. Magdysyuk, Moataz M. Attallah, ***Synchrotron Characterisation of Ultra-Fine Grain TiB2/Al-Cu Composite Fabricated by Laser Powder Bed Fusion***, Acta Metallurgica Sinica (English Letters (2021).

https://doi.org/10.1007/s40195-021-01317-y.

Papers in Preparation

6. **Lei Tang**, Fuqing Jiang, Huibin Liu, Saurabh Kabra, Biao Cai, ***In situ neutron diffraction reveals the effect of Cu on cryogenic mechanical performance of TWIP steels*****.** To be submitted to Acta Materialia.

7. **Lei Tang**, Fuqing Jiang, Bin Liu, Saurabh Kabra, Moataz M. Attallah, Biao Cai, ***Mechanical performance and deformation mechanisms of 316L stainless steel processed by laser powder bed fusion at cryogenic temperatures: in situ neutron diffraction*****.** To be submitted to Scripta Materialia.

Nomenclature

Roman Symbols

$\boldsymbol{b}$	Burger's vector
a	Lattice Parameter
G	Shear modulus
E	Young's modulus
R	Gas constant
T	Temperature in Kelvin
N	Avogadro's number
P	Number of phases in thermodynamically equilibrium state
F	Degree of freedom
M	Taylor factor
k	Boltzmann constant
A	Fitting parameter
B	Fitting parameter
l	Twin spacing
e	Thickness of twins
D	Crystalline size
L	Distance between diffraction planes in real space
s	Diffraction vector
H	Lorentzian width of the peak profile

Greek Symbols

γ	Face-centred cubic austenite
ε	Hexagonal close-packed martensite
α'	Body-centred tetragonal martensite
ν	Poisson's ratio
ρ	Dislocation density
α	A constant for scaling the interaction strength between dislocations
μ	Normalized homogenization parameter

Ω	Phase determination parameter

Acronyms

AM	Additive Manufacturing
APT	Atom Probe Tomography
ASS	Austenite Stainless Steel
BCC	Body-Centred Cubic
BCT	Body-Centred Tetragonal
CALPHAD	CALculation of PHAse Diagram
CE	Cluster Expansion
CPA	Coherent Potential Approximation
DBTT	Ductile-to-Brittle Temperature
DFT	Density Functional Theory
EBSD	Electron Back Scatter Diffraction
FCC	Face-Centred Cubic
FDA	Frequency Distribution Analysis
FFT	Fast Fourier Transform
FWHM	Full Width at Half Maximum
GGA	Generalized Gradient Approximation
GPA	Geometric Phase Analysis
HAADF	High-Angular Dark-Field
HAGB	High-Angle Grain Boundary
HCP	Hexagonal-Close-Packed
HEAs	High Entropy Alloys
HRSTEM	High-Resolution Scanning Transmission Electron Microscope
HRTEM	High-Resolution Transmission Electron Microscope
ICP-MS	Inductively Coupled Plasma Mass Spectrometry
IPF	Inverse Pole Figure
K-S	Kurdjumov-Sachs
LAGB	Low-Angle Grain Boundary
LD	Loading Direction
L-PBF	Laser Powder-Bed-Fusion

MC	Monte-Carlo
MCAs	Multi-Component Alloys
MEAs	Medium Entropy Alloys
OM	Optical Microscope
RD	Rolling Direction
SAED	Selected Area Electron Diffraction
SEM	Scanning Electron Microscope
SFE	Stacking Fault Energy
SFP	Stacking Fault Probability
SFs	Stacking Faults
SHR	Strain Hardening Rate
SIMT	Strain-Induced Martensite Transformation
S-N	Shoji-Nishiyama
SRO	Short-Range Order
STEM	Scanning Transmission Electron Microscope
TCH	Thomson–Cox–Hasting pseudo-Voigt function
TEM	Transmission Electron Microscope
TOF	Time-of-Flight
TRIP	Transformation Induced Plasticity
TWIP	Twinning Induced Plasticity
UTS	Ultimate Tensile Strength
VASP	Vienna Ab-initio Simulation Package
VEC	Valence Electron Concentration
WHC	Work Hardening Capacity
YS	Yield Strength

Other Symbols

g_0	A scaling factor
$\sigma_{Athermal}$	Athermal component of yield strength
r_i	Atomic radius
$\overline{r}$	Average atomic radius

$\overline{C}_{h00}$	Average contrast factor for $\{h00\}$ peak
μ_B	Bohr magneton
b_p	Burgers vector for partial dislocations
$\Delta G_{\rho}^{\gamma\to\varepsilon}$	Change of Gibbs free energy of each element during phase transformation from γ to ε
E_N^{γ}	Configurational energies of the interstitial N atoms in γ phase
E_N^{ε}	Configurational energies of the interstitial N atoms in ε phase
ΔS_{config}	Configurational entropy
S_{Calc}^{SS}	Configurational molar entropy
$\Delta G_{seg(\mathrm{int})}^{\gamma\to\varepsilon}$	Contribution from interstitial atoms such as carbon and nitrogen to Gibbs free energy change during phase transformation from γ to ε
τ_{tw}	Critical shear stress for twinning
σ_{tw}	Critical stress for twinning
$\partial\sigma_{dis}/\partial\varepsilon$	Dislocation-induced hardening rate
β_{GD}	Distorsion broadening effects of Gaussian component
β_{LD}	Distorsion broadening effects of Lorentzian component
A_i	Elastic anisotropy parameter
ΔH_{mix}	Enthalpy of a solid solution alloy
ΔS_{mix}	Entropy of a solid solution alloy
σ_{exp}	Experimentally measured flow stress
$\Omega_{\varphi\phi}^{\gamma\to\varepsilon}$	First-order interactions between two different element φ and ϕ
ΔG	Free energy of overcoming barriers
ΔK	Full width at half maximum
β_{Gg}	Gaussian component of instrumental broadening
β_G	Gaussian component of intrinsic broadening
β_{Gh}	Gaussian component of measured diffraction profile
δ^2	Gaussian width of the peak profile
G_{mix}	Gibbs Free Energy of a solid solution alloy

$\Delta G^{FCC \rightarrow HCP}$	Gibbs free energy of the martensite phase transformation from FCC to HCP
σ_{GB}	Grain boundary hardening
K_{GB}	Hall-Petch coefficient
ΔK^2_{inst}	Instrumental broadening effects
$\sigma^{\gamma/\varepsilon}$	Interfacial energy per unit of the γ/ε boundaries
d^0_{hkl}	Inter-planar spacing from *hkl* grain plane under stress
d^0_{hkl}	Inter-planar spacing from *hkl* grain plane without stress
σ_f	Lattice friction stress
ε^{exp}_{hkl}	Lattice strain of *hkl* grain plane
β_{Lg}	Lorentzian component of instrumental broadening
β_L	Lorentzian component of intrinsic broadening
β_{Lh}	Lorentzian component of measured diffraction profile
$\varepsilon^{strain}_{hkl}$	Macro-strain of *hkl* grain plane
$\Delta G^{\gamma \rightarrow \varepsilon}_{mg}$	Magnetic contribution to the Gibbs free energy change during phase transformation from γ to ε
β^{Φ}	Magnetic moment of the phase divided by the Bohr magneton
b_p	Magnitude of the Burgers vector of the Shockley partial dislocations
$\langle \varepsilon^2 \rangle_{111}$	Mean square strain, root-mean-square microstrain of the deformed FCC matrix at the close-packed {111} plane
ε^{exp}_{hkl}	Measured lattice strain of *hkl* grain plane
ΔK^2_{meas}	Measured peak broadening
σ_0	Mechanical threshold stress to overcome the lattice friction without thermal activation at 0 K
ΔV_n	Misfit Volume
χ_i	Molar fraction of constituent element *i*
G^{γ}_{φ}	Molar Gibbs free energy of the pure elements in γ phase
$G^{\varepsilon}_{\varphi}$	Molar Gibbs free energy of the pure elements in ε phase

ρ_m	Molar surface density
$T_{Néel}^{\Phi}$	Néel temperature
σ_{PP}	Precipitation hardening
σ_{mod}	Predicted flow stress
$\dot{\varepsilon}_0$	Reference strain rate
$\vec{F}_e$	Repulsive elastic force between two partial dislocations
$\vec{F}_s$	Restorative force between two partial dislocations
ΔK_{sample}^2	Sample-induced peak broadening
α_{DBT}	Screw-to-edge ratio
r_e	Separation distance between two partial dislocations
a_s	Shape factor for cubic-symmetric spherical crystals
G_0	Shear modulus at 0 K
G_T	Shear modulus at temperature T
σ_{SRO}	Short-range-ordering hardening
β_{GS}	Size broadening effects of Gaussian component
β_{LS}	Size broadening effects of Lorentzian component
m_{dis}	Slope of hardening rate curves of dislocation
m_{twin}	Slope of hardening rate curves of twinning
$\partial SFP/\partial\varepsilon$	Speed of forming stacking faults
ε_{hkl}^{sf}	Stacking fault induced strain of *hkl* grain plane
$\dot{\varepsilon}$	Strain rate
$\sigma_{dis}^{\varepsilon}$	Strength contribution from dislocations at strain of ε
σ_{dis}^{0}	Strength contribution from initial dislocations
σ_{twin}	Strengthening contribution from twinning
σ_{dis}	Strengthening contribution of dislocations
σ_{diff}	The difference between experimentally measured flow stress and modelling results

M_d	The outer cutoff radius of dislocation
$\sigma_{Thermal}$	Thermal component of yielding strength
E_{isf}	Total energy of the faulted supercell
E_0	Total energy of the pristine supercell
$\sigma_{0.4}$	True stress at a true strain of 0.4
$\partial\sigma_{twin}/\partial\varepsilon$	Twinning-induced hardening rate
σ_{UTS}	Ultimate tensile strength
v_e	Velocity of edge dislocations
v_s	Velocity of screw dislocations
σ_{YS}	Yield strength
ΔE_b	Zero-stress energy barrier
τ_{y_0}	Zero-temperature flow stress
A_D	Distortion component of Fourier transform coefficients
A_s	Size component of Fourier transform coefficients
A_s	Total area of the stacking fault at the close-packed plane
C_{ij}	Elastic constants
E_{hkl}	*hkl*-specific Young's modulus
F_t	Twin volume fraction
K_{twin}	Hall-Petch coefficient of twinning
L_0	Width of the twin embryo
N_c	Number of Components
R_{dis}	Increase rate of dislocation density
V_0	Volume of the undistorted cell
V_{alloy}	Atomic Volume
V_{hkl}	*hkl*-specific Poisson's ratio
γ_{sf}	Stacking Fault Energy
θ_p	Angle between the dislocation line and the Burgers vector of the perfect dislocation

List of Figures

List of Tables

Abstract

The rapid advancement of cryogenic technology is now boosting the demand for strong and ductile structural materials for low-temperature applications ranging from familiar natural gas storage/transmission to advance superconductivity realization.

In this thesis, *in situ* neutron diffraction and tensile testing were performed at the low-temperature range (e.g., from 373 to 10 K) to investigate the mechanical and microstructural responses of several promising face-centred cubic alloys, including high Mn steels, multi-component alloys, and an additively manufactured austenite stainless steel. Meanwhile, correlative post-mortem microscopy characterizations were utilized to reveal the microstructure evolution and assist the determination of various strengthening effects.

The qualitative and quantitative analysis revealed that the superior cryogenic mechanical performance of these advanced alloys originates from a variety of concurrent strengthening mechanisms including dislocation motion, strain-induced twinning, and phase transformation, not only building a more fundamental understanding of the strengthening effects at cryogenic conditions but also revealing the relationship among deformation mechanisms, chemical composition, stacking fault energy, and deformation temperature. This study shows a very promising way of achieving superior combinations of strengthening mechanisms by tailoring stacking fault energy, thus shedding a light on developing new alloys with lower production cost and excellent combinations of strength and ductility for cryogenic applications.

Chapter 1. Introduction

Cryogenic technology is now gaining importance in many areas ranging from applications such as food storage, liquid natural gas transition/storage to superconductivity realization, outer-space exploration, and nuclear fusion devices [1–3]. This leads to the soaring demand for low-cost structural alloys with superior mechanical performance in cryogenic conditions.

With the decrease of deformation temperature, many alloys may undergo ductile-to-brittle transition, where the fracture mode can be transferred from ductile to brittle. The brittle fracture requires less energy, and the crack can propagate rapidly with minimal plastic deformation [3,4]. This is very dangerous and undesirable in most applications. Some conventional cryogenic alloys were developed, such as aluminium alloys [5–8], titanium alloys, and Ni-based Invar alloys [8]. These alloys, however, find it very difficult to maintain the strength-ductility balance, which means either strength or ductility will be sacrificed due to the very limited strain hardening effect.

Two emerging intriguing deformation mechanisms, twinning-induced plasticity (TWIP) and transformation-induced plasticity (TRIP) in FCC alloys can provide continuous high strain hardening effects during plastic straining and thus significantly improve both strength and ductility. The TWIP and TRIP effects are all based on the dissociation of perfect dislocations and the following motion of partial dislocations and stacking faults. The stacking fault energy (SFE), which measures the energy barrier of dissociating perfect dislocations, thus plays a critical role in determining deformation mechanisms and deciding the mechanical performance. With the decrease of SFE, the dominant deformation mechanisms can sequentially shift from dislocation motion

(SFE > 45 mJm^{-2}) to TWIP (45mJm^{-2} > SFE > 18 mJm^{-2}) and TRIP (SFE < 18 mJm^{-2}). With suitable SFE, three alloys with great potential in activating multiple strengthening effects and thus achieving excellent strength-ductility combinations in cryogenic conditions have been identified: multi-component alloys, high Mn steels, and austenite stainless steels.

However, the investigations concerning these new types of alloys, especially at ultra-low temperature conditions, are still very rare. Most of them are based on theoretical modelling/prediction in need of experimental validation, while many experimental observations are based on *ex situ* methods, and very few *in situ* observations reflecting the real-time microstructural and mechanical responses, especially with *in situ* neutron diffraction at cryogenic temperatures, were performed.

This thesis endeavours to utilize *in situ* neutron diffraction and post-mortem microscopic characterizations to investigate the microstructural and mechanical features of three promising FCC alloys at cryogenic conditions, with the aim to (i) develop more advanced cryogenic alloys with excellent strength-ductility combinations and lower production costs; (ii) build a more fundamental understanding about the relationship among microstructural/mechanical responses, deformation mechanisms, SFE, and chemical composition of these alloys at the ultralow-temperature range; and (iii) determine the strengthening contributions of multiple deformation mechanisms at the cryogenic temperatures and how they evolve with temperature decreasing.

The thesis outline is described as follows:

Chapter 1 briefly introduces the project background, content, and aims of this thesis.

Chapter 2 gives the theoretical background related to cryogenic technology, cryogenic deformation, and the soaring demand for strong and ductile alloys in cryogenic

environments. The promising solution with two deformation mechanisms (TWIP and TRIP) was introduced. The important role of SFE and the formation mechanisms of the faulted structures were also discussed. Three new promising cryogenic alloys (high Mn steels, multi-component alloys, and austenitic stainless steels) were also introduced focusing on the deformation mechanisms. Furthermore, different methods to determine SFE, including theoretical prediction and experimental measurement (X-ray/neutron diffraction and TEM observation), were also briefly compared.

Chapter 3 investigated the mechanical performance and microstructural evolution of a high Mn steel deformed at the temperature range of 373 and 77 K. The temperature dependence of SFE and its role in controlling the dominant deformation mechanism was revealed. The evolution of multiple strengthening effects (e.g., dislocation motion and twinning) at different strains and temperatures were also determined and discussed in detail.

Chapter 4 investigated the dominant deformation mechanism transition of several high Mn steels with different chemical compositions, focusing on the role of Cu in tailoring SFE and thus adjusting strengthening effects. The SFE measured with neutron diffraction and predicted with thermodynamical calculation was compared. The strengthening effects of dislocation motion, TWIP, and TRIP (from FCC austenite to HCP martensite) were determined and compared in detail.

Chapter 5 revealed the superior mechanical properties of a $FeCoCrNiMo_{0.2}$ high entropy alloy at both 293, 77, and 15 K. The temperature-dependent deformation behaviour, microstructure evolution, and SFE were investigated with *in situ* neutron diffraction. The hardening effects were analysed with the strain-induced phase transformation.

Chapter 6 systematically investigated a high-strength equal-molar FeCrNi medium entropy alloy at 293 and 15 K with *in situ* neutron diffraction and correlated microscopic observation. The temperature-dependent mechanical performance was interpreted in terms of DFT theoretical simulation and neutron diffraction experimental measurement. Multiple strengthening effects including severe lattice distortion and dislocation motion were calculated with the assistance of microscopic observation and DFT simulation.

Chapter 7 investigated the mechanical and microstructural responses of an additively manufactured austenitic stainless steel (316 L) during deforming at the low-temperature range (from 373 to 10 K). The influence of temperature and microstructure on SFE was revealed. The temperature-dependent strengthening effects mainly originating from the TRIP effect (from FCC to BCT/HCP) were also discussed with the corresponding strain hardening behaviours.

Chapter 8 summarizes the results of the above studies and outlines the promising directions for future investigations.

Chapter 2. Literature Review

2.1 Cryogenic Technology

Cryogenic technology is nowadays playing an essential role in a variety of areas including aerospace exploration, medical diagnosis, transportation, biological conservation, materials processing, et al [2,9,10]. By creating low-temperature environments, cryogenic technology was originally applied for commercial or industrial inert gas production and wind tunnel tests [1,2]. Decades of development and investigation revealed many discoveries and mechanisms concerning low temperatures.

For example, cryogenic technology is widely used in the transmission/storage of liquified gases [11–13]. Cryogenic fuels are very critical in machinery that operates in outer-space exploration (e.g., rockets and satellites) [14]. The cryogenic fuels generally contain liquefied hydrogen and oxidizer, both of which are stored at very low temperatures and high-pressure conditions [15]. Additionally, natural gas liquefaction achieved by cryogenic technology is critical in solving the growing serious air pollution. The soaring energy consumption and the over-reliance on traditional fossil fuels have led to severe air pollution and the greenhouse gas effect [3]. Natural gases are now emerging as a promising solution to this problem and their consumption is now soaring. During the last decade, the consumption of natural gas in the UK maintained a very high level of > 37 bcm (billion cubic meters) per year [16]. For other developed countries and areas (such as the United States and Europe), the consumption is all above 500 bcm/year since 2010 [17]. The consumption of natural gases all over the world increased from 3150.8 bcm in 2010 to 3976.2 bcm in 2019 [16]. To reduce the

production cost and improve efficiency, the liquefaction of natural gas via cryogenic technology is necessary during storage and long-distance transportation.

Another benefit of cryogenic technology is the realization of superconductivity, such as superconducting electromagnets [18]. Real-time and high-resolution magnetic resonance imaging equipment is emerging as a critical method in diagnosing diseases with ultra-high accuracy. To obtain reliable results, they mainly rely on large superconducting magnets working in an ultra-low temperature of 4.2 K maintained by a closed-cycle refrigeration system [19]. The superconducting electromagnets are also widely used in the magnetic levitation (Maglev) train technology, which is considered as a convenient, environment-friendly, low maintenance, and reliable transportation method [20]. Besides, various applications of Maglev technology have been developed, such as spacecraft, military weapons, the centrifuge of the nuclear reactor, magnetic bearing, elevator, compressor, wind turbines, geothermal heat pumps, heart pump, automotive engineering, etc [21].

In summary, cryogenic technology is expanding its application rapidly, including cryogenic liquid level controllers, cryogenic line regulators, cryopumps, nuclear radiation testing, and recycling [2]. The advancements of cryogenic technology thus boost the demand for cost-effective structural materials that could resist ultra-low temperature and exhibit excellent strength-ductility combinations.

2.2 Cryogenic Deformation

Indeed, the rapid advance of cryogenic technology lays the foundation for developing many advanced technologies. Its realization has been a huge challenge to the structural

materials due to the very high requirement in both desirable mechanical performance and the ability to resist the harsh serving conditions: ultralow temperatures.

The decrease of temperature can lead to many changes of the alloy, such as the microstructure change, the occurrence of cracks on the surface, shrinkage and change in dimensions, and increase of hardness etc [22,23]. The most serious issue is that many alloys can suffer from the severe reduction of mechanical performance [24] and the fracture mode can be transferred from ductile to brittle (so-called ductile-to-brittle transition phenomenon) as the temperature decreases [25,26]. Unlike the ductile fracture, where the alloy is torn apart after considerably large plastic deformation, the brittle fracture requires less energy, and the crack can propagate rapidly with minimal plastic deformation [27]. Although the strength can be improved significantly, their ductility can be decreased to a very low level [28–30].

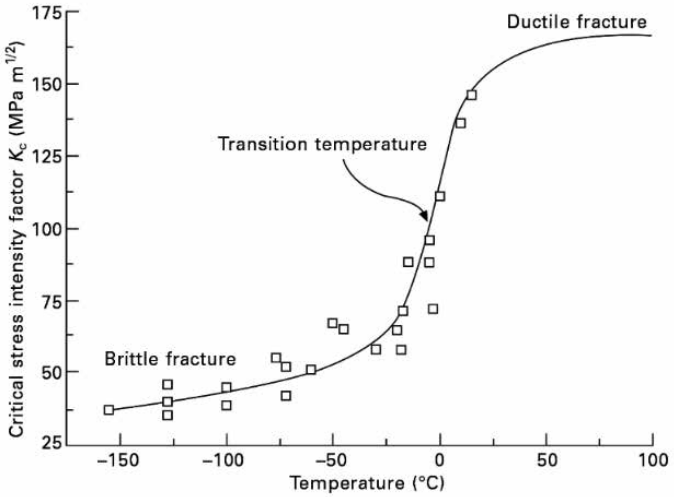

Fig. 2-1 Critical stress intensity factor of medium-strength steel plotted as a function of environmental temperature, showing the transition of fracture mode (from ductile to brittle), after Ref. [31].

Fig. 2-1 shows the evolution of the critical stress intensity factor of a medium-strength steel as a function of deformation temperature. The fracture toughness decreased rapidly as the temperature decreased from 5℃ to -20℃, switching fracture mode from ductile to brittle with the transition point appearing at ~0℃. Fig. 2-1 indicates that the

severe reduction in ductility and fracture mode transition is temperature-dependent. At high temperatures, the dislocation movement is aided by both sufficient internal thermal energy and externally applied stress. This allows the massive gliding of mobile dislocations and following dislocation multiplication, withstanding larger plastic strain. The low temperature reduced the internal thermal energy, dislocation mobility, and thus the ductility and fracture toughness [32].

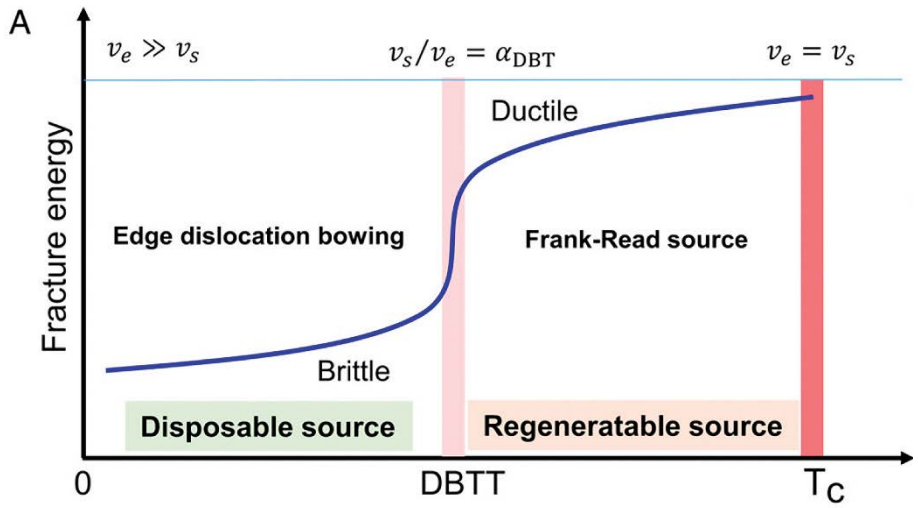

Fig. 2-2 The relationship among temperature, relative dislocation mobility, Frank-Read source, and the ductile-to-brittle temperature (DBTT), after Ref. [33].

During deformation at low temperatures, many alloys (e.g., tungsten, tin, molybdenum, chromium, zinc, and magnesium alloys) with body-centred cubic (BCC, α) or hexagonal close-packed (HCP, ε) structures, showed very poor ductility and can undergo the ductile-to-brittle transition as temperature decreases [34–36]. The ductile-to-brittle transition can result from the very high lattice friction stress (Peierls stress) at low-temperature conditions [37]. Lu et al. [33] revealed that the transition from ductile to brittle in BCC alloys is closely related to the screw-to-edge velocity ratio ($\alpha_{DBT} = v_s/v_e$), which measures the efficiency of the dislocation source and the ability to produce abundant dislocations to maintain the plastic deformation. The activity of screw dislocation strongly relies on thermal activation and the decrease of temperature

leads to inactive screw dislocation gliding and thus low α_{DBT} . As shown in Fig. 2-2, if the temperature drops to below ductile-to-brittle temperature (DBTT) and α_{DBT} decreased to a very low level, the bowing part of the edge dislocation can be a disposable and low efficient dislocation source. Contrarily, when the temperature increases to higher than DBTT and $v_e = v_s$, the edge dislocation can bow out into a half loop and produce high effective Frank-Read sources.

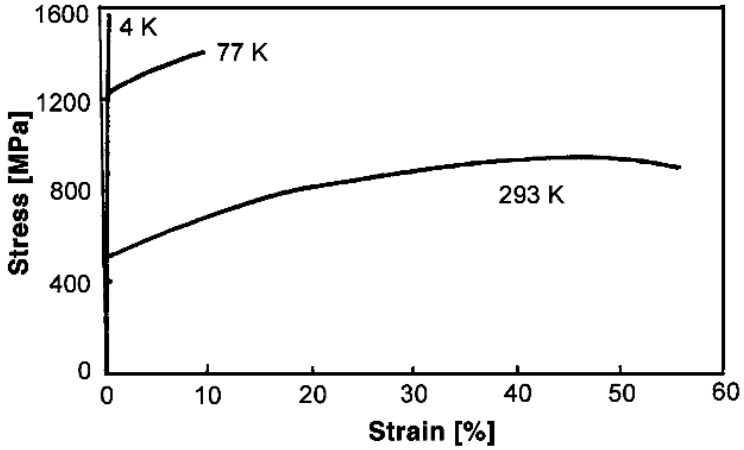

Fig. 2-3 Stress-strain curves of the 18Cr-18Mn-N steel at 293, 77, and 4 K, after Ref. [38].

The ductile-to-brittle transition was also observed in some FCC alloys. For example, according to Ref. [38], 18Cr-18Mn-0.7N austenitic steel showed an excellent combination of the tensile strength (with yield strength, YS, of ~540 MPa) and ductility (with total elongation of ~58%) at 293 K. As shown in Fig. 2-3, with the drop of deformation temperature, the ductility of the alloy was decreased sharply to 10% at 77 K and to even less than 0.2% at 4 K.

The ductile-to-brittle transition severely limited the serving temperature of most steels to above 253 K. The brittle deformation behaviours are very dangerous and unsuitable for use in safety-critical structures at cryogenic environments requiring exceptional structural reliability (transport/storage of liquefied natural gas at 77 K, high field

superconducting magnets working at 4 K, etc.) [2]. For example, during the winter months between 1943 and 1944 (World War II), almost 160 Liberty ships broke in half due to the low-temperature brittle fracture [39]. In January 2021, at least 6 people were killed due to the leak of liquid nitrogen from a poultry plant in Georgia, US [40]. In April 2008, the outer jacket of a 60,000-litre liquid nitrogen tank, which was made of carbon steel, suffered from a brittle fracture after 9 years of operation, ejecting steel fragments to the surrounding area [41]. Therefore, developing structural materials with low-cost, high stability, and desirable strength-ductility balance for cryogenic applications is very important. Meanwhile, it is also of great importance to build a fundamental understanding of the deformation mechanisms, mechanical behaviours, and microstructure evolution of the alloys during deforming at a low-temperature range (< 293 K).

2.3 Two Intriguing Deformation Mechanisms

To improve the strength, ductility, and strain hardening of the alloys, the combination of various strengthening mechanisms has been utilized, such as fine-grain strengthening and precipitation strengthening [42,43]. Even though these strengthening mechanisms can largely improve the tensile strength, the strain hardening effects are still very limited and the ductility sometimes is sacrificed [44].

A very promising way to resolve the strength-ductility trade-off is to design full-face-centred cubic (FCC, γ) structured alloys or enhance the volume fraction of FCC phases [45–50]. Sohn et al. [45] investigated the mechanical performance and Charpy impact of a series of FCC-structured austenitic high Mn steels with different Mn and Al contents at both room temperature and 77 K. Interestingly, the Fe-22Mn and Fe-22Mn-

2Al steels showed very high ultimate tensile strength (UTS of ~997 MPa and ~828 MPa) and very large ductility of ~73.8% and ~71.6% at room temperature. When deforming at 77 K, the excellent strength-ductility balance was maintained with UTS of ~1509 MPa and ~1403 MPa, total elongation of ~53.5% and ~67.2 for Fe-22Mn and Fe-22Mn-2Al steel, respectively. Fig. 2-4 shows the SEM images of the tensile sample fractured at 77 K. For the Fe-19Mn alloy, the fracture surface mainly consists of quasi-cleavage fracture, indicating a deterioration of ductility. The fractured surface of the Fe-22Mn and Fe-19Mn-2Al alloy is a mixture of quasi-cleavage and ductile fractures, while the fractured surface of the Fe-22Mn-2Al alloy only shows many ductile dimples.

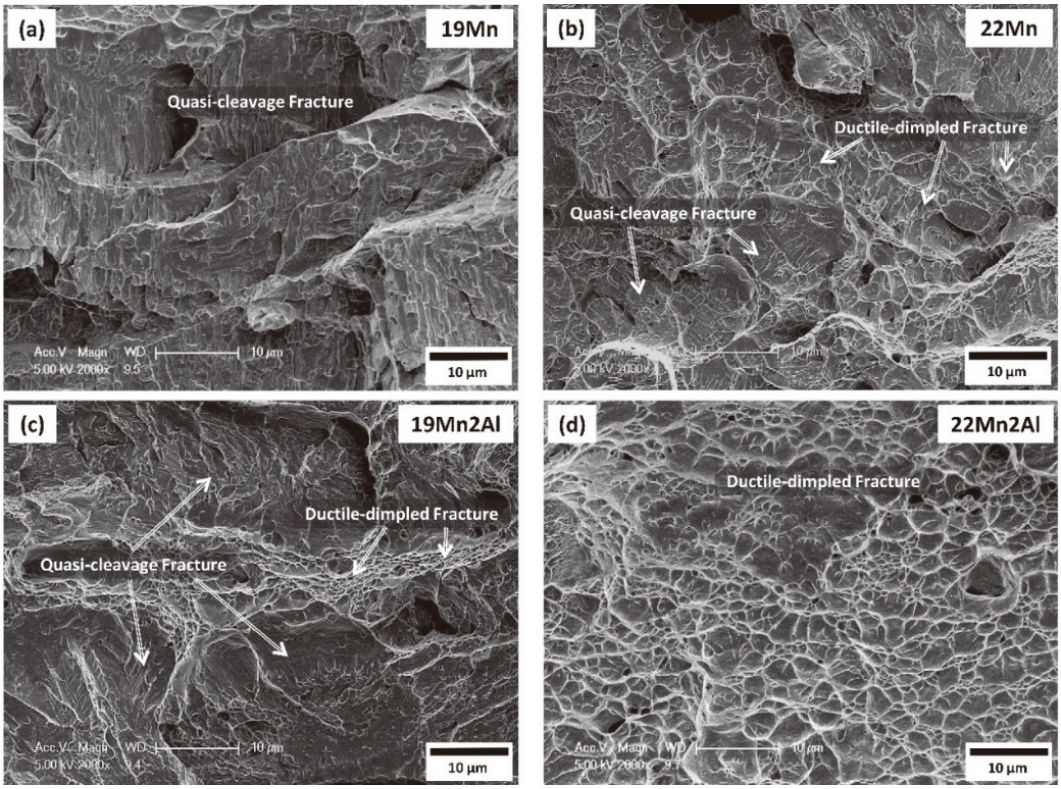

Fig. 2-4 SEM fractography of the (a) Fe-19 Mn, (b) Fe-19Mn-2Al, (c) Fe-19Mn-2Al, and (d) Fe-22Mn-2Al alloy fractured at 77 K, after Ref. [45].

Similar enhancement at both elongation and strength with temperature decreasing to the cryogenic range was also observed in some other FCC alloys, such as 304L stainless steel [49], Fe-(0.4, 1.0)C-18 Mn steel [46], aluminium alloys [51,52], medium entropy alloys [47,53], and high entropy alloys [48,54].

The mechanical improvement in these cases can be ascribed to the ability of FCC phases to trigger two intriguing strengthening mechanisms: TWinning Induced plasticity (TWIP) and Transformation Induced Plasticity (TRIP) effect [55–59]. These two effects usually come with high work hardening rates, large uniform elongation, and superior tensile strength. For the TWIP effect, high density of intersecting twin boundaries can be produced, serving as both strain carriers and dislocation motion barriers [60,61]. For the TRIP effect, the parent FCC-γ matrix can be transformed into two types of martensite with HCP or BCT (body-centred tetragonal, α′) lattice structure [62–64]. The newborn martensite serves as hard phases locally and can effectively impede further plastic deformation. Plastic strain can thus be passed to other soft and untransformed FCC phases, providing larger and more homogeneous plastic deformation [65,66].

These two effects are based on the reaction/motion of partial dislocations and stacking faults arrangement. Huge research interest was aroused in these two deformation mechanisms, and it is very promising to achieve premier strength-ductility combinations of alloys at cryogenic temperatures via activating multiple deformation mechanisms, including dislocation strengthening, TWIP, and TRIP.

2.3.1 Twinning Induced Plasticity Effect

As indicated in Ref. [67], five independent shear systems are required to activate general deformation for polycrystalline. For many crystalline structures with a limited number of slip systems, such as HCP, twinning not only serves as an important alternative deformation mechanism for shearing, but also provides dense barriers to dislocation motions, providing sites for dislocation pile-up, fracture nucleation, and cross slip. For alloys with high-symmetry lattices, e.g., BCC and FCC, the pronounced

twinning was also observed [60,68–76]. This can be ascribed to the higher flow stress for slip (Peierls stress for perfect dislocation motion) than the flow stress for twinning (stress for partial dislocation motion). For example, deformation twins have been observed in deforming single-crystal copper at 77 K and below on the principle slip plane of $(11\bar{1})$ along the shear direction [77]. After decades of investigation, the TWIP effect is now emerging as a very promising method in providing some heavily alloyed austenitic alloys (e.g., Mn or Ni) with continuous, effective, and high strain hardening effect during straining, thus guaranteeing high strength and large elongation simultaneously [78].

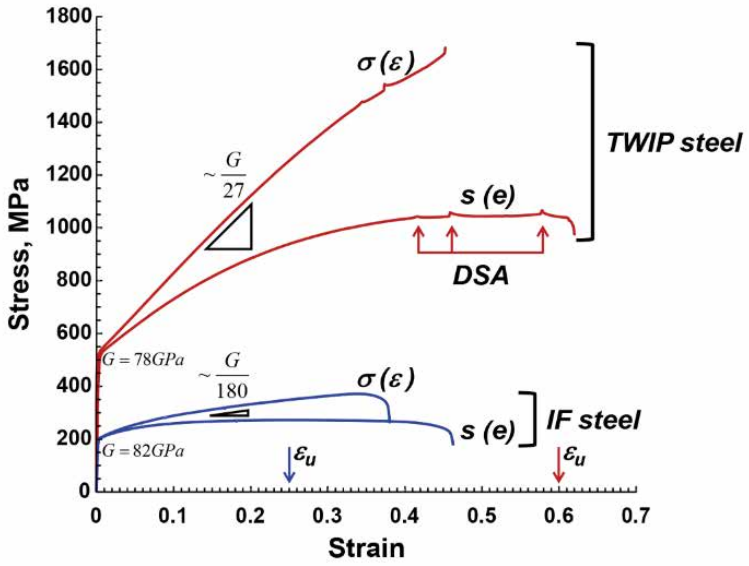

Fig. 2-5 The tensile engineering and true stress-strain curves of a TWIP steel (Fe-18%Mn-0.6%C-1.5%Al) with full-FCC structure and a Ti-stabilized IF steel, after Ref. [79].

One typical group of alloys strengthened by strain-induced twinning is noted as TWIP steels with high Mn contents, showing a wide range of excellent mechanical combinations [80]. Grässel et al. [81,82] and Frommeyer et al. [83] investigated the mechanical performance and microstructural responses of a series of Fe-Mn-Si-Al steels with Mn content higher than 25 wt.%, Al content larger than 3 wt.% and Si content in the range of 2-3 wt.%. A series of desirable strength-ductility combinations

were obtained, enhancing the product of UTS and total elongation of the alloy to an ultra-high level of 50,000 MPa·%. The UTS of the Fe-25Mn-3Al-3Si TWIP steel exceeded 1200 MPa, with a very large total elongation of ~0.6 [83]. The microstructural observation revealed that very active deformation twinning occurred during deforming these TWIP steels. To show the advantages of TWIP steels compared with other traditional steels, the stress-strain curves of one TWIP steel (Fe-18%Mn-0.6%C-1.5%Al) and one Ti-stabilized interstitial-free (IF) steel were both plotted in Fig. 2-5 [79]. Compared with the IF steel, which is considered as the most formable steel in industries, the TWIP steel shows much higher YS (~500 MPa), strain hardening effect, UTS (~1 GPa), and larger uniform elongation. At high strain levels, the TWIP steel also shows some serrations, which is related to the dynamic strain ageing effect [79].

The mechanical performance comparison among a wide range of traditional alloys and TWIP-assisted alloys (e.g., austenitic stainless steels and high Mn steels) is shown in Fig. 2-6. The excellent strength-ductility combinations are rarely observed in conventional steels, the TWIP-assisted steels show significant improvement in both strength and ductility, indicating the huge potential of the TWIP effect in overcoming the strength-ductility trade-off.

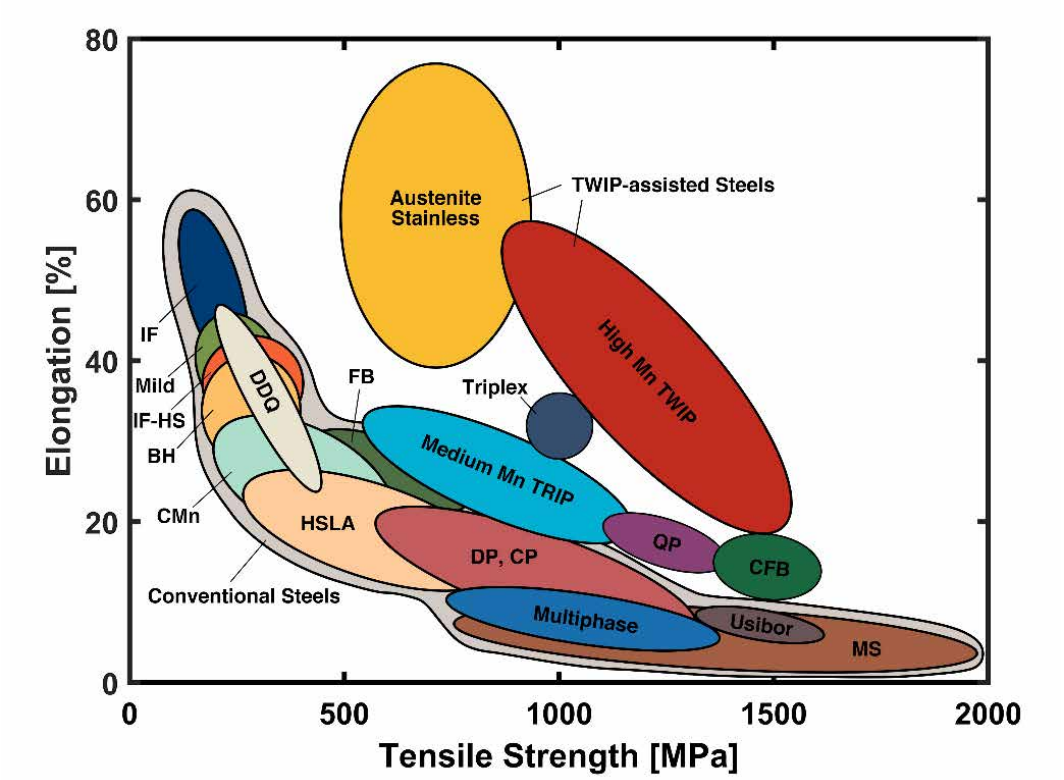

Fig. 2-6 Mechanical performance (tensile strength and elongation) comparison among conventional alloys with TWIP-assisted alloys (austenitic stainless steels and high Mn TWIP steel) at room temperature. Conventional steels include interstitial-free (IF) steel, mild steel, deep drawing quality (DDQ) steel, interstitial-free high strength (IF-HS) steel, bake-hardening (BH) steel, carbon manganese (CMn) steel, high-strength low alloy (HSLA), ferritic-bainitic (FB) steels, dual-phase (DP), transformation-induced plasticity (TRIP), complex phase (CP) steel, martensite steels (MS), medium Mn transformation-induced plasticity (TRIP) steel, quenching and partitioning (QP) steels, Carbide-free bainitic (CFB) steels, usibor steel, and triplex steels, after Ref. [84].

The improvement in both strength and ductility originates from the extensive occurrence of strain-induced twinning behaviour in FCC-structured grains. Unlike some conventional alloys (e.g., aluminium alloys) [85,86], whose strain hardening behaviour is mainly decided by intense dislocation motions (multiplication, interaction, and annihilation), the TWIP effect enables the continuous formation of additional planar dislocation barriers.

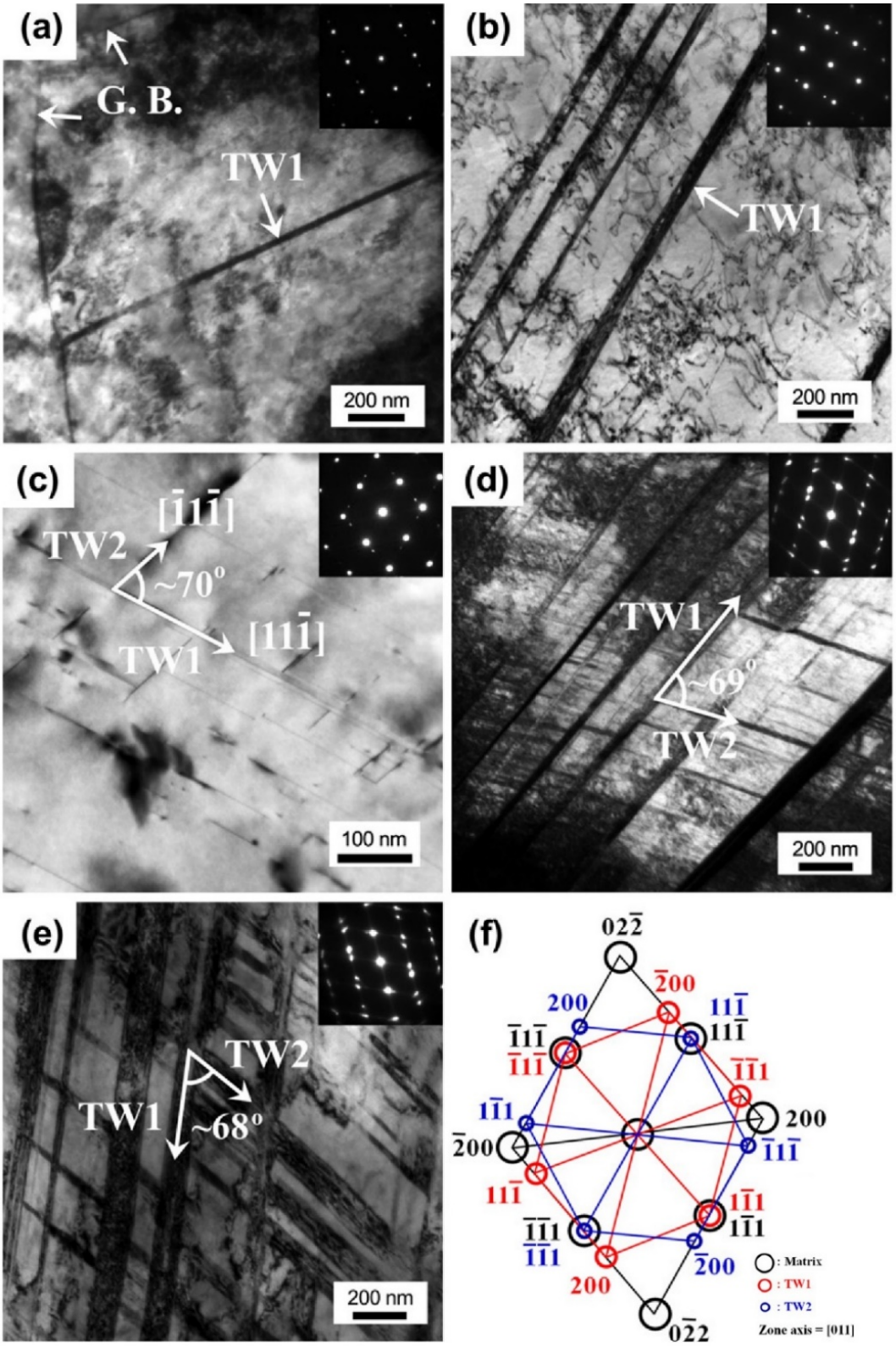

Fig. 2-7 Typical bright-field TEM images and corresponding selected area electron diffraction (SAED) pattern of the Fe-18Mn-0.6C alloy deformed to different strain levels: (a) 0.02; (b and c) 0.05; (d) 0.1 and (e) 0.25. (f) Index of the SAED pattens of the strain-induced twins at true strain of 0.05, after Ref. [87].

Fig. 2-7 shows the typical bright-field TEM images of the Fe-18Mn-0.6C TWIP steel deformed to different strains of 0.02, 0.05, 0.1, and 0.25 [87]. The strain-induced twins are identified as bands with two parallel boundaries and are produced by changing the stacking sequence of atoms in close-packed (111) grain planes during deformation. Primary and secondary twins were identified with the corresponding selected area electron diffraction (SAED) patterns. It is generally accepted that the strain-induced twinning can increase strain hardening rate by continuously creating twin boundaries, which serve as effective barriers for dislocation gliding during plastic deformation (so-called “dynamic strain hardening effect” or “dynamic Hall-Petch effect”) [70,88–92].

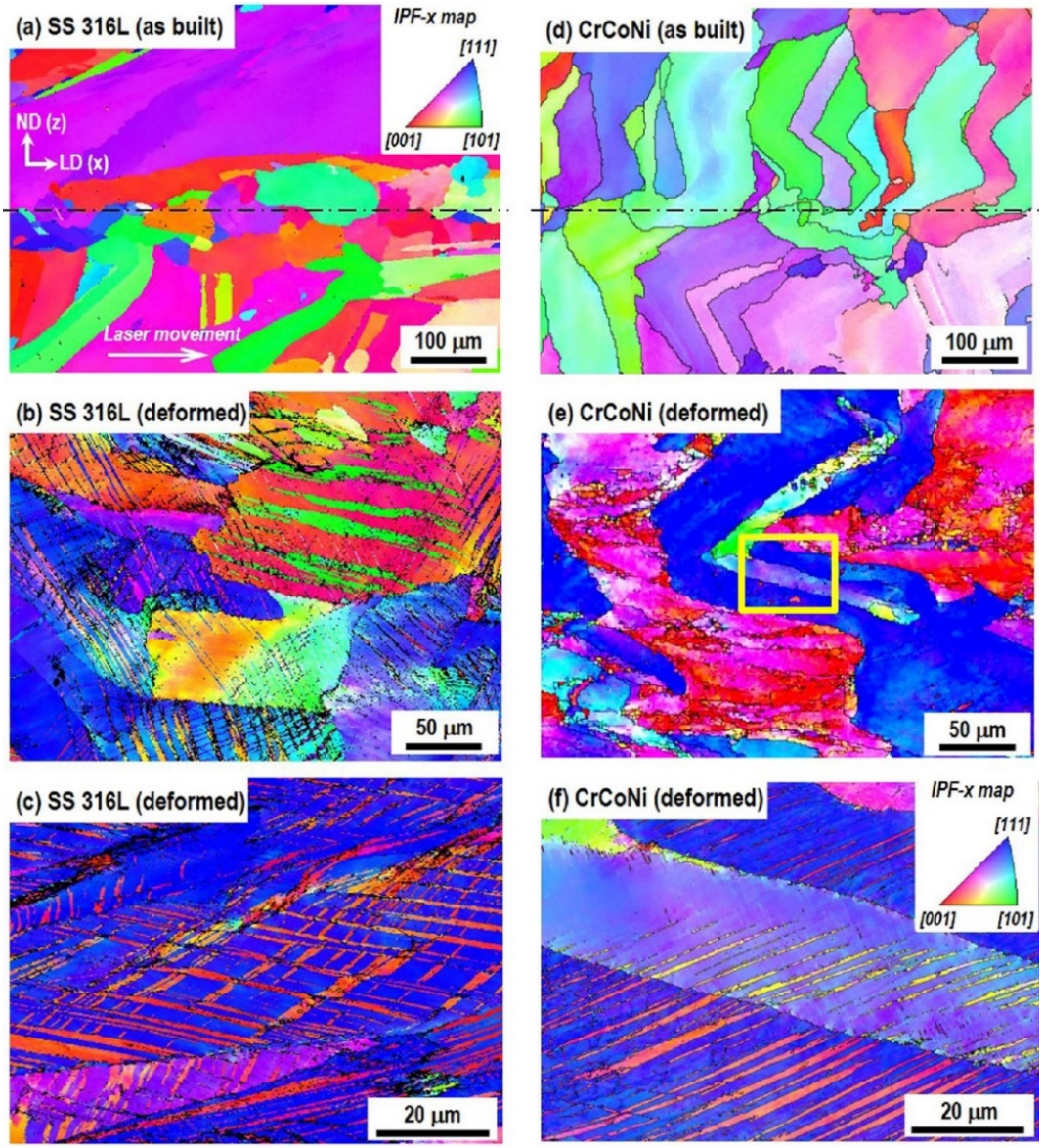

Fig. 2-8 Typical inverse pole (IPF) maps (at the loading direction-normal direction plane) of two FCC alloys, additive manufactured 316 stainless steel and medium entropy alloy CrCoNi before and after deformation: (a) as built; (b and c) deformed of 316L stainless steel; (d) as built and (e and f) deformed CrCoNi alloy, after Ref. [93].

Except high Mn steels (such as Fe-18Mn-0.6C TWIP steel [87], Fe-22Mn-0.6C [94], Fe-17.74Mn-2.96Si-0.44Al-0.57C), similar prominent strengthening effects resulted from twinning were also reported in deforming other austenitic alloys: stainless steels (e.g., 316L stainless steel [95,96]), medium entropy alloys (e.g., CrCoNi [93], CoCrMo [97], and $Ni_{57.6}Cr_{19.2}Fe_{19.2}Nb_4$ [98]), and high entropy alloys [99–102]. For example, before deformation, the as-built CrCoNi alloy shows the columnar grain structure without twins (Fig. 2-8a and d). After deformation, abundant twins were produced and

the twinning preferably from in grains with [111] parallel to the loading direction. At a strain of 0.58 (Fig. 2-8f), 85% of misorientation angles rotated about 60° about the [111] direction, which is defined as ∑3 type twin boundaries [103,104].

As shown in Fig. 2-9 [71], the occurrence of crossing twin boundaries during deformation can interact with dense dislocations and serve as barriers to impede the dislocation motion via reducing the mean free path of dislocations, whose inverse is the sum of the inverse distances between different impenetrable burdens (e.g., grain boundaries). The number of original large grains was then reduced after the progressive segmentation effect from twinning boundaries.

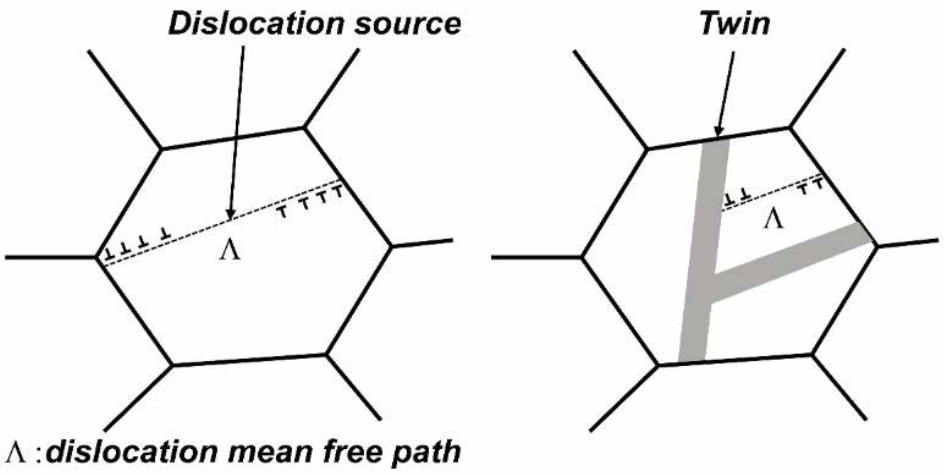

Fig. 2-9 Schematic illustrations of the dynamic Hall-Petch effect. The occurrence of strain-induced twin boundaries can effectively reduce the mean free path of multiple dislocations, after Ref. [71].

2.3.2 Transformation Induced Plasticity Effect

Serving as an important deformation mechanism, the transformation-induced plasticity (TRIP) effect can not only significantly raise the work hardening rate but also postpone the fracture at the necking region. As compared in Fig. 2-6, the TRIP-assisted steels (such as QP steel, medium Mn TRIP steels, complex phase steels, austenitic stainless steels) show great advantages in achieving excellent combinations of strength-ductility.

Therefore, the TRIP effect is now widely used as a promising method in enhancing the strength-ductility balance of multiple alloys, such as dual-/multi- phase steels [105–107], austenitic stainless steels [49,108], bainite steels [109], etc.

It is well-known that the high strain hardening effects can originate from the transformation from original FCC phases to martensites with HCP or BCT structures. Cios et al. [110] investigated the mechanical responses of an AISI 304 stainless steel with different extents of TRIP effect by controlling the deformation temperature. The true stress-strain and strain hardening rate (SHR) curves of the AISI 304 stainless steel can be seen in Fig. 2-10a and b, respectively. As indicated in Fig. 2-10c, the low deformation temperature can effectively promote the transition from FCC to BCT phases (the highest SHR increases with temperature decreasing), producing higher strain hardening effects at lower deformation temperatures (Fig. 2-10b).

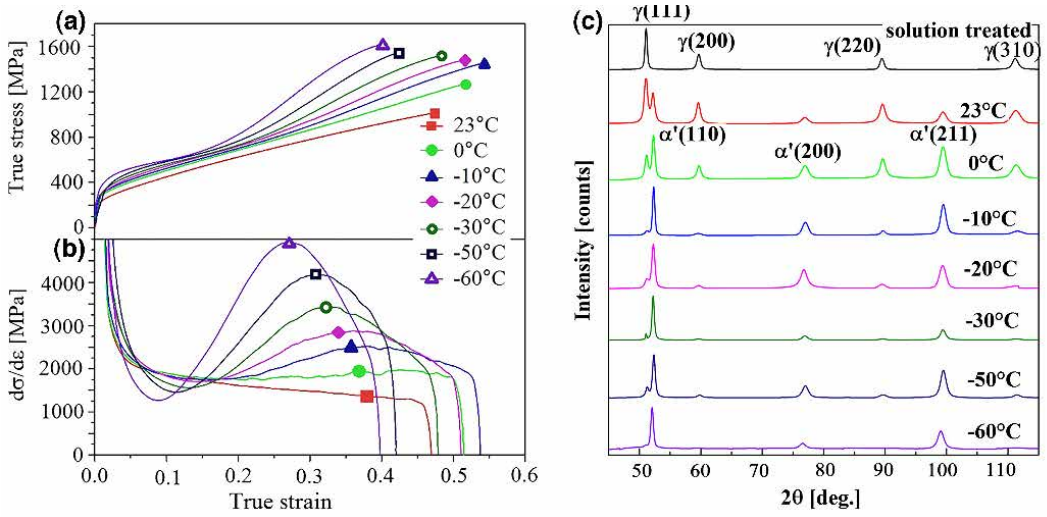

Fig. 2-10 The relationship between mechanical performance, temperature, and TRIP effect of the AISI 304 stainless steel: (a) True stress-strain curves, (b) strain hardening rate (SHR) curves, and (c) X-ray diffraction patterns of the solution heat-treated and the samples deformed at different temperatures, after Ref. [110].

On the other hand, the TRIP effect can also improve ductility by postponing the fracture at high strain levels. The schematic illustration of the TRIP effect during deforming is

shown in Fig. 2-11. As the strain increased to high levels, the phase transformation can strengthen the alloys at the necking stage hence postponing the final fracture [64].

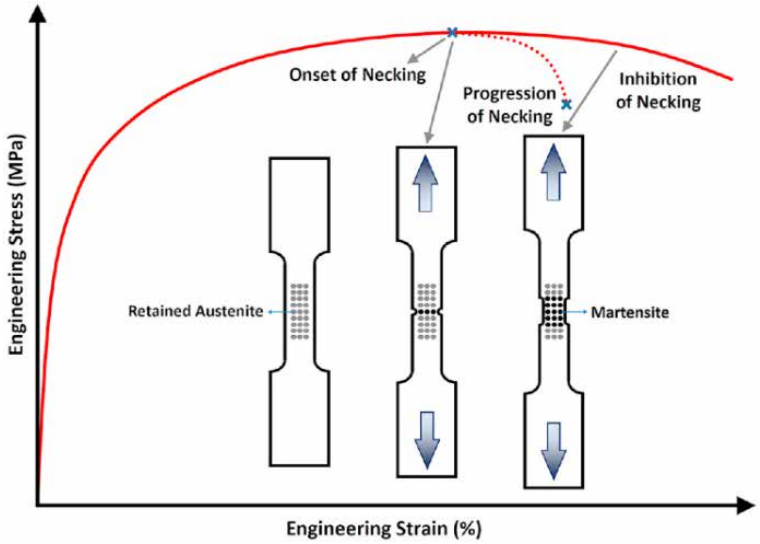

Fig. 2-11 The schematic illustration of postponing necking of TRIP effect during tensile straining, after Ref. [64].

Due to its excellent ability to strengthen the alloys and improve ductility, the TRIP effect has attracted huge research interest. This process can occur in a direct manner (from FCC to BCT, where the intersection of shear bands and twins are favourable nucleation sites) or in an indirect manner (from FCC to HCP to BCT, where the HCP phases serve as medium phase) [111].

The strain-induced martensite phase transformation was also captured by TEM observation (Fig. 2-12). Fig. 2-12a, b, and c show the typical bright-field TEM image, dark-field TEM image, and SAED pattern of 10%-strained Fe-0.4C-15Mn steel. In Fig. 2-12a and b, high density of twins can be observed, and some newborn hexagonal close-packed (HCP) ε-martensite phases were identified by the SAED pattern shown in the left corner of Fig. 2-12b. Meanwhile, the dark-field image in Fig. 2-12c also shows some α'-martensite with BCT lattice structure were produced. The parent austenite phase keeps the Shoji-Nishiyama (S-N) relationship with the ε-martensite phases as the

$(111)_\gamma \parallel (0001)_\varepsilon$ and $[111]_\gamma \parallel (2\bar{1}\bar{1}0)_\varepsilon$. The orientation relationship between the austenite phase and α'-martensite maintains the Kurdjumov-Sachs (K-S) relationship: $(111)_\gamma \parallel (110)_{\alpha'}$ and $[011]_\gamma \parallel (\bar{1}111)_{\alpha'}$ [69]. This phase-related deformation mechanism can be activated at high stress/strain levels and related to stress transfer and dynamic strain partitioning among different phases. The high strain hardening rate is related to the newborn two hard martensite phases (HCP and BCT) as well as the mechanical incompatibility such as the strain partitioning among different phases with various flow stresses [105–107].

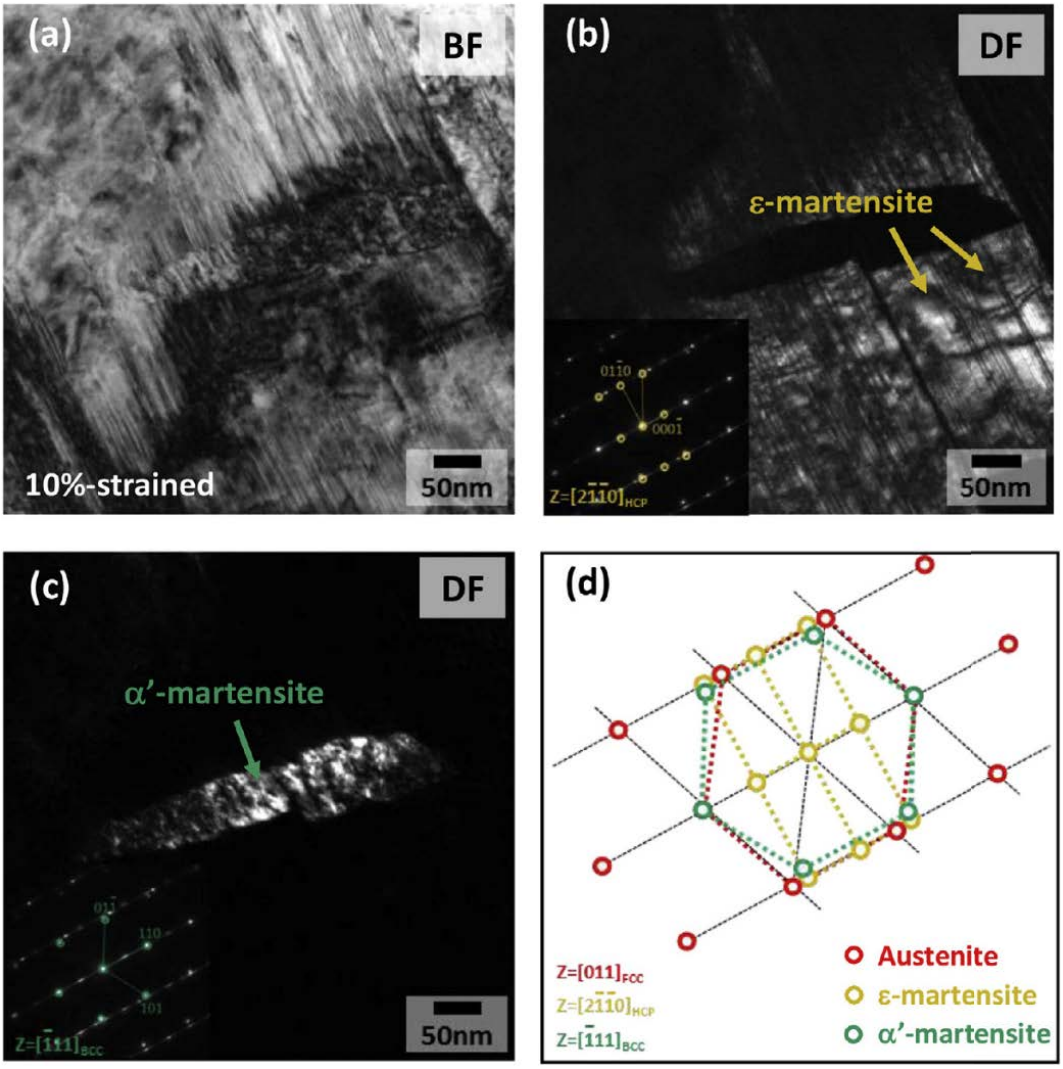

Fig. 2-12 TEM characterization of phase transformation of a TWIP steel (Fe-0.4C-15Mn) at strain level of 10%: (a) typical bright-field image; (b and c) dark-field images; (d) SAED (selected area electron diffraction) pattens, after Ref. [69].

The significant strengthening effects of the new born BCT phases were widely observed, its working mechanisms, however, were still under debate. Spencer et al. [65] observed the high dislocation density in the deformed austenite phases while the dislocation density in BCT phases is low. The strain induced BCT phases then act as a reinforcing phase in two ways. First, the BCT phases were considered as an elastic reinforcing phase and withstanding higher stress than the austenite [65,66]. On the other hand, the BCT phases can deform with FCC phases while they contribute more to the total flow stress due to their higher temperature sensitivity to the decrease of temperature [112,113]. Shintani et al. [114] introduced a strengthening model based on the dislocation type and density of the FCC and BCT phases. The strength of the steel mainly depends on the BCT phases due to their inherent high dislocation density at low strain levels (< ~0.3). At high strain levels (> ~0.3), the dislocation density of FCC phases reached saturation and the FCC phases are as strong as BCT phases. Galindo-Nava et al. [115] theoretically predicted the mechanical performance of several austenitic steels based on the dislocation strengthening theory. The BCT phases have much higher strength than the FCC phases and the strain is withstood by the HCP laths and FCC phases, while Maréchal et al. [66] argued that the strain hardening effects measured by experiments are too high to be explained only by dislocation forest hardening effects, indicating that a part of the BCT phases can contribute to the total flow stress by deforming elastically.

2.4 Formation Mechanisms of SFs, Twins, HCP, and BCT

Fig. 2-13 illustrates the pathways of forming stacking faults, twins, and HCP structure with the motion of Shockley partial dislocation ($b = 1/6\langle 11\bar{2} \rangle$) in FCC materials [116].

The close-packed FCC structure is generated by sequentially stacking close-packed planes (111) along the close-packed direction $\langle 110 \rangle$. The stacking sequence of FCC and HCP structure can be described as ABCABC and ABABAB, respectively [67], where A, B, and C refer to {111} planes. The stacking faults refer to the interruption of the perfect stacking sequence of crystals. Two types of stacking faults can be classified: intrinsic and extrinsic. The gliding of the Shockley partial on one {111} plane creates one intrinsic stacking fault, moving all {111} planes above by a vector of $1/6\langle 11\bar{2} \rangle$. The stacking sequence was then transferred into ABCABC|BCABC, which means the intrinsic stacking fault can also be treated as removing one {111} plane. The gliding of a second Shockley partial on the adjacent plane creates an extrinsic stacking fault, with a stacking sequence of ABCABC|B|ABCABC, which is equivalent to inserting one {111} plane to the original matrix [117].

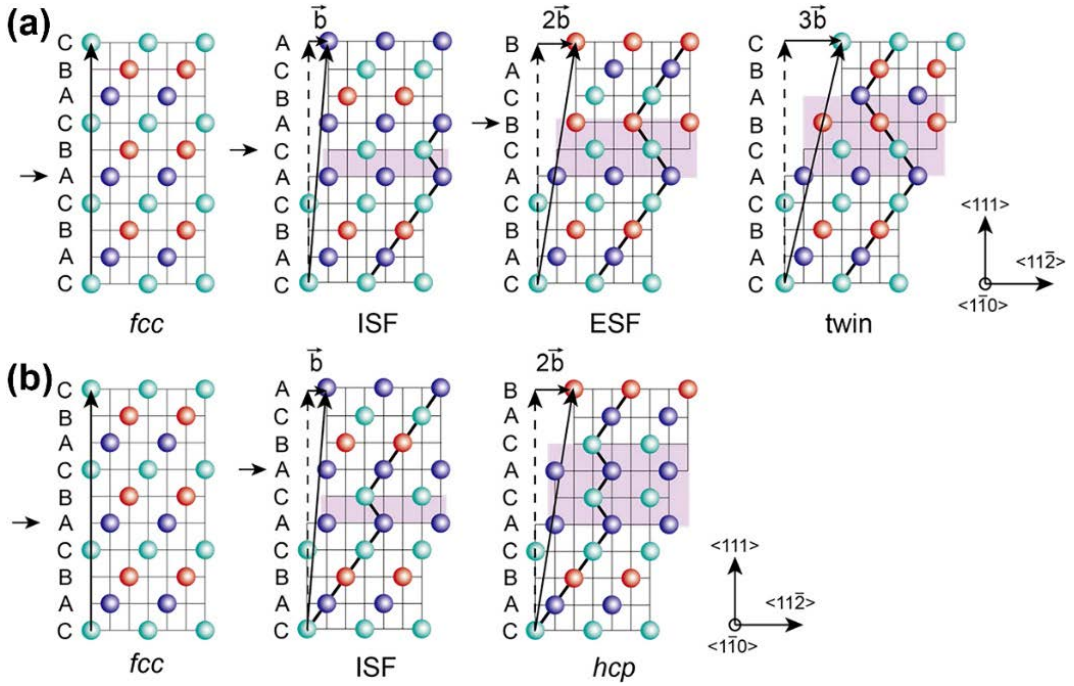

Fig. 2-13 The atomic configuration of the FCC structure, intrinsic stacking fault, two-layer extrinsic stacking fault, three-layer twin, and HCP phase. Formation procedure of (a) three-layer twin and (b) HCP phase, after Ref. [116].

According to the classical dislocation theory, stacking faults, twins, and HCP structure is created by the dissociation of perfect dislocations and the following reactions/motion among perfect/partial dislocations [67]. As shown in Fig. 2-14, when a perfect dislocation ($\boldsymbol{b}_I=\frac{a}{2}[\bar{1}01]$) dissociates into two glissile Shockley partial dislocations of the type of $1/6\langle 112\rangle$ on $\{111\}$ planes, an enclosed stacking fault in between (green zone) can be created [67]:

$$\frac{a}{2}[\bar{1}01]\rightarrow\frac{a}{6}[\bar{1}\,\bar{1}2]+\frac{a}{6}[\bar{2}11] \qquad \text{Eq. 2-1}$$

, in which a is the lattice parameter.

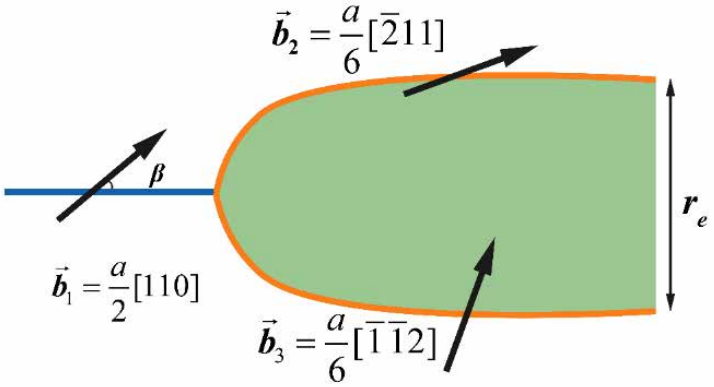

Fig. 2-14 The schematic illustration of the dissociation of a perfect dislocation into two Shockley partials, after Ref. [67].

For the twin formation, it can be simply described as the glide of the third partials on consecutive (111) planes, forming a three-layer twin and two twin boundaries, with a stacking sequence of CABCACBABC (Fig. 2-13). A variety of mechanisms were proposed to rationalize their nucleation and growth. Initially, the nucleation of twins was considered to be homogeneous at regions with high-stress concentrations [67]. Its heterogeneity, however, was envisaged by the following researches [118]. A pole mechanism was proposed by Venables [119] to describe the twinning system and its orientation dependence. On the slip plane of $\{111\}$, a perfect dislocation can split into

two mobile Shockley partials ($a/6\langle 11\bar{2}\rangle$ and $a/6\langle 2\bar{1}\,\bar{1}\rangle$). On the conjugate $(11\bar{1})$ plane, a perfect dislocation ($a/2\langle 011\rangle$) can split into two glissile Shockley partials ($a/6\langle 11\bar{2}\rangle$ and $a/6\langle \bar{1}21\rangle$). Meanwhile, the $a/2\langle 011\rangle$ dislocation can be dissociated into one sessile Frank partial dislocation (pole dislocation) and one Shockley partial dislocation under external stresses [119] or impeded by strong barriers (e.g., Lomer-Cottrell locks) [120] with:

$$a/2\langle 110\rangle \rightarrow a/3\langle 111\rangle + a/6\langle \bar{2}11\rangle \qquad \text{Eq. 2-2}$$

In this mode, the glissile Shockley partial dislocation can glide away from the sessile Frank partial dislocation, leaving a stacking fault in between. Generally, this procedure is not energetically favourable as the total energy remains constant before and after the reaction. The high density of dislocations can be gathered near the head of the dislocation pile-up sites, bringing two Shockley partial dislocations close and making the reaction in Eq. 2-2 possible. When considering many barriers and this procedure occurs on successive (111) planes, a twin can thus be formed. Besides, the moving Shockley partials can also react with perfect dislocations and form sessile Frank dislocations on the interface plane with:

$$a/2\langle \bar{1}0\,\bar{1}\rangle + a/6\langle 121\rangle = a/3\langle \bar{1}1\,\bar{1}\rangle \qquad \text{Eq. 2-3}$$

, where the Frank dislocations were considered as ‘secondary polar sources’. Furthermore, Fujita and Mori [121] proposed the stair-rod cross-slip mechanism, where a Shockley partial dislocation in the $\langle 111\rangle$ plane can be split into a new Shockley partial dislocation (on the conjugate plane) and a stair-rod sessile dislocation anchoring at the intersection of primary glide plane and conjugate plane:

$$a/6\langle \bar{2}11\rangle_{(111)} \rightarrow a/6\langle \bar{1}\,\bar{1}0\rangle_{sessile} + a/6\langle \bar{1}21\rangle_{(\bar{1}\bar{1}1)} \qquad \text{Eq. 2-4}$$

Mahajuan and Chin [118] proposed another model based on the presence of an extrinsic stacking fault. Two co-planar perfect dislocations ($a/2\langle 110\rangle$) can dissociate into three Shockley partial dislocations on three consecutive {111} planes, creating an extrinsic stacking fault serving as a three-layer twin embryo:

$$a/2\langle 011\rangle_{(1\bar{1}1)} + a/2\langle \bar{1}0\bar{1}\rangle_{(1\bar{1}1)} \rightarrow 3\times a/6\langle \bar{1}12\rangle_{(1\bar{1}1)} \qquad \text{Eq. 2-5}$$

In the model proposed by Miura, Takamura, and Narita [122], the extended dislocation can pile up and interact with a Lomer dislocation at the Lomer-Cottrell barrier in the primary plane, producing one $a/3\langle 111\rangle$-type Frank sessile partial dislocation, two $a/6\langle 112\rangle$-type partial dislocations, and two-layer stacking faults acting as a twin nucleus.

Meanwhile, the active motion of Shockley partial dislocations can also lead to martensite phase transformation, where the original FCC matrix can be transferred into HCP/BCT martensite. The HCP phase with a stacking sequence of CABCACACAB can be formed based on an intrinsic stacking fault and continue creating stacking faults on every other {111} plane (Fig. 2-13).

Fujita and Ueda [123] envisaged the important role of the stair-rod cross-slip mechanism in FCC-HCP phase transformation, where the leading Shockley partial dislocation can be split into a stair-rod and a Shockley partial on the intersecting {111} plane with the aid of high stress. The HCP structure can then be formed if this process occurs repeatedly on every second parallel {111} plane. According to Ref. [124], two coplanar $a/6\langle 110\rangle$-type perfect dislocation can interact and form a six-layer HCP phase with:

$$a/2\langle 1\bar{1}0\rangle_{(111)} + a/2\langle 10\bar{1}\rangle_{(111)} \rightarrow 3\times a/6\langle 2\bar{1}\bar{1}\rangle_{(111)} \qquad \text{Eq. 2-6}$$

The higher thermodynamic stability of the HCP structure can rearrange the atoms in the cores of the Shockley partials, forming a four-layer HCP structure. The transformation from the four-layer HCP structure into a six-layer HCP structure may arise if: (i) the $a/2\langle 10\bar{1}\rangle$ and $a/2\langle 1\bar{1}0\rangle$ partials glide at adjacent {111} plane, (ii) $a/2\langle 10\bar{1}\rangle$ partial dislocation cross slip, or (iii) $a/6\langle \bar{1}2\bar{1}\rangle$ and $a/6\langle 2\bar{1}\bar{1}\rangle$ Shockley partial loops can nucleate on the appropriate planes. The nucleation sites initially locate at different strain levels within a localized high-stress zone and then grow into each other, forming macroscopic HCP phases.

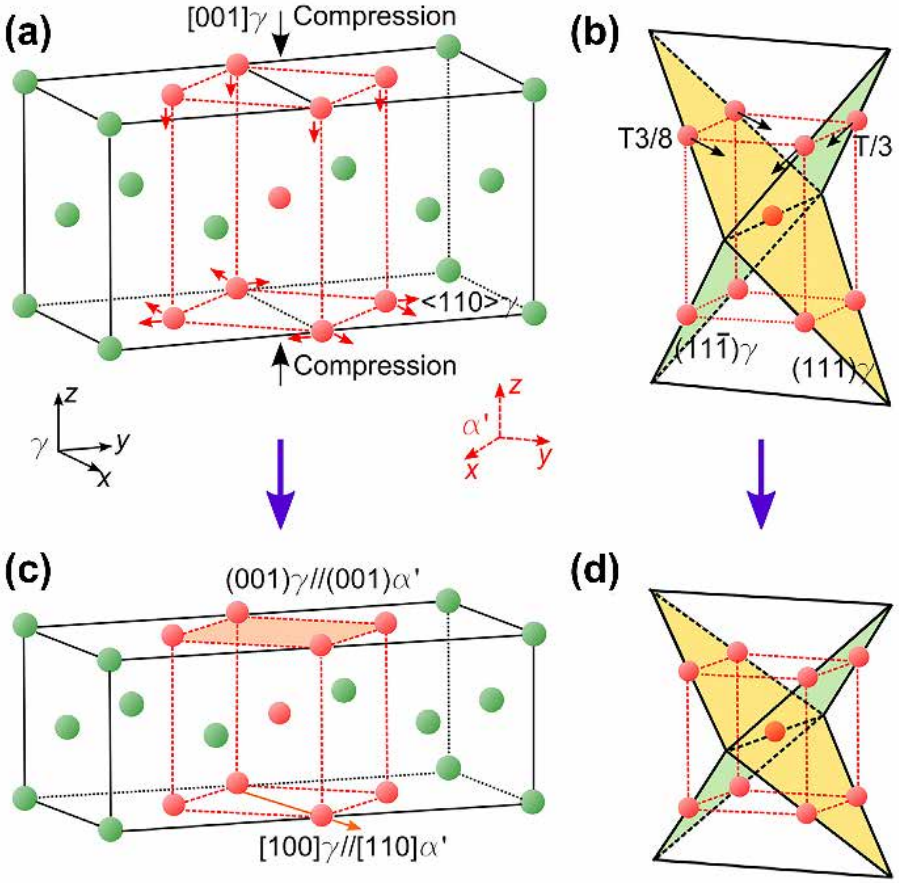

Fig. 2-15 Schematic illustrations of the Bogers and Burgers model for the transition from FCC to BCT martensite: (a) The Bain correspondence between FCC (green) and BCT (red) lattice structure. The (a) FCC lattice can be converted to (c) BCT lattice via a compression of 20% along [001]-FCC and an expansion of 12% along <110>-FCC. Alternatively, this procedure can also be the result of gliding of partial dislocation $a/18[1\bar{2}\bar{1}]$ on every $(11\bar{1})$ -γ plane and $a/16[\bar{1}2\bar{1}]$ on every (111)-γ. T represents a Shockley partial dislocation with Burgers of $a/6[11\bar{2}]$, after Ref. [125].

In the Bogers-Burgers model [126] shown in Fig. 2-15, the FCC to BCT transition can be accomplished by compression of 20% along [001]-γ and expansion of 12% along $\langle 110 \rangle_\gamma$. The orientation relationship is $(001)_\gamma \,/\!/\, (001)_{\alpha'}$ and $[100]_\gamma \,/\!/\, [110]_{\alpha'}$. This transition can thus be accomplished by the gliding of partial dislocations: on every $(11\bar{1})$-γ plane and $a/16[\bar{1}2\bar{1}]$ on every (111)-γ plane (Fig. 2-15). Olson and Cohen [127] emphasized the role of plastic deformation, indicating that the BCT phases could nucleate at the intersection of two HCP laths (slip bands) or by the intersection of HCP lath with a twin or grain boundary (Fig. 2-16).

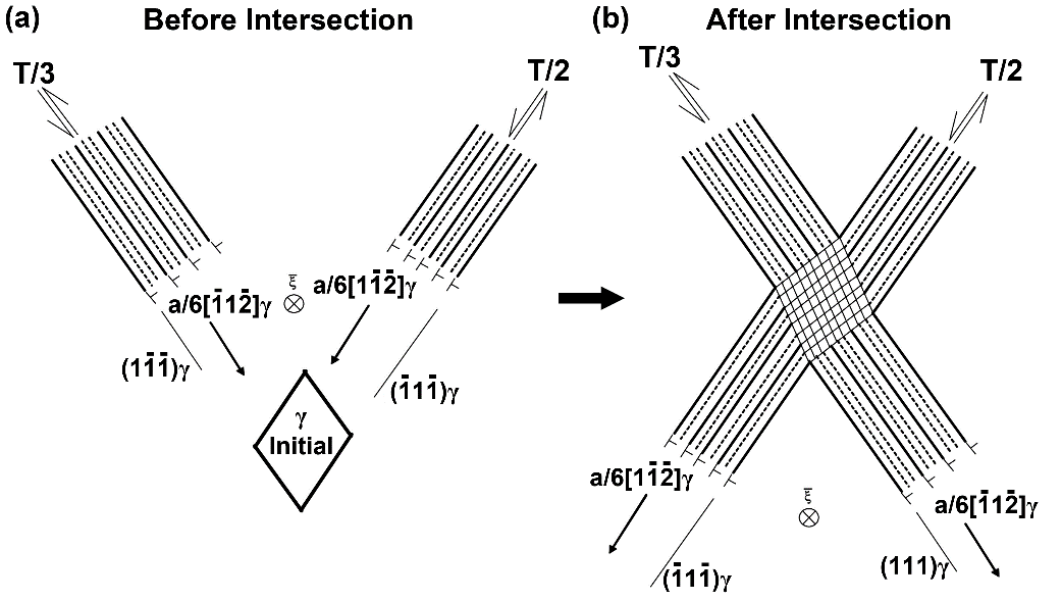

Fig. 2-16 The model for strain-induced BCT phases at the intersection of two localized slip bands: (a) before and (b) after the intersection, after Refs. [128].

The phase transformation can be accomplished by two shears named as *T*/3 and *T*/2, where *T* represents FCC twinning shears with Burgers vector of $a/6[11\bar{2}]$. The first shear, *T*/3, can be achieved by an array of $a/6[112]$ in every third {111}-FCC plane. The second shear component, *T*/2, can be described as $a/12[112]$ in the FCC matrix and $a/8[110]$ in the BCC matrix. Likewise, the *T*/2 shear component can be

accomplished by an array of $a/6[112]$ partial dislocations but at every second {111}-FCC plane. The two arrays of $a/6[112]$ partial dislocations can result in a perfect BCC structure in the doubly-faulted intersection. This transition mechanism was experimentally verified with HRTEM in characterizing deformed high Mn steel [128] and AISI 304 austenitic stainless steel (Fig. 2-17) [129].

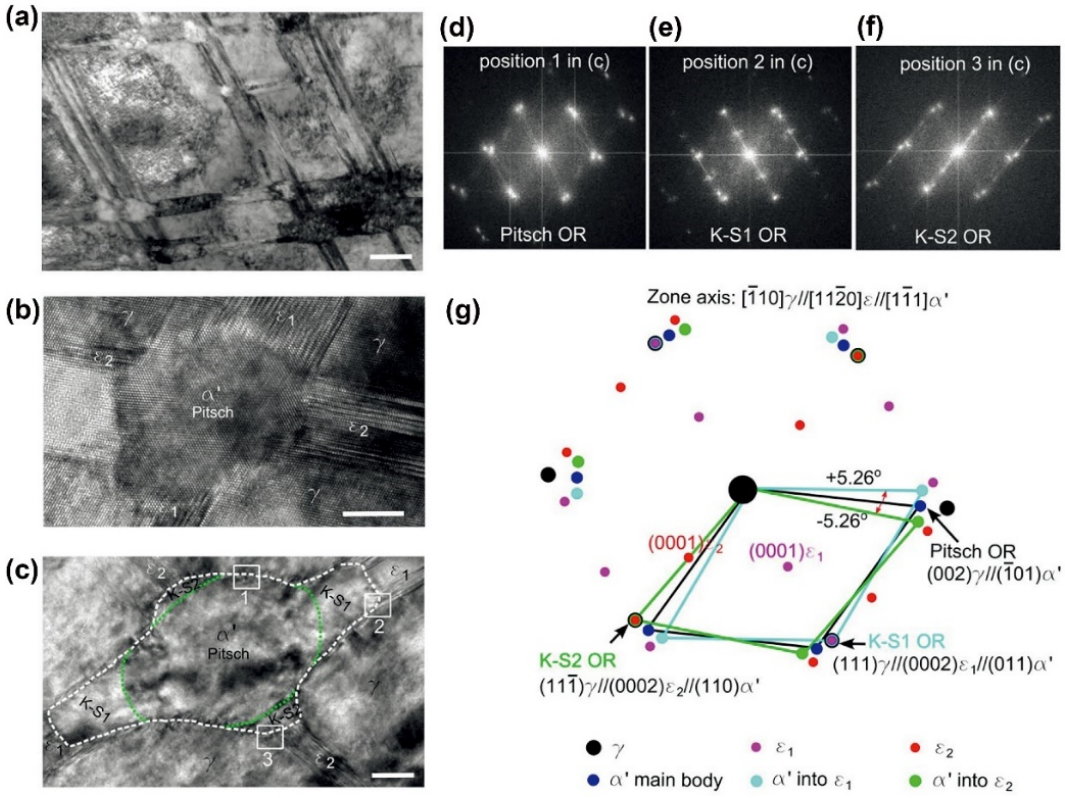

Fig. 2-17 TEM characterization of the formation of BCT phases via intersecting two HCP laths at a deformed 304 stainless steel: (a) bright-field TEM image showing the high density of BCT phases formed at the intersection of HCP laths; (b-f) TEM images and their corresponding live fast Fourier Transformation (FFT) spot patterns taken along the zone axis of $[\bar{1}10]\gamma \,//\, [11\bar{2}0]\gamma \,//\, [1\,\bar{1}1]\gamma$. (g) schematically illustration of the diffraction spots taken from the interfacial transition regions among γ, ε, and α′. The scale bar in (a), (b), and (c) is 200 nm. Note: Pitsch OR indicates the $(00\bar{2})_{\gamma} \,//\, (\bar{1}01)_{\alpha'}$ orientation relationship, after Ref. [129].

Strain-induced α′ were found at the intersection zones of two slip bands showing the well- known Kurdjumov-Sachs (K-S) orientation relationships between γ and α′ phases and Bogers-Burgers relationship between ε and α′ phases, indicating the close-packed planes and close-packed directions are parallel in these three phases [129]:

$$\{111\}\gamma \,/\!/\, \{110\}\alpha' \,/\!/\, \{0001\}\varepsilon$$
$$\langle 110\rangle\gamma \,/\!/\, \langle 111\rangle\alpha' \,/\!/\, \langle 2\bar{1}\bar{1}0\rangle\varepsilon \qquad \text{Eq. 2-7}$$

Meanwhile, Pitsch orientation relationship ($(002)_\gamma \,/\!/\, (\bar{1}01)_{\alpha'}$) was also observed in the new born α′ phases with respect to γ matrix (Fig. 2-17a) [129]. The α′ phases can grow along with the two ε laths and change the original Pitsch into two K-S orientation relationships ($(111)_\gamma \,/\!/\, (0002)_{\varepsilon_1} \,/\!/\, (011)_{\alpha'}$ and $(11\bar{1})_\gamma \,/\!/\, (0002)_{\varepsilon_2} \,/\!/\, (110)_{\alpha'}$).

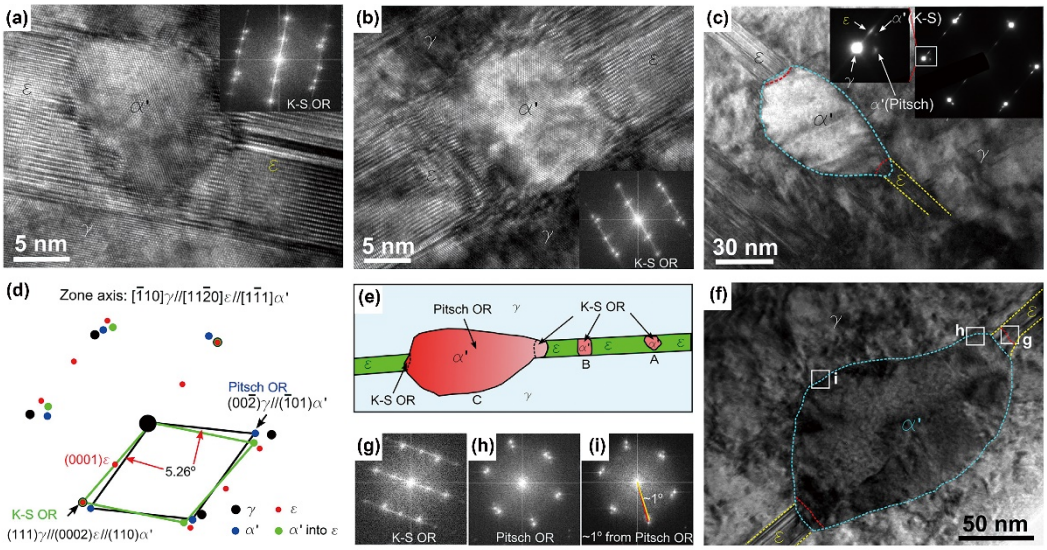

Fig. 2-18 The formation of α′ phase inside the single ε laths. (a-c) The morphologies and the corresponding SAED patterns of the γ matrix, ε laths, and newborn α′ inclusions inside a single ε lath. (d) Schematical illustration of the diffractions spots from the three phases and their orientation relationships. (e) Schematically illustration of the formation of α′ and its orientation relationship with ε phase and γ phase. (g-i) the corresponding FFT patterns from locations marked in (f), supporting the orientation relationship shown in (e), after Ref. [125].

Meanwhile, the new born BCT phases can nucleate independently in cases where the formation of HCP phases is suppressed, such as grains orientated along the tensile direction and HCP phases are not thermodynamically stable [127]. Yang et al. [125], observed the inclusions formed inside a single ε laths ~10 nm in length and ~15 nm in width. As shown in Fig. 2-18, the new born α′ phases can nucleate at single ε laths without intersecting slip bands/ε laths. As shown in Fig. 2-18c, it can then grow into the parent γ matrix and exhibit wider width (~70 nm) than the ε laths. The FFT and

SAED patterns (projected along $[\bar{1}10]_\gamma \,/\!/\, [11\bar{2}0]_\varepsilon \,/\!/\, [1\,\bar{1}1]_{\alpha'}$) in Fig. 2-18a-c identified the coexistence of the two orientation relationships: Pitsch ($(00\bar{2})_\gamma \,/\!/\, (\bar{1}01)_{\alpha'}$) and K-S ($(111)_\gamma \,/\!/\, (0002)_\varepsilon \,/\!/\, (110)_{\alpha'}$). The K-S orientation relationship was maintained in the initial nucleation α′ phases before following coarsening, indicating the original close-packed $(111)_\gamma$ plane smoothly transited to $(0002)_\varepsilon$ and the $(110)_{\alpha'}$ plane without rotation during nucleation. When the α′ starts to grow, the orientation of α′ phases will occur and the Pritch orientation relationship was maintained at the main body region while the interface connecting the ε laths was switched to the K-S orientation.

2.5 Role of Stacking Fault Energy

An ideal intrinsic stacking fault is created by infinitely separating two partial dislocations or removing one layer of close-packed {111} plane from the perfect FCC matrix. The equilibrium state between the two partial dislocations can be maintained under the restorative force created by the stacking fault energy (SFE) and the repulsive elastic force of the two partial dislocations [78]. After considering interactions between their edge ($\vec{F}_e$) and screw ($\vec{F}_s$) components, the forces between the two parallel partial dislocations (***b₂*** and ***b₃*** in Fig. 2-14) can be expressed by [67]:

$$\vec{F}_e = \frac{Gb_{2e}b_{3e}}{2\pi(1-\nu)r_e} \qquad \text{Eq. 2-8}$$

$$\vec{F}_s = -\frac{Gb_{2s}b_{3s}}{2\pi r_e} \qquad \text{Eq. 2-9}$$

, in which G is the shear modulus. Combining Eq. 2-8 and Eq. 2-9 yields:

$$\vec{F} = -\frac{G(\vec{b}_{2s}\cdot\vec{b}_{3s})}{2\pi r_e} + \frac{G(\vec{b}_{2e}\cdot\vec{b}_{3e})}{2\pi(1-\nu)r_e} \approx \frac{G(\vec{b}_2\cdot\vec{b}_3)}{2\pi r_e} = \frac{Gb_p^2}{4\pi r_e} \qquad \text{Eq. 2-10}$$

, where $b_p = a/\sqrt{6}$. As the expansion of the stacking fault region was impeded by the SFE, the force acting on a unit length of the dislocations equals $\vec{F}$. Therefore, the SFE of the alloy can be measured in terms of the separation distance (r_e) at equilibrium state [67]:

$$r_e \approx \frac{Gb_p^2}{4\pi SFE} \quad \text{Eq. 2-11}$$

According to Sections 2.3.1 and 2.3.2, the activating of TWIP and TRIP effects are strongly dependent on the formation and subsequent activities of partial dislocations. Since SFE measures the difficulty of creating stacking faults, SFE can serve as a critical parameter for interpreting the plastic deformation behaviours and governing multiple strengthening mechanisms. The relationship between SFE and the dominant deformation mechanism is well accepted in various FCC alloys [68,130–134]. When SFE is higher than 45 mJm^{-2}, dislocation motions take a majority role in withstanding strain as the dissociation of perfect dislocations is impeded due to the high SFE [135]. Meanwhile, if the Gibbs free energy of the martensite phase transformation ($\Delta G^{FCC \rightarrow HCP}$) is positive and the SFE of the alloy decreases to be within the range of 18~45 mJm^{-2}, the occurrence of twinning (TWIP effect) becomes more favourable [135–137]. If the SFE is further decreased to be lower than ~18 mJm^{-2} and $\Delta G^{FCC \rightarrow HCP}$ decreased to negative, dense activating of partial dislocation can create dense HCP laths and promote the transition from FCC to BCT phase (TRIP effect).

The SFE, however, can be determined by a variety of factors including chemical composition, grain size, deformation temperature, texture, and strain rate [135,138–140]. Zambrano et al. [141] investigated the influence of deformation temperature, grain size, and chemical composition on the SFE of the Fe-Mn-Al-C-Si steels. They

indicated that the SFE can be reduced by decreasing deformation temperature, increasing austenite grain size, and adding low-SFE elements, which favours the activation of TWIP and TRIP effects. These results were also consistent with that obtained in other alloys such as TWIP steels [135,142,143] and high entropy alloys [144].

2.6 SFE Determination

Considering the important role of SFE, the determination of the SFE of the alloys can be critical in building a more comprehensive understanding of the mechanical performance and multiple strengthening effects and thus developing new advanced alloys with improved mechanical properties. To predict/calculate the SFE, several methods were developed: thermodynamic/first principal prediction [145–149], TEM observation [150,151], X-ray/neutron diffraction [152,153].

2.6.1 Theoretical Prediction

TWIP and TRIP effects can be interpreted in terms of energy change as additional energy is required to motivate the dislocation dissociation due to the self-energy of dislocation [132,147]. For example, this energy can be provided by the assistance of local stress concentration and the Gibbs free energy between the two phases: FCC and HCP ($\Delta G^{\gamma\to\varepsilon}$). A thermodynamic modelling approach to predict SFE was therefore proposed by Olson and Cohen [136]. The detailed calculation procedure can be found in Fig. 2-19. When a stacking fault is considered as a thin layer of HCP lath separating the perfect FCC matrix, the SFE can be expressed with $\Delta G^{\gamma\to\varepsilon}$ and the interfacial energy between γ and ε phases ($\sigma^{\gamma/\varepsilon}$) [154]:

$$SFE = 2\rho\Delta G^{\gamma\to\varepsilon} + 2\sigma^{\gamma/\varepsilon} \quad \text{Eq. 2-12}$$

, in which $\sigma^{\gamma/\varepsilon}$ is the interfacial energy per unit of the two boundaries, ρ is the molar surface density (the density of atoms in a closely packed plane in a mole per unit area), which can be calculated with:

$$\rho = \frac{4}{\sqrt{3}}\frac{1}{a_0^2 N} \quad \text{Eq. 2-13}$$

, in which N is the Avogadro's number, a_0 is the lattice parameter. In Eq. 2-12, the $\Delta G^{\gamma\to\varepsilon}$ is the sum of $\Delta G_{\rho}^{\gamma\to\varepsilon}$ (the change of Gibbs free energy of each element during phase transformation), $\Omega_{\varphi\phi}^{\gamma\to\varepsilon}$ (the first-order interactions between two different element φ and ϕ), and $\Delta G_{mg}^{\gamma\to\varepsilon}$ (magnetic contribution to the Gibbs free energy) and $\Delta G_{seg(\text{int})}^{\gamma\to\varepsilon}$ (the contribution from interstitial atoms such as carbon and nitrogen) [155]:

$$\Delta G^{\gamma\to\varepsilon} = \sum_i \chi_i \Delta G_i^{\gamma\to\varepsilon} + \sum_{ij} \chi_i \chi_j \Omega_{ij}^{\gamma\to\varepsilon} + \Delta G_{mg}^{\gamma\to\varepsilon} + \Delta G_{seg(\text{int})}^{\gamma\to\varepsilon} \quad \text{Eq. 2-14}$$

, where χ_i is the molar fraction of each constituent element. The first item on the right side can be expressed with:

$$\Delta G_{\varphi}^{\gamma\to\varepsilon} = G_{\varphi}^{\varepsilon} - G_{\varphi}^{\gamma} \quad \text{Eq. 2-15}$$

, in which $G_{\varphi}^{\varepsilon}$ and G_{φ}^{γ} represents the molar Gibbs free energy of the pure elements in different phases, HCP and FCC. The second term in Eq. 2-14 is the sum of the excess free energy and can be calculated based on a subregular modelling approximation:

$$\Omega_{\phi\varphi}^{\gamma\to\varepsilon} = \left({}^0L^{\varepsilon} - {}^0L^{\gamma}\right) + \left({}^1L^{\varepsilon} - {}^1L^{\gamma}\right)\left(\chi_{\varphi} - \chi_{\phi}\right) \quad \text{Eq. 2-16}$$

, where ${}^0L^{\varphi}$ is a linear function of temperature while ${}^1L^{\varphi}$ is a constant [156,157]. The magnetic contribution to Gibbs free energy can be calculated with:

$$G_{mg}^{\gamma\to\varepsilon} = RT\ln(\beta^{\Phi}+1) f^{\Phi}(\tau^{\Phi}) \quad \text{Eq. 2-17}$$

, in which R is the gas constant, T is the temperature, β^{Φ} is the magnetic moment of the phase divided by the Bohr magneton μ_B, and $f^{\Phi}(\tau^{\Phi})$ is a function of the scaled Néel temperature ($\tau^{\Phi} = T/T_{Néel}^{\Phi}$). The last item, Gibbs free energy change due to the interstitial atoms can be obtained by determining the change of configurational energies of the interstitial atoms surrounded by atoms in substitutional matrix positions during the martensite phase transformation [135]:

$$\Delta G_{N(\text{bulk})}^{\gamma\to\varepsilon} = E_N^{\varepsilon} - E_N^{\gamma} \qquad \text{Eq. 2-18}$$

, with E_N^{ε} and E_N^{γ} are the configurational energies of the interstitial atoms (carbon or nitrogen) in the HCP and FCC phase, respectively.

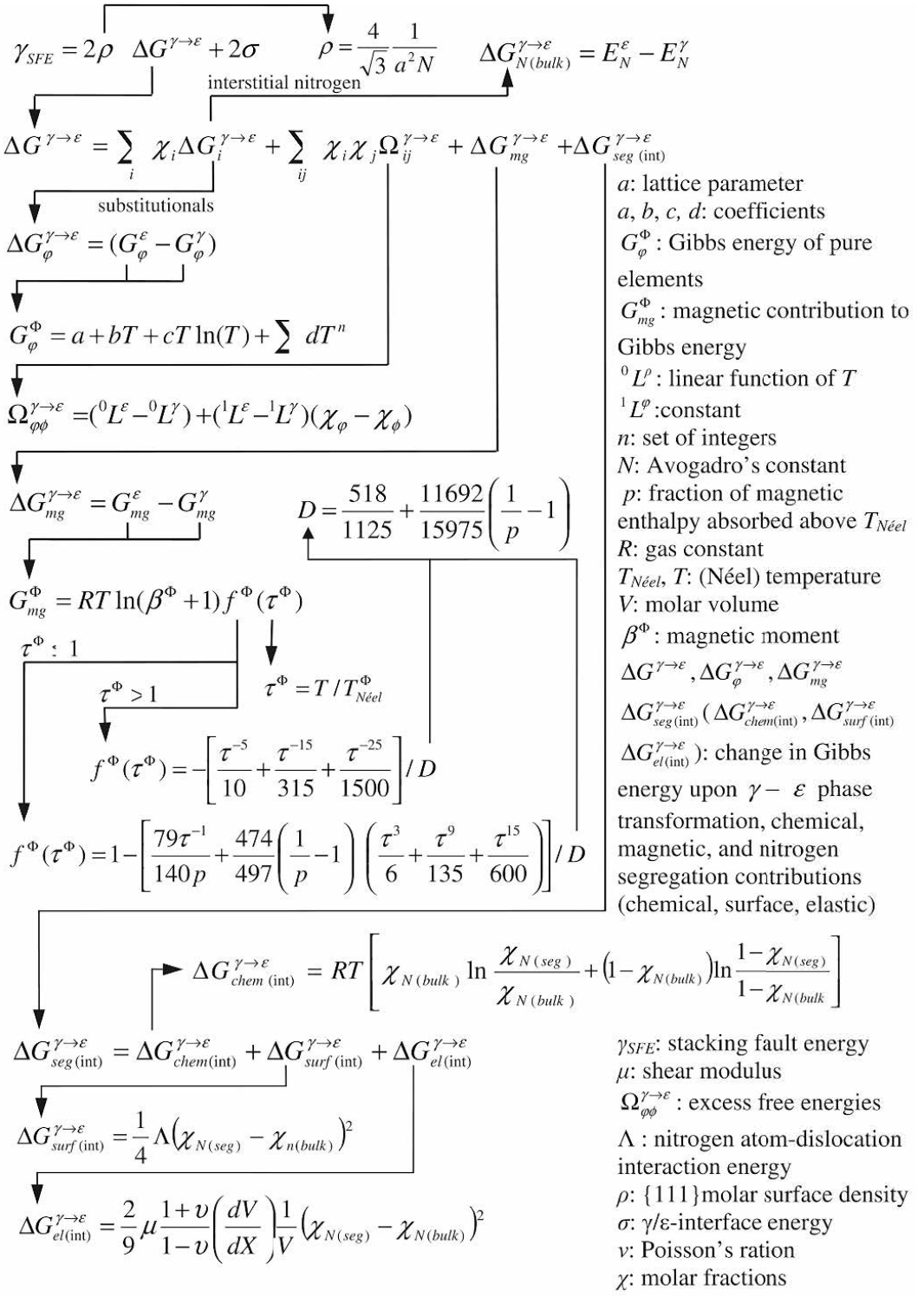

Fig. 2-19 Flow chart of calculating SFE with thermodynamics, after Ref. [155].

Recently, the first principal calculation is emerging as a promising method in the prediction of SFE. Many first-principle calculations are conducted within the frame of

the density functional theory with the VASP code [148] and the projector-augmented wave method [158]. Generally, the SFE calculation proceeds with building supercells:

$$\gamma_{sf} = \frac{E_{isf} - E_0}{A_t} \quad \text{Eq. 2-19}$$

, in which E_{isf} and E_0 are the total energy of the faulted and pristine supercell, A_t is the total area of the stacking fault at the close-packed plane [159]. The first-principle calculation achieved success in predicting the SFE of a variety of traditional alloys (e.g., Co alloys [159] and Ni alloys [149]) and some complex multi-component alloys, such as Mo-added CoCrNi [149] and CoCrMnNiFe [160]. Besides, other theoretical approaches to calculate SFE were also proposed and gained their importance in modelling/predicting the strengthening effects and mechanical performance of various alloys, such as molecular dynamics [161] and machine learning [162]. Molecular dynamics serves as an ideal approach to build a more fundamental understanding of materials properties and show good agreement with experimental results in determining SFE [163]. The machine learning also emerging as a powerful tool in SFE predicting by extracting information from multi-dimensional data and modelling various properties of the alloys [163].

The advantages and disadvantages of theoretical modelling methods in determining/predicting SFE are also obvious. The theoretical modelling methods are generally considered as they are the straightforward methods to calculate the SFE. They are more efficient, and the costs and time can be significantly reduced since they are not suffering from sample preparation and measurement techniques and are capable of providing accurate structural modelling results without experimental inputs when dealing with conventional alloys [163,164]. On the other hand, there are still many limits to the theoretical determination of SFE. For example, thermodynamical

simulations successfully determined SFE of many alloys, such as TWIP/TRIP steels and stainless steels [135,143,155,165], the accuracy of the results, however, are still in need of improvement. Geissler et al. [132] doubted the accuracy of measuring SFE with thermodynamics. For example, the interfacial energy is in the range of 5-27 mJm^{-2}, which is inconsistent with the physical meaning of an interface created by intrinsic stacking faults. On the other hand, the thermodynamical calculation is based on many empirical equations, most of which are suitable for a confined composition and the accuracy strongly depends on the quality of CALculation of PHAse Diagram (CALPHAD) database. The data used also includes extrapolations of different parameters at the low-temperature range, making the results unreliable. Furthermore, in most of the previous investigations based on thermodynamics simulation, the SFE determination, and Gibbs free energy functions are utilized in steels with only 2-3 elements. The simulation results for alloys with a wide composition range are still leaving unverified [135,165,166]. Limits also exist in other theoretical modellings. When dealing with complex multicomponent alloys, the calculation of chemical and magnetic energy contribution in the first principal calculation is challenging and time-consuming [132]. This can lead to the underestimation of the SFE and even negative SFE values were reported [160,167]. Therefore, to gain a better understanding of the relationship between micro-mechanical performance and modelling results, the experimental validation and determination of SFE are necessary and of great importance.

2.6.2 Experimental Measurement

The determination of SFE was mainly based on two methods: direct TEM observation of extended dislocation nodes and analysing X-ray/neutron diffraction profiles. For the

TEM method, the width of the dissociated dislocations can be measured in weak beam observation of the two separated partial dislocations. When the two partial dislocations are visible with weak beams, the vector from the incident to the exciting spot is parallel to the Burgers vector of the perfect dislocation. The SFE can thus be measured with the following equation [168]:

$$SFE = \frac{Gb_p^2}{8\pi w} \cdot \frac{2-\nu}{1-\nu}\left(1 - \frac{2\nu\cos 2\theta}{2-\nu}\right) \quad \text{Eq. 2-20}$$

, in which b_p is the magnitude of the Burgers vector of the Shockley partial dislocations, ν is the Poisson ratio of the alloy, w is the width of partial dislocation separation, and θ is the angle between the dislocation line and the Burgers vector of the perfect dislocation. With this method, Liu et al. [169] determined the SFE of three multi-component alloys, NiCoCr (18±4 mJm^{-2}), FeCONiCr (27±4 mJm^{-2}), and FeCoNiCrMn (26.5±4.5 mJm^{-2}). The weak beam dark-field images were shown in Fig. 2-20 [169]. Similar observation and calculation can also be found at many other alloys, e.g., high Mn TWIP steels [170].

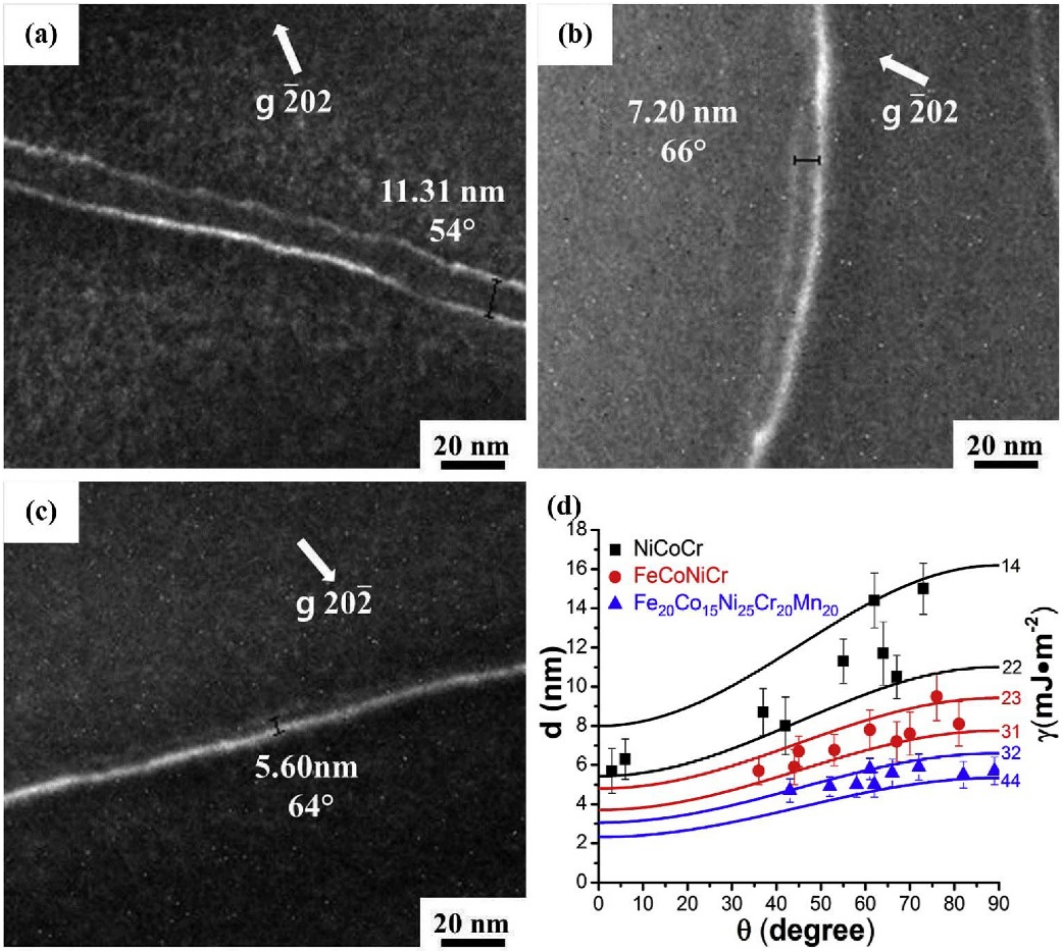

Fig. 2-20 The weak beam dark-field images of separated partial dislocations in (a) NiCoCr, (b) FeCoNiCr, (c) FeCoNiCrMn, and the separation distance of partial dislocations plotted as a function of the angle between dislocation and the perfect dislocation's Burgers vector, θ, after Ref. [169].

Another SFE measurement is realized by analysing diffraction peaks obtained in X-ray/neutron diffraction. The calculation was based on a model proposed by Reed and Schramm [171]:

$$SFE = \frac{6.6a_0}{\pi\sqrt{3}} \frac{\left\langle \varepsilon^2 \right\rangle_{111}}{SFP} \left(\frac{2C_{44}}{C_{11} - C_{12}} \right)^{-0.37} \left(\frac{C_{44} + C_{11} - C_{12}}{3} \right) \qquad \text{Eq. 2-21}$$

, where a_0 is the lattice parameter, $\left\langle \varepsilon^2 \right\rangle_{111}$ is the mean square strain, i.e., root-mean-square microstrain of the deformed FCC matrix at the close-packed {111} plane. SFP stands for the stacking fault probability and C_{11}, C_{12}, and C_{44} are the three basic elastic

constants for the FCC alloy. The critical parameters in Eq. 2-21, such as $\left\langle \varepsilon^2 \right\rangle_{111}$, elastic constants, and SFP, can be obtained by analysing X-ray/neutron diffraction peaks.

The experimental validation of the SFE is necessary for validating the simulation results and understanding the fundamentals of the relationship between microstructure evolution and mechanical performance. However, experimentally determining the SFE is time-consuming and complex, which also delays the process of discovering new materials.

First, the procedures of preparing the samples are very long and complex. For traditional methods of preparing samples, ingots with different elements need to be melted, casted into a mould, and cooled down before different heat-treatment and cold/hot working. For the microscopic characterization, mechanical cutting, grinding, and polishing are required before final preparation with twin-jet electropolishing, ion milling, or focused ion beam (FIB) cutting. Its accuracy depends on the statistical analysis of the separation distance at different positions of the dissociated dislocation [50,172]. Moreover, traditional TEM observations of dissociated dislocations are usually *ex situ* experiments, which means the samples were pre-deformed to create stacking faults and then prepared for observation. Preparing, handling, and transferring samples can exert different influences (stress, strain, temperature, etc.) on the sample. The initial dislocation morphology of the sample can be ruined and cause ambiguity, especially when measuring the SFE at cryogenic conditions, where the samples need to be warmed up to room temperature and then polished. To overcome this shortcoming, the *in situ* TEM characterization [173–175] was proposed, where the real-time microstructure of the sample can be captured under real-world conditions, such as during deforming at cryogenic conditions [175]. However, performing *in situ* TEM

observation is even more difficult and time-consuming. First, a specially designed sample holder and extra equipment are required to apply stress/temperature change to the sample and carry the sample simultaneously. Meanwhile, the sample preparation is still a challenge as well as placing the sample within the operating zone of the *in situ* holder.

Nevertheless, the *in situ* X-ray/neutron diffraction can also capture the real-time microstructural evolution at various temperature/stress/strain conditions and their sample preparation is much easier as they are non-destructive techniques and no extra preparation procedures are needed [93,176–178]. Meanwhile, compared to the nanosized observation area in TEM, the X-ray/neutron diffraction can collect the diffraction pattern averaged from a very large gauge volume in the level of cubic millimetres. The accuracy of the measurement can thus be effectively improved. In addition, the *in situ* X-ray diffraction has ultrafast data acquisition rates of the order of seconds or milliseconds, thus allowing capturing of some fast-transient or short-lived processes and continuous monitoring microstructure evolution under different operating conditions [179]. For example, collecting one diffraction pattern in I12 beamline of the Diamond Light Source (DLS, UK) consumes only less than 1s [180]. However, X-ray diffraction generally suits the fine-grained polycrystalline to guarantee the quality of diffraction data due to its very limited penetration ability, especially for alloys consisting of high atomic numbers where the penetration ability of X-ray drops rapidly in this regime. The *in situ* neutron diffraction shows much higher penetration ability and solution than synchrotron X-ray diffraction. A neutron can penetrate a few centimetres into the bulk material and create a good diffraction signal, thus it is very suitable for the measurement of the residual stress of alloys with high atomic numbers [181–184], while neutron diffraction data collection usually consumes a longer time

than X-ray diffraction. For example, it usually takes over 15 mins to collect a diffraction pattern with high quality at the beamline ENIGN-X at ISIS spallation neutron source, the Rutherford Appleton Laboratory, UK [185].

Even with many merits in data collecting and accuracy, there are still many limits in synchrotron X-ray/neutron diffraction. First, *in situ* X-ray diffraction is based on a large synchrotron which can produce high energy X-ray (53-150 keV at beamline I12 of the Diamond Light Source), while the neutron diffraction relies on the large neutron spallation sources, such as ISIS neutron and muon source in UK and Spallation Neutron Source in the US. The accessibility of these large facilities is very limited as there are only around 40 large synchrotron light sources and 23 neutron sources around the world. Meanwhile, the *in situ* observation with X-ray/neutron diffraction required several different types of equipment (tensile rig, cryogenic system, vacuum chamber, ion irradiation, etc.) built integrally to create different service conditions, such as low temperature and high strain levels, to capture the real-time microstructural features. Furthermore, the interpretation of diffraction peaks can also induce ambiguity since the diffraction data mainly relies on the single peak fitting with different methods, e.g., Pseudo-Voigt peak fitting.

In summary, the *in situ* neutron diffraction can reflect the real-time microstructure evolution during deforming at different conditions, e.g., temperature and strain rate, with the high gauge volume and thus accuracy. It is one of the most desirable and powerful tools in exploring the relationship among microstructure (such as SFE and dislocation density) evolution, strengthening mechanisms, and mechanical performance at the cryogenic range.

2.7 Promising Cryogenic Materials

The rapid advancement of cryogenic technology put forward ever-increasing demand and thus many challenges for the alloys that could resist low-temperature and various service conditions.

The first challenge is the ultra-low temperatures. Some emerging applications of cryogenic technology, such as energy storage, nuclear fusion, superconducting magnets for medical diagnosis, and Maglev, require the ultra-low working temperature at around 4K. The conventional low-temperature materials, such as aluminium alloys [5–8], low carbon steels containing 3.5% nickel or higher, titanium alloy, nickel alloys, 9%Ni steels, and Fe-Ni-based Invar alloys [8]), and highly alloyed steels, however, showed undesirable mechanical performance in the cryogenic zone. The designed working temperature for the present developed low-temperature alloys is generally higher than 77 K. Many aluminium alloys can only be used at temperatures higher than 231 K, except 7075 and 7178 alloy [5–8]. The ideal working temperature for low carbon steels (containing 3.5 wt.% nickel or higher) is in the range of 173 to 198 K. Some aluminium alloys (such as 2024-T4, 7039-T6, 5456-T6, and 5456-H343) and maraging steels with the addition of 20-25 wt.% nickel, cobalt, molybdenum, titanium, and niobium are generally designed for working temperature down to 77 K [5–8]. For conditions lower than 77 K, only a few highly alloyed austenitic stainless steels with 18-21 wt.% chromium and 9-14 wt.% nickel (such as 304 and 310 stainless steel) were developed [8].

The second challenge is the ever-increasing higher requisitions for the mechanical properties at cryogenic conditions. The mechanical performance for the traditional low-temperature alloys is not very desirable and the very limited alloy type cannot meet the

expanding applications. As shown in Fig. 2-21, conventional alloys generally cannot achieve high strength and large ductility simultaneously at low temperatures due to the lack of continuous strain hardening effects during plastic deformation. For example, titanium alloys generally show very high YS and UTS while their ductility was sacrificed: their elongation was usually lower than 20%. The aluminium alloys, however, showed even worse mechanical performance at 77 K with YS and UTS < 800 MPa and elongation < 20%. For the expensive nickel alloys, although the strength is high (YS < 1500 MPa and UTS < 1700 MPa), their ductility is only slightly improved compared to the titanium alloys and remains at a very low level (elongation < 30%).

Another challenge for low-temperature alloys is their high production cost. It is critical and of great significance in reducing the production cost of cryogenic alloys due to the soaring demand. The massive production for the present low-temperature alloys, however, is not economically viable. Many of the low-temperature alloys are relying on the high nickel concentration to maintain the stability of lattice structure and mechanical performance [8,186]. The addition of nickel is very expensive (13.81 £/kg) compared to other elements, such as copper (5.3 £/kg), manganese (1.5 £/kg) and aluminium (0.45 £/kg).

Recently, several types of alloys were developed with many intriguing merits (such as low-production cost, excellent strength-ductility balance) for cryogenic conditions, attracting huge research interest and showing promising solutions to this dilemma. The mechanical performance (YS, UTS, and elongation) of conventional low-temperature alloys (aluminium alloys, titanium alloy, and nickel alloys) at 77 K were compared with the promising alloys: (austenitic stainless steels, high Mn alloys, and multi-component alloys) in Fig. 2-21 [5–8,45,48,186–202]. These alloys exhibit high strength and large elongation simultaneously due to their potential in activating a variety of concurrent

strengthening mechanisms, i.e., dislocation motions, TWIP, and TRIP. As shown in Fig. 2-21, multi-component alloys, high-Mn steels, and austenitic steels show premier mechanical performance and great potential in achieving the combination of higher strength and larger elongation.

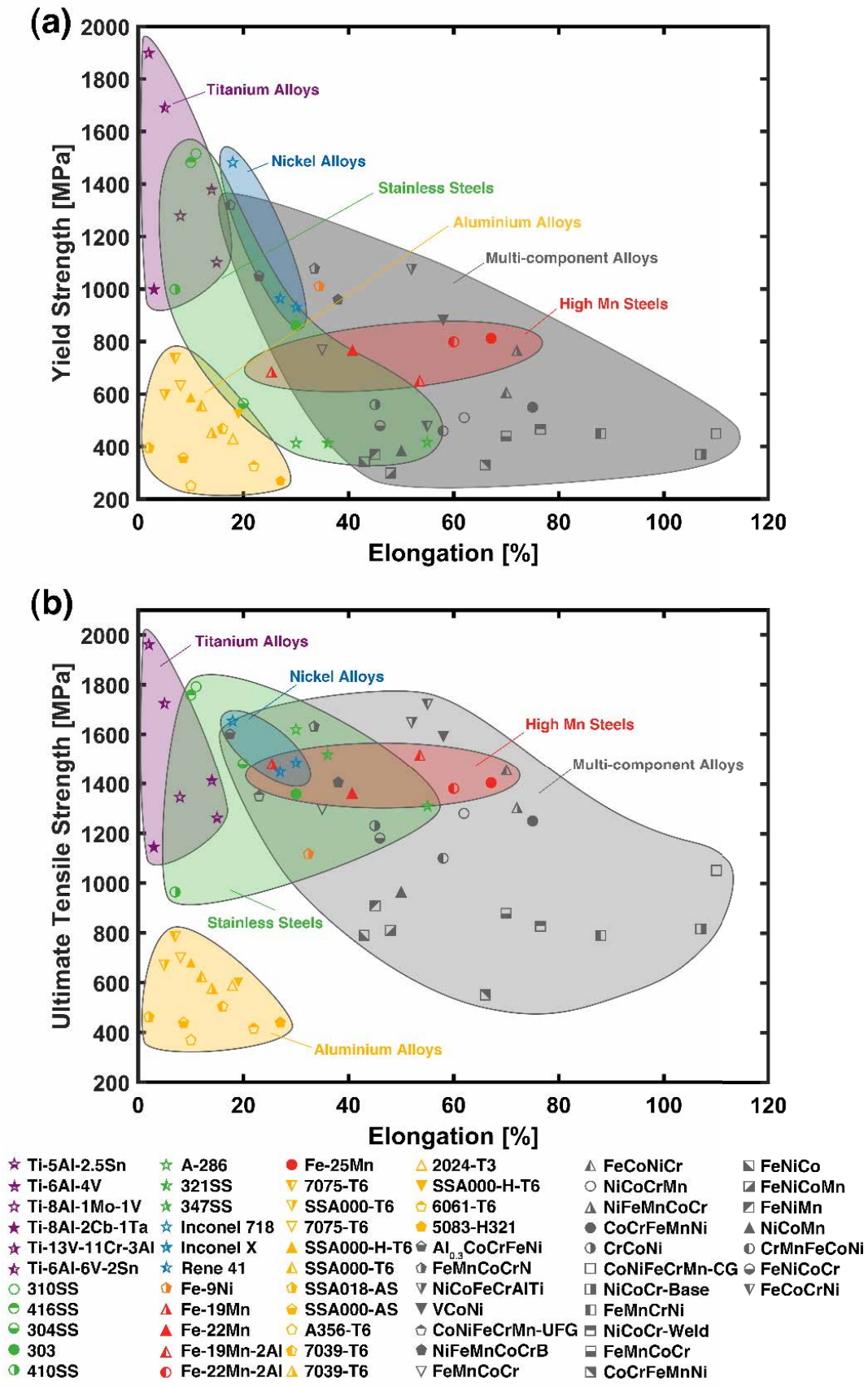

Fig. 2-21 The comparison of mechanical performance of various cryogenic alloys at 77 K: titanium alloys, aluminium alloys, nickel alloys, high Mn steels, stainless steels, multi-component alloys. (a) Yield strength plotted with elongation. (b) Ultimate tensile strength plotted with elongation [5–8,45,48,186–202].

2.7.1 High Mn Steels

The Fe-Mn steels were firstly discovered by Sir Robert Hadfield in 1888 [203] (also called Hadfield steel, containing 1.35% of C, 0.69% of Si, 12.76% of Mn in wt.%). The Hadfield steel showed high stiffness, surface wear resistance, and extended service life. It first achieved great success in tramline in 1892, after which its application expanded to a very wide range and has been playing an irreplaceable role in multiple industries such as mining, electrical power, construction, agricultural machinery, metallurgical industries, and many other high impact and wear environments [204].

This great potential and important role of Fe-Mn steels also boosted the related investigation [205–208]. Many new high-Mn steels were found with the ever-improving strength-ductility combination (as shown in Fig. 2-22) and great commercial value in various industries [203].

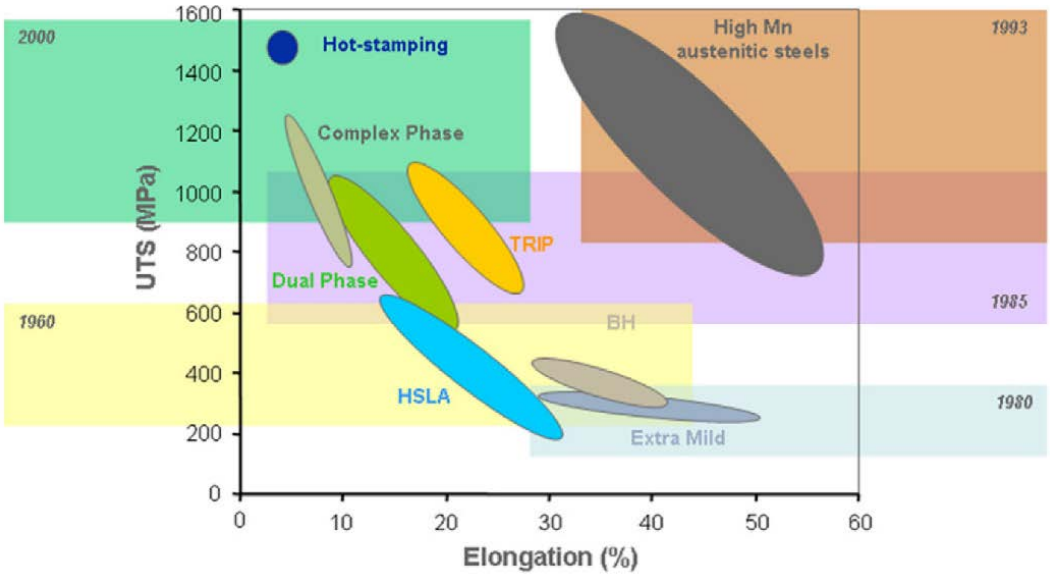

Fig. 2-22 The ultimate tensile strength and total elongation comparison of different steels, after Ref. [203].

Initially, in 1929, Hall and Krivobok [203] revealed the full austenite microstructure of Hadfield's steels after thermal treatment higher than 500 ℃ and subsequent quench.

After that, the important role of Mn concentration was found as high Mn content can promote the formation of FCC single-phase structure of austenite, making high-Mn steels very promising candidates for various industrial applications. In 1936, Tofaute and Linden [209] indicated that the alloys can maintain FCC lattice structure when:

$$wt.\%Mn+13wt.\%C \geq 17 \quad \text{Eq. 2-22}$$

This equation revealed the role of Mn in stabilizing austenite phases and high Mn steels can be cheaper alternatives for Ni-containing steels. Therefore, many series of high-Mn steels attracted huge research interest due to their low cost, high strength, large elongation, and good workability [210]. Fe-xMn-ySi-zAl alloys serve as a very promising series of high-Mn steels and were systematically investigated by Grässel et al. [81,82,211] in terms of deformation mechanisms and mechanical behaviours. The results revealed these alloys own very high strain hardening rate thus significantly improving tensile properties and uniform elongation (as shown in Fig. 2-23). Among all the tested alloys, the Fe-25Mn-3Si-3Al showed a high UTS of ~650 MPa and a very large elongation of 95%. Meanwhile, they also observed extensive strain-induced twinning and a certain amount of martensite phase transformation (from γ to ε/α′), indicating that the dense twin boundaries and new born α′ phases can not only act as strong barriers to dislocation motions but also enhance tensile elongation by retarding local necking. The role of Al and Si was also revealed: Al can effectively increase the SFE of the alloy and sustain the stability of the austenite phases while the Si can decrease the SFE and promote γ to ε transformation [211–213]. This means the SFE of the alloys can be modified via tunning concentrations of Mn, Al, and Si. Furthermore, in order to achieve better mechanical properties and exploit the strengthening mechanisms, more Fe-Mn-Al-Si series alloys with different SFE were developed by adding a trace amount of other elements, such as Ni and C [90,214–217]. Meanwhile,

many variants of Fe-Mn alloys were also developed, such as AISI 201 and 202 (Fe-Mn-Cr series stainless steels), Ni-free Cr-Mn-N stainless steels [216,218,219]. These alloys were then widely used as heat-resistant, non-magnetic, and low-temperature materials in many applications.

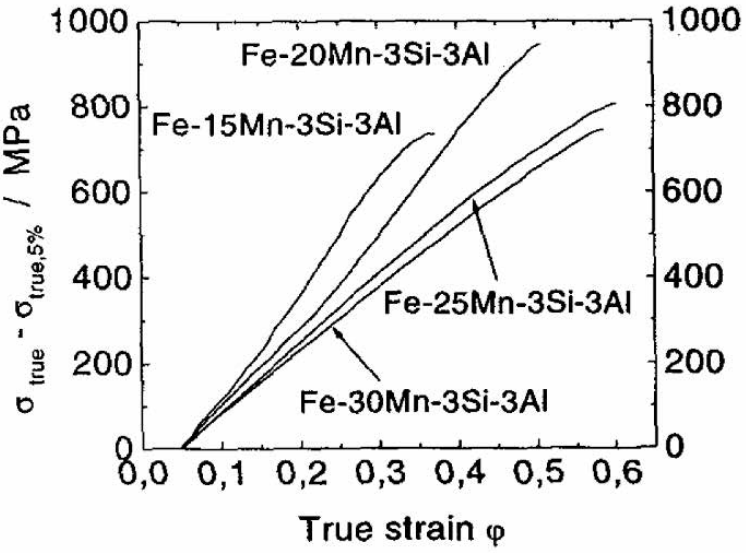

Fig. 2-23 Strain hardening increment of several Fe-xMn-3Si-3Al during straining at room temperature, after Ref. [81].

On the other hand, the outstanding mechanical performance of high-Mn steels during low-temperature straining was also reported in Refs. [220]. In 1977, Remy et al. [220] investigated the twinning and phase transformation (from γ to ε) of a Fe-Mn-Cr-C alloy and emphasized their increasing importance in enhancing work-hardening rate and elongation during decreasing deformation temperature. Curtze et al. [68] reported the temperature dependence of a series of high-Mn steels at the temperature range of 223 to 298 K. As shown in Fig. 2-24, decreasing temperature witnessed a steady increase in tensile strength in all tested high-Mn steels.

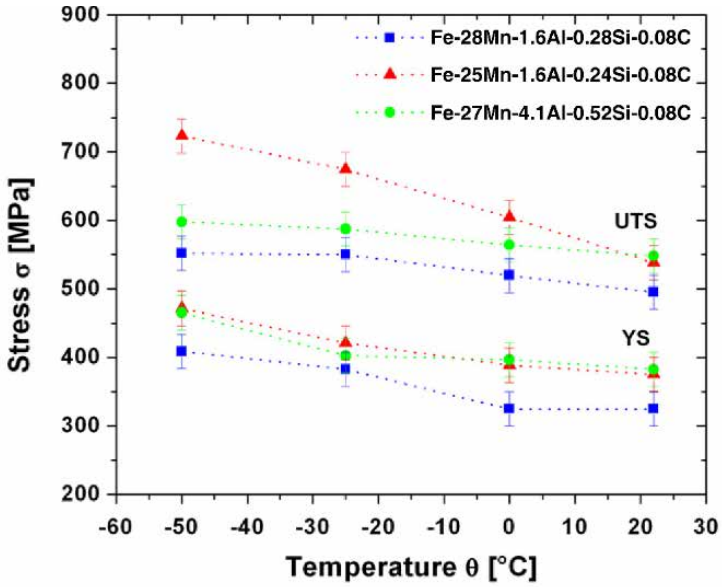

Fig. 2-24 YS and UTS of several high-Mn steels as a function of deformation temperature, after Ref. [68].

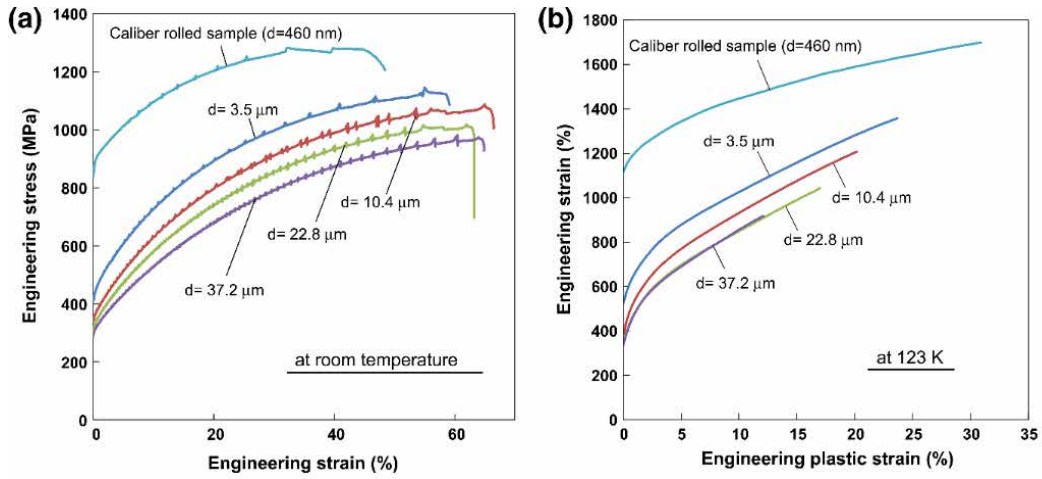

Fig. 2-25 Engineering stress-strain curves of the Fe-17Mn-0.6C steels with different grain sizes during deforming at room temperature and 123 K, after Ref. [221].

Motomichi et al. [221] explored the mechanical performance of a series of high-Mn steel (Fe-17Mn-0.6C, wt.%) in a lower temperature of 123 K. The stress-strain curves of the alloys at room temperature and 123 K are shown in Fig. 2-25. The evolution of the strain hardening rate of the alloys with different grain sizes during tensile testing at room temperature and 123 K is shown in Fig. 2-26. The dotted lines show the flow stress equals the strain hardening rate, indicating the plastic instability and the

occurrence of fracture. The low temperatures can effectively improve the strain hardening rate and avoid fracture.

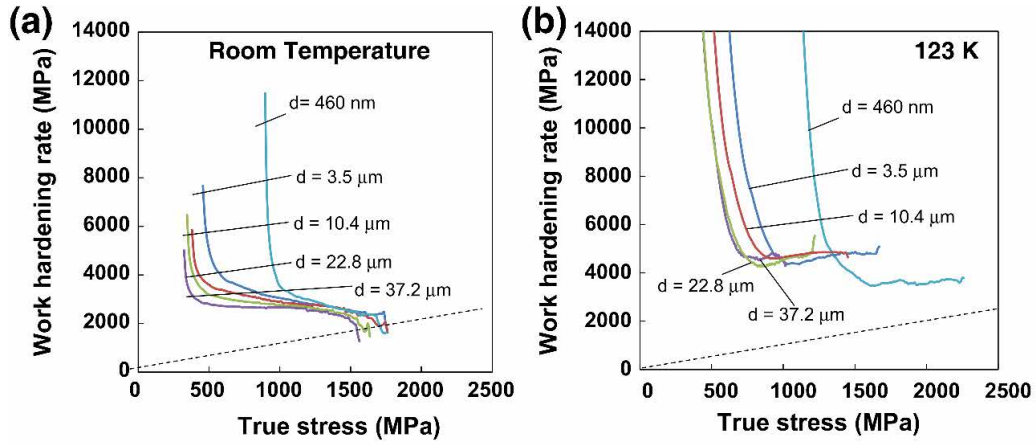

Fig. 2-26 Work hardening rate of the alloys with different grain sizes during deforming at (a) room temperature and (b) 123 K, after Ref. [221].

In summary, these results indicate that the huge potential of high Mn steels in cryogenic environments as their superior ability in fully exploiting TWIP and TRIP effects. More importantly, the production cost of high Mn steels is significantly lower than other Ni-containing alloys due to the high concentration of Mn, which serves as a critical element in adjusting the stability of austenite and thus the deformation mechanisms.

2.7.2 Multi-component Alloys

Traditional alloys, such as aluminium alloys, copper alloys, basically consist of one main element and several minor elements. An alloy family with a variety of mechanical performances can be achieved by modifying the ratio of minor elements. Multi-component alloys, consisting of several (≥ 3) elements with near equiatomic ratio [222–225], are designed to break the concept of one principal element, which was widely employed by conventional alloys (e.g., binary and quaternary alloys). Their uniqueness of consisting of multiple equal ratio elements endows them with significant lattice

distortion, many other intriguing features (e.g., sluggish effect, cock tail effect, etc.) as well as a very promising mechanical performance [226–228].

On the other hand, the core concept of one main element severely limited developing alloys with better mechanical performance, leaving a relatively very narrow space for other elements [229]. The multi-component alloys abandoned this principle and revealed the huge potential of unexplored alloys. According to Cantor [230], the total number of possible alloys (N) can be calculated with the number of components (C) and composition difference between each alloy (x%):

$$N = \left(100 / x\right)^{C\text{-}1} \qquad \text{Eq. 2-23}$$

After excluding the radioactive, toxic elements, it can yield a huge number of possible alloys (~10^{177}), which is overwhelmingly larger than the alloys we now have investigated. According to the available phase diagrams [231], the total number of isomorphous binary and the ternary system reaches only 153 and 248, respectively. As shown in Fig. 2-27, the binary, ternary, and quaternary alloy systems are located at the corner and the vast realm was left in the centre of higher-order phase diagrams [230]. Therefore, a new concept of producing alloys with several equal ratio elements has been popularized in 2004 by Yeh [232]. This new concept attracted enormous interest for investigating all around the world during the past decade [101,233–235].

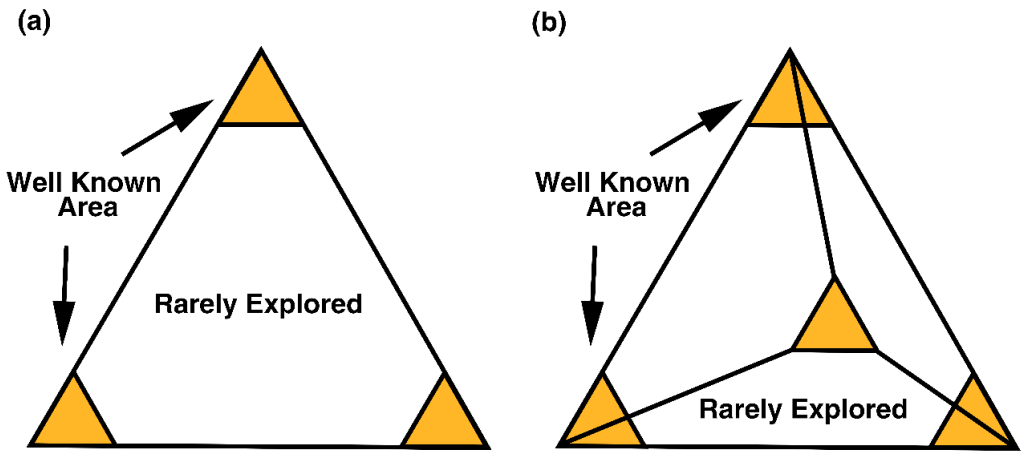

Fig. 2-27 Schematic illustrations of the (a) ternary and (b) quaternary systems. The corner regions marked with yellow represent the traditional alloys based on one major element, which are well-known; The blank areas are relatively less known, after Ref. [230].

This new design concept can also be interpreted in terms of the configurational entropy of the alloy. According to the general Gibbs free energy equation, the relationship between Gibbs free energy (G_{mix}) and entropy (ΔS_{mix}) of a solid solution alloy can be expressed as follows [222,223]:

$$G_{mix} = \Delta H_{mix} - T\Delta S_{mix} \qquad \text{Eq. 2-24}$$

, in which the T is the temperature in Kelvin and ΔH_{mix} is the enthalpy of an ideal solution. For a binary alloy, the maximum of the configurational entropy can be obtained when the two elements are mixed with an equiatomic ratio: $\Delta S_{config} = -R\left(X_A \ln X_A + X_B \ln X_B\right)$, where R is the gas constant [229,236]. For general solutions, the enthalpy can still be regarded as 0 since the deviation is small, so the configurational entropy of mixing (S^{SS}) can be simply written as [237]:

$$S^{SS} = -R\sum X_i \ln\left(X_i\right) \qquad \text{Eq. 2-25}$$

, where X_i corresponds to the atom fraction of element i. Therefore, the maximum configurational entropy of any alloy system can be roughly written as $\Delta S_{conf,\max} = R \ln N$. According to Ref. [232], the increase of the constituent number can

lead to the increase of configurational molar entropy (S_{Calc}^{SS}) of the alloy and therefore entropy. Generally, multiple alloys can be divided into three categories based on their entropy values: low ($S_{Calc}^{SS} < 0.69R$), medium ($0.69R < S_{Calc}^{SS} < 1.61R$), and high entropy ($S_{Calc}^{SS} > 1.61R$) alloys. As proposed by Yeh [238], the multi-component alloys were designed consisting of five or more principal elements with each of them having a concentration between 5 and 35 at.%. This unique design concept leads to a very high entropy value according to Eq. 2-25, so these alloys are more commonly described as high entropy alloys (HEAs). During the past decade, huge research interest was devoted to developing more types of complex concentrated alloys, leading to a growing number of new alloys: such as non-equiatomic HEAs, multiple phase HEAs, metastable HEAs, and MEAs. Fig. 2-28 shows the formation of a quinary equiatomic system via mixing 5 types of atoms [239]. According to Eq. 2-25, the configurational entropy is calculated to be 1.61R. The deviation from the equiatomic state can lead to the dropping of entropy.

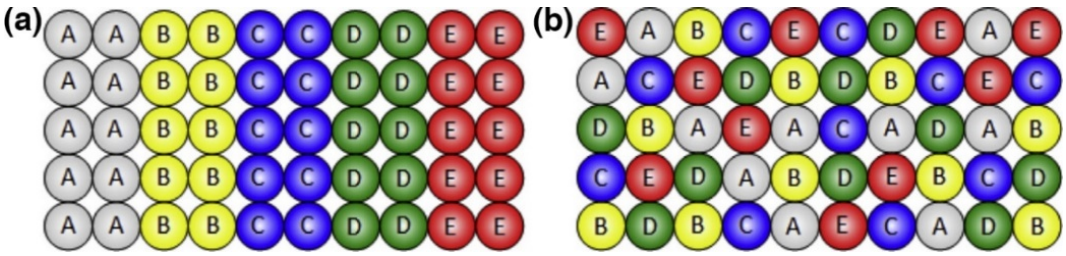

Fig. 2-28 Schematic illustrations of five equiatomic elements (a) before and (b) after mixing. The atom size was assumed to be the same just to show the randomness of the matrix, after Ref. [239].

Four special effects were found at HEAs: the high entropy effect, lattice distortion effect, sluggish effect, and the cocktail effect [240]. which favours the formation of stable, single-phase, and severely distorted solid solutions [241].

The high entropy effect is the most symbolic feature for HEAs. Compared with traditional alloys having only one dominant element and low entropy value, the high entropy value enhances the formation of stable, single-phase substitutional solid

solutions with severely distorted lattice [238,242]. Gibbs phase rule depicts the relationship among the number of phases in thermodynamically equilibrium state (*P*), the degree of freedom (*F*), and the number of components (*N*) at constant pressure can be written as:

$$P = N - F + 1 \qquad \text{Eq. 2-26}$$

The maximum value for the phase number could be *N+1* with *F* having a minimum value of 0, any slight change in composition and/or temperature can decrease the equilibrium phase number. The minimum phase number could be 1 when *F* = *N*. Even the number of the existing phases in multiple component alloy is not certain (ranging from 1 to *N+1*). However, HEAs can violate the founding principle due to their high entropy [243,244]. HEAs have medium negative ΔH_{mix} and the highest ΔS_{mix} compared with other states: elemental phase, compounds, and intermediate phases [245]. Therefore, the ΔG_{mix} is a larger negative for HEAs according to Eq. 2-24, indicating HEAs can be more stable at random solid solution state.

The lattice distortion effect stems from the difference in atom size, bonding energy, and crystal structure, leading to a complex and highly distorted matrix [246,247]. The randomness of occupying the lattice site by different types of atoms causes severe local displacement, which is much higher than the solid solution effects in traditional alloys. This phenomenon is related to the shear modulus mismatch between constituent atoms, which can give a rise of friction stress, postpone the initiation of dislocation, and realize significant hardening effects [248,249]. Fig. 2-29a shows the conventional solid solution in which the solute atoms are trapped by solvent atoms due to their minor amount. The boundary between the solution and the solvent atom will disappear for multi-component alloys (shown in Fig. 2-29b), in which the atom positions show great deviation from mean lattice positions [241].

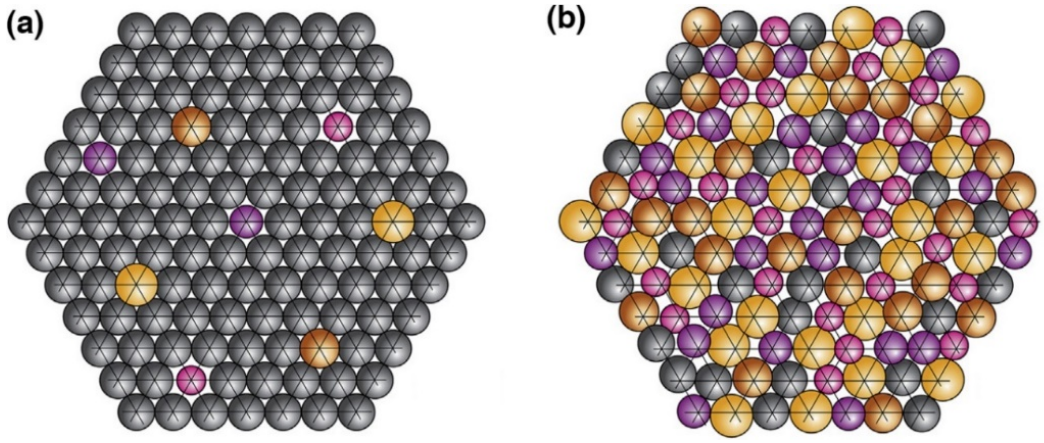

Fig. 2-29 Comparison between the (a) conventional dilute solid solution and (b) a complex, concentrated solution, after Ref. [241].

The severely distorted lattice can effectively influence the thermal part of initiation dislocation motion, increasing the YS and hardness of the alloy significantly. This is because the Peierls-Nabarro energy barriers for initiating dislocation motion at conventional alloys are more periodic [250].

The sluggish effect means the diffusion in HEAs is sluggish [251]. Atom diffusion plays an important role in some phase transformation processes. The heavily distorted lattice can not only impede the dislocation motion but also slow down the atom diffusion. Therefore, the nucleation/growth of new phases and even the morphology of the new phases can be influenced.

The cocktail effect means the synergistic mixture result is unpredictable and has a greater result than the sum of each part [229]. The phase number of HEAs may vary since the difference in composition and processing procedures, the total property enhancement can be decided by mixing of all constituents. The improvement can be significantly better than the sum of each phase since each phase can be regarded as an atomic scale composite (due to the highly distorted matrix) and the variety in size, shape, distribution, phase interfaces among each phase [252,253].

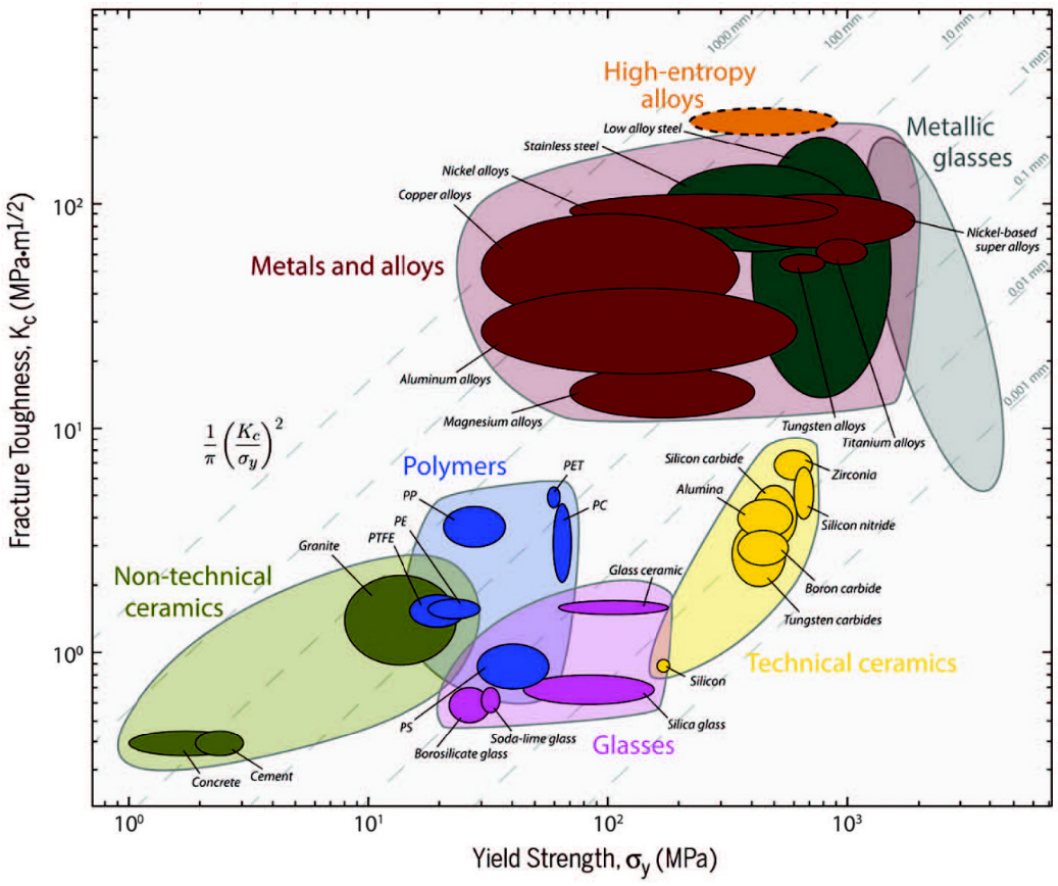

Fig. 2-30 Ashby map plotting fracture toughness with respective to yielding strength for comparing high entropy alloys with other materials, after Ref. [254].

The new design concept also brings the MEAs/HEAs with better mechanical properties (e.g., YS, hardness, toughness, elongation, etc.) compared with conventional alloys (Fig. 2-30). As shown in Fig. 2-30, Gludovatz et al. [254] compared the fracture toughness and YS with a wide variety of materials. The result shows the superior combinations of YS and toughness of HEAs. Among all the investigated HEAs, CrMnFeCoNi has been found to have the best combination of a high toughness (with the plane-strain fracture toughness reaching 200 MPa·m$^{-0.5}$) and a high UTS of ~1 GPa.

On the other hand, as shown in Fig. 2-31, HEAs also show high mechanical performance at the elevated temperature range (from 473 to 1273 K) [255]. This can be ascribed to the sluggish diffusion effect and second phase strengthening. For example, the hardness of an AlCoCrFeMo$_{0.5}$Ni alloy can maintain a very high Vickers hardness

of 347 at 1273 K, which is much higher than traditional high-temperature alloys like Inconel 718 alloy (with a hardness of 220 HV) [256].

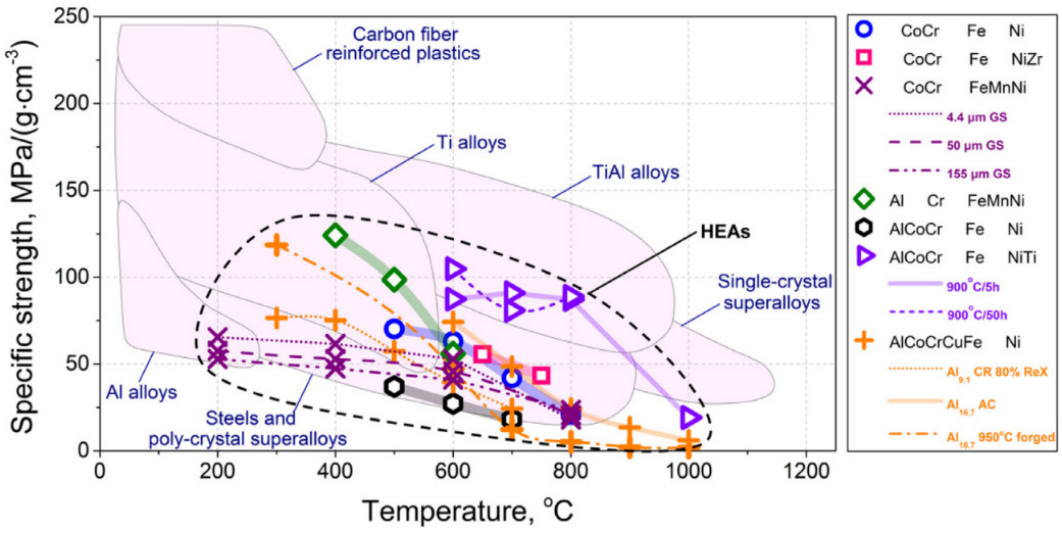

Fig. 2-31 The mechanical properties of HEAs and other compels concentrated alloys at the low- to high- temperature range, after Ref. [255].

Recently, the investigation concerning MEAs/HEAs has expanded to the low-temperature range and more prominent mechanical performance has attracted huge research interest for cryogenic applications [193,257–259]. As indicated in Ref. [254], decreasing deformation temperature from 293 to 77 K led to significant improvement in mechanical performance: the YS and UTS of CrMnFeCoNi alloy were simultaneously improved by ~85% and ~70%, reaching very high values of 759 and 1280 MPa, respectively. Meanwhile, Wang et al. [200] also reported a similar phenomenon at a HEA with 4 principal elements (FeCoCrNi). Fig. 2-32a shows the true stress-strain curve of the alloy deforming at 293 and 77 K while the strain hardening rate (SHR) was calculated at Fig. 2-32b. The result shows that a good combination of high UTS (~1725 MPa) and large elongation (~0.55) were obtained at 77 K.

The superior mechanical properties of some multi-component alloys were compared with other conventional alloys at 77 K in Fig. 2-21. This reveals the huge potential of

multi-component alloys in achieving excellent strength-ductility combinations. Meanwhile, it is also worth noting that the multi-component alloys have a very wide adjustment space for mechanical performance due to their unique design concept of consisting of several near-equiatomic elements. This sheds a light on designing different multi-component alloys with varied mechanical properties for different service conditions and reducing the production cost.

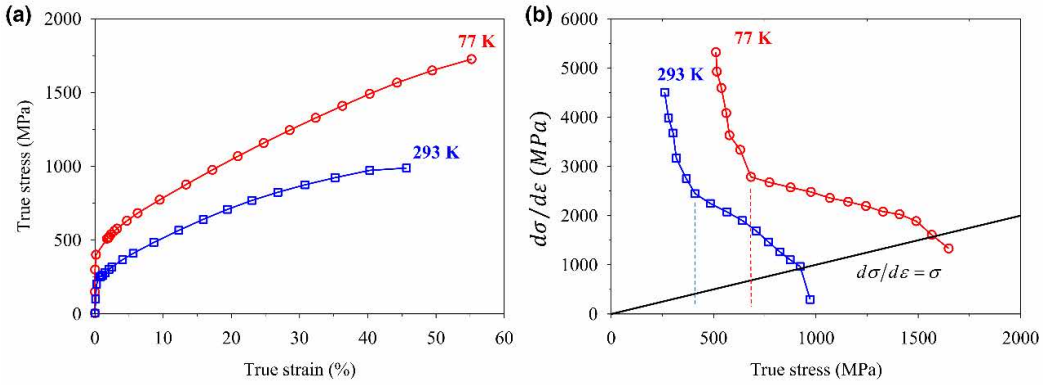

Fig. 2-32 Mechanical performance of a FeCoCrNi HEA at 293 and 77 K: (a) True stress-strain curve and (b) the corresponding strain hardening rate, after Ref. [200].

2.7.3 Austenitic Stainless Steels

With desirable corrosion resistance, toughness, biocompatibility, and weldability, austenitic stainless steels (ASSs) have found a very wide range of applications ranging from low-end applications such as cooking utensils and tableware to some sophisticated areas (such as automobile production and aerospace vehicles) to advanced cryogenic applications in outer-space exploration and high-resolution detectors [65,153,260,261]. For example, in nuclear power industries, AISI 304L ASS shows great resistance to irradiation and has been used to build main irradiation-facing components in the light water reactors or some sodium-cooled fast reactor, e.g., EBR-II [262]. To create an

adherent, self-healing layer and achieve superior corrosion resistance, the chromium content of ASSs is generally higher than 11 wt.% [263].

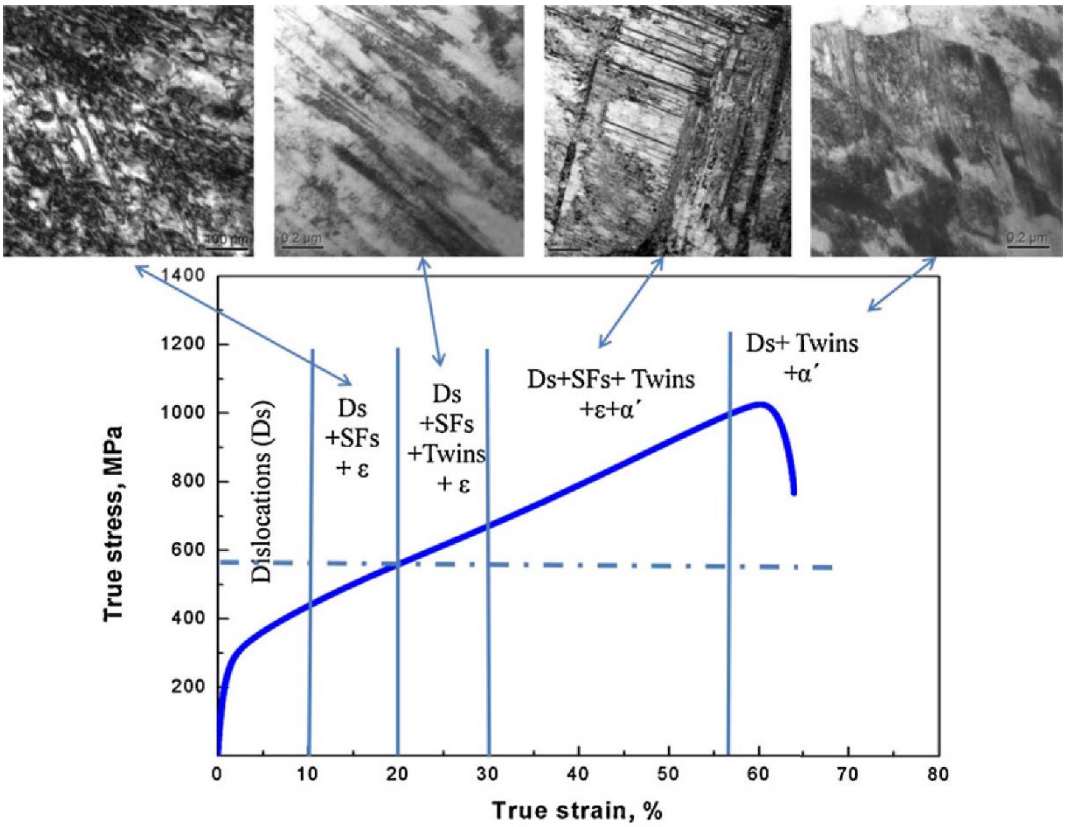

Fig. 2-33 The microstructure evolution of the 304SS during deforming at room temperature, after Ref. [264].

Meanwhile, the chemical composition also endows the ASSs with low SFE and the metastable FCC structured austenite, thus both TWIP and TRIP effects were frequently observed in the ASSs even during deforming at room temperature [264,265]. As shown in Fig. 2-33, Shen et al. [264] indicated that different deformation structures (dislocations, stacking faults, twins, HCP laths, and BCT phases) were formed during plastic deformation. Consequently, the 304 SS shows both a high strain hardening effect and extraordinary ductility. The YS of the 304 ASS is ~320 MPa while the following newborn microstructures sustainably contributed to the strain hardening effect, yielding a very high UTS of ~870 MPa and large elongation of ~63%. More importantly, as indicated in Refs. [108,110,153], ASSs exhibit more prominent strain hardening effects

and thus improved mechanical properties (high toughness, excellent strength, and extraordinary ductility) with the decrease of deformation temperature. The mechanical properties of several traditional ASSs at 77 K were compared with other conventional alloys in Fig. 2-21, making them very intriguing in cryogenic applications.

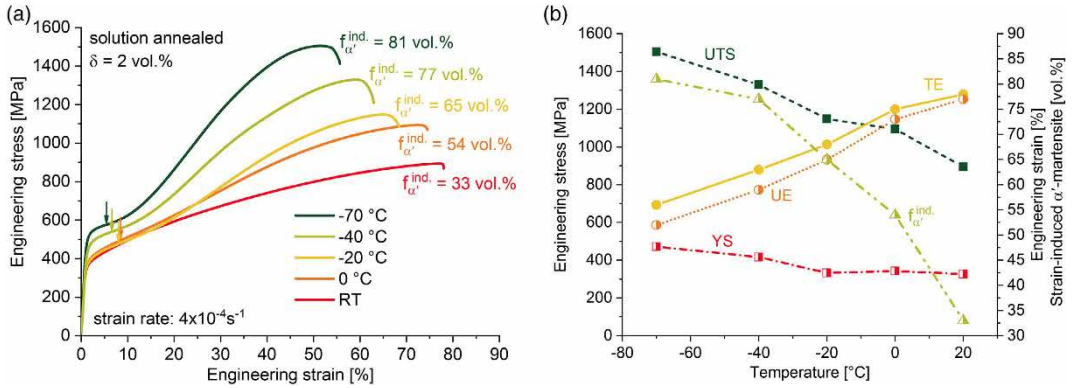

Fig. 2-34 (a) Engineering stress-strain curves of the Cr19NC15.15 ASS during decreasing deformation temperature, after Ref. [266].

For example, Alsultan et al. [266] applied *in situ* magnetic measurements to investigate the mechanical performance and the TRIP effect of an ASS (Fe-19Cr-4Ni-3Mn-0.15N-0.15C) at the low-temperature range (from room temperature to -70°C). The mechanical performance of the alloy during deforming at different temperatures was shown in Fig. 2-34. The YS and UTS of the alloy are 327 MPa and 895 MPa at room temperature, which was gradually enhanced to 472 MPa and 1505 MPa at -70°C. As summarized in Fig. 2-34b, both YS and UTS of the alloy increased almost linearly with the temperature dropping, accompanied by a decline in elongation, from 78% at room temperature to 56% at -70°C.

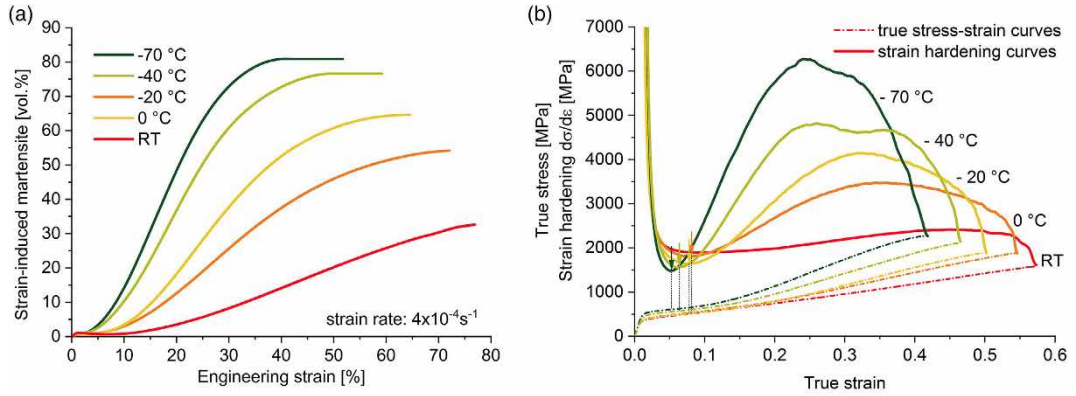

Fig. 2-35 (a) The evolution of volume fraction of strain-induced martensite with engineering strain and (b) true stress-strain curves and the corresponding strain hardening curves, after Ref. [266].

The evolution of volume fraction of strain-induced martensite was plotted as a function of engineering strain in Fig. 2-35. The formation of BCT martensite can be promoted by the decreasing of temperature and thus the highest volume fraction of BCT martensite of 81% was observed at -70°C. Consequently, the strain hardening effect of the alloy was significantly improved (as shown in Fig. 2-35b) since the new born BCT phase serves as the hard/strengthening phase in the soft FCC austenite matrix [267,268].

Recently, due to their excellent toughness, paramagnetic, weldability, and low thermal conductivity, the ASSs have attracted even higher research interest and shown more potential applications since they are ideal raw materials for additive manufacturing [95,269–271]. Metal additive manufacturing is an advanced technology to fabricate end-use metallic components for critical applications and is considered as the next-generation manufacturing method. Many investigations [95,269,270] reported that the unique layer-by-layer building method and the resulting complex thermal cycles are usually involved during the metal additive manufacturing, which can induce several heterogeneous microstructures, (such as heterogeneous grain structures, sub-grain cellular structure, and texture) and anisotropy to the fabricated alloys. These structures can provide effective barriers for the dislocation motion thus significantly enhancing the YS of the alloys.

In summary, the ASSs are a promising candidate for the various complex service conditions (cryogenic and other harsh environments) due to their excellent corrosion resistance, toughness, weldability, biocompatibility. On the other hand, their low SFE at cryogenic conditions can induce multiple strengthening microstructures and thus trigger multiple deformation mechanisms, guaranteeing superior mechanical performance. Furthermore, ASSs serve as the desirable raw material for additive manufacturing, paving a new way of manufacturing complex components with improved mechanical performance for cryogenic applications.

2.8 Summary

In conclusion, the need for cryogenic materials with superior mechanical properties and lower production costs is soaring due to the rapid advancement of cryogenic technology (Chapter 2.1). However, the change of deformation temperature, especially at the ultralow range, can easily result in ductile to brittle transition phenomenon in many alloys with BCC or HCP structures (Chapter 2.1). Activating multiple strengthening mechanisms (dislocation motion, TWIP, and TRIP) in FCC alloys is considered as a very promising method to achieve excellent strength-ductility combinations even at the cryogenic conditions (Chapter 2.3). The SFE of the alloys serves as a critical parameter in activating the deformation mechanisms (Chapter 2.5) and needs accurate experimental validation, especially at the cryogenic temperatures (Chapter 2.6). From previous profound findings, three types of FCC alloys (multi-component alloys, high Mn steels, and austenitic stainless steels) exhibit great potential in adjusting the SFE to the desirable range and thus realizing different strengthening mechanisms (Chapter 2.7).

To develop more advanced cryogenic alloys with premier mechanical properties and lower production costs, it is urgently needed to build a more fundamental understanding of the relationship among microstructural/mechanical responses, deformation mechanisms, SFE, and chemical composition of these alloys at the low-temperature range. Even with great previous findings in conventional cryogenic alloys, the investigations concerning these new types of alloys, especially at ultra-low temperature conditions, are still very rare. Most of them are based on theoretical modelling/prediction or *ex situ* observation. Many theoretical simulations need experimental validation and very few *in situ* observation, especially the *in situ* neutron diffraction at cryogenic temperatures, were performed. In addition, the strengthening contribution of multiple deformation mechanisms, dislocation, TWIP, and TRIP, is not yet fully exploited and their evolution with decreasing temperature needs more comprehensive studies.

Chapter 3. Superior Cryogenic Performance of a High Mn Steel

Published Article

Lei Tang[a] **,** Li Wang[b,c], Minshi Wang[a], Huibin Liu[d], Saurabh Kabra[e], Yulung Chiu[a], Biao Cai[a], ***Synergistic deformation pathways in a TWIP steel at cryogenic temperatures: In situ neutron diffraction***, Acta Mater. 200 (2020) 943–958.

https://doi.org/10.1016/j.actamat.2020.09.075.

Acknowledge of Collaborative Work

Lei Tang conceived and designed the experiment, performed the experiment, interpreted the data, and wrote the manuscript. Li Wang, Minshi Wang, Saurabh Kabra, and Yulung Chiu assisted in performing experiments. Biao Cai assisted with designing the experiments, revising the manuscript, and data analysis. Huibin Liu assisted with the preparation of the material.

[a] School of Metallurgy and Materials, University of Birmingham, B15 2TT, United Kingdom
[b] State Key Laboratory of Powder Metallurgy, Central South University, Changsha, 410083, China
[c] Institute of Materials Research, Helmholtz-Zentrum Geesthacht, Max-Planck-Strasse 1, Geesthacht, D-21502, Germany
[d] BAOSHAN IRON & STEEL CO., LTD, Shanghai 201900, China
[e] ISIS Facility, Rutherford Appleton Laboratory, Didcot OX11 0QX, United Kingdom

3.1 Abstract

High manganese steels are promising candidates for applications in cryogenic environments. In this study, we investigate the mechanical and microstructural responses of a high manganese twinning induced plasticity (TWIP) steel at a low-temperature range (from 373 to 77 K) via in situ neutron diffraction quantification and correlative microscopy characterization. During plastic deformation, stacking fault probability and dislocation density increased at a faster rate at a lower temperature, hence, higher dislocation density and denser mechanical twins were observed, confirmed by microscopic observation. Stacking fault energy was estimated, dropping linearly from 34.8 mJm^{-2} at 373 K to 17.2 mJm^{-2} at 77 K. A small amount of austenite transferred to martensite when deforming at 77 K. The contributions to flow stress from solutes, grain boundary, dislocation, and twinning were determined at different temperatures, which shows that the high work strain hardening capacity of the TWIP steel originates from the synergetic strengthening effects of dislocations and twin-twin networks. These findings reveal the relationship among stacking fault energy, microstructure, and deformation mechanisms at the low-temperature range, paving the way in designing TWIP steels with superb mechanical performance for cryogenic applications.

3.2 Introduction

There is a rapidly growing demand for the development of metallic materials to be used at cryogenic temperatures such as liquified gas (e.g. natural gas and hydrogen) storage and transportation, nuclear fusion devices, and outer-space exploration [68,79,272]. High Mn austenitic steels are promising candidates not only due to their superior ability

to resist low-temperature cracking, excellent work hardening capacity, and the associated superb strength-ductility combination [68,79,273,274] but also because that their costs are lower compared to austenitic stainless steels [275], 9% Ni steels [13] and medium/high entropy alloys [200,276].

High Mn austenitic steels with Mn content in the range of 15 to 30 wt.% are known to trigger nano-twinning during deformation [79,277], achieving excellent mechanical performance with high strain hardening. The activation of twinning effects is closely related to the temperature- and composition-dependent stacking fault energy (SFE) [138–140]. When SFE is higher than 45 mJm^{-2}, dislocation sliding takes the main role, whereas twinning is favoured when SFE drops to the range of 18~45 mJm^{-2}. If the SFE is further decreased to a very low level (< 18 mJm^{-2}), phase transformation can be triggered due to the negative value of molar Gibb's energy of the transition from FCC-austenite to HCP-or/and BCT-martensite. Although this relationship between SFE and deformation mechanisms is well known, the measurement of SFE in high Mn steels at the low-temperature regime has rarely been reported. Theoretical calculation based on thermodynamics [273] and first principle [278] was used to determine the temperature dependence of SFE, but experimental measurements are rare and critically needed for model validation.

Measurement of SFE of high Mn steels at cryogenic temperature is, hence, valuable for alloy development and understanding of deformation mechanisms. SFE can be obtained usually from transmission electron microscope (TEM) micrographs of unloaded specimens deformed to a certain strain [279,280]. This means that for cryogenic deformed specimens, we have to raise the temperature of the frozen samples to room temperature for sample preparation and TEM observation, which could lead to a significant change of the stacking fault structure hence the SFE measurement may not

be reliable. Recently, *in situ* methods for mapping microstructure evolution during cryogenic deformation have been developed, such as *in situ* TEM [281] and *in situ* neutron diffraction [102,200,282]. *In situ* TEM shows remarkable advantages in observing the dislocation motion, slip band formation, and primary/secondary twinning formation during deformation and should be a promising approach for SFE measurement, although implementation of *in situ* TEM at extremely low temperature is difficult [281,283]. *In situ* neutron diffraction combined with loading at cryogenic temperatures, on the other hand, not only can quantitatively depict the microstructural evolution of bulk materials (e.g., interplanar crystal lattice spacing [273], phase identification [284], and dislocation density [200,285]), but also allows us to measure SFE at extremely low temperatures as low as 15 K [282].

Although twinning is known to occur during the deformation of high Mn steels with SFE between 18 to 45 mJm^{-2}, the contribution of deformation-induced twins to their high work hardening capacity is under debate. It is widely accepted that during deformation, strain-induced twinning boundary serves as an effective barrier to impede dislocation gliding by reducing their mean-free path. This leads to substantial strength enhancement under progressing strain, which is best known as the "dynamic Hall-Petch effect" [286,287], providing a sustained high work hardening rate. However, this concept was challenged recently. Liang et al. [72] demonstrated that dislocation motion is the main source for the high work hardening rate of TWIP steels while the twinning contribution is insignificant. Therefore, it is important to further shed light on the contributions of twinning and dislocation towards the work hardening.

Herein, we investigated the cooperative strengthening effects from dislocation motion and mechanical twinning in a high Mn TWIP steel (Fe-24Mn-4Cr-0.5C-0.5Cu) at a low-temperature range (from 373 to 77 K). The *in situ* neutron diffraction and tensile

testing were performed to capture the microstructure evolution during deformation. The diffraction spectra were analysed to obtain manifold microstructural parameters (e.g., lattice strain, stacking fault probability, SFE, and dislocation density). After the tensile tests, microscopic observation has been carried out on the fractured samples to characterize the microstructure. Additionally, the strengthening contributions from various strengthening mechanisms have been determined at different deformation temperatures. This work provides an in-depth micro-mechanical understanding of the superior mechanical properties via dislocation-TWIP collective deformation mechanism.

3.3 Experimental Methods

3.3.1 Materials Processing

The material was provided by Baosteel company. High purity metals (purity ≥ 99.9%) were melted to cast an ingot with a composition of Fe-24Mn-4Cr-0.5Cu-0.5C (wt.%) by vacuum induction melting and casting. After homogenization at 1473 K for 48 h, the ingot was then subjected to hot rolling at 1200 K, followed by water quenching to room temperature.

3.3.2 *In Situ* Neutron Diffraction

In situ time-of-flight (TOF) neutron diffraction measurements during tensile tests were carried out on the ENGIN-X diffractometer with a stress rig, provided by ISIS spallation neutron source, the Rutherford Appleton Laboratory, UK [185]. The schematic illustration of the *in situ* TOF neutron diffraction experiment is shown in Fig. 3-1a. The incident beam, containing pulses of neutrons with a continuous range of speed

and therefore wavelength, travelled through the moderator and was defined by slits with a size of 4 × 4 mm^2. Two ±90° detector banks, radial (north) and axial (south) one, were mounted perpendicularly to the incident beam direction. They are capable of continuously collecting diffracted neutron beams from crystallographic grain planes subjected to compressing and tensile force, respectively. The intersection of the incident beam and 4 mm diffraction beam (defined by the width of the collimator) determined the scattering gauge volume to be 4 × 4 × 4 mm^3. Dog-bone tensile samples (Fig. 3-1c) with gauge volume of Φ 8 × 32 mm^3 were placed at a cryogenic chamber, which provides a high-vacuum environment (< 10^{-5} Pa) (Fig. 3-1b). The deformation temperature change was achieved by a built-in heater and two liquid helium tubes [288]. The temperature was stabilized for 30 minutes at the high vacuum state before tensile loading and collecting diffraction signals. The tensile forces were provided by an Instron stress rig with a load capability of ±100 kN mounted horizontally and 45° to the incident beam. A series of measurements were performed during the tensile tests and each diffraction pattern collection consumes 20 minutes between tensile loading steps, iterating until sample fracture. An extensometer was used to measure the strain during tensile loading. Prior to data collection, a standard sample (CeO_2) was used for precise calibration of the experimental geometry (e.g., primary and secondary flight path distance) and subtraction of the instrumental broadening effect. The GSAS software package was applied to perform peak fitting (with pseudo-Voigt function) and Rietveld refinement, allowing the determination of peak position, full width at half maximum (FWHM), and lattice parameter.

The lattice strain is defined as the change of inter-planar distance of a given grain family due to the applied stress. The inter-planar spacing from different crystallographic plane

$\{hkl\}$ without stress (d_{hkl}^{0}) and under different stress conditions (d_{hkl}) were applied to evaluate the evolution of lattice strain (ε_{hkl}^{exp}) via:

$$\varepsilon_{hkl}^{exp} = \frac{d_{hkl} - d_{hkl}^{0}}{d_{hkl}^{0}} \quad \text{Eq. 3-1}$$

To estimate the contribution of dislocation multiplication to the strength enhancement, the quantitative analysis of dislocation density was necessary. We performed dislocation density calculation based on a modified Williamson-Hall method [289,290]. The detailed calculation procedure can be found in Section A.1.1 of the Appendices.

3.3.3 Microstructure Characterization

Samples for microstructure observation were sectioned from the fractured tensile bars after the tensile tests. After mechanical grinding and polishing, a solution consisting of dilute hydrochloric acid and iron chloride was used for etching before optical microscope (OM) observation. Electron backscatter diffraction (EBSD) was performed on a field emission gun scanning electron microscope (FEI Sirion 200) equipped with an HKL EBSD detector and Channel 5 software. The EBSD maps of the as-received material are shown as image quality maps and inverse pole figure (IPF) maps perpendicular to the rolling direction (RD). The RD was marked in EBSD maps. The scanning electron microscope (SEM) beam parameters were set to a voltage of 20 kV, current of 25 nA, a spot size of 6.5, a working distance of 168 mm, and the scanning step size was set to 0.7 μm for the as-fabricated sample and 0.03 μm for deformed samples. The EBSD data was then analysed with a MATLAB package, MTEX [291]. Misorientation angle less than 2° were ignored during the analysis to avoid ambiguous grain boundaries. For transmission electron microscope (TEM) and scanning transmission electron microscope (STEM) characterization, thin foils obtained by

grinding and polishing were prepared by twin jet electropolishing with a constant current of ~150 mA in a solution of 5% perchloric acid and 95% methanol cooled to -30 ℃. TEM and STEM characterization was then performed on a JOEL 2100 and FEI TITAN 30-800, respectively.

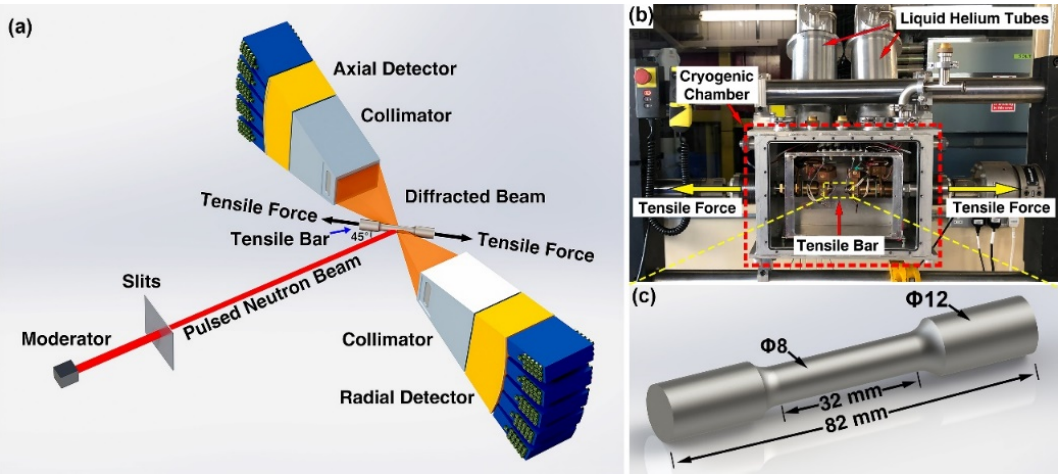

Fig. 3-1 (a) Schematic illustration of *in situ* neutron diffraction facility at ISIS, neutron and muon source; (b) the size of the tensile bar; and (c) the cryo-chamber and hydraulic system.

3.4 Results

3.4.1 Microstructure of the As-fabricated Material

The typical IPF map in Fig. 3-2a shows the grain structure of the as-fabricated TWIP steel, which mainly consisted of large equiaxed grains with a small fraction of recrystallized grains. The average grain size was 14.0±1.2 μm determined by performing the line-intercept method on several optical micrographs, which is consistent with the EBSD results. Corresponding misorientation distribution was plotted in Fig. 3-2b, showing that its average grain misorientation angle was 28.3% with the fraction of low angle grain boundary (i.e., grain misorientation angle in the range of 2-15°) reaching a high level of 47.6%. Dislocation tangling and dislocation-free zones were observed and shown in Fig. 3-2c and d, respectively. The dislocation

networks, unevenly distributed, might be induced during the hot rolling and following quenching process.

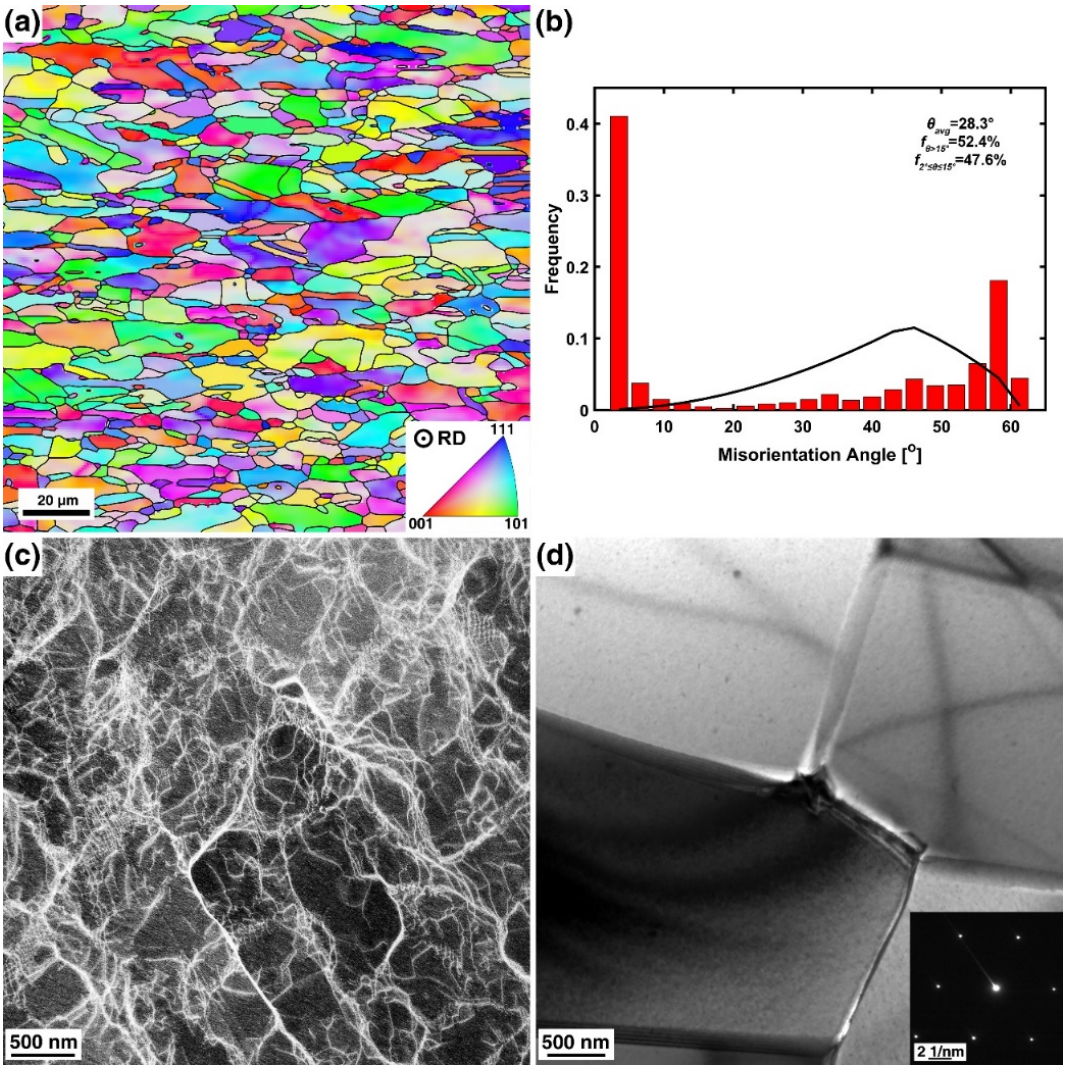

Fig. 3-2 The microstructure of the as-fabricated TWIP alloy: (a) typical IPF map; (b) grain misorientation distribution (The black line shows the random distribution misorientation); (c) HAADF-STEM image of a dislocation tangling zone and (d) typical bright-field image and selected area diffraction pattern of a dislocation-free zone.

3.4.2 Mechanical Performance

Fig. 3-3a shows the engineering/true stress-strain curves of the alloy deformed at different temperatures. Corresponding mechanical properties (yield strength (σ_{YS}), ultimate tensile strength (σ_{UTS}), total elongation, and work hardening capacity (WHC))

were summarized with respect to deformation temperature in Fig. 3-3b. The WHC was calculated with the following equation [60]:

$$WHC = \frac{\sigma_{0.4} - \sigma_{YS}}{MG} \quad \text{Eq. 3-2}$$

, where $\sigma_{0.4}$ is the true stress at a true strain of 0.4, G is the shear modulus and M=3.06 is the Taylor factor. At 373 K, the steel showed a very large elongation of 0.68 and relatively low strength (σ_{YS} of 354 MPa and σ_{UTS} of 796 MPa). The σ_{YS}, σ_{UTS}, and WHC increased almost linearly with the dropping of temperature (as shown in Fig. 3-3b). An excellent combination of mechanical properties was achieved at 77 K, reaching σ_{YS} of 760 MPa, σ_{UTS} of 1312 MPa, and total elongation of 0.56. The WHC increased from 3.46×10^{-3} at 373 K to 4.99×10^{-3} at 77 K. The alloy showed good ductility across the temperature range, with the total elongation remaining at a high level of ~0.55 or higher.

In order to further analyse the hardening behaviour at different temperatures, the strain hardening rate (SHR, $d\sigma/d\varepsilon$) at different temperatures was plotted with respect to true stress in Fig. 3-3c. The SHR curves can be roughly divided into three stages (separated by dashed lines). At 373 K, the SHR curve kept dropping with the increase of true stress, but the dropping speed varied among stages. At 293, 173, and 77 K, the SHR curves shared a very similar pattern: the SHR dropped rapidly at the first stage due to an elastic-plastic transition; Then they increased slightly at Stage II but dropped again at Stage III. The length of Stage II increased with decreasing temperature. At 293 K, Stage II ranged from 614 to 841 MPa and it was then expanded at 173 K (from 804 to 1200 MPa). At 77 K Stage II lasted from 1008 to 1700 MPa until almost approaching failure. Besides, as shown in Fig. 3-3c, the dropping of deformation temperature also pushed the elastic-plastic transition stress (from Stage I to Stage II) to higher stress

levels (521 MPa at 373 K, 614 MPa at 293 K, 804 MPa at 173 K and 1008 MPa at 77 K). The Young's modulus (*E*) as shown in Table 3-2 was determined by the slope of the linear fitting function of the true stress/strain curve at the elastic stage. There are small variations of Young's modulus between different temperatures, which can be resulted from the sample shrinkage as the temperature decreases.

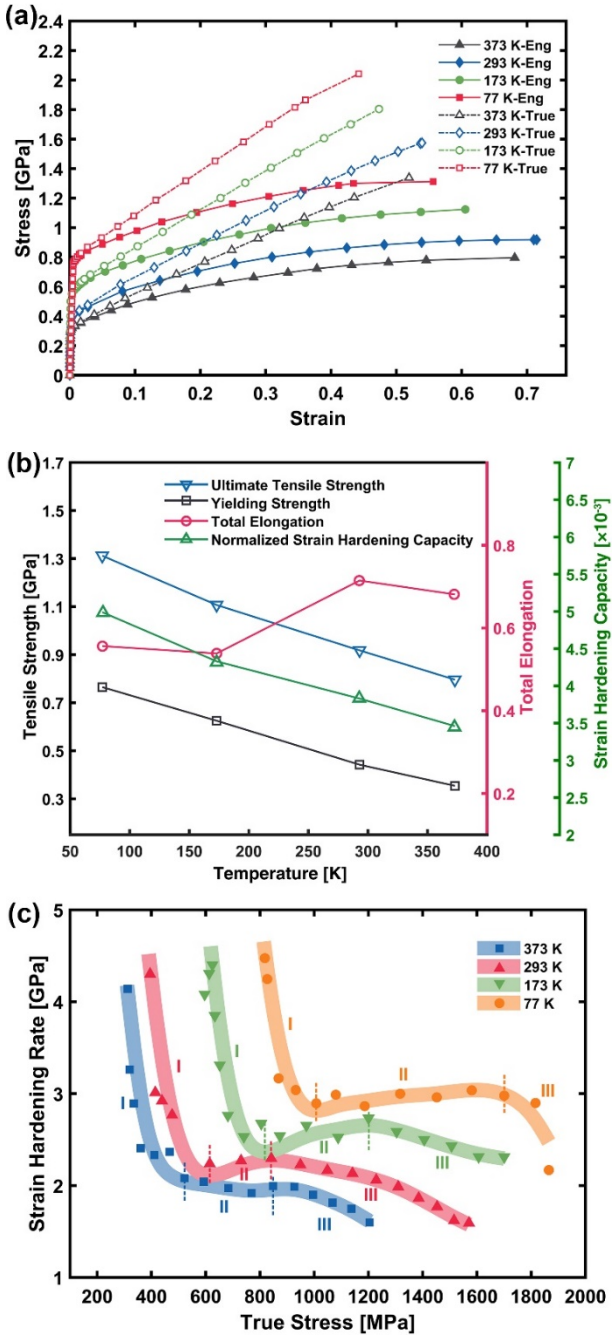

Fig. 3-3 Mechanical performance of the TWIP steel at different temperatures: (a) true stress-strain curves; (b) mechanical properties versus temperatures; and (c) strain hardening rate.

Table 3-1 Mechanical properties of the alloy deformed at different temperatures.

Temperature [K]	σ_{YS} [MPa]	σ_{UTS} [MPa]	Total elongation	WHC [$\times 10^{-3}$]
373	354	796	0.68	3.46
293	442	918	0.72	3.83
173	625	1107	0.54	4.33
77	760	1312	0.56	4.99

3.4.3 Diffraction Data Analysis

In situ neutron diffraction tests were carried out at four deformation temperatures (373, 293, 173, and 77 K). The normalized diffraction patterns during tensile testing at 373 and 77 K (axial detector) were plotted against the true stress in Fig. 3-4a and b, respectively. FCC austenite phase (γ) was confirmed to be the matrix phase and did not transform during cooling. The lattice parameter of the austenite phase versus temperature was determined by performing Rietveld refinement. The lattice parameter at 373 K is 3.619 Å and almost linearly decreases to 3.610 Å at 77 K (Table 3-2).

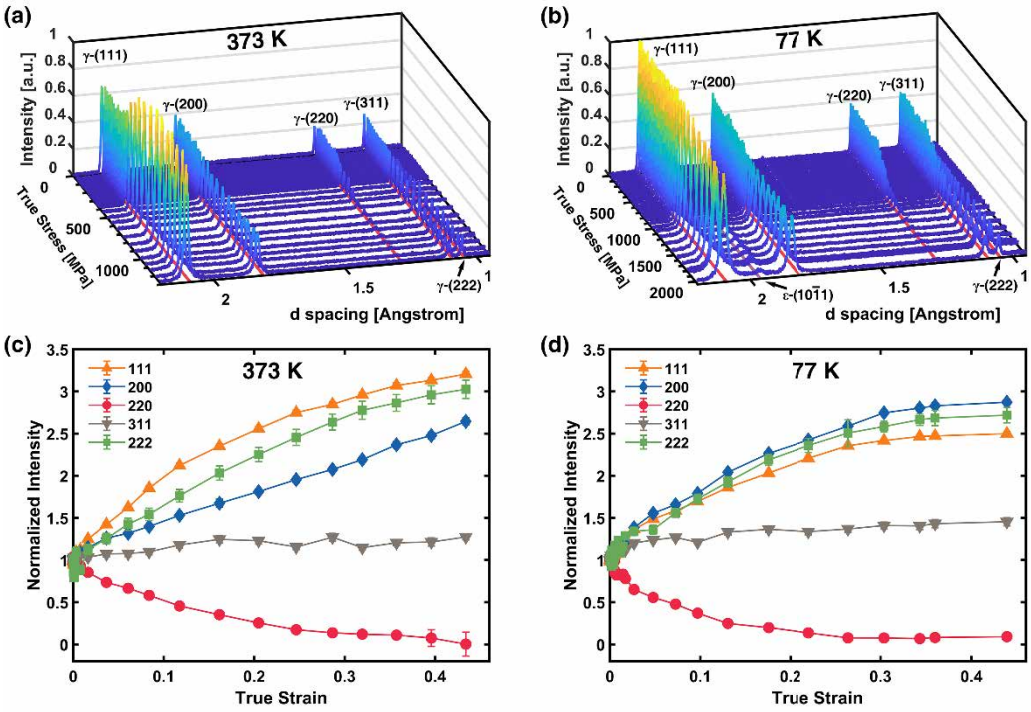

Fig. 3-4 Diffraction patterns with respect to true stress when deforming at (a) 373 K and (b) 77 K; Normalized intensity as a function of true strain at (c) 373 K and (d) 77 K.

The integrated intensity of each orientation during deforming at 373 and 77 K was normalized with that at the undeformed state and plotted with strain in Fig. 3-4c and d, respectively. The texture is almost unchanged during elastic deformation, after which the evolution of each orientation varies due to the inherent anisotropy of the alloy. The intensity of γ-(111), γ-(222), and γ-(200) peaks kept increasing, indicating grains with these orientations gradually rotated to tensile axis. Contrarily, the γ-(220) intensity decreased and γ-(311) changed only slightly since (220) grains rotated away from the tensile axis while (311) grains are stable during straining. It is worth mentioning that the intensity curves at both temperatures appeared to stabilize at the end of the deformation while 77 K showed an earlier turning point than 373 K. The saturation of the texture indicates the limited dislocation behaviours and activation of a new deformation mechanism. Besides, no new reflection peaks were found when deformation temperature is between 373 and 173 K, indicating that the structure of the alloy is stable and remained as FCC structure during deformation. At 77 K, the intensity of all 5 reflection peaks of the γ phase decreased initially and stabilized at large strain conditions (> 0.3). One new peak indexed as the $(10\bar{1}1)$ plane of the HCP phase [49] appeared. This shows that there is not only texture change but also FCC-to-HCP martensitic transition that occurred during deformation at 77 K.

3.4.4 Lattice Strain Evolution

In Fig. 3-5, the lattice strain evolution of five grain families ({111}, {200}, {220},{311} and {222}) from the axial and radial direction was plotted as a function of true stress at 373, 293, 173, and 77 K. The uncertainty of the measured strain is constrained to less than 30 microstrain [292]. Fig. 3-5a shows that at 373 K, the lattice strain curves from all crystallographic grain planes increased linearly with true stress up to its yielding

point (354 MPa). Then a nonlinear relationship was observed at all crystallographic grain planes since the stress transferred from some stiff grain families (e.g., 220) to compliant grain families (e.g., 200) after yielding. Similar behaviour was also observed at the other three temperatures, as shown in Fig. 3-5b-d. Besides, the maximum lattice strain values (both axial and radial directions) for all 5 grain planes increased with the dropping of deformation temperature.

Table 3-2 Lattice parameter, elastic properties, and stacking fault energy of the TWIP steel at different temperatures.

Temp. (K)	a_0 (Å)	E (GPa)	E_{111} (GPa)	E_{200} (GPa)	E_{220} (GPa)	E_{311} (GPa)	v	v_{111}	v_{200}	v_{220}	v_{311}	G (GPa)	SFE (mJm^{-2})
77	3.610	179.4	258	131	203	171	0.257	0.207	0.344	0.284	0.289	71.4	17.2±1.1
173	3.613	179.8	243	130	195	158	0.261	0.181	0.321	0.271	0.273	71.3	21.7±1.1
293	3.616	179.9	235	129	191	156	0.267	0.176	0.317	0.257	0.251	71.0	30.5±1.3
373	3.619	179.7	225	138	203	154	0.284	0.166	0.292	0.256	0.229	70.2	34.8±1.6

The elastic constants at the tensile and compressive directions were obtained from the linear fitting of the lattice strain of axial and radial directions before the yielding of each grain plane (Fig. 3-5), respectively. The lattice parameter evolution with stress at radial and axial directions were determined with Rietveld refinement. At the elastic stage, the lattice parameters at radial and axial directions increased and decreased linearly with true stress, respectively. Their slopes were linearly fitted to determine the tensile and compressive Young's modules. The ratio of the two was the Poisson's ratio (v). The shear modulus (G) was calculated via $G = E/2(1+v)$. The Poisson's ratio and shear modulus at different temperatures are shown in Table 3-2. Likewise, we determined the elastic constants of each orientation (E_{111}, E_{200}, $E_{220,}$ and E_{311}) as shown in Table 3-2. The ratio of elastic constants between the radial and axial directions was used to determine Poisson's ratios at each orientation. At all temperatures, E_{111} and E_{200} have the highest and lowest values, respectively. As the temperature decreased, the stiffness of the alloy increased. E_{111} and E_{311} were enhanced while E_{200} and E_{220}

remained at the same level. This phenomenon can be ascribed to the shrinkage of atomic bonds during temperature dropping [293].

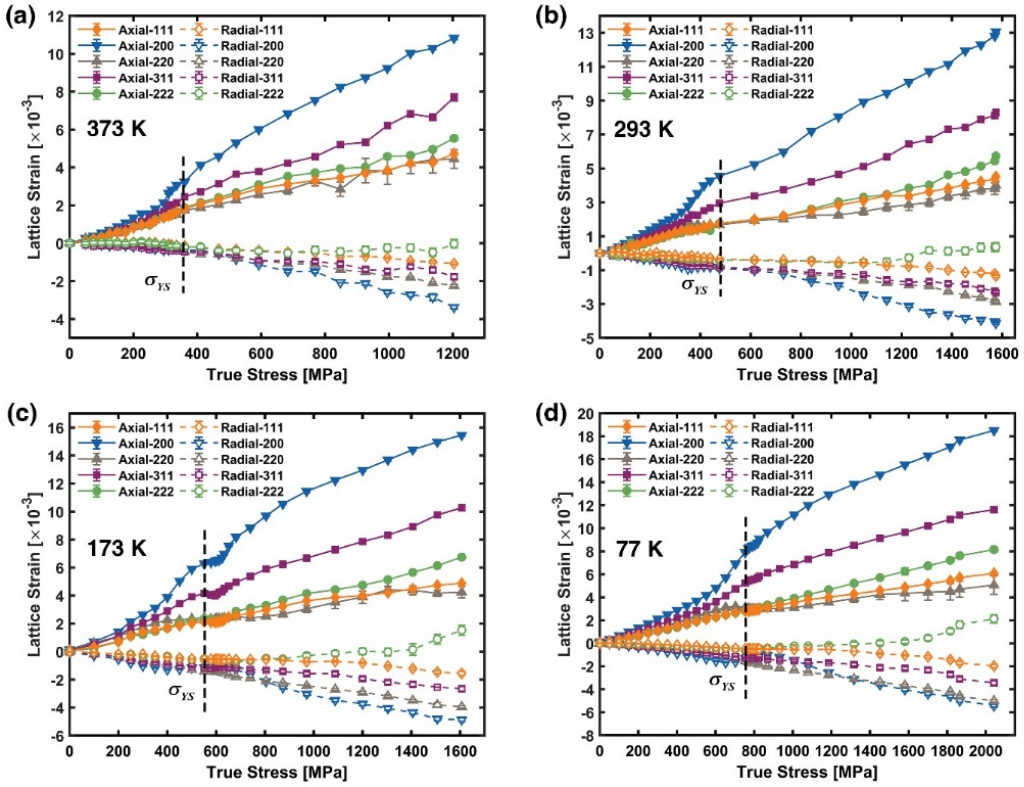

Fig. 3-5 Lattice strain curves of crystallographic planes {111}, {200}, {220}, {311}, and {222} obtained from the axial and radial detectors during deforming at different temperatures: (a) 373 K (b) 293 K (c) 173 K and (d) 77 K.

3.4.5 SFP and SFE Calculation

Many studies [282,285,292] demonstrated that stacking faults accumulation at FCC alloys can lead to the shifting of two consecutive crystallographic grain planes (e.g., {111} and {222}) differently. Therefore, stacking fault probability (SFP), which evaluates the density of stacking faults, can be calculated by measuring the splitting distance between the lattice strain curves of {111} and {222}. Lattice strain curves of two successive grain families {111} and {222} at the four temperatures (373, 293, 173, and 77 K) were then plotted with respect to true strain in Fig. 3-6a-d, respectively. Separation of lattice strain curves of {111} and {222} grain families at four deformation

temperatures can be clearly observed, indicating the formation of stacking faults, which is used to calculate the SFP as follows.

To calculate the SFP, an equation considering the strain induced by macro-strain ($\varepsilon_{hkl}^{strain}$) and stacking faults (ε_{hkl}^{sf}) has been proposed in Ref. [274]:

$$\varepsilon_{hkl}^{exp} = \varepsilon_{hkl}^{strain} + \varepsilon_{hkl}^{sf} = \varepsilon_{hkl}^{strain} - \frac{\sqrt{3}}{4\pi} \frac{\sum b \pm (h+k+l)}{(u+b)(h^2+k^2+l^2)} SFP \qquad \text{Eq. 3-3}$$

, where *u* and *b* are the numbers of non-broadening and broadened components due to stacking faults [274]. Since successive grain families are equivalent in the crystallographic directions, their lattice strain change should be the same when only macro-strain is considered. Therefore, the SFP can be derived from the lattice strain of {111} and {222} via [274]:

$$SFP = \frac{32\pi}{3\sqrt{3}} \left(\varepsilon_{222}^{exp} - \varepsilon_{111}^{exp} \right) \qquad \text{Eq. 3-4}$$

The calculated SFP at different temperatures was plotted against strain in Fig. 3-6a-d. SFP fluctuates at a very low level when the true strain is small. Sometimes the values are even negative, due to small errors induced by peak fitting. When SFP reached 0, they increased almost linearly with true strain. A linear equation was then fitted to the SFP versus true strain after considerable stacking faults have formed (when SFP is higher than 0.01). The slope of the fitted line of SFP (∂SFP/$\partial\varepsilon$) indicates the speed of stacking fault formation, which was plotted against deformation temperature in Fig. 3-7a. It started from 3.3×10^{-2} at 373 K and almost linearly increased to 7.7×10^{-2} at 77 K. This indicates that stacking faults form much more quickly at cryogenic temperatures than at higher temperatures (e.g., 373 K).

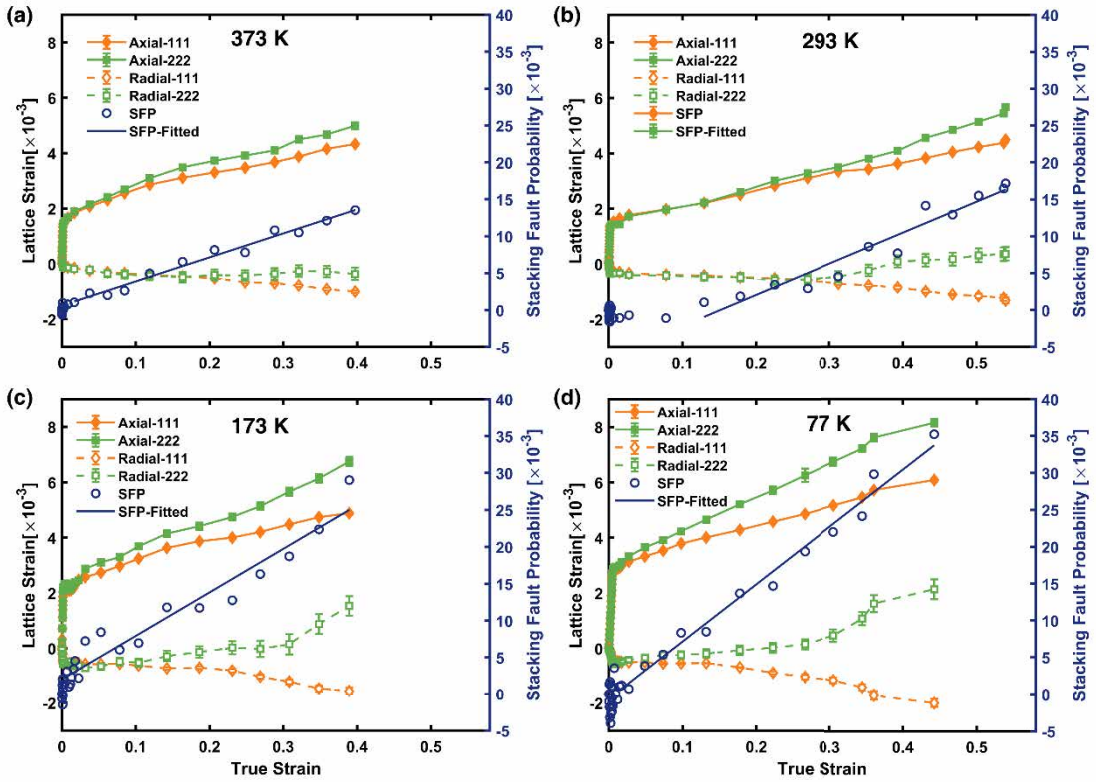

Fig. 3-6 Evolution of lattice strain and stacking fault probability as a function of true strain at different temperatures: (a) 373 K, (b) 293 K, (c) 173 K, and (d) 77 K.

According to Reed and Schramm [171], SFE measures the easiness of dissociation of a perfect dislocation into partial dislocations and creating stacking faults. The relationship between SPF and SFE is depicted with:

$$\gamma_{isf} = \frac{6.6a_0}{\pi\sqrt{3}} \frac{\langle \varepsilon^2 \rangle_{111}}{SFP} \left(\frac{2C_{44}}{C_{11}-C_{12}} \right)^{-0.37} \left(\frac{C_{44}+C_{11}-C_{12}}{3} \right) \qquad \text{Eq. 3-5}$$

, in which a_0 is the lattice parameter and γ_{isf} is the intrinsic stacking fault energy. The mean-square strain, $\langle \varepsilon^2 \rangle_{111}$, was calculated by deconvoluting size and strain broadening effects with the double-Voigt method [294]. The detailed procedure to calculate the mean-square strain can be found in Section A.1.2 in the Appendices. The single-crystal elastic constants (C_{11}, C_{12}, and C_{44}) of Fe-24wt%Mn-4wt%Cr alloy, a close composition to ours, were calculated based on the *ab initio* simulation results of Ref. [295]. It was found that C_{11}=222 GPa, C_{12}=159 GPa, and C_{44}=150 GPa. Single-

crystal elastic constants are temperature-dependent but only vary slightly between 77 and 373 K [296–298]. The coefficient $\left(\frac{2C_{44}}{C_{11}-C_{12}}\right)^{-0.37}\left(\frac{C_{44}+C_{11}-C_{12}}{3}\right)$ in Eq. 3-5 is even less temperature-sensitive within the temperature range according to our analysis on Fe [296], CrCoNi medium entropy alloy [298], and Cr-Mn-Fe-Co-Ni high-entropy alloy [299] (see Section A.1.3 of the Appendices). Here, we used single-crystal elastic constants of Fe-24wt%Mn-4wt%Cr alloy at room temperature to estimate SFE of various temperatures using Eq. (5), as shown in Table 3-2. It is expected that a precise measurement of the single crystal elastic constants of the alloy as a function of temperatures via experiments and *ab initio* simulation could increase the accuracy of SFE calculation.

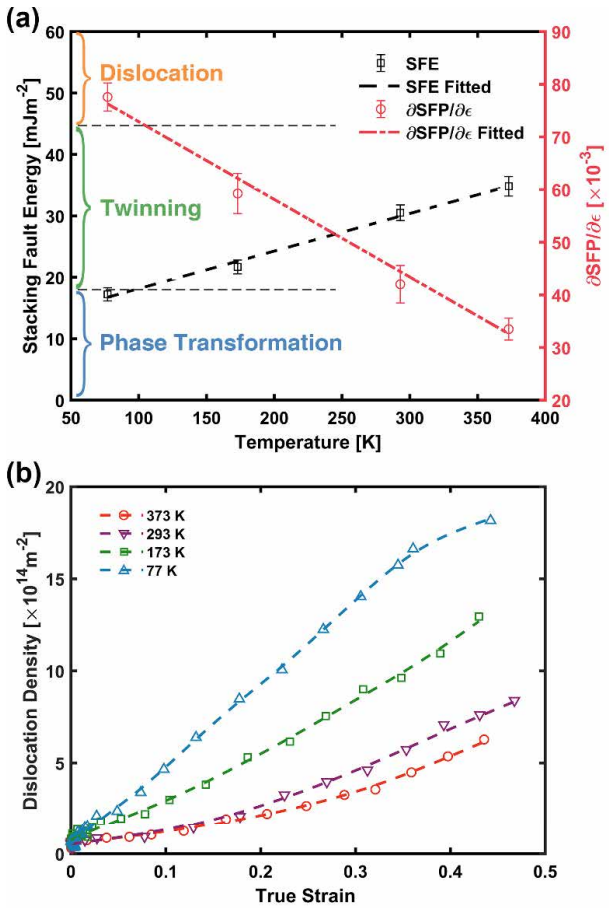

Fig. 3-7 (a) Temperature dependence of stacking fault probability and stacking fault energy and (b) dislocation density evolution with true strain at different temperatures.

The evolution of SFE with deformation temperature is shown in Table 3-2 and Fig. 3-7a. The different deformation mechanism regimes defined by SFE [139,140], as stated in the introduction, were overlapped in Fig. 3-7a. In our study, SFE of the alloy started from 34.8 mJm^{-2} at 373 K and almost linearly declined to 17.2 mJm^{-2} at 77 K. The linear relationship between SFE and temperature was also predicted by thermo-dynamic simulation [273] and first-principle calculation [278]. According to Fig. 3-7a, for this alloy, twinning would occur and play an important role during deformation at all four temperatures. At 373 K, the SFE value was close to the regime boundary separating dislocation slipping and twinning, therefore, dislocation motion might be still the major deformation mechanism. As the test temperature decreased, the role of twinning became more pronounced. At 77 K, SFE dropped to the boundary of twinning and phase transformation, indicating that phase transformation could occur but at a low extent. This result agrees well with the highest SFP rate and the formation of HCP-ε phase at 77 K observed in neutron reflections (Fig. 3-4b).

3.4.6 Dislocation Density Evolution

To estimate the contribution of dislocation multiplication to the strength enhancement, a quantitative analysis of dislocation density was necessary. Fig. 3-7b shows the calculated dislocation density (ρ) evolution during tensile testing at different test temperatures. Initially, the dislocation density at all temperatures was around 7×10^{13} m^{-2}, indicating that the fabrication processes induced pre-existing dislocations (Fig. 3-2c), which did not change significantly when the temperature dropped. During elastic deformation, dislocation density did not change much. After yielding, the dislocation density increased with strain. Fig. 3-7b shows that the lower the deformation temperature, the higher the dislocation density at the same strain level. There appears

to be a saturation period at high strain levels before failure at 77 K. Saturation of dislocation density was also observed in an Al-alloyed TWIP steel that the dislocation density saturated at 1×10^{15} m^{-2} at a strain of ~0.35 [76], which is of similar magnitude as ours. The highest dislocation density of 1.82×10^{15} m^{-2} was reached when deforming at 77 K to a true strain of 0.44, while the corresponding dislocation density was only 0.63×10^{15} m^{-2} at 373 K when deforming to a similar strain level. The dislocation density curves against strain between yielding and saturation appeared to be almost linear. By linearly fitting the curves, the slope of the fitted lines represents the increased rate of dislocation density (R_{dis}). At high temperatures, R_{dis} was low, about 1.1×10^{15} m^{-2} at 373 K and 1.6×10^{15} m^{-2} at 293 K. It increased to 4.3×10^{15} m^{-2} when the test temperature was decreased to 77 K. Decreasing of test temperatures accelerated dislocation formation, especially at low strain conditions.

3.4.7 Microstructure Characterization

Fig. 3-8 shows OM images taken from the fractured samples deformed at 293 and 77 K to different strain levels (~0.1, ~0.2, and ~0.3). When deformed at 293 K with a low strain of ~0.1 (Fig. 3-8a), the twinning formation was inhomogeneous. Most of the grains were twin-free and only a very limited number of grains, which probably have preferred orientation for twinning, showed features of primary twinning. These twins were short and had a wide twin spacing. A similar phenomenon was also reported in [300], showing that twinning was preferably initiated from grains with orientations such as $\langle 111 \rangle$ //tensile axis, while the orientation, $\langle 001 \rangle$ //tensile axis, is much harder for twinning. De Cooman et al. [71] pointed out that mechanical twinning prefers to occur in grains with a high dislocation density. Our TEM observation shows that some grains of the as-fabricated sample have dense dislocation networks (Fig. 3-2c), at which

twinning could prefer to occur first. With the increase of strain, these primary twins gradually occupied the grain interior and grew denser. Only very few secondary twinning can be observed at a strain of ~0.2 (Fig. 3-8b). Then twins propagated to other grains at higher strain conditions (Fig. 3-8c). Compared with the situation at 293 K, twinning was more prominent at 77 K. At all three strain levels at 77 K, more grains were twinned with a higher twin density. Meanwhile, there are more secondary twinning, intersecting with the primary twins when deforming at 77 K (Fig. 3-8d-f). This is consistent with the measurement of SFP (Fig. 3-7). Since stacking faults serve as the embryo of twinning, SFP curves could be used to predict the formation of mechanical twins. Higher SFP was achieved at a lower temperature at a faster rate, hence, more mechanical twins are expected at 77 K than 293 K.

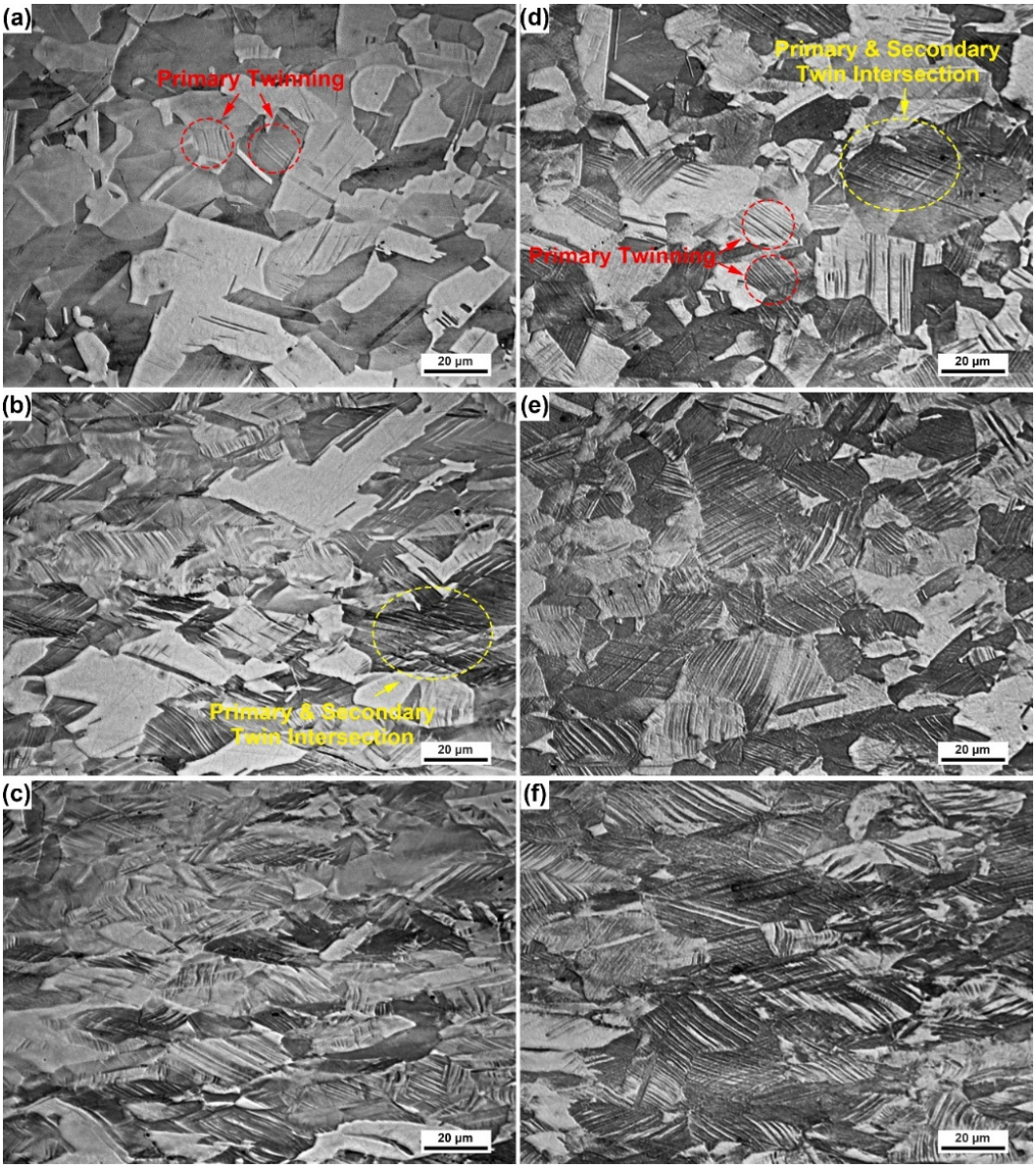

Fig. 3-8 Grain morphology observed by OM in TWIP steel deformed at 293 K and 77 K with different true strain: (a) 293 K, ε=~0.1; (b) 293 K, ε=~0.2; (c) 293 K, ε=~0.3; (d) 77 K, ε=~0.1; (e) 77 K, ε=~0.2; (f) 77 K, ε=~0.3.

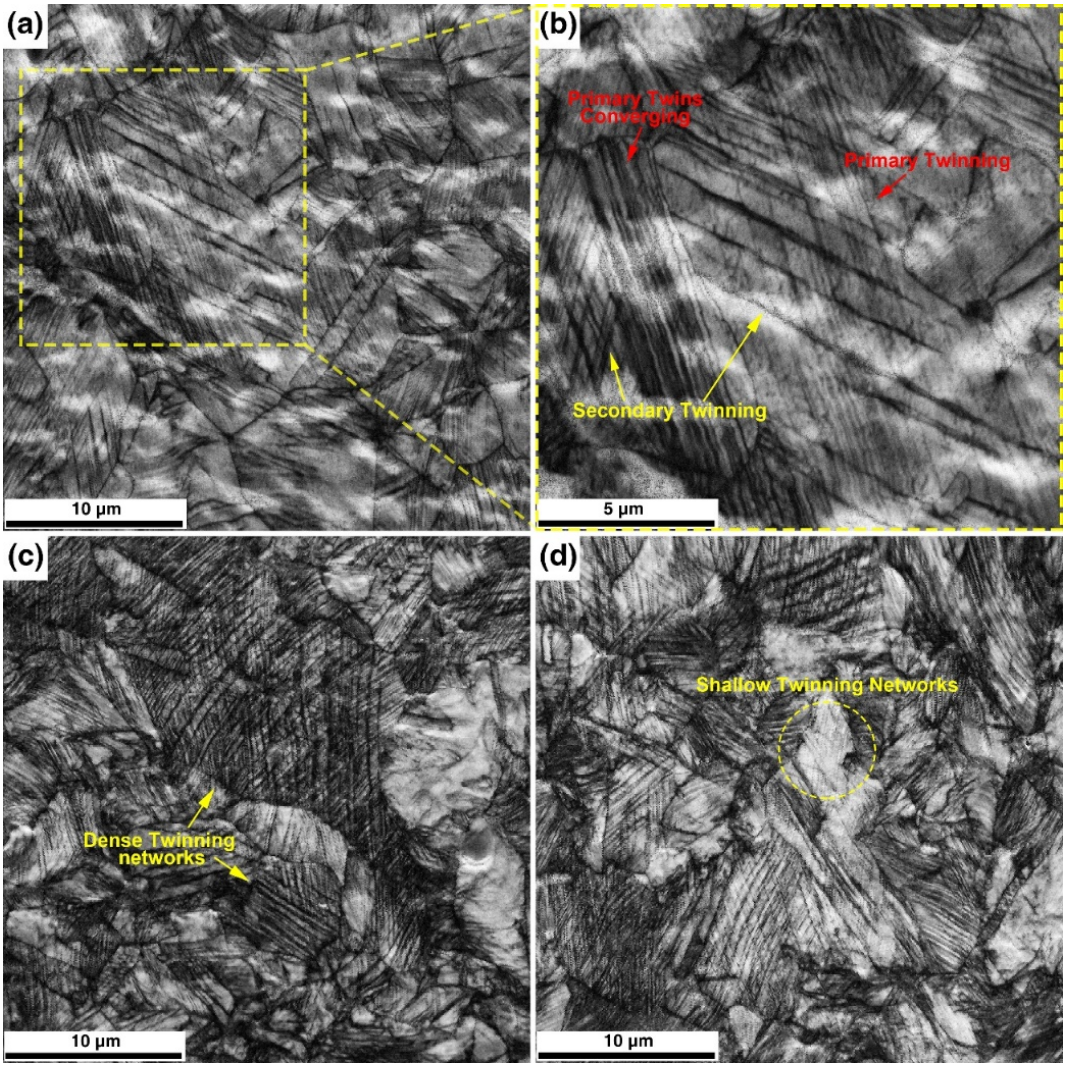

Fig. 3-9 EBSD image quality maps showing the twinning gathering process with increasing tensile strain at 77 K: (a) strain of 0.05; (b) higher magnification of the rectangle zone in (a); (c) strain of ~0.1; (d) strain of ~0.2.

To further investigate the twinning process at 77 K, high-resolution EBSD image quality maps were obtained at different strain levels of ~0.05, ~0.1, and ~0.2 (Fig. 3-9). Even with very a very small strain (~0.05, Fig. 3-9a), most grains were dominated by dense primary twins or primary/secondary twin networks. The rectangle area in Fig. 3-9a was magnified in Fig. 3-9b. Primary and secondary twins were both observed at the low strain level, which could benefit the formation of dense hierarchical twinning networks during subsequent straining. The propagation of twinning usually started from grain boundaries, implying that grain boundaries were the preferable nucleation locations for mechanical twins [301]. As shown in Fig. 3-9b, the primary twins were

very thin and distributed discretely. Then the converge of multiple thin twins was also observed, forming one thick twinning band. As the strain raising to ~0.1, dense twinning networks consisting of thick twins formed, and twins propagated to nearly every grain interior (Fig. 3-9c). When the strain reached ~0.2, more dense twinning networks were observed while some intersecting twinning networks, though very thin, also started to grow in grains with unfavourable orientations (as shown with the yellow circle in Fig. 3-9d).

To further study the influence of temperature on the morphology of the twinning and dislocation, TEM examination was performed on samples deformed to ~0.3 strain at 373 and 77 K, as shown in Fig. 3-10. Twins were observed at both temperatures, which were confirmed by the twin reflections in the associated selected area diffraction patterns (SAED) recorded along the $\langle 011 \rangle$ direction (Fig. 3-10b and d). Based on the distribution and density of twins and dislocations, Fig. 3-10a can be divided into four regions: (1) dense twin zone, (2) dislocation-twin tangling zone, (3) discrete twin zone, and (4) dense dislocation zone. At the dense twin region, high density of nanosized twins were observed starting at grain boundaries and being prolongated through the grain interior. At the discrete twin zone, much fewer twins with a wide twin spacing (~600 nm) were formed. The dislocation-twin tangling zone shows the interaction between dense dislocations and twins, indicating that the dense twin boundaries act as columns trapping dislocations in between. In the dense dislocation zone, some grains remained untwinned and dislocation motion is still the main deformation mechanism, forming thick dislocation walls and large dislocation cells (~3 μm).

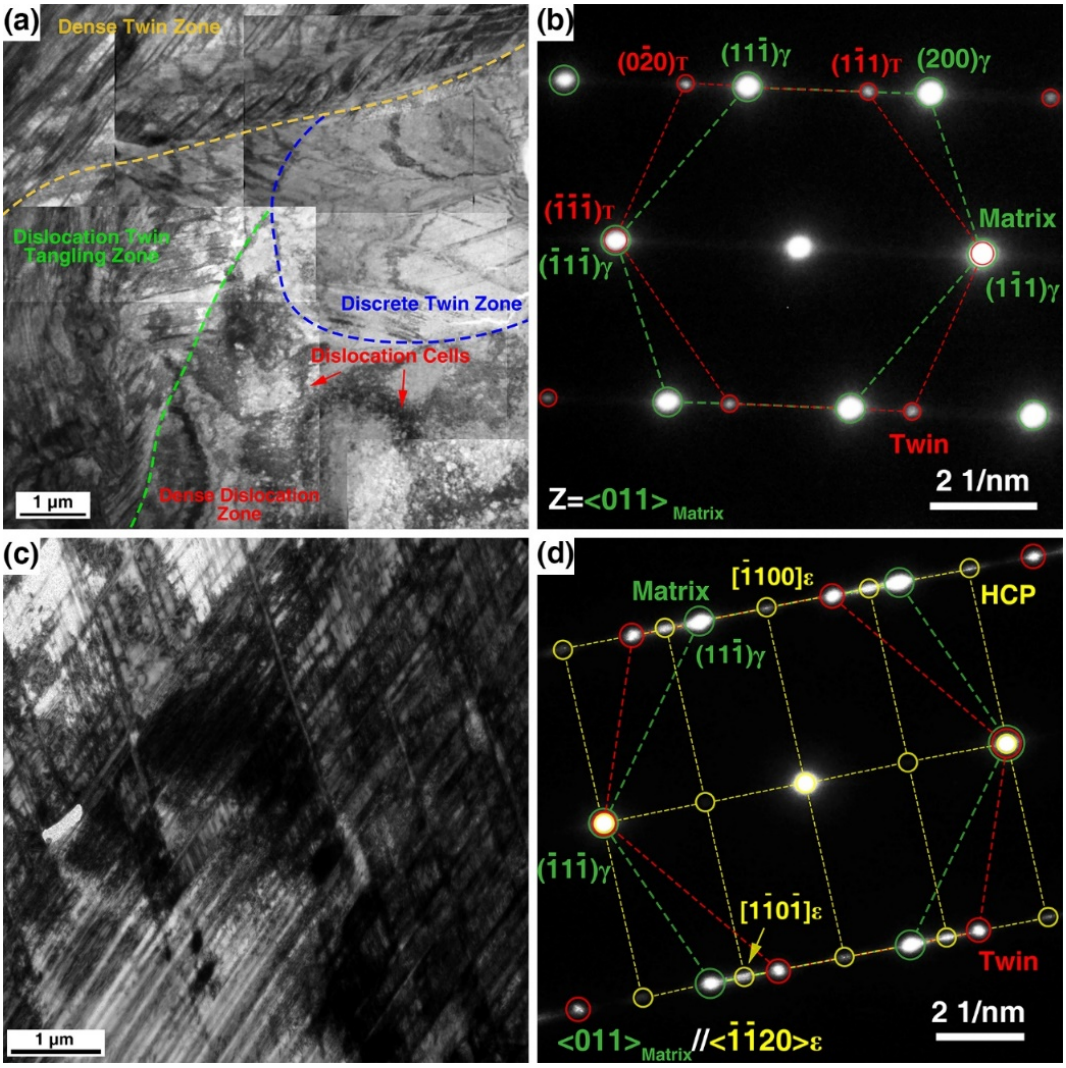

Fig. 3-10 TEM images taken from the sample deformed to true strain ~0.3 at 373 K and 77 K. (a and c) bright-field image at 373 K and 77 K, respectively; (b and d) SAED patterns of (a and c), respectively; shows that the twin density increases with the deformation temperature decreasing and FCC-γ to HCP-ε transition occurred at 77 K.

On the other hand, at 77 K the enhanced twinning activity led to hierarchical twin-twin intersections, trapping dense dislocation in intra-twin regions in Fig. 3-10c. This indicates more effective 3-dimensional twin networks were formed in impeding dislocation motion. Besides, phase transformation was confirmed by the SAED pattern at 77 K (Fig. 3-10d). This is consistent with the previous results obtained from *in situ* neutron diffraction (Fig. 3-10b). The experimental result suggests the gradual transition of deformation behaviour from dislocation motion to twin-twin/dislocation interaction

and even to phase transformation as the test temperature dropped. This agrees well with the SFE-temperature map developed (Fig. 3-7a).

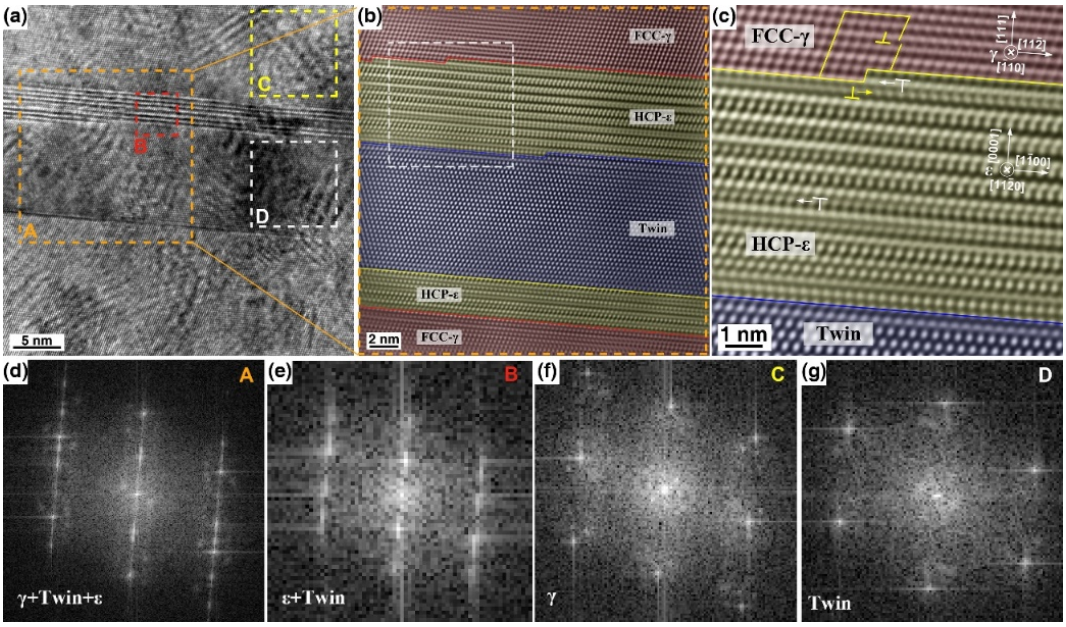

Fig. 3-11 Twinning formation and γ→ε phase transformation of the alloy during deformed at 77 K to a true strain of ~0.3: (a) HRTEM image; (b) atomic image of A area in (a); (c) higher magnification of the white rectangle areas in (b) and (d-g) FFT images at areas of A, B, C and D in (a).

The twin growth and martensite phase transformation (FCC-γ to HCP-ε) at 77 K were further revealed by HRTEM. The TEM sample was extracted from the failed sample at a strain of ~0.3. Fig. 3-11a-c show the HRTEM images focusing on the γ/ε/twin interfaces, viewed along $[\bar{1}10]_\gamma \,//\, (11\bar{2}0)_\varepsilon$ directions. The fast Fourier transformation (FFT) images (shown in Fig. 3-11d-g) were obtained from the marked areas in Fig. 3-11a, identifying the existence of twins and HCP-ε laths. In Fig. 3-11a, one nanosized twin with a thickness of 9 nm was observed, as well as two HCP-ε laths (with a width of 0.7 and 4 nm, respectively) located at the twin-matrix interface. The rectangle area in Fig. 3-11b was magnified in Fig. 3-11c, which shows that several Shockley partial dislocations with different Burger's vectors glided at the edge of HCP-ε laths, creating new stacking faults and leaving HCP-ε laths behind. These results indicate that the FCC-γ to HCP-ε phase transformation preferably occurs at the twin boundaries and the

two microstructural features (twinning and phase transformation) are closely related to perfect dislocations dissociation, following (partial) dislocation reaction and related stacking faults motion. The interaction of two leading partials of two stacking faults on two {111} grain planes can create a stair-rod dislocation via:

$$\frac{a}{6}[2\bar{1}\bar{1}]+\frac{a}{6}[\bar{1}21]\rightarrow\frac{a}{6}[110] \qquad \text{Eq. 3-6}$$

The new born stair-rod dislocation is sessile and can serve as Lomer-Cottrel lock [302] since its Burgers vector is perpendicular to the dislocation line and does not lie on the two {111} planes of the adjacent stacking faults [57]. According to Ref. [90], the Shockley partial dislocations ($b:\frac{a}{6}[\bar{1}21](111)_{\gamma}$) could interact with perfect dislocations ($b:\frac{a}{2}[10\bar{1}](111)_{\gamma}$) during their movement and create straight Frank sessile dislocations ($b:\frac{a}{3}[11\bar{1}](111)_{\gamma}$) lying at the twin-matrix interface. These dense Frank dislocations can affect the dynamic of the twinning and twin boundary expansion, maintaining the high stability of twins and making twin boundaries hard to be penetrated by dislocations. On the other hand, the partial dislocation motion and the newborn stacking faults also play a decisive role in mechanical twin formation and martensite phase transformation. Yang et al. [75] proposed three types of partial dislocations and indicated that the mechanical (de)twinning is caused by gliding one partial dislocation on consecutive $(111)_{\gamma}$ planes. Regarding martensitic phase transformation, when partial dislocations glide from plane B and consecutively on every second $(111)\gamma$ planes, the parent stacking sequence of …ABCABC…(FCC-γ matrix) will transfer into …ACACAC…(HCP-ε laths). These HCP laths preferably initiate at the interface of the twin-matrix. Similar phenomena were also found at other TWIP steels [273,303], where the expansion and growth of HCP laths gradually fulfilled the intra-twin regions.

In summary, the microstructure evolution observed at different temperatures agrees well with the neutron diffraction results (Fig. 3-4) and SFE-deformation mechanism evolution map (Fig. 3-7a). At a high-temperature regime (e.g., 373 K), intensive dislocation motion and multiplication played a major role in accommodating strain due to its high SFE. Twinning-induced hardening was not significant until reaching very high strain conditions. As the test temperature drops, SFE decreases, dislocation preferably to dissociate rather than glide to cater to plastic straining. This enables active partial dislocation motion and rapid SFs formation (i.e., higher SFP rate, Fig. 3-7a), making twinning a more favourable deformation mechanism at cryogenic conditions. When SFE is low enough (e.g., 18.3 mJ/m^{-2} at 77 K) phase transformation from parent FCC phase to HCP laths can be triggered.

3.5 Discussion

In the following, the dependence of yield strength (Fig. 3-3b) and the contribution of dislocation and twinning to flow stress (Fig. 3-3c) will be discussed with dislocation slip system-driven modelling.

3.5.1 Temperature-dependent Yield Strength

The yield point corresponds to the initiation of macroscopic unpinning and gliding of mobile dislocations. As shown in Fig. 3-3a and b, σ_{YS} of the alloy was linearly enhanced by dropping deformation temperature. Prior to the detailed analysis of the temperature dependence of σ_{YS}, it is important to classify the strengthening contributors towards yielding strength. Generally, σ_{YS} is the result of the synergetic effects of

multiple strengthening effects which can be decomposed into athermal ($\sigma_{Athermal}$) and thermal ($\sigma_{Thermal}$) parts:

$$\sigma_{YS} = \sigma_{Athermal} + \sigma_{Thermal} \quad \text{Eq. 3-7}$$

The athermal component is generally related to strengthening resources of a long-range order (> 10 Å), such as initial dislocation density (σ_{dis}), precipitate hardening (σ_{PP}), and grain boundary hardening (σ_{GB}). In our case, the contribution from precipitates (σ_{PP}) can be ignored since the SAED pattern (Fig. 3-2d) and the neutron diffraction spectra (Fig. 3-4) did not show the presence of precipitates, and the alloy remained single-phases (FCC) before yielding. Therefore, $\sigma_{Athermal}$ is determined from the rest two resources: initial dislocation density and grain boundaries.

The hardening effect from dislocation (σ_{dis}) can be calculated with Taylor equation [304]:

$$\sigma_{dis} = M\alpha Gb\rho^{1/2} \quad \text{Eq. 3-8}$$

, in which M=3.06 is the Taylor factor, α is a constant for scaling the interaction strength between dislocations and a value of 0.26 was used here [87,305,306]. It is noted that different α values have been used in TWIP steels, such as 0.136 [72], 0.26 [87,305], and 0.4 [307]. We will show later that α=0.26 is a reasonable value for our TWIP steel. The temperature dependence of Burger's vector (b) has been ignored since the lattice parameter decreases only slightly during cooling down (Fig. 3-12a). The dislocation density of the as-fabricated state (7×10^{13} m^{-2}) was used and the strength contribution from initial dislocations (σ_{dis}^{0}) was estimated to be 124 MPa.

The contribution from grain boundaries was calculated with the classical Hall-Petch formula [308] in which the strength contribution keeps a linear relationship with the inverse square root of average grain size (d):

$$\sigma_{GB} = K_{GB} d^{-1/2} \quad \text{Eq. 3-9}$$

Hall-Petch coefficient (K_{GB}) of 0.357 MPa·m$^{0.5}$ was used based on Ref. [214], yielding the strength improvement from grain boundaries to be 95 MPa.

Meanwhile, barriers inhibiting dislocation gliding in a short range (< 10 Å) can give a rise to the thermal part of Eq. 3-7 [309]. It mainly derives from the thermally initiated dislocation gliding overcoming Peierls lattice potential friction and the pinning effect from solid solution atoms (e.g., carbon) [60,310]. Decreasing temperature can reduce atom vibration frequency and consequently increase the critical stress for the initiation of dislocation gliding. The strain rate $\dot{\varepsilon}$ can be expressed by the Arrhenius relationship [311]:

$$\dot{\varepsilon} = \dot{\varepsilon}_0 \cdot \exp\left(\frac{\Delta G}{kT}\right) \quad \text{Eq. 3-10}$$

, where $\dot{\varepsilon}_0$ is the reference strain rate and a value of 10^8 s^{-1} was assumed according to Ref. [312], k is the Boltzmann constant. ΔG is the free energy of overcoming barriers and can be well described with a phenomenological relation [311]:

$$\Delta G = Gb^3 g_0 \left[1 - \left(\frac{\sigma_{Thermal}}{\sigma_0} \cdot \frac{G_0}{G_T}\right)^p\right]^q \quad \text{Eq. 3-11}$$

, where G_0 and G_T is the shear modulus of the alloy at 0 K and at temperature T, p and q are two constants describing the characteristics of the obstacles, g_0 is a scaling factor and a material constant, σ_0 is the mechanical threshold stress to overcome the

lattice friction without thermal activation at 0 K. The temperature dependence of the shear modulus was fitted with an equation proposed by Y. P. Varshni [313]:

$$G_T = G_0 - A/\left[\exp\left(B/T\right) - 1\right] \quad \text{Eq. 3-12}$$

The two adjustable parameters (A and B) were determined to be 77.5 and 1574, respectively, by fitting the shear modulus versus temperature curve (Fig. 3-12a). G_0 of 71.36 GPa was obtained by extrapolating Eq. 3-11 to 0 K (Fig. 3-12a). Similar temperature dependence of shear modulus of three Fe–18Mn–0.6C–xAl TWIP steels was reported in Ref. [60], where the shear modulus is slightly higher than our study. Combining Eq. 3-10 and Eq. 3-11 yields the relationship between deformation temperature and $\sigma_{Thermal}$:

$$\sigma_{Thermal} = \sigma_0 \left(\frac{G_T}{G_0}\right)\left[1 - \left(\frac{kT}{g_0 G_T b^3} \ln\frac{\dot{\varepsilon}_0}{\dot{\varepsilon}}\right)^{\frac{1}{q}}\right]^{\frac{1}{p}} \quad \text{Eq. 3-13}$$

This indicates the mechanical threshold value at 0 K, σ_0 can be decreased by the increasing thermal activation as a result of temperature rise. The strain rate is 9×10^{-4} s^{-1} in the present study and the two constants (p and q) were set to be 0.5 and 1.5 [314], respectively. Therefore, the normalized temperature-related component $\left(\frac{\sigma_{Thermal}}{G_T}\right)^p$ of σ_{YS} and the normalized temperature $\left(\frac{kT}{G_T b^3} \ln\frac{\dot{\varepsilon}_0}{\dot{\varepsilon}}\right)^{\frac{1}{q}}$ was linearly fitted in Fig. 3-12b. All measured data points can be well fitted into a line, indicating that the high-temperature sensitivity of the σ_{YS} (Fig. 3-12b) originates from the increase in the lattice friction stress which is estimated to be 898 MPa at 0 K by extrapolating the fitted straight line to 0 K (Fig. 3-12b). The temperature sensitivity of σ_{YS} observed in our

study is very similar to that in Ref. [310], where the effect of carbon content is emphasized. The thermal component of a TWIP steel with 0.6% C can be significantly improved by ~350 MPa (which is 318 MPa in our case) when decreasing temperature from room temperature to 77 K.

In summary, the strengthening contributions to yield strength from different sources were calculated. The contribution from grain boundaries was 95 MPa at all tested temperatures. The contribution from dislocations was 124 MPa. The lattice friction stress increased from 135 MPa to 541 MPa as the deformation temperature dropped from 373 K to 77 K, which is the main reason for the increase of yield strength at lower test temperatures.

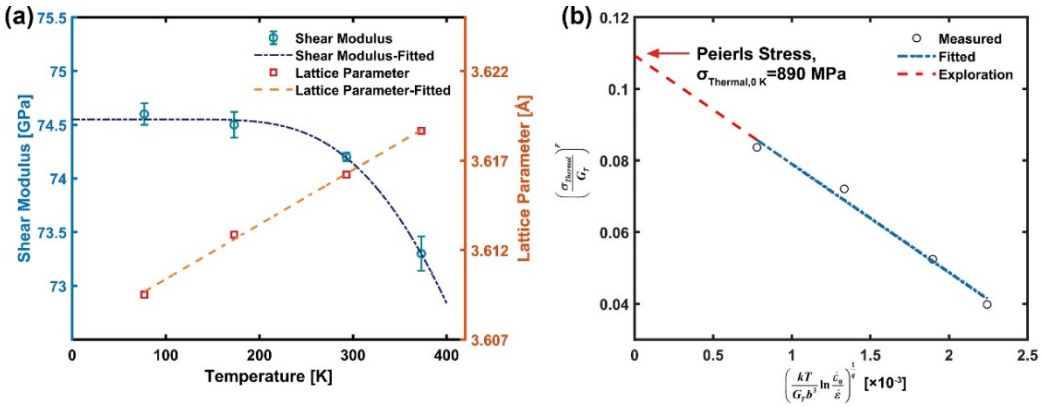

Fig. 3-12 (a) Temperature dependence of the shear modulus and lattice parameter of the alloy and (b) normalized thermally activated component of the yielding stress with respect to the normalized temperature.

3.5.2 Plastic Deformation

At the plastic stage, in addition to grain boundary strengthening and lattice friction stress (σ_f), there are two additional contributors to the flow stress: (1) dislocation multiplication, and (2) twinning formation, and martensite phase transformation. The strengthening effect from dislocation density (σ_{dis}) can be calculated using Eq. 3-8. The dislocation density was measured from the *in situ* neutron diffraction pattern and shown

in Fig. 3-7b. This allows us to calculate σ_{dis} as a function of strain (e.g., a at 77 K) using Eq. 3-8. With regarding phase transformation, the fraction of transformed HCP-ε laths is very small and is prone to locate at the twinning boundaries (Fig. 3-11b and c). Meanwhile, stand-alone HCP-laths have a wide spacing distance and thin thickness (< 5 nm), leading to the very limited ability of impeding dislocation motion and thus low contribution towards strength [315]. Hence, we ignored the contribution from phase transformation. Therefore, the strengthening contribution from twinning (σ_{twin}) can be calculated indirectly as follows:

$$\sigma_{twin} = \sigma - \sigma_f - \sigma_{GB} - \sigma_{dis} \quad \text{Eq. 3-14}$$

, where σ is the measured true stress. σ_{twin} versa true strain at 77 K was plotted in Fig. 3-13a.

Alternatively, twin boundaries act as grain boundaries and its strengthening effect can be calculated with the Hall-Petch model directly [315]:

$$\sigma_{twin} = FK_{twin}l^{-0.5} \quad \text{Eq. 3-15}$$

, where F is the volume fraction of twins, l is the twin spacing, K_{twin} is the Hall-Petch coefficient of twinning. According to Refs. [70,316], the Hall-Petch constant for twinning is about equal to that for the slip in Fe-22Mn-0.6C TWIP steel. In our study, K_{twin} is also assumed to be the same as K_{GB} [272]. This value has been widely used to model twin contribution to the strength of TWIP steels with different compositions (e.g. in Refs. [61,317,318]) with great success. Another study by Kusakin et al. [74] shows that K_{GB} =0.35 MPa·m$^{0.5}$ via data fitting of various TWIP steels, which is close to 0.357 MPa·m$^{0.5}$ used by De las Cuevas et al. [214] and those reported in Cr-Ni austenitic steels [319]. Therefore, we used K_{twin} =0.357 MPa·m$^{0.5}$. F can be estimated with the stereological analysis of Fullman [320]:

$$\frac{1}{l}=\frac{1}{2e}\frac{F}{1-F} \quad \text{Eq. 3-16}$$

, in which *e* is the thickness of twins. Twin boundary density is usually calculated from TEM [87,91] or SEM [321] images. Based on TEM images, *l* was measured to be 212 nm and *e* was 95 nm when the strain was ~0.2 at 77 K. With strain increased to ~0.3, twin spacing distance decreased to 153 nm and their thickness increased to 110 nm. Based on Fig. A-4a and Fig. A-4b, *F* was equivalent to 0.474 and 0.589 at strains of ~0.2 and ~0.3, yielding the twin contribution of 376 and 538 MPa, respectively. In Fig. 3-13a, the twinning contribution calculated from TEM images at a true strain of 0.2 and 0.3 was compared with the indirect calculation with Eq. 3-14 . The two methods agree very well.

As we stated before, various α values were used in Eq. (8) in literature, among which, we chose to use $\alpha = 0.26$. This also allows us to verify the use of $\alpha = 0.26$ in our study. The stress level after yielding can be predicted by Eq. 3-17:

$$\sigma_{\mathrm{mod}} = \sigma_{twin} + \sigma_{dis}^{\varepsilon} - \sigma_{dis}^{0} + \sigma_{YS} \quad \text{Eq. 3-17}$$

, in which σ_{mod} is the predicted flow stress. $\sigma_{dis}^{\varepsilon}$ is the strengthening contribution from dislocations at strain ε, while σ_{dis}^{0} is the strengthening contribution from initial dislocations in the as-received sample, both of which can be calculated from Eq. 3-8. The difference (σ_{diff}) between experimentally measured stress (σ_{exp}) and modelling results (σ_{mod}) can be calculated by Eq. 3-18:

$$\sigma_{diff} = |\sigma_{\mathrm{exp}} - \sigma_{\mathrm{mod}}| \quad \text{Eq. 3-18}$$

Combining Eq. 3-8, Eq. 3-15, Eq. 3-17, and Eq. 3-18, we can determine σ_{diff} with different α values as shown in Table 3-3. When α=0.26, σ_{diff} is the smallest among the three commonly used α values.

Table 3-3 σ_{diff} at two strain levels using different α values.

K_{twin} [MPa·m$^{0.5}$]	α	Strain	σ_{diff} [MPa]
0.357	0.136	0.2	88.1
0.357	0.136	0.3	167.0
0.357	0.26	0.2	65.3
0.357	0.26	0.3	33.1
0.357	0.4	0.2	238.7
0.357	0.4	0.3	259.0

Fig. 3-13a displays the contribution from various strengthening resources at 77 K, showing the growing strength enhancement from both twinning (σ_{twin}) and dislocation (σ_{dis}) as the plastic strain increases. The twinning contribution was not significant at low strain due to its low density. However, during tensile deformation, it increased faster than dislocation contribution. Twinning gradually became a comparable strengthening resource as dislocations at very large strain (higher than around 0.4). When strain reached 0.34, 507 MPa was from twinning while dislocations contributed 574 MPa. This phenomenon can be ascribed to that the dynamic recovery curbed dislocation multiplication at high strain conditions even at an extremely low temperature of 77 K, but nano-twins continuously increased during the deformation of the low-SFE TWIP steel.

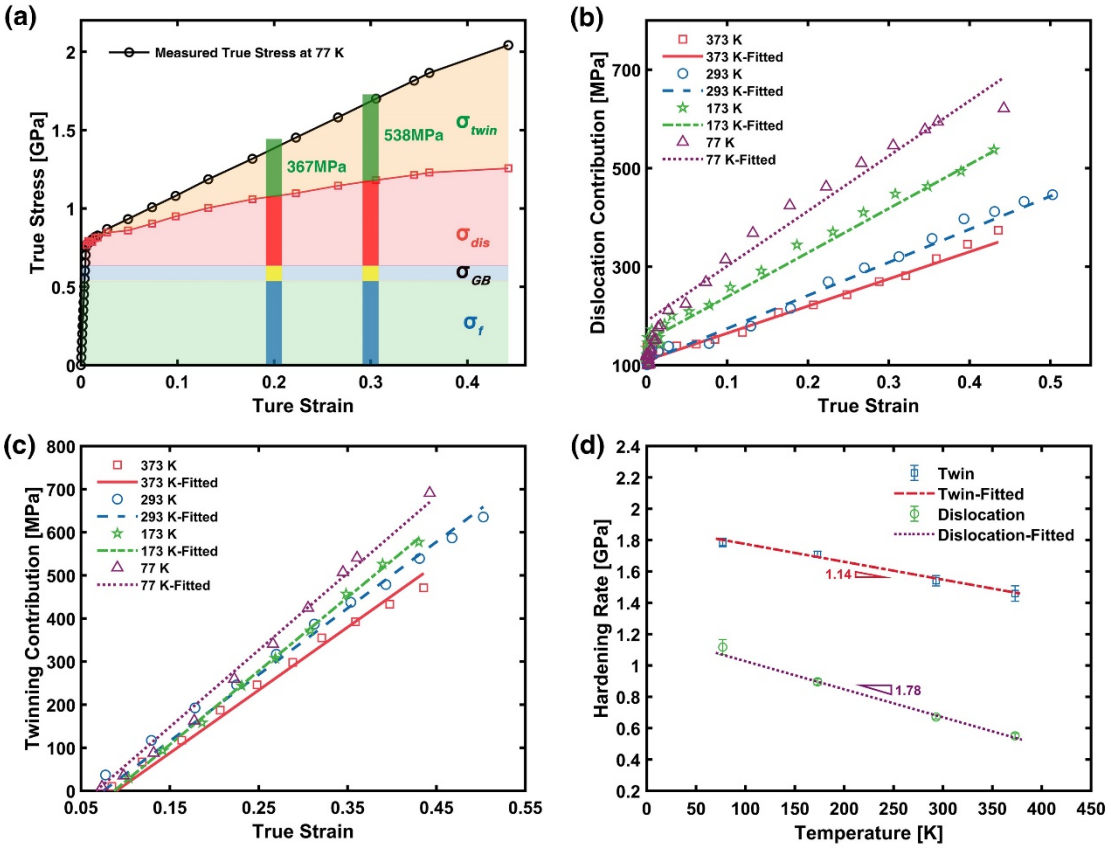

Fig. 3-13 (a) The respective contribution of multiple resources to the total flow stress; strain hardening contribution from (b) dislocation and (c) twin density at different temperatures; (d) temperature dependence of the hardening rate from dislocation and twinning. Note: σ_{twin}, σ_{dis}, σ_{GB}, and σ_{f}, represents the strengthening effects from twins, dislocations, grain boundaries, and lattice friction stress.

The strengthening contributions from dislocations and twins at different temperatures were plotted against true strain in Fig. 3-13b and c, respectively. Due to the pre-existing dislocations, dislocation contribution started at around 124 MPa for all 4 temperatures. It increased almost linearly with strain after yielding. The curves were fitted with linear functions and the slopes of the fitted lines were defined as dislocation-induced hardening rate ($\partial\sigma_{dis}/\partial\varepsilon$). The twinning contribution was also shown to be linearly increasing with true strain (Fig. 3-13c). Similarly, the slope of the fitted line is defined as the twinning-induced hardening rate ($\partial\sigma_{twin}/\partial\varepsilon$). These two figures show a synergetic hardening mode of twinning and dislocation at the low-temperature range (from 373 to 77 K). The strain hardening capacity of this TWIP steel comes from both

dislocation-induced hardening and twinning-induced hardening. As the deformation temperature decreased, the strengthening contributions from dislocation and twinning both increased. On the one hand, temperature dropping inhibited some thermally activated processes (such as thermally driven cross-slip) and dynamic recovery [322], maintaining a high level of dislocation density and slowing down dislocation motion. Thus, the dislocation capacity (the maximum dislocation density) can be improved, achieving higher strengthening effects. On the other hand, a growing number of twins was produced as the SFE was reduced from 34.8 mJm^{-2} at 373 K to 17.2 mJm^{-2} at 77 K. It is also worth noting that although the twinning contribution at 293 K is less significant than at 77 K, it still grew rapidly with strain and contribute significantly to strength: 316 MPa is from dislocations while twins contributed 394 MPa at a strain of 0.36. This is contrary to Ref. [72], where the twinning contribution to flow stress at 293 K is small and almost constant during deformation. This can be ascribed to the different compositions of the two TWIP steels and therefore the disparity in SFE. Meanwhile, the ductility of the alloy was decreased from 0.72 at 293 K to 0.56 at 77 K even with multiple strengthening mechanisms activated. The high density of dislocations and twinning boundaries can bring high strength by providing dense new dislocation motion barriers. However, the high density of barriers can evolve into dislocation walls, newborn phases [323], and the intersection of twinning [324], which can significantly increase the internal stress and serve as weak positions for crack initialization, hence reducing the ductility. A similar phenomenon can also be found at Ref. [325].

Fig. 3-13d shows the hardening rates of twinning and dislocation as a function of temperatures, interestingly, both of which show an almost linear relationship with respect to deformation temperature. Therefore, their relationship can be described as:

$$\frac{\partial \sigma_{dis}}{\partial \varepsilon \partial T} = -m_{dis} \quad \text{Eq. 3-19}$$

$$\frac{\partial \sigma_{twin}}{\partial \varepsilon \partial T} = -m_{twin} \quad \text{Eq. 3-20}$$

, where m_{dis} and m_{twin} are slopes of the hardening rate curves of dislocation and twinning respectively. With the help of linear curve fitting, m_{dis} was found to be about 1.78 MPa·K^{-1}, which is higher than m_{twin}=1.14 MPa·K^{-1}. The reason why the hardening rates of twinning and dislocation versus temperatures are both linear is unclear. This could be related to the linear relationship between SFE and temperature (Fig. 3-7a). More work would be needed to verify this observation on other alloys with the TWIP effect. If validated, new analytic and numerical models could be developed to predict the flow stress evolution of TWIP alloys.

3.6 Conclusions

In this study, we investigated the temperature dependence of the deformation mechanisms operating in a high Mn TWIP steel (Fe-24Mn-4Cr-0.5Cu-0.5C). *In situ* neutron diffraction was employed to map the evolution of multiple microstructure features (e.g., lattice strain, stacking fault probability, stacking fault energy, and dislocation density) and record real-time mechanical responses. The microstructure evolution was then confirmed via post-mortem microscopy characterization. The investigation leads to the following conclusions:

(1) A steady increase in the tensile strength was observed as the test temperature dropped, maintaining high ductility (over 50%). The superior combination of engineering tensile strength (σ_{YS} of 760 MPa, σ_{UTS} of 1312 MPa) was obtained at 77 K, which is significantly higher than that at 373 K (σ_{YS} of 354 MPa, σ_{UTS} of 796 MPa).

(2) Via *in situ* neutron diffraction measurement, the stacking fault probability at different strain conditions was calculated. It increased almost linearly with the strain. Its increase rate became higher at lower test temperatures.

(3) SFE values of the alloy as a function of temperature were estimated, which was 34.8 mJm^{-2} at 373 K and decreased to 17.2 mJm^{-2} at 77 K, resulting in a significant increase in twin density and even triggering martensitic transformation from FCC-γ to HCP-ε at 77 K.

(4) The dislocation density evolution was calculated using the modified Williamson-Hall method. The as-fabricated samples had a dislocation density of around 7×10^{13} m^{-2}. The dislocation density increased during tensile straining after yielding. Its rate of increase was higher at lower temperatures. The maximum value of 1.82×10^{15} m^{-2} was obtained when deforming at 77 K with a true strain of 0.44.

(5) The respective contributions of the flow stress from twins, dislocations, grain boundaries, and solid solution during elastic, and plastic deformation were calculated. The increase of yield strength at lower temperatures was due to a significant increase of lattice friction stress (from 135 MPa at 373 K to 541 MPa at 77 K).

(6) During plastic deformation, dislocation hardening and TWIP effects worked synergistically in addition to grain boundary and solute strengthening. With a very high strain hardening rate, the strength contribution from twinning increases rapidly, making twinning becomes a comparable strength contributor of dislocations at large strain conditions.

Chapter 4. TWIP-TRIP Transition of High Mn steels: the role of Cu

Paper in Submission

Lei Tang[a], Fuqing Jiang[b], Huibin Liu[c], Saurabh Kabra[d], Biao Cai[a], ***In situ neutron diffraction reveals the effect of Cu on cryogenic mechanical performance of TWIP steels***, to be submitted to Acta Materialia.

Acknowledgement of Collaborative Work

Lei Tang conceived and designed the experiment, performed the experiment, interpreted the data, and wrote the manuscript. Saurabh Kabra and Fuqing Jiang assisted in performing experiments. Biao Cai assisted with designing the experiments, revising the manuscript, and data analysis. Huibin Liu assisted with the preparation of the material.

[a] School of Metallurgy and Materials, University of Birmingham, B15 2TT, United Kingdom
[b] Shenyang National Laboratory for Materials Science, Institute of Metal Research, Chinese Academy of Sciences, Shenyang 110016, China
[c] BAOSHAN IRON & STEEL CO., LTD, Shanghai 201900, China
[d] ISIS Facility, Rutherford Appleton Laboratory, Didcot OX11 0QX, United Kingdom

4.1 Abstract

High manganese steels are emerging as promising structural materials for cryogenic applications due to their low production cost and great potential in achieving an excellent strength-ductility combination. Micro-alloying serves as a desirable method in manipulating stacking fault energy (SFE) of the steels and thus tailoring the mechanical performance. In this study, we investigated the dedicate role of Cu addition played on the mechanical and microstructural responses of high manganese steels at the low-temperature range (293, 173, and 77 K) via *in situ* neutron diffraction and microscope characterizations. The addition of 1wt.%Cu to the steel not only effectively improved the yield strength (YS) and elongation but also increased the SFE thus postponing the martensite formation. For both high Mn steels, as deformation temperature decreased, the tensile strength was increased linearly, the formation of stacking faults and dislocation was promoted, and the SFE almost linearly decreased with a slope of about 0.06 $mJm^{-2}\cdot K^{-1}$. For the non-Cu-added steel, the best mechanical properties appeared at 77 K with YS of 700 MPa, ultimate tensile strength (UTS) of 1361 MPa, and elongation of 0.68. The dominant deformation mechanism transformed from twinning at 293 K when SFE is 26.8±0.5 mJm^{-2} to martensite phase transformation at 77 K while SFE is 15.5±1.7 mJm^{-2}. In the 1%-Cu-added steel, the best mechanical performance was also achieved at 77 K (YS: 793 MPa, UTS: 1323 MPa, and elongation: 0.86). Twinning and dislocation multiplication were the main deformation mechanisms across the three temperatures. The contributions to YS and flow stress from lattice friction, grain boundary, dislocation, deformation twins, and phase transformation were determined. The work revealed the critical role of Cu addition in tailoring the SFE and the resulting deformation mechanisms, paving the way in designing new high manganese steels with superb mechanical properties for cryogenic applications.

4.2 Introduction

High-Mn (15-30 wt.%) steels are exhibiting ever-growing importance in multiple applications for liquid natural gas storage/transmission, and have the potential to be used as structural materials for superconducting magnets due to their excellent strength-ductility balance, desirable strength/weight ratio [326] and lower cost compared to other austenitic steels [153], and 9 % Ni steels [13]. Recently, more prominent strengthening effects and excellent strength-ductility combinations of high Mn steels in a low-temperature range was reported [135,141,327]. The superior mechanical performance of high-Mn steels originates from their ability to synergistically activate multiple strengthening mechanisms, including dislocation motions, TWinning-Induced-Plasticity (TWIP) and TRansformation-Induced-Plasticity (TRIP) effects. TWIP effect can be achieved by introducing high density of strain-induced twin boundaries to impede dislocation motion, while the TRIP effect can be activated when the parent austenitic face-centred cubic (FCC) austenite is transferred into martensite with hexagonal close-packed (HCP)/body-centred tetragonal (BCT) structure under strain. The dominant deformation mechanism of the high-Mn steels is strongly dependent on their inherent stacking fault energy (SFE) [135,138,259,328], which is defined as the excess energy required to dissociate perfect dislocations and separate partial dislocations infinitely. The decrease of SFE can lead to the shifting of the dominant deformation mechanism: from dislocation motion (SFE > 45 mJm^{-2}) to TWIP (45 mJm^{-2} > SFE > 18 mJm^{-2}) and TRIP (SFE < 18 mJm^{-2}).

SFE can be determined by many factors including strain rate, deformation temperature, grain size, and chemical composition [60,135,141,329,330]. SFE decreases significantly with the decrease of temperature [135,282,327]. The high SFE at high

temperatures can limit the strain hardening effect due to the inability to activate multiple deformation mechanisms [135]. The low SFE at low temperatures, sometimes, can be detrimental to the mechanical performance, e.g., yield strength (YS) and ductility [63,282,331]. Wang et al. [63] indicated that the abundance of strain-induced martensite phases can reduce the YS due to the imposed pre-yield transformation stress. Saeed-Akbari [331] showed that when SFE dropped from 35 mJm^{-2} to ~0 mJm^{-2}, the elongation to fracture of high Mn steels was significantly decreased from 0.28 to 0.08. Notably, there is also a need to avoid the formation of ferromagnetic martensite phases during loading, which can be induced when the SFE is very low, particularly for applications in superconducting magnets [2]. Therefore, precisely controlling the SFE to a desirable range is critical in tailoring the strengthening mechanisms and designing the mechanical performance for specific working conditions, e.g., cryogenic applications. This requires the combination of effective SFE-adjusting methods and accurate SFE measurement. *In situ* neutron diffraction coupled with tensile testing at cryogenic temperatures, which can be used to accurately depict SFE evolution as a function of temperature [102,185,282], is a powerful tool to study the relationship between mechanical responses and deformation mechanisms of high Mn steels [327].

Recently, Cu alloying is emerging as a low-cost and high effective method to increase the SFE of TWIP steels [329,330,332,333]. Dumay et al. [334] indicated that the SFE of the high-Mn steel can be increased by 1.52 mJm^{-2} for 1 wt.% of Cu addition. Gonzalez et al. [335] found out that the uniform elongation of an austenitic stainless steel is improved and the martensite formation is suppressed by Cu addition. The effects of Cu on mechanical performance, however, is still under debate. Lee et al. [329] indicated that the addition of Cu has almost no influence on the YS of the Fe-Mn-C-Al steel, while the kinetics of twin formation was suppressed and the ultimate tensile

strength (UTS) was decreased. On the contrary, Choi et al. [69] found out that both YS and UTS can be decreased with increasing Cu content. Peng et al. [330] showed that the YS of Fe-20Mn-1.3C increased from 470 MPa to 538 MPa after adding 3 wt.% Cu due to the solid solution strengthening. Therefore, it is important to further shed a light on the effects of Cu on SFE, deformation mechanisms, and mechanical behaviours, especially in cryogenic conditions where the effects of Cu addition [69] have rarely been explored.

Herein, we investigated the deformation mechanisms and mechanical properties of two high Mn steels with different Cu concentrations (Fe-24Mn-4Cr-0.5C and Fe-24Mn-4Cr-0.5C-1Cu, weight percent and hereafter) at low temperatures (293, 173, and 77 K). The *in situ* neutron diffraction and tensile tests were performed to track the microstructure evolution and mechanical responses during deformation. The neutron diffraction spectra analysis allowed us not only to determine key materials parameters, e.g., lattice parameter, elastic moduli, single-crystal elastic constants, and SFE as a function of temperature, but also to observe the evolution of multiple microstructural features during straining, such as lattice strain, stacking fault probability (SFP), and dislocation density. Meanwhile, post-mortem TEM characterization was performed on the fractured samples to observe the deformed microstructures. The strengthening contributions from different resources, including grain boundaries, dislocations, twins, and martensite phases were then calculated and compared. Based on these results, the effects of Cu addition on SFE, deformation mechanisms, and mechanical performance at the low-temperature range were then discussed in detail.

4.3 Materials and Methods

4.3.1 Materials Processing

The two high-Mn steels with different Cu concentrations, Fe-24Mn-4Cr-0.5C and Fe-24Mn-4Cr-1Cu-0.5C wt.% steels (marked as the 0-Cu and 1-Cu steels, respectively), were provided by Baowu steel company. High purity metals (purity ≥99.9%) were melted to cast ingots with vacuum induction melting and casting. The casted ingots were hot-rolled at 1200 K after homogenization treatment at 1473 K for 48 h. Then the ingots were cooled down to room temperature by water quenching.

4.3.2 *In Situ* Neutron Diffraction

In situ time-of-flight neutron diffraction and tensile tests were performed at the beamline of ENGIN-X, ISIS spallation neutron source, the Rutherford Appleton Laboratory, UK [185]. The schematical illustration of the *in situ* neutron diffraction experiments can be seen in Ref. [327]. Before reaching the tensile bars, the incident neutron beam with a continuous range of speed was modified by the moderator and slits (with a size of 4×4 mm^2). The axial and radial signal detectors (correspond to the north and south detector, respectively) were mounted perpendicularly to the incident beam, collecting the diffracted neutrons from crystallographic planes subjected to tensile and compressive stress, respectively. The size of the diffracted neutron beams was defined by the two collimators, deciding the scattering gauge volume of $4 \times 4 \times 4$ mm^3. Dog-bone tensile bars with a gauge volume of $\Phi 8 \times 32$ mm^3 as well as an Instron stress rig were mounted 45° to the incident beam. Tensile tests were carried out in a high-vacuum ($< 10^{-5}$ Pa) chamber equipped with built-in heaters and a liquid helium circulation system to achieve cryogenic deformation. The high-vacuum and low-temperature

environments were stabilized for 30 mins before straining. The sequential signal collection was performed during the tensile tests and each consumes 20 mins between tensile loading intervals. An extensometer was used to measure the strain. Before tensile tests, a standard CeO_2 sample was used to calibrate the experimental geometry and subtract the instrumental broadening effect.

The single peak-fitting was performed with pseudo-Voigt function and the Rietveld refinement were performed on the TOPAS software (Coelho Software, Australia), allowing the determination of peak intensity, full width at half maximum (FWHM), peak position, and lattice parameter (a). The lattice strain (ε_{hkl}^{exp}) is defined as the change of the spacing distance of a given crystallographic plane in response to external stress. It then can be determined with:

$$\varepsilon_{hkl}^{exp} = \frac{d_{hkl} - d_{hkl}^{0}}{d_{hkl}^{0}} \qquad \text{Eq. 4-1}$$

, where d_{hkl}^{0} and d_{hkl} is the inter-planar distance of $\{hkl\}$ grain plane without stress and under different stress conditions, respectively. The approaches we used to calculate the stacking fault probability (SFP), stacking fault energy (SFE) and dislocation density can be found in Ref. [327].

4.3.3 SFE Prediction Based on Thermodynamics

The SFE of the two steels were explored with both experimental measurement based on neutron diffraction (see details at Refs. [282,327]) and theoretical calculations (based on thermodynamics).

The thermodynamic modelling approach of calculating the SFE was first proposed by Olson and Cohen [154]. Formed by the dissociation of perfect dislocations, the stacking faults can disrupt the normal sequence of the {111} plane. Therefore, this model treats

the stacking faults as a thin layer of HCP lath separating the normal stacking matrix into two parts. The ideal SFE can then be expressed with:

$$SFE = 2\rho\Delta G^{\gamma\to\varepsilon} + 2\sigma, \qquad \text{Eq. 4-2}$$

where ρ is the molar surface density along {111} planes, $\Delta G^{\gamma\to\varepsilon}$ is the molar Gibbs energy of the phase transformation ($\gamma \to \varepsilon$), and σ=5 mJm^{-2} is the interfacial energy per unit area of phase boundary as its value is generally taken between 5 and 15 mJm^{-2} for transition metals [146,336,337]. The molar surface density ρ can be calculated with the lattice parameter a and Avogadro's constant N:

$$\rho = \frac{4}{\sqrt{3}}\frac{1}{a^2 N}. \qquad \text{Eq. 4-3}$$

In this model, the steels were assumed to be in a regular solid solution state, the substitutional atoms were at the lattice sites while interstitial atoms locate at the octahedral site of the FCC and HCP lattice. The $\Delta G^{\gamma\to\varepsilon}$ in Eq. 4-11 includes the chemical contribution of all substitution elements to Gibbs free energy of $\gamma \to \varepsilon$ phase transformation ($\Delta G^{\gamma\to\varepsilon}_{FeMnX}$), the contribution of interstitial carbon ($\Delta G^{\gamma\to\varepsilon}_{FeMnX/C}$), and atom magnetic contribution of Gibbs free energy ($\Delta G^{\gamma\to\varepsilon}_{mg}$) originating from the Néel transition (paramagnetic to antiferromagnetic) [338]:

$$\Delta G^{\gamma\to\varepsilon} = \Delta G^{\gamma\to\varepsilon}_{FeMnX} + \chi_C \Delta G^{\gamma\to\varepsilon}_{FeMnX/C} + \Delta G^{\gamma\to\varepsilon}_{mg}, \qquad \text{Eq. 4-4}$$

in which χ_i is the molar fraction of each alloying element.

According to Ref. [135], the chemical contribution $\Delta G^{\gamma\to\varepsilon}_{FeMnX}$ and the contribution from carbon addition $\Delta G^{\gamma\to\varepsilon}_{FeMnX/C}$ can be calculated with [334]:

$$\begin{aligned}\Delta G^{\gamma\to\varepsilon}_{FeMnX} = {} & \chi_{Fe}\Delta G^{\gamma\to\varepsilon}_{Fe} + \chi_{Mn}\Delta G^{\gamma\to\varepsilon}_{Mn} + \chi_{Cr}\Delta G^{\gamma\to\varepsilon}_{Cr} + \chi_{Cu}\Delta G^{\gamma\to\varepsilon}_{Cu} + \chi_C\Delta G^{\gamma\to\varepsilon}_{C} + \\ & \chi_{Fe}\chi_{Mn}\Delta\Omega^{\gamma\to\varepsilon}_{FeMn} + \chi_{Fe}\chi_{Cr}\Delta\Omega^{\gamma\to\varepsilon}_{FeCr} + \chi_{Fe}\chi_{Cu}\Delta\Omega^{\gamma\to\varepsilon}_{FeCu} + \chi_{Fe}\chi_C\Delta\Omega^{\gamma\to\varepsilon}_{FeC}\end{aligned} \qquad \text{Eq. 4-5}$$

$$\Delta G_{FeMnX/C}^{\gamma\to\varepsilon} = \frac{1246}{\chi_C}\left(1-e^{-24.29\chi_C}\right) - 17.175\chi_{Mn} \quad \text{Eq. 4-6}$$

The magnetic contribution to the Gibbs free energy change $\Delta G_{mg}^{\gamma\to\varepsilon}$ was calculated with

$$\Delta G_{mg}^{\gamma\to\varepsilon} = G_{mg}^{\varepsilon} - G_{mg}^{\gamma} \quad \text{Eq. 4-7}$$

, where $G_{mg}^{\varphi}(\varphi = \gamma, \varepsilon)$ is represented by

$$\Delta G_{mg}^{\varphi} = RT\ln(1+\beta^{\Phi}) f^{\Phi}(\tau^{\Phi}), \mu = \gamma, \varepsilon \quad \text{Eq. 4-8}$$

, where R is the gas constant, T is the temperature, β^{Φ} is the magnetic moment of the phase φ divided by the Bohr magneton μ_B, and $f^{\Phi}(\tau^{\Phi})$ is a polynomial function of the scaled Néel temperature $\tau^{\Phi} = T / T_{Néel}$ of phase φ [339]. The magnetic moment of the γ phase was determined with the simple mixing rule of the magnetic moment of each element:

$$\beta^{\gamma} = \chi_{Fe}\beta_{Fe} + \chi_{Mn}\beta_{Mn} - \chi_{Cr}\beta_{Cr} - \chi_{Fe}\chi_{Mn}\beta_{FeMn} - \chi_C\beta_C, \quad \text{Eq. 4-9}$$

in which β_{Fe}=0.7, β_{Mn}=0.62, β_{Cr}=0.8, β_{FeMn}=0.64, and β_C=4 [334,339,340] are empirical values for the pure elements' magnetic moments. The magnetic moments of the martensite phase ε can be calculated with the following equation [334,341]:

$$\beta^{\varepsilon} = \chi_{Mn}\beta_{Mn} - \chi_C\beta_C \quad \text{Eq. 4-10}$$

The magnetic transition temperature of each phase $T_{Néel}^{\Phi}$ was calculated with empirical expressions in Refs. [340,341]:

$$T_{Néel}^{\gamma} = 251.71 + 681\chi_{Mn} - 272\chi_{Cr} - 1740\chi_C \quad \text{Eq. 4-11}$$

$$T_{Néel}^{\varepsilon} = 580\chi_{Mn} \quad \text{Eq. 4-12}$$

According to Ref. [155], the term $f^{\Phi}(\tau^{\Phi})$ in Eq. 4-8 can be expressed with the following equation:

$$f^{\Phi}(\tau^{\Phi})=\begin{cases}1-\left[\dfrac{79\tau^{-1}}{140p}+\dfrac{474}{497}\left(\dfrac{1}{p}-1\right)\right]\left(\dfrac{\tau^{3}}{6}+\dfrac{\tau^{9}}{135}+\dfrac{\tau^{15}}{600}\right)\Big/D & (\tau\le 1)\\ -\left[\dfrac{\tau^{-5}}{10}+\dfrac{\tau^{-15}}{315}+\dfrac{\tau^{-25}}{1500}\right]\Big/D & (\tau>1)\end{cases}, \quad \text{Eq. 4-13}$$

, where p=0.28 and D=2.342456517 for FCC and HCP phases [147].

Table 4-1 Numerical values and functions used for the thermodynamical calculations.

Parameter	Functions [J·mol^{-1}]	Ref.
$\Delta G_{Fe}^{\gamma\to\varepsilon}$	$-2243.38+4.309T$	[338]
$\Delta G_{Mn}^{\gamma\to\varepsilon}$	$-1000.00+1.123T$	[338]
$\Delta G_{Cr}^{\gamma\to\varepsilon}$	$-1370.00-10T$	[342,343]
$\Delta G_{Cu}^{\gamma\to\varepsilon}$	$600+0.2T$	[343]
$\Delta G_{C}^{\gamma\to\varepsilon}$	-22166	[343]
$\Delta\Omega_{FeMn}^{\gamma\to\varepsilon}$	$2873+717(\chi_{Fe}-\chi_{Mn})$	[344]
$\Delta\Omega_{FeCr}^{\gamma\to\varepsilon}$	2095	[345]
$\Delta\Omega_{FeCu}^{\gamma\to\varepsilon}$	7506	[334]
$\Delta\Omega_{FeC}^{\gamma\to\varepsilon}$	42500	[339]

4.3.4 Post-mortem Microstructure Characterization

The as-received samples were metallographically polished before the microscopic characterization. The electron backscatter diffraction (EBSD) was performed on an HKL EBSD detector based on a field emission gun scanning electron microscope (FEI Sirion 200), which was set to a voltage of 20 kV, current of 25 nA, and step size of 0.5 μm. The EBSD data analysis was performed with HKL Channel 5 software, during which the misorientation angles less than 2° were ignored to avoid ambiguity. The samples for microscope observation were sectioned from the fractured sample with electrical discharge machining. For the transmission electron microscope (TEM) and scanning TEM (STEM) observation, thin foils were mechanically polished to a thickness of ~60 μm before the twin-jet electropolishing with a current of 150 mA in a solution of 5% perchloric acid and 95% methanol after cooling down to -30℃. The

bright-field TEM observation was carried out on a Technai G2 F30 microscope with an accelerating voltage of 300 kV. The high-resolution TEM images (HRTEM) and atomic-resolution high-angle annular dark-field STEM (HAADF-STEM) images were collected on an aberration-corrected Titan 60-300 microscope. The collection half-angle of the HAADF detector ranging from 60 to 290 mrad was used, with the convergence half-angle of 21.4 mrad, giving a probe size of ~1.2 Å.

4.4 Results and Discussion

4.4.1 Microstructure of the As-fabricated Steels

The as-fabricated 0-Cu and 1-Cu steel shared very similar microstructure thus only the images of the 0-Cu steel were presented here. Fig. 4-1a shows the typical EBSD inverse pole figure (IPF) of the virgin 0-Cu steel. Most of the grains were large equiaxed grains after the hot rolling. The mean grain size of 14.5±1.3 μm was determined by the line-intercept method excluding twinning boundaries. The low-angle grain boundaries (LAGBs, $2° \leq \theta \leq 15°$), high-angle grain boundaries (HAGBs, $15° < \theta$), and Σ3{111} twinning boundaries of Fig. 4-1a were marked and overlapped with the band contrast map in Fig. 4-1b. The LAGBs have a relatively low fraction of 13.8% accompanied by 86.2% of HAGBs. Fig. 4-1b shows the high density of Σ3{111} annealing twinning boundaries, which contributed to the high fraction of HAGBs at around 60° (Fig. 4-1c). In addition to the twinning boundaries, the grain misorientation distribution followed a pattern of the random misorientation distribution (Fig. 4-1c). A typical bright-field TEM image is shown in Fig. 4-1d, showing the microstructure consists of dense-dislocation and dislocation-free zones. The dislocation cells and dislocation entanglements can be observed in the dense dislocation zone. The dislocation free zone

mainly consists of equiaxed recrystallized grains and parallel-sided annealing twins, which initialized from the grain boundaries and expanded into the grain interior.

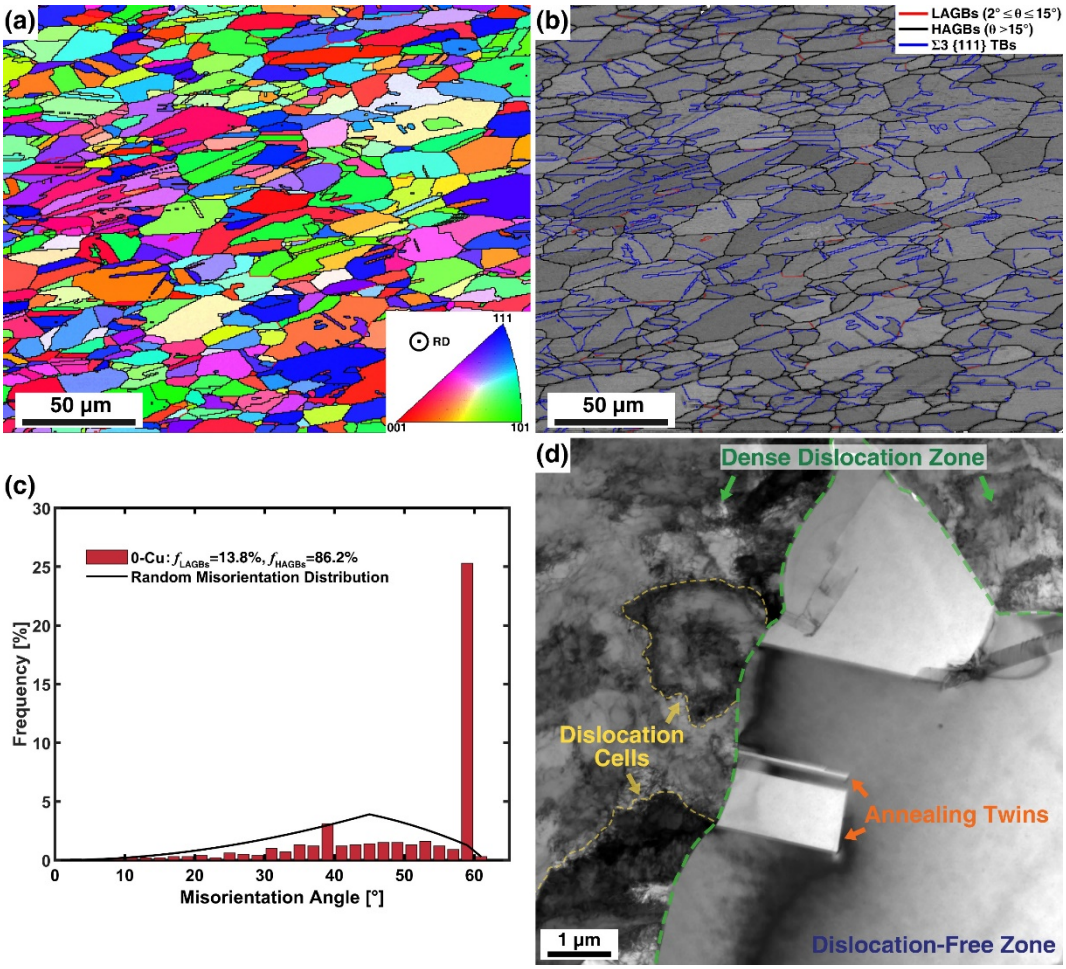

Fig. 4-1 Initial microstructure of the two alloys: (a) EBSD inverse pole figure (IPF) map, (b) Band contrast map overlapped with boundaries map, (c) sample and random misorientation, and (d) typical bright-field TEM image.

4.4.2 Mechanical Performance

The engineering stress-strain curves of the 0-Cu and 1-Cu steel deformed at 293, 173, and 77 K were shown in Fig. 4-2a and b, respectively. The stress relaxation was due to the paused straining for neutron diffraction data collection. The mechanical properties of the 0-Cu and 1-Cu steel were compared in Fig. 4-2c. At 293 K the YS and UTS of the 0-Cu steel were 336 MPa and 930 MPa, respectively (Table 4-1). As the deformation temperature decreased, both YS and UTS witnessed a substantial and

almost linear increase to 700 MPa and 1361 MPa, respectively. The ductility, however, decreased linearly from an ultrahigh value of 104% at 293 K to 68% at 77 K. The mechanical property of the 0.5-Cu and 1-Cu steel showed very similar temperature dependence. The Cu addition witness a steady increase in YS as the 1-Cu steel showed higher YS (~100 MPa) but slightly lower UTS (less than 50 MPa) than the 0-Cu steel at all three temperatures. Besides, the total elongation of the 1-Cu steel was maintained at a very high level at the low-temperature range and increased from 78% at 293 K to 86% at 77 K.

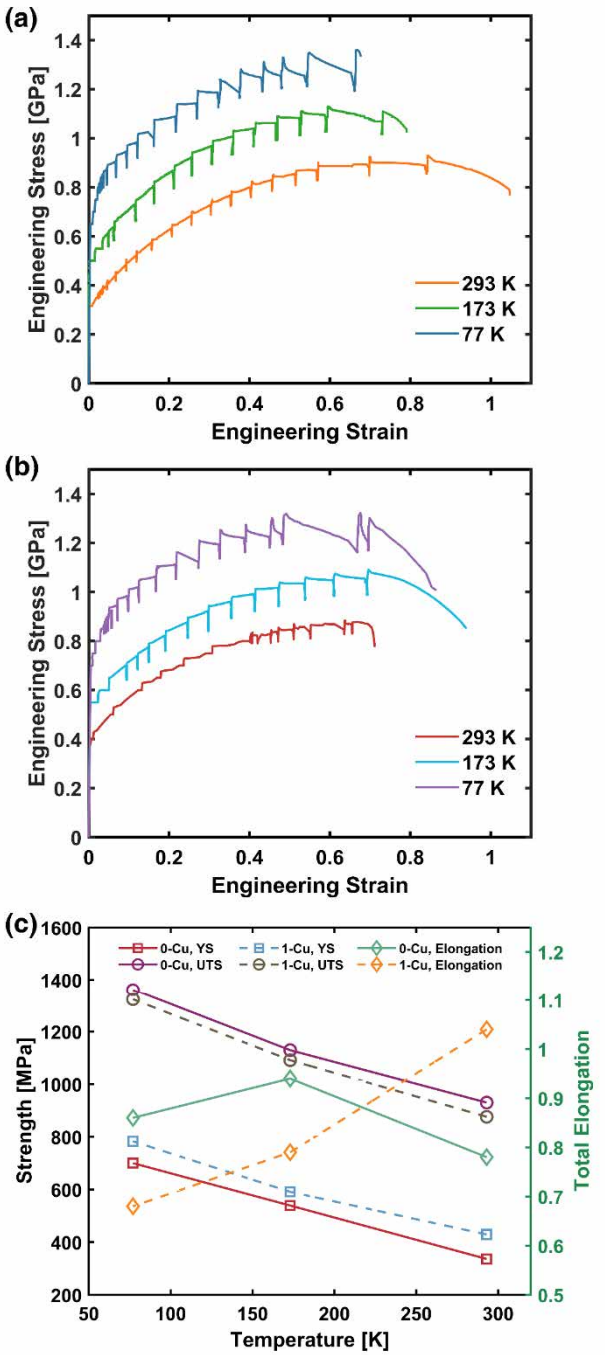

Fig. 4-2 Mechanical performance of the two high Mn steel at 293, 173, and 77 K: (a) and (b) Engineering stress-strain curves of the 0-Cu and 1-Cu alloy, respectively; (c) The evolution of mechanical properties with deformation temperature.

Defined as the derivative of true stress *v.s.* true strain, $d\sigma/d\varepsilon$, the strain hardening rate (SHR) of the two steels during deforming at different temperatures are plotted as a function of true stress in Fig. 4-3a (0-Cu) and b (1-Cu), respectively. For the 0-Cu steel, the SHR curves at the three deformation temperatures shared a similar pattern and they

can be categorized into three stages (separated with dash lines in Fig. 4-3a). Initially, the SHR curve dropped rapidly (Stage I), followed by a stable period during which the SHR increased slightly (Stage II), indicating the emergence of new and steady strengthening effects. At the last stage (Stage III), the SHR curve dropped again until fracture. The SHR curves of the 1-Cu steel (Fig. 4-3c) are also temperature-dependent and can also be divided into three stages. At 293 K, the SHR curve kept decreasing during straining, but the dropping rate varied with stages. When decreasing temperature to 173 and 77 K, the strengthening effects were improved significantly and both SHR curves show an increasing trend at Stage II while gradually decrease during the following Stage III.

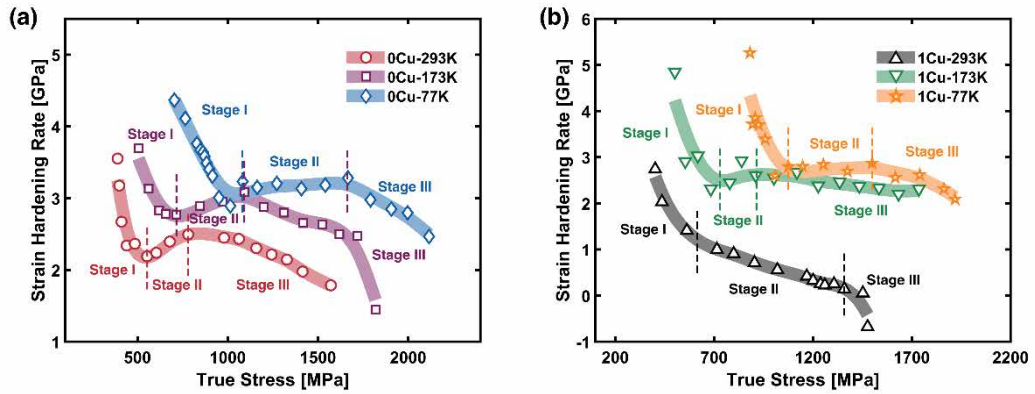

Fig. 4-3 Strain hardening rate (SHR) curves of the (a) 0-Cu and (b) 1-Cu steel during deforming at 293, 173, and 77 K.

Table 4-2 Mechanical properties of the steels at different temperatures.

Steels	0-Cu			0.5-Cu			1-Cu		
Temperature [K]	293	173	77	293	173	77	293	173	77
YS [MPa]	336	539	700	442	625	760	457	643	793
UTS [MPa]	930	1159	1361	918	1107	1312	876	1115	1323
Total elongation [%]	104	79	68	72	54	56	78	94	86

4.4.3 *In Situ* Neutron Diffraction Spectra

Fig. 4-4 shows the *in situ* neutron diffraction patterns of the two steels collected during tensile tests at different temperatures. The two steels maintained a single FCC structure as they are cooled down to cryogenic temperatures as only five diffraction peaks of

FCC phase were identified. During deformation, the FCC structure of both steels was stable at 293 K as no other peaks appeared. When deforming the 0-Cu steel at 77 K, a new diffraction peak appeared after yield point and its intensity grew stronger with straining (marked with a green line in Fig. 4-4b). This peak was identified as the $(10\bar{1}1)$ peak of the HCP phase [327]. This indicates the low temperature reduced the stability of the original FCC phases and strain-induced phase transformation from FCC to HCP occurred. A similar phenomenon was observed when deforming the 1-Cu steel at 77 K, but the new peak has a very weak peak intensity, indicating that a trace amount of the newborn HCP phases was produced.

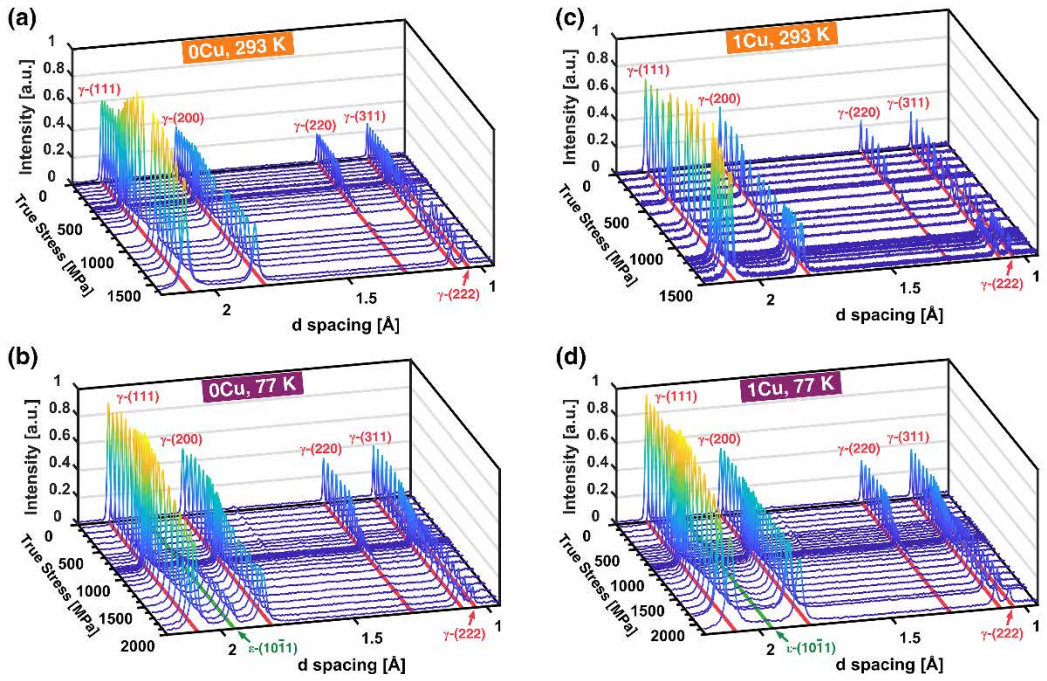

Fig. 4-4 *In situ* neutron diffraction spectra of the two austenitic steels during tensile testing at different temperatures: (a) 0-Cu, 293 K; (b) 0-Cu 77 K; (c) 1-Cu, 293 K; (d) 1-Cu, 77 K.

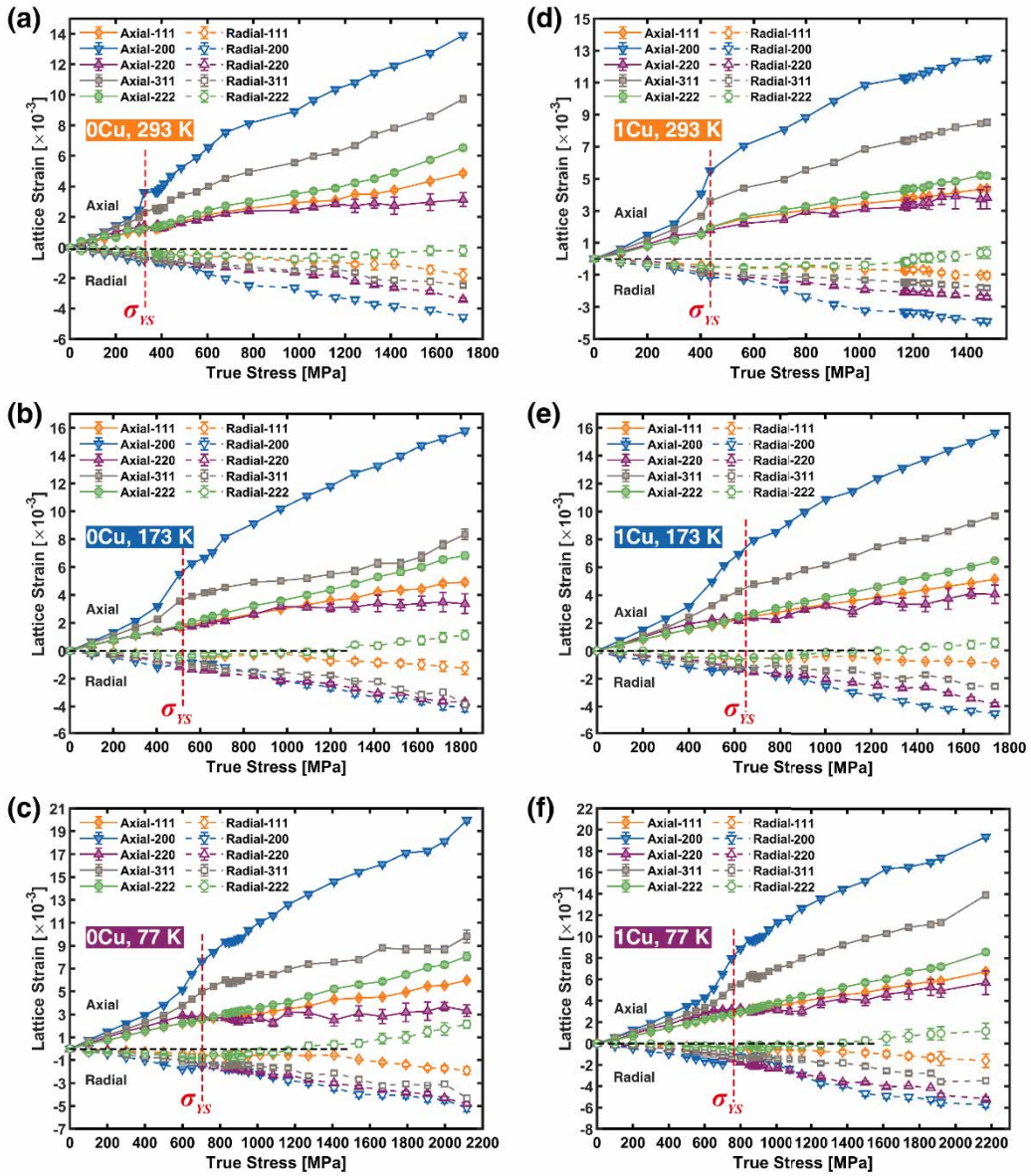

Fig. 4-5 Lattice strain evolution of five crystallographic planes ({111}, {200}, {220}, {311}, and {222}) of two TWIP steels (0-Cu and 1-Cu) during deforming at different temperatures: (a) 0-Cu, 293 K; (b) 0-Cu, 173 K; (c) 0-Cu 77 K; (d) 1-Cu, 293K; (e) 1-Cu, 173 K; (f) 1-Cu, 77 K.

The macroscopic and *hkl*-specific elastic moduli were measured by analysing the neutron diffraction patterns. The macroscopic Young's modulus (E) was determined by linear fitting the applied stress as a function of true strain at the elastic stage. The small variations of Young's modulus can be resulted from the sample shrinkage as the temperature decreases. The lattice parameters of the two steels are very close (3.615 Å for 0-Cu and 3.616 Å for 1-Cu) and they both decreased almost linearly with the decreasing of temperature (Table 4-2). With the increase of true stress, the lattice

parameter obtained from radial and axial signals increased and decreased almost linearly at the elastic stage, respectively. The macroscopic Poisson's ratio (ν) was determined by the ratio of the two fitted lines. Then the bulk shear modulus (G) can be obtained via $G=E/(1+\nu)$. The lattice strain evolution of four grain families ({111}, {200}, {220}, and {311}) along axial and radial direction at different temperatures was calculated with Eq. 4-1 and shown in Fig. 4-5. The *hkl*-specific lattice strain also increased/decreased linearly with stress before yielding and showed varied yield behaviours. After linear fitting at the elastic stage, their slopes determine the *hkl*-specific diffraction elastic moduli (E_{111}, E_{200}, E_{220}, and E_{311}). The ratio of elastic moduli between the radial and axial direction determined the Poisson's ratio of different grain families (ν_{hkl}). Among all the orientations, E_{111} and E_{200} shows the highest and lowest values, respectively. Meanwhile, the low temperature can increase the stiffness of the steel. With the temperature decreasing, the shear modulus and all elastic moduli (except E_{311}, which remained at the same level) of the two steels increased. The Poisson's ratio showed a decreasing trend (Table 4-3). During the following plastic deformation, the lattice strain increased non-linearly with the applied stress since the stress gradually transferred from some stiff orientations, e.g., (220)//LD (loading direction) to some compliant orientations, e.g., (200)//LD.

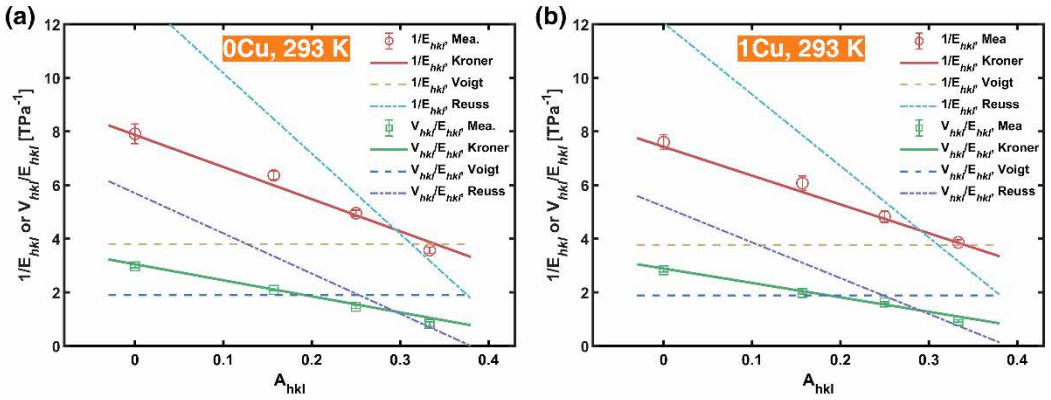

Fig. 4-6 Plots of the reciprocal diffraction moduli ($1/E_{hkl}$ and ν/E_{hkl}) of differently oriented crystals as a function of the elastic anisotropy factor ($A_{hkl} = \left(h^2k^2 + h^2l^2 + k^2l^2\right) \Big/ \left(h^2 + k^2 + l^2\right)^2$) and the fitting results based on Kroner, Voigt, and Reuss model of the (a) 0-Cu and (b) 1-Cu TWIP steel at 293 K.

Fig. 4-6 shows the elastic moduli of grains with different orientations plotted as a function of the elastic anisotropy factor and the fitted lines with the Voigt, Reuss, and Kroner models at 293 K. The details of the calculation can be found at Section A.2.1 of the Appendices. The fitting results indicate that the self-consistent Kroner model has the best agreement with the experimental results as compared with the Voigt and Reuss model. According to Refs. [346,347], these two theoretical models were generally used to estimate the upper and lower bounds of the diffraction and macroscopic elastic moduli as they only assume all grains are subjected to a homogeneous strain (Voigt) or stress (Reuss) but failed to meet the equilibrium (Voigt) and continuity (Reuss) at grain boundaries during loading. The *hkl*-specific diffraction elastic moduli obtained from neutron diffraction were used to determine the single-crystal elastic constants (C_{11}, C_{12}, and C_{44}) with the Kroner's model at different temperatures (Table 4-3).

Table 4-3 Multiple properties of the 0-Cu and 1-Cu steel at 293 K.

Steel	0-Cu			1-Cu		
Temperature [K]	293	173	77	293	173	77
a [Å]	3.615	3.611	3.610	3.616	3.612	3.611
E [GPa]	191.3	192.1	193.4	191.5	191.1	193.6
E_{111} [GPa]	280.1	282.5	283.5	259.1	272.6	279.3
E_{200} [GPa]	126.4	129.0	133.2	135.1	136.7	138.5
E_{220} [GPa]	202.0	202.8	208.2	207.6	203.4	205.3
E_{311} [GPa]	157.2	156.2	156.7	152.1	156.0	156.6
G [GPa]	73.35	75.45	77.17	75.57	76.20	78.76
v	0.304	0.273	0.253	0.267	0.254	0.229
v_{111}	0.231	0.225	0.223	0.241	0.226	0.215
v_{200}	0.375	0.368	0.375	0.371	0.380	0.367
v_{220}	0.295	0.312	0.300	0.336	0.337	0.332
v_{311}	0.329	0.306	0.305	0.325	0.321	0.323
C_{11} [GPa]	223	227	231	240	243	250
C_{12} [GPa]	170	172	175	182	186	190
C_{44} [GPa]	129	132	132	128	128	134

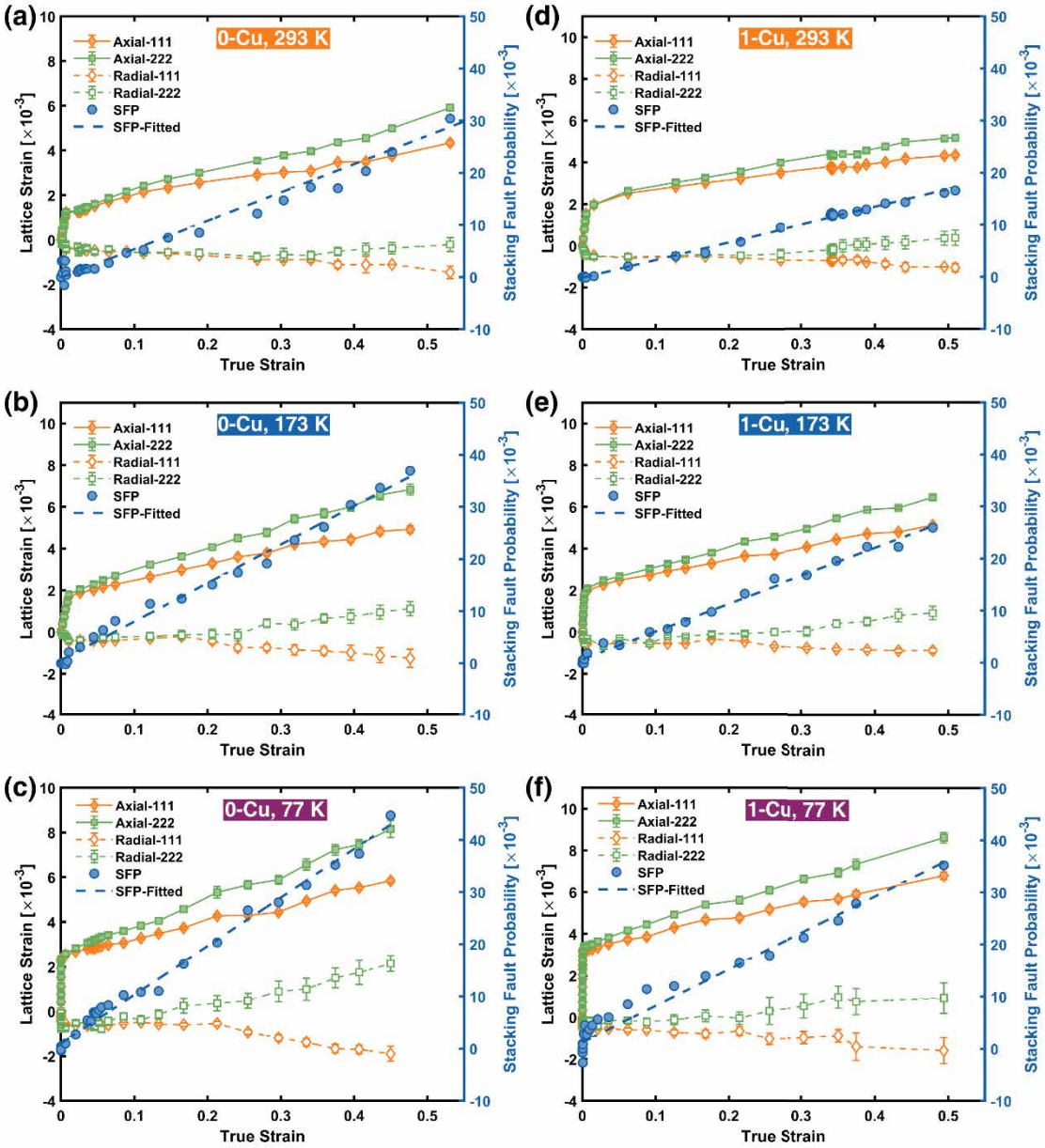

Fig. 4-7 Lattice strain evolution of {111} and {222} grain planes along axial and radial direction and the corresponding stacking fault probability change of the two TWIP steels during deforming at different deformation temperatures: (a) 0-Cu, 293 K; (b) 0-Cu, 173 K; (c) 0-Cu 77 K; (d) 1-Cu, 293 K; (e) 1-Cu, 173 K; (f) 1-Cu, 77 K.

4.4.4 SFE Evolution

The lattice strain of {111} and {222} grain families increased with strain but a growing split between them was observed (Fig. 4-5). This is a signature of the formation of stacking faults, which causes extra strain and separates lattice strain curves from different orders of Miller indices [282,327,348]. Stacking fault probability (SFP), a

parameter that measures the amount of formed stacking faults, can thus be determined by measuring the separating distance between the lattice strain curves from two consecutive grain planes. The detailed calculation procedure can be found at Refs. [282,327]. In Fig. 4-7, the lattice strain evolution of {111} and {222} grain families and the calculated SFP of the two steels were plotted against true strain at different temperatures. At the low strain regime, the SFP fluctuates at around 0 and the negative value was caused by the small errors introduced during peak fitting. SFP increases almost linearly with true strain and a linear function was applied to depict the stacking fault multiplication during straining. After linear fitting, the slopes ($\partial SFP/\partial \varepsilon$) of these lines define the speed of stacking faults production (Fig. 4-7) [327]. The low temperature can effectively promote the SF formation and increase $\partial SFP/\partial \varepsilon$. The $\partial SFP/\partial \varepsilon$ of the 0-Cu steel is 4.63×10^{-2} at 293 K and almost linearly increased to 8.41×10^{-2} at 77 K (Fig. 4-9). The 1-Cu steel showed a very similar pattern but with a lower increase rate, which is 3.39×10^{-2} at 293 K and 7.0×10^{-2} at 77 K. The evolution of $\partial SFP/\partial \varepsilon$ and measured SFE were plotted as a function of deformation temperature in Fig. 4-8. For the 0-Cu steel, its SFE started from 26.8±0.5 mJm^{-2} at 293 K and almost linearly decreased to 15.5±1.7 mJm^{-2} at 77 K. The 1-Cu steel showed a higher level of SFE from 33.8±1.8 mJm^{-2} at 293 K to 20.7±0.7 mJm^{-2} at 77 K (~5-7 mJm^{-2}) higher than the 0-Cu steel within the whole temperature range. Their slopes also showed a very close value with 0.056±0.006 $mJm^{-2}K^{-1}$ for the 0-Cu steel and 0.059±0.008 $mJm^{-2}K^{-1}$ for the 1-Cu steel. The values are also very close to 0.061 $mJm^{-2}K^{-1}$ observed in the Fe-24Mn-4Cr-1Cu-0.5C steel reported in Ref. [327]. According to the SFE-deformation mechanism map overlapped in Fig. 4-8 [138,259], the SFE of the 0-Cu steel stayed at the twinning-dominant region at ~125-373 K, while it dropped to the phase transformation region at 77 K. The SFE of the 1-Cu steel showed similar temperature

dependence but it remained at the twinning zone at the three tested temperatures. This indicates the transition of the dominant deformation mechanism, which agrees well with the diffraction results shown in Fig. 4-4, where observable diffraction peaks of $(10\bar{1}1)$ were formed when deforming the 0-Cu steel at 77 K.

Besides, the measured SFE shows an acceptable match with the thermodynamical prediction (Table 4-4). The disparity between the two SFE-determination methods is relatively small (~2 mJm^{-2}) except for the results of the 1-Cu steel at 293 K (~5 mJm^{-2}). The difference between theoretical calculation and experimental measurement can be originated from that the SFE can be influenced by several factors (e.g., strain rate [135] and grain size [328]), which, however, were not considered in the thermodynamical modelling.

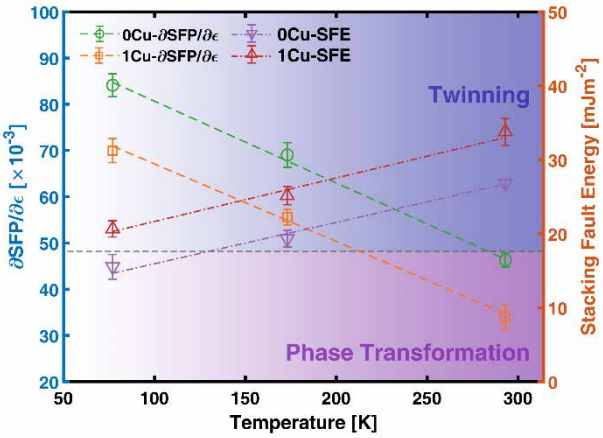

Fig. 4-8 Temperature dependence of stacking fault probability (SFP) increase rate and stacking fault energy (SFE) of the two TWIP steels (measured with neutron diffraction patterns).

Table 4-4 Temperature-dependent SFE of the 0-Cu and 1-Cu steel determined with thermodynamics and neutron diffraction.

Steel	Temperature [K]	SFE [mJm^{-2}] (Neutron Diffraction)	SFE [mJm^{-2}] (Thermodynamics)
0-Cu	293	26.8±0.5	26.4
	173	19.3±1.1	20.3
	77	15.5±1.7	16.6
1-Cu	293	33.8±2.2	28.8
	173	25.2±1.2	23.0
	77	20.7±0.7	19.2

4.4.5 Dislocation Density Calculation

To analyse the strengthening contribution of forest hardening effects, it is necessary to quantitatively determine the evolution of dislocation density during straining. The dislocation density was calculated with the neutron diffraction patterns based on the modified Williamson-Hall model [289,349]. The detailed calculation process can be found in Ref. [327]. The dislocation density evolution of the two steels at 293, 173, and 77 K was plotted with respect to true strain in Fig. 4-9. As shown in Fig. 4-9a, at three deformation temperatures, the dislocation density of the two steels was ~7 × 10^{13} m^{-2}, and it increased almost linearly with the increase of true strain after yielding. The decrease of deformation temperature promoted the speed of dislocation accumulation: at a true strain of 0.5, the dislocation density at 293 K reached ~1.00 × 10^{15} m^{-2} and it increased to ~1.52 × 10^{15} m^{-2} at 173 K and ~2.41 × 10^{15} m^{-2} at 77 K. Similar phenomena was also observed in the 1-Cu steel.

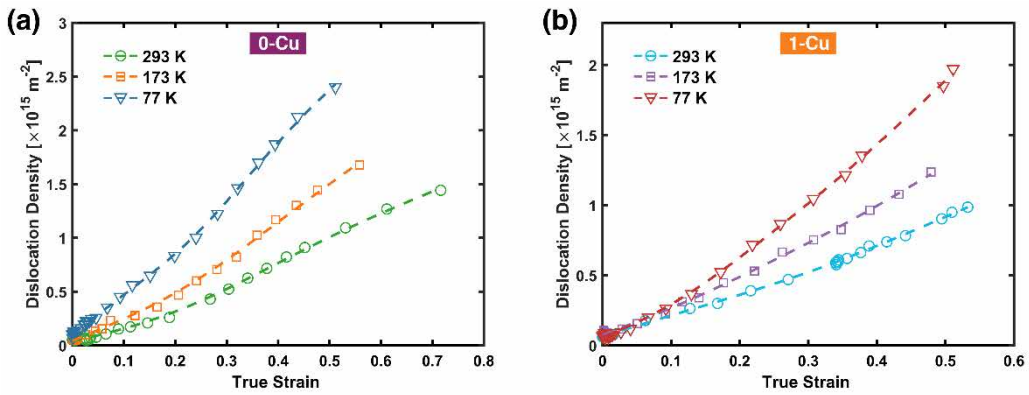

Fig. 4-9 The evolution of dislocation density of the two high Mn alloys deformed at 293, 173, and 77 K: the (a) 0-Cu and (b) 1-Cu steel.

The varied increasing speeds of dislocation density of the two steels originates from the varied SFE and deformation temperature. The increased dislocation density is the concurrent result of dislocation generation and dynamic recovery [60]. Due to the low SFE, the perfect dislocations tend to slip on parallel slip planes or dissociate into two

Shockley partials with stacking faults existing in between. Dense planar dislocation arrays and stacking faults on parallel {111} slip planes are thus highly expected, contributing to significant dislocation accumulation. The dynamic recovery, on the other hand, can be reduced significantly by lowering deformation temperature. Dynamic recovery is generally caused by diffusional processes including cross slip and climb. When the temperature decreases to below 0.3 T_m (T_m: melting temperature), the dynamic recovery is very limited and dominated by cross slip [350]. The low temperature can even reduce the thermal activation of cross slip and create more extended dislocation cores to hinder cross slip [328]. Hence, the growth speeds of dislocation density increased as the deformation temperature was decreased.

4.4.6 Microscopic Characterization

To reveal the relationship among the chemical composition, temperature, and deformation mechanisms, the microstructure of the two steels after deforming to different strains at 293 and 77 K were characterized with TEM. Fig. 4-10a and b show the typical bright-field TEM micrograph of the 0-Cu steel deformed to a true strain of ~0.3 at 293 K. The corresponding selected area diffraction pattern (SAED) was shown in Fig. 4-10c. After deformation, high density of dislocations and closely packed lamellae structures, which were identified as nano-sized primary twins accompanied with thin HCP laths (identified with SAED), were produced (Fig. 4-10a). These well-defined twins and HCP clusters penetrated the grain interior and subgrains, leading to the continuous segmentation of grains. The mean free path of dislocations was reduced effectively and high density of dislocations (Fig. 4-10b) were trapped among them, thus providing significant strain hardening effects (so-called “dynamic Hall-Petch effect”)[327].

As shown in Fig. 4-10d, the introduction of new interfaces (i.e., twinning boundaries) and similar dislocation-twin interaction were also observed in the deformed 1-Cu steel at 293 K (Fig. 4-10d). The twinning activity of the 1-Cu steel is more active than that of 0-Cu steel as both primary and second twin system was observed (Fig. 4-10e). The two intersecting twin systems introduced a higher density of twinning boundaries, forming a hierarchical twin substructure. The structure of the hierarchical twin system was further revealed via HRTEM in Fig. 4-10f. The primary twins were typically arranged in the form of parallel bundles and their boundaries consist of stacking faults. The second twins formed from closely packed stacking faults intersecting with the primary twin. Apart from the crossing twinning networks, the active formation and following reaction of stacking faults, e.g., Lomer-Cottrell (L-C) locks, were also observed during the plastic straining.

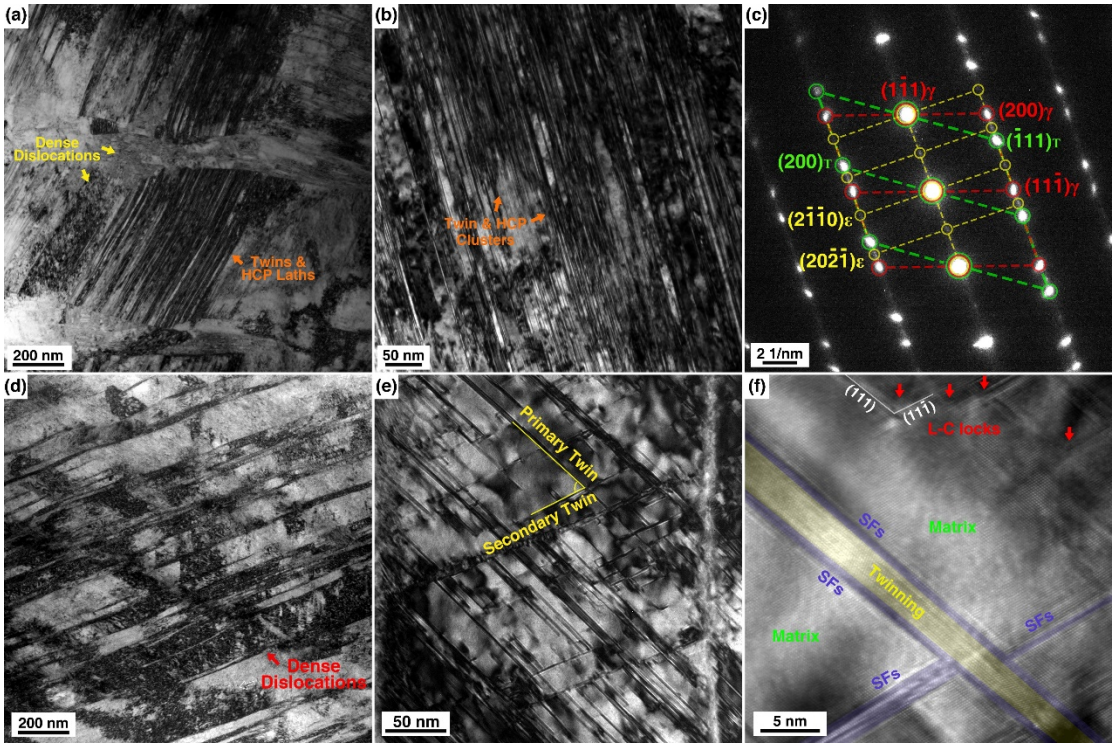

Fig. 4-10 Microstructure of the 0-Cu and 1-Cu steel deformed to a true strain of ~0.3 at 293 K: (a) typical bright-field TEM image, 0-Cu; (b) higher magnification of (a); (c) Selected area diffraction pattern of (a); (d) typical bright-field image, 1-Cu; (e) higher magnification of (d); (f) HRTEM image of the rectangle area in (e).

The formation of twins, martensitic phase transformation, and L-C locks are closely related to the activity of stacking faults. Due to the low SFE of the steel, the dissociation of perfect dislocations can easily occur on two 60° inter-crossing crystallographic planes of (111) and $(11\bar{1})$, where numerous closely-packed stacking faults can be observed [67]. Twins can be formed by the glide of $\frac{a}{6}\langle 11\bar{2}\rangle$-type Shockley partial dislocations on consecutive (111) planes of the FCC matrix. When partial dislocation glide on every second (111) plane, the parent FCC phases with stacking sequence of …ABCABC… will transfer into HCP phases with …ACACAC… stacking sequence. Continuously produced partial dislocations on surrounding (111) planes can thicken the twins or HCP laths [117,348]. Meanwhile, after the dissociation of perfect dislocations, the reaction of two leading partial dislocations from different slip systems can further lead to a high formation probability of a stair-rod dislocation via [57]:

$$\frac{a}{6}\langle 2\bar{1}\bar{1}\rangle + \frac{a}{6}\langle \bar{1}21\rangle \rightarrow \frac{a}{6}\langle 110\rangle \qquad \text{Eq. 4-14}$$

, the Burgers vector of stair-rod dislocation is perpendicular to the dislocation line and does not locate at the two {111} planes, making them sessile and hard to glide. These stair-rod dislocations are known as Lomer-Cottrell locks (marked with arrows in Fig. 4-10f) [351]. It is indicated that L-C locks play an important role in the strain hardening of FCC alloys [352]. The L-C locks show a high capability of accumulating dislocations as four dislocation segments can be pinned by each L-C lock [353]. As the L-C locks are usually very short in length and can equivalently act as pinning points, the strengthening effects of L-C locks are very similar to Orowan's strengthening based on the orientation-dependent line tension model [354]. Meanwhile, the L-C locks can also become unlocked after interacting with travelling dislocations driven by external stress [174].

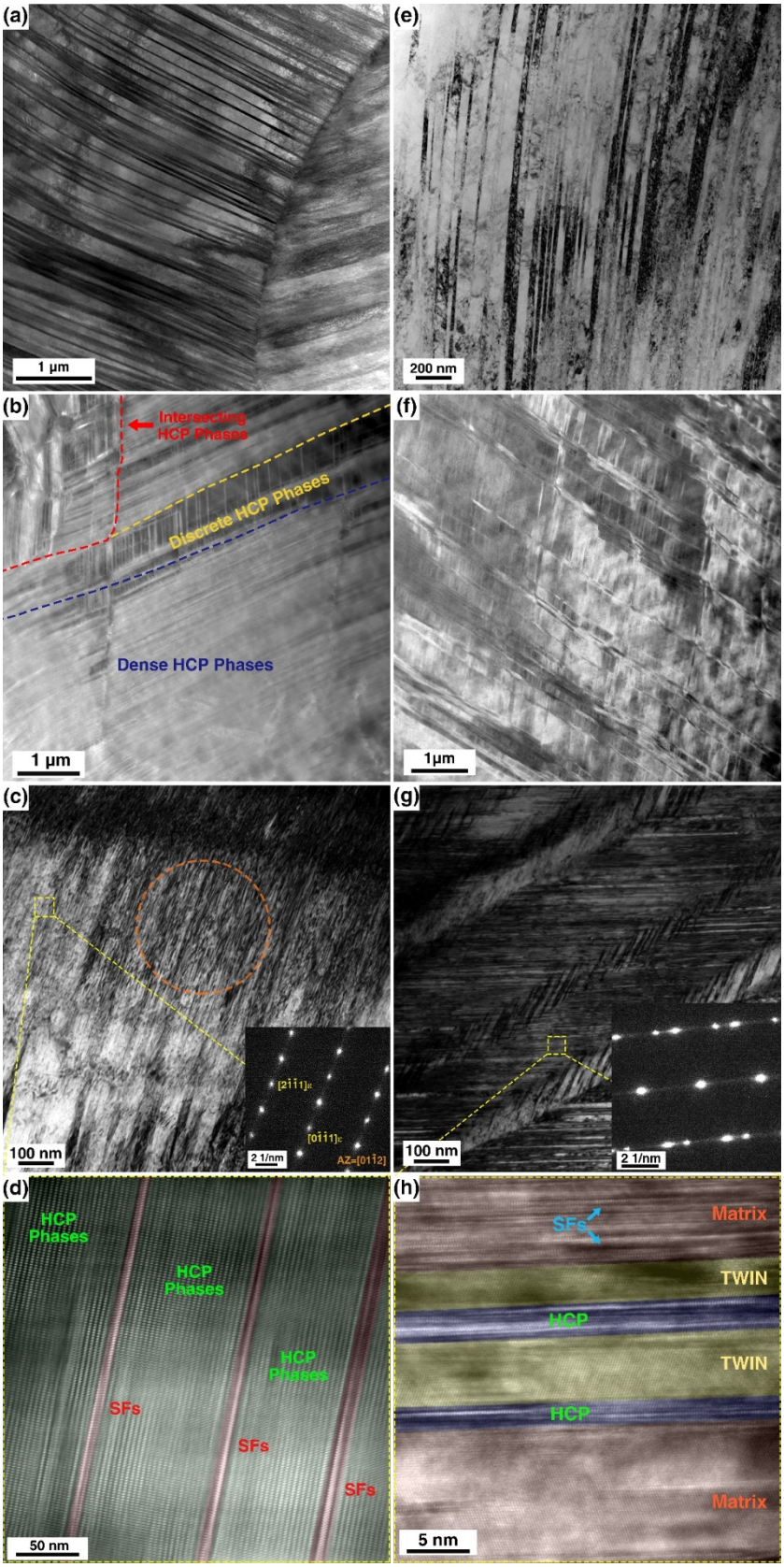

Fig. 4-11 The microstructure of the 0-Cu and 1-Cu steel deformed to different strain levels at 77 K: (a) and (e) typical bright-field TEM image of the 0-Cu and 1-Cu steel with a strain of ~0.15, respectively; (b) and (f) HAADF image of the 0-Cu and 1-Cu steel with a strain of ~0.3, respectively; (c) and (g) Bright-field image of the 0-Cu and 1-Cu steel with a strain of ~0.3, respectively; (d) HRTEM image of the yellow square area in (c); (h) HRTEM image of the yellow square area in (g).

The microstructure of the two steels deformed to similar strain levels of ~0.15 and ~0.3 at 77 K was compared in Fig. 4-11. Fig. 4-11a and e show the high density of mechanical twins formed in the 0-Cu and 1-Cu steels deformed to a true strain of ~0.15, respectively. Fig. 4-11b presents the HAADF image of the 0-Cu steel at a true strain of ~0.3, showing the massive transition from the parent FCC phases into HCP-martensite in different forms: the dense HCP phases, discrete HCP lamellae, and thin HCP laths intersecting with each other. The HCP phases can be identified with the SAED pattern inserted in Fig. 4-11c, where HCP phases were entangled with dense dislocations. The martensite transformation can be ascribed to the lowered SFE caused by temperature decreasing, motivating the overlapping of the stacking faults on every other {111} plane [355]. The microstructure of the newborn HCP phases (the yellow square area in Fig. 4-11c) was revealed by HRTEM in Fig. 4-11d. It shows that the HCP phases exist in the form of parallel thin laths, separated by one or two stacking faults. This indicates that with the decrease of temperature (from 293 to 77 K) and SFE (from 26.8±0.5 to 15.5±1.7 mJm^{-2}), the martensite phase transformation gradually became the main deformation mechanism of the 0-Cu steel. This result is in good accordance with the neutron diffraction results in Fig. 4-5 and SFE-deformation mechanism map in Fig. 4-8.

The deformation microstructure of the 1-Cu steel (at a true strain of ~0.3, 77 K) was revealed with HAADF image in Fig. 4-11f and bright-field TEM image in Fig. 4-11g. As the deformation temperature decreased to 77 K, the density of the hierarchy twin structure increased significantly compared to that at 293 K (Fig. 4-10). The abundance of primary and secondary twins introduced a much higher density of interfaces than that at 293 K, leading to more significant segmentation of the grains into ultrafine microstructural entities. The square frame area in Fig. 4-11g was further analysed with HRTEM in Fig. 4-11h. It is a nanotwin-HCP lamella consisting of two parallel twins

with thin HCP laths located at their boundaries. The twinning boundaries can serve as preferable nucleation sites for HCP phases [104,356]. The extended dissociated dislocations can react with coherent twinning boundaries: the leading partial dislocation can decompose into a stair-rod partial and a glissile partial along the boundaries, forming a favourable site for the HCP formation [104]. The HCP phase has a very narrow width (~2 nm) and a low volume fraction at ~0.3 true strain, which may explain that only a very weak diffraction peak of ε-$(10\bar{1}1)$ was detected in the neutron diffraction spectra (Fig. 4-4). Besides, a high density of stacking faults was also observed among the FCC matrix. This indicates that twinning is still the main deformation mechanism of the 1-Cu steel at 77 K as only a very trace amount of HCP phases can be identified. The decrease of deformation temperature from 293 to 77 K largely promoted the formation of (primary and secondary) twins, thus providing a higher strain hardening effect.

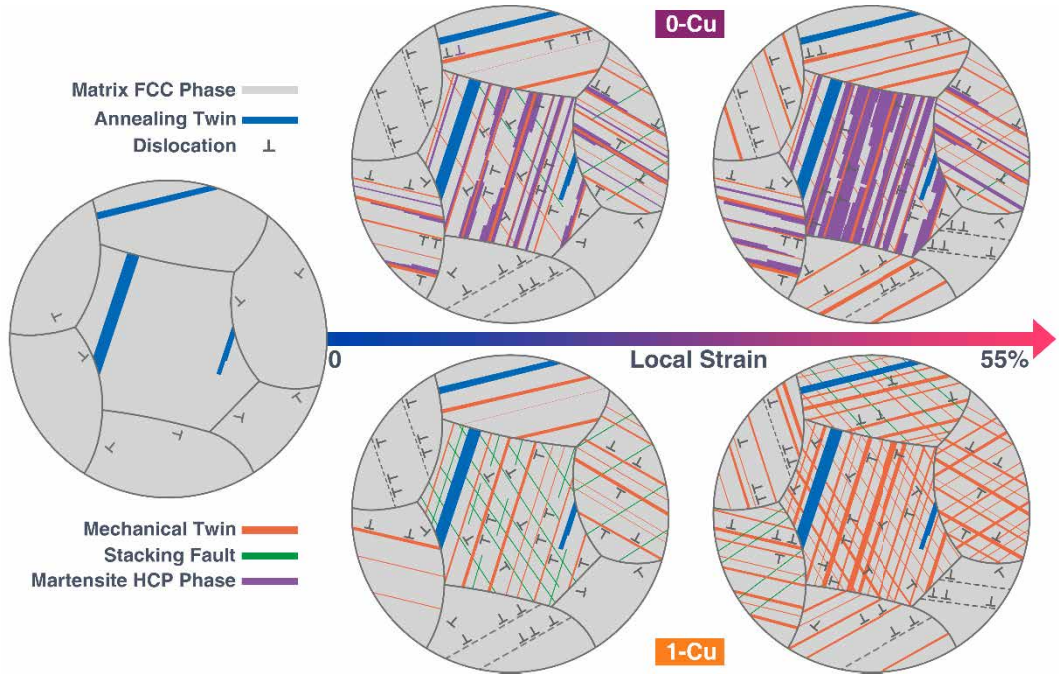

Fig. 4-12 Schematic sketches illustrating the sequence of microstructure evolution in the 0-Cu and 1-Cu steel deformed at 77 K.

Therefore, the deformation behaviours of the two steels at 77 K can be summarized and schematically illustrated in Fig. 4-12. Originally, both steels showed low dislocation density and a high fraction of annealing twins distributed among the grain interiors. For the 0-Cu steel, dislocation multiplication/gliding, the primary twinning, and slight phase transformation dominated the strain hardening behaviour at low strain levels. When at high strains, in addition to the continuous increase of dislocation density, the formation and thicken of twins and HCP laths became the main deformation mechanisms, playing an important role in withstanding external stress and providing larger ductility. For the 1-Cu steel, it produced a high density of twins, stacking faults, dislocations, and L-C locks at low strains. The following deformation promoted the formation and thicken of primary/secondary twins, forming three-dimensional hierarchical twinning systems and trapping dense dislocations in the intra-twin zones.

4.4.7 Strengthening Mechanisms

The neutron diffraction and post-mortem TEM characterization indicate that the deformation behaviour of the 0-Cu steel is a mixture of dislocation multiplication, twinning (at low strain levels) and phase transformation (at high strain levels). But for the 1-Cu steel, which has an overall higher SFE than the 0-Cu steel, dislocation motion and twinning are the dominant deformation mechanism during the whole plastic stage. Therefore, the total flow stress (σ_{flow}) of the two TWIP steels should generally combine the contribution of the yield stress (σ_y) and an incremental strain hardening effects (σ_{sh}) during plastic deformation [198]:

$$\sigma_{flow} = \sigma_y + \sigma_{sh} \qquad \text{Eq. 4-15}$$

First, we address the first term on the right, σ_y. According to Ref. [198], the yield stress is a combination of various strengthening effects:

$$\sigma_y = \sigma_{y0} + \sigma_p + \sigma_{dis}^0 + \sigma_{gb} \quad \text{Eq. 4-16}$$

, where σ_{y0} is the lattice friction stress, i.e., intrinsic lattice resistance and the solid solution strengthening effects [357], σ_p represents the precipitation hardening, σ_{dis}^0 is the forest hardening effects due to the initial dislocation density of the virgin samples, σ_{gb} is the grain boundary hardening. For the two steels used in the present study, the σ_p can be eliminated since no precipitates were characterized, at least from the neutron diffraction spectra (Fig. 4-3) and TEM observation (Fig. 4-11 and Fig. 4-12). According to Ref. [304], the forest strengthening effect of dislocations can be calculated with the Taylor equation:

$$\sigma_{dis} = M\alpha Gb\rho^{1/2}, \quad \text{Eq. 4-17}$$

where M=3.06 is the Taylor factor, α=0.26 is a constant for scaling the inter action strength between dislocations [358]. According to the neutron diffraction results, the dislocation density of the two as-fabricated steels was about 7×10^{13} m^{-2}, contributing ~106 MPa to the YS. The hardening effects of grain boundaries can be well described with the Hall-Petch equation [67]:

$$\sigma_{GB} = \sqrt{\frac{G(T)}{G(RT)}} K_{gb} d^{-1/2}, \quad \text{Eq. 4-18}$$

where the Hall-Petch coefficient (K_{gb}) of 0.357 MPa·$m^{0.5}$ was used according to Refs. [214,327], *G(T)* and *G(RT)* are the shear modulus at a given temperature and room temperature, respectively. Based on the average grain size of 14.5±1.3 μm, the grain boundaries contributed ~95 MPa to the yield stress. Therefore, the lattice friction stress of the two steels can be calculated with Eq. 4-16. As shown in Fig. 4-13, with the

decrease of deformation temperature, the lattice friction stress of the two steels can increase almost linearly with very similar slopes (1.651 MPa·K^{-1} for 0-Cu steel and 1.717 MPa·K^{-1} for 1-Cu steel). It is worth noting that the 1-Cu steel shows overall higher (~90 MPa) lattice friction stress than the 0-Cu steel at all three temperatures. This can be ascribed to the stronger solid solution strengthening effects brought from Cu addition [43].

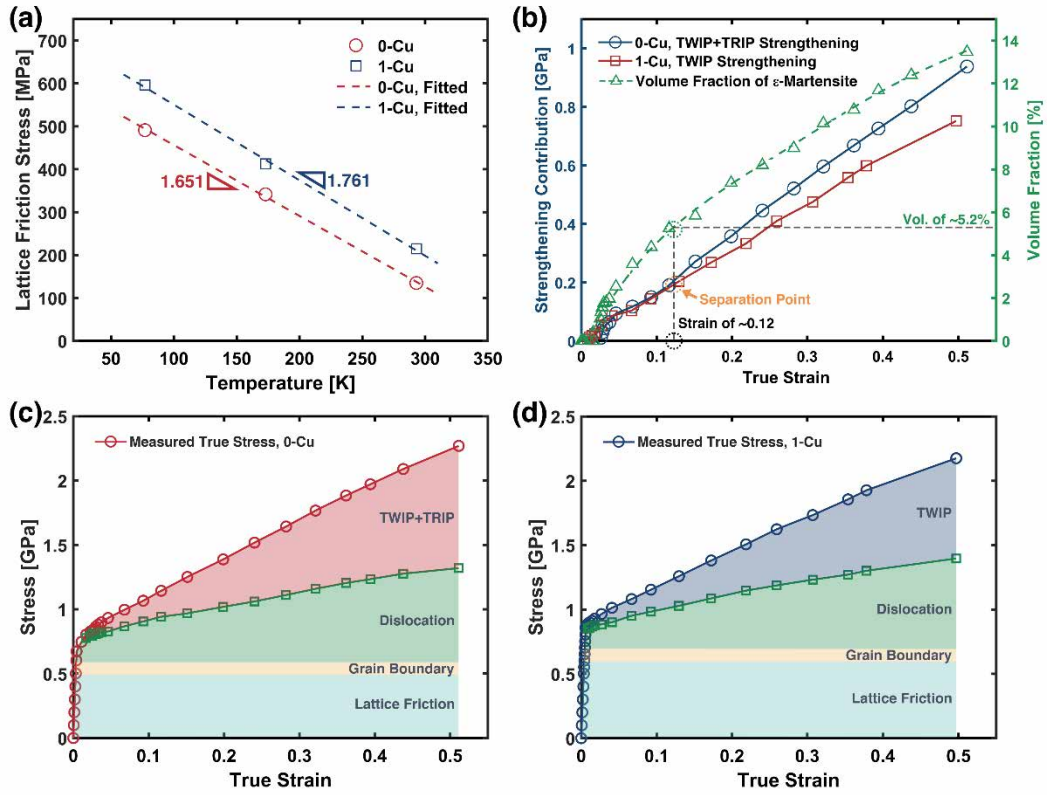

Fig. 4-13 Strengthening effects of the 0-Cu and 1-Cu steel during deforming at 77 K: (a) The lattice friction stress evolution plotted as a function of temperature; (b) The evolution of strengthening contribution of deformation twinning of the 1-Cu steel and TWIP+TRIP of the 0-Cu steel with respect to true strain; (c) and (d) The respective contribution of multiple strengthening mechanisms to the total flow stress of the 0-Cu and 1-Cu steel at 77 K, respectively.

Next, we address the strengthening effects during plastic deformation. According to Refs. [198,327], several strengthening effects including (1) dislocation multiplication, (2) twinning, and (3) martensite phase transformation (σ_{tr}) can collaboratively contribute to the incremental stress at the plastic stage:

$$\sigma_{sh} = \sigma_{dis}^{p} + \sigma_{tw} + \sigma_{tr} \quad \text{Eq. 4-19}$$

, where σ_{dis}^{p} is the strengthening contribution from the dislocations produced during straining. Combining Eq. 4-15, Eq. 4-16, and Eq. 4-19, the contribution from twinning (σ_{tw}) and/or phase transformation (σ_{tr}) can be calculated with:

$$\sigma_{tw} + \sigma_{tr} = \sigma - \sigma_{gb} - \sigma_{fr} - \sigma_{dis}. \quad \text{Eq. 4-20}$$

For the 1-Cu steel, a trace amount of the transformed ε-martensite phase has been identified (not detectable via neutron diffraction) and preferably exist with a very wide spacing distance and thin thickness (< 5 nm) (Fig. 4-4 and Fig. 4-11f). According to Ref. [315], these stand-alone HCP laths have a very limited ability to impede dislocation motions and produce strengthening effects. The contribution from martensite phase transformation is thus neglected for the 1-Cu steel. However, when deforming the 0-Cu steel at 77 K, strain-induced hard HCP laths serve as an additional strengthening source, which can introduce extra FCC/HCP interfaces with high-stress concentration and reduce the mean free path of dislocation motions [359,360]. Therefore, a synergistic strengthening effect of TWIP and TRIP was considered in deforming the 0-Cu steel at 77 K. The evolution of volume fraction of HCP phases of the 0-Cu steel and strengthening contribution of the TWIP effect (for the 1-Cu steel) and TWIP+TRIP effect (for the 0-Cu steel) at 77 K were plotted as a function of true strain in Fig. 4-13b. Starting from a very low level (~50 MPa), the two curves increased linearly with true strain and were almost overlapped before strain reaching 0.12 and the volume fraction of HCP martensite reaching ~5.2% (separation point). This indicates the strengthening effects of HCP laths is negligible with a limited volume fraction (lower than 5.2%), where most of them were distributed distantly or along with twinning boundaries. The two curves then gradually separated, and the difference became wider with the increase of strain. At the true strain of ~0.5, extensive twinning

boundaries contributed ~810 MPa in 1-Cu steel, while the twin and HCP-martensite/austenite interfaces in 0-Cu steel provided ~940 MPa to the total flow stress. This indicates that the abundance of HCP phases in the 0-Cu steel can provide more significant strain hardening effects than hierarchy twin networks produced in the 1-Cu steel.

According to our SHR results in Fig. 4-3, both twinning and martensite phase transformation can provide steady and significant strengthening effects and improve the ductility of the steels. But they may influence the mechanical performance differently. Mechanical twins have both hardening and softening effects. On one hand, the abundance of strain-induced twinning boundaries can penetrate the grain interior and form dense three-dimensional networks, subdividing the grains into nano-scaled substructures. The dislocation-twin, dislocation-dislocation, and twin-twin interactions were significantly promoted, thus offering substantial work-hardening effects [95]. Due to the segmentation of the grains, the strengthening effects of twinning boundaries are generally considered analogous to grain boundaries. The twin spacing dependent strengthening effect is thus represented similar to the classical Hall-Petch relation [91]:

$$\sigma_{tw} = k_{TB} / \sqrt{t}\,, \qquad \text{Eq. 4-21}$$

where t is the average twin spacing and k_{TB} is a constant. Meanwhile, due to the inhabitation of twinning boundaries to dislocations, high-density orderly arranged interfacial dislocation can be observed along with twinning boundaries. The dynamic recovery of dislocations can be effectively reduced by dense hierarchical twin networks. This may explain the higher dislocation density when deforming at lower temperatures (Fig. 4-9). It is also worth noting that twinning boundaries can be penetrated by dislocations with decreasing the twin lamella thickness and higher external stress [91]. For the present study, the strain-induced twinning boundaries, especially the secondary

twins, has a very narrow width (less than ~5 nm, Fig. 4-10 and Fig. 4-11), which may relieve the stress concentration along with twinning boundaries and reduce the strain hardening effect. On the other hand, the softening effect of twinning originates from its role as an effective and supportive deformation mechanism. twinning boundaries can serve as adequate pathways for easy glide and cross-slip of dislocations, enabling the alloy to accommodate extensive plastic deformation at high strain levels and postpone necking [352,361].

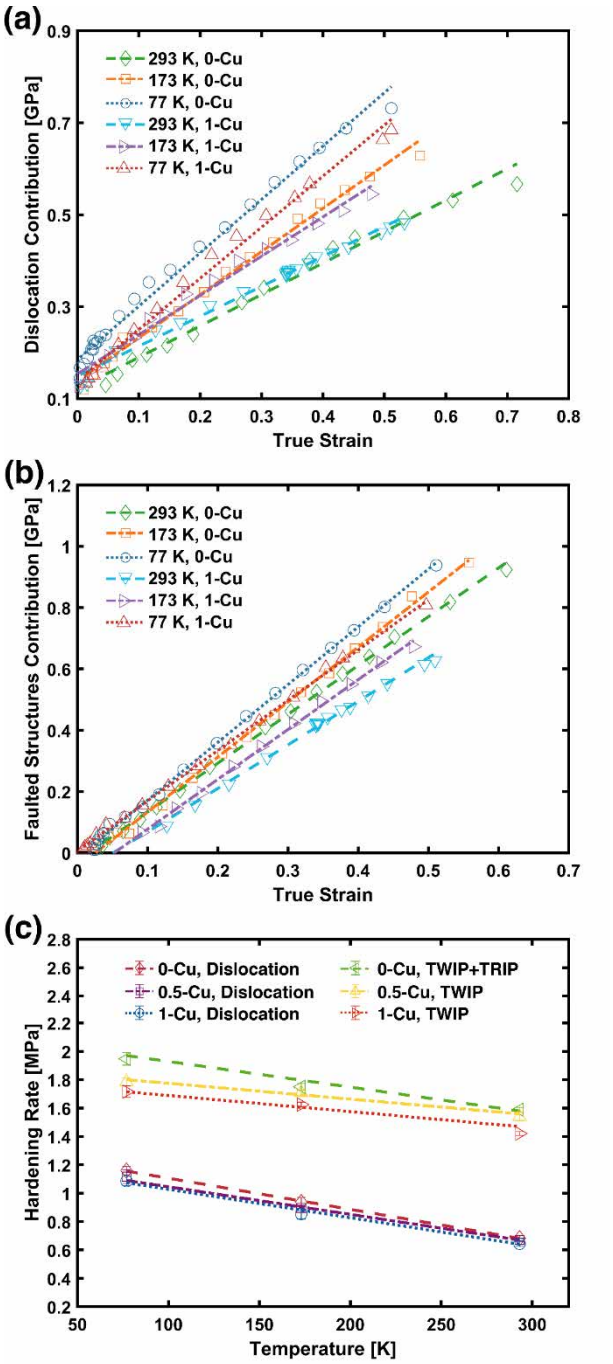

Fig. 4-14 Strengthening hardening effect of (a) dislocation and (b) TWIP and TRIP; (c) temperature dependence of the hardening rate from dislocation and faulted structures.

Similarly, the strengthening effects of strain-induced HCP laths are based on continuous segregating grains by introducing extra phase-matrix interfaces, where dislocations pile up can be significantly promoted after massive dislocation motions. This can create significant back stresses, which are capable of reducing the mobility of dislocations, dynamic recovery, and thus improving work hardening rate [362]. Unlike

the thin twins, the lamellar structure of HCP phases serves as stronger dislocation barriers due to either <c> or <c+a> dislocations are needed for passing edge dislocations into the HCP phase, and the critical resolved shear stress of motivating these dislocations are very high [363]. Meanwhile, the transformation from FCC to HCP laths is expected to produce a significant strengthening effect. More importantly, the HCP laths can also create very strong barriers for twinning on impinging slip systems, and motivating intragranular rotations [104]. A large amount of martensite phase transformation, however, can deteriorate ductility, since the quasi-cleavage fracture can be activated [69].

The strengthening effects of dislocation and faulted structures (TWIP and TRIP) were plotted as a function of true strain in Fig. 4-14a and b, respectively. When deforming the 0-Cu steel to a true strain of ~0.5, the strengthening contribution from dislocation (σ_{dis}) increased from ~493 MPa at 293 K to ~690 MPa at 77 K. Meanwhile, the contribution from the faulted structures (σ_{fs}) was ~780 MPa at 293 K (from TWIP), which increased to ~940 MPa at 77 K (from TWIP and TRIP). The strengthening effect is less significant in the 1-Cu steel at a similar strain level: σ_{dis} was ~470 MPa at 293 K and ~770 MPa at 77 K while σ_{fs} was ~640 MPa at 293 K and 810 MPa at 77 K. The hardening effects showed an almost linear increase with true strain. After linear fitting, their slopes were defined as the dislocation-induced ($\partial\sigma_{dis}/\partial\varepsilon$) and faulted structures-induced ($\partial\sigma_{fs}/\partial\varepsilon$) hardening rates, respectively. This indicates that the high strengthening effects can be ascribed to concurrent strengthening effects from dislocation, TWIP, and TRIP, which can be enhanced with the decrease of deformation temperature and SFE. The influence of temperature on the hardening rates of the three steels, the 0-Cu, 0.5-Cu [327], and 1-Cu steel, was also illustrated in Fig. 4-14c. This

indicates that both $\partial\sigma_{dis}/\partial\varepsilon$ and $\partial\sigma_{fs}/\partial\varepsilon$ increased almost linearly with temperature decreasing. Their relationship can thus be described as:

$$-m_{dis} = \frac{\partial\sigma_{dis}}{\partial\varepsilon\partial T} \quad \text{Eq. 4-22}$$

$$-m_{fs} = \frac{\partial\sigma_{fs}}{\partial\varepsilon\partial T} \quad \text{Eq. 4-23}$$

, where the m_{dis} and m_{fs} are the slopes of the hardening rate-temperature curves of the dislocation and faulted structures, respectively. After linear fitting, m_{dis} of the three high Mn steels maintained at a very similar level of ~2.0 MPa·K^{-1}. The 1-Cu and 0.5-Cu steels have m_{fs} = ~1.1 MPa·K^{-1}, lower than that of the 0-Cu steel, m_{fs} = 1.89 MPa·K^{-1}. This is due to the synergistic hardening effects of TWIP and TRIP of the 0-Cu steel at 77 K.

4.5 Conclusions

The mechanical performance, microstructural evolution, and deformation mechanisms of two high Mn steels with different Cu contents (Fe-24Mn-4Cr-0.5C and Fe-24Mn-4Cr-0.5C-1Cu) at a low-temperature range (from 293 to 77 K) were investigated with *in situ* neutron diffraction tensile tests and correlated post-mortem microscopic characterization. The investigation leads to the following conclusions:

(1) The tensile strength increased steadily with temperature decreasing. At 293 K, the YS and UTS of the 0-Cu steel are 336 MPa and 930 MPa, respectively, while the 1-Cu steel showed a higher YS of 429 MPa but lower UTS of 876 MPa. At 77 K, the 0-Cu steel showed a high YS of 700 MPa and UTS of 1358 while the corresponding data of the 1-Cu steel can reach 793 MPa and 1323 MPa. Meanwhile, the large elongation was

maintained even at 77 K with total elongation of ~0.68 and ~0.86 for the 0-Cu and 1-Cu steel, respectively.

(2) The stacking fault energy of the two steels were determined with both thermodynamical modelling and neutron diffraction measurement. The results show that the SFE decreased linearly with the drop of temperature (with a slope of ~0.06 $mJm^{-2}K^{-1}$). The SFE of the 0-Cu steel decreased from 26.8±0.5 mJm^{-2} at 293 K to 15.5±1.7 mJm^{-2} at 77 K. The dominant deformation mechanism of the 0-Cu steel switched from twinning (at 293 and 173 K) to martensite phase transformation (at 77 K). The 1wt.% Cu addition enhanced the SFE with ~5 mJm^{-2}, making twinning the main deformation mechanism of the 1-Cu steel.

(3) The dislocation density of the two steels was calculated with the modified Williamson-Hall method. The dislocation density was at around 7×10^{13} m^{-2} before deformation. The dislocation density increased almost linearly with strain after yielding. Its increase rate was higher at lower deformation temperatures. The deformed 0-Cu steel showed a higher level of dislocation density than the 1-Cu alloy. When deforming at 77 K to a true strain of ~0.5, the highest dislocation density of both steels was achieved (~2.5×10^{15} m^{-2} for the 0-Cu steel and ~2.0×10^{15} m^{-2} for the 1-Cu steel).

(4) The lattice friction stress can be improved by decreasing temperature and Cu alloying. The 1wt.% of Cu addition can enhance ~82 MPa of the lattice fraction stress. Starting from 135 MPa (0-Cu) and 215 MPa (1-Cu), the lattice friction stress increased linearly with the temperature dropping with a slope of 1.651 $MPa \cdot K^{-1}$ (0-Cu) and 1.761 $MPa \cdot K^{-1}$ (1-Cu).

(5) The strengthening effects of both dislocation and faulted structures (twins and martensite) are significant and increase as the temperature/SFE decreased. For the 0-

Cu steel deformed to a true strain of ~0.5, dislocation contributed ~470 MPa at 293 K and ~730 MPa at 77 K, while the faulted structures contributed ~770 MPa at 293 K (from TWIP only), which increased to ~940 MPa at 77 K (from both TWIP and TRIP).

Chapter 5. Cryogenic Deformation of a $FeCoCrNiMo_{0.2}$ High Entropy Alloy

Published Article

Lei Tang[a], Kun Yan[b], Biao Cai[a], Yiqiang Wang[c], Bin Liu[d], Saurabh Kabra[e], Moataz M Attallah[a], Yong Liu[d], ***Deformation mechanisms of FeCoCrNiMo0.2 high entropy alloy at 77 and 15 K***, Scr. Mater. 178 (2020) 166–170.

https://doi.org/10.1016/j.scriptamat.2019.11.026.

Acknowledge of Collaborative Work

Lei Tang conceived and designed the experiment, performed the experiment, interpreted the data, and wrote the manuscript. Kun Yan assisted in the data interpretation. Biao Cai assisted with designing the experiments, revising the manuscript, and data analysis. Yiqiang Wang, Bin Liu, Moataz M Attallah, and Yong Liu assisted in the preparation of the material. Saurabh Kabra assisted with performing experiments.

[a] School of Metallurgy and Materials, University of Birmingham, B15 2TT, United Kingdom
[b] School of Materials, University of Manchester, M13 9PL, United Kingdom
[c] United Kingdom Atomic Energy Authority, Culham Science Centre, Abingdon OX14 3DB, United Kingdom
[d] State Key Laboratory for Powder Metallurgy, Central South University, 410083, P.R. China
[e] ISIS Facility, Rutherford Appleton Laboratory, Didcot OX11 0QX, United Kingdom

5.1 Abstract

Deformation mechanisms of high entropy alloys (HEAs) at cryogenic temperatures have attracted extensive research interest. We used *in situ* neutron diffraction to study the tensile behaviour of a face-centred-cubic HEA at 77 and 15 K and compared its stacking fault energy (SFE) at ambient and cryogenic temperatures. The SFE dropped from 28 mJm^{-2} at 293 K to 11 mJm^{-2} at 15 K, leading to the transition of the deformation mechanism from deformation-induced twinning to martensite phase transformation. As a result, an excellent balance of strength and ductility was achieved at both temperatures. This finding highlights the importance of SFE for cryogenic alloy design.

5.2 Introduction

Differing from traditional alloys, which are mainly based on only one principle element, high entropy alloys (HEAs) were designed to consist of near-equimolar multi-components and single-phase to maximize their configurational entropy [232,364–366]. The unique features of HEAs (sluggish diffusion, cocktail effects, and high lattice distortion [232,364]) usually come with eminent mechanical performance [367–371]. Researches have shown that at cryogenic temperatures several HEAs [200,254,372] (FeCoCrNi, CrMnFeCoNi, FeCoNiCr, etc.) with single face-centred cubic (FCC) phase have an excellent combination of high strength and elongation, making them very attractive for low-temperature applications, such as liquified natural gas industry, structural material for superconductor in fusion reactors and outer space.

Two athermal transformations are known to significantly improve HEAs' mechanical performance: deformation-induced twinning and phase transformation [259]. It is well established that deformation-induced nano-twinning can activate the dynamic Hall-

Petch effect, leading to significant increments in both strength and ductility [135]. Phase transformation also serves as an important origin of strength and ductility in FCC alloys by inducing (transformation-induced-plasticity) TRIP effect [53]. The dominant factor in deciding the strengthening mechanisms in HEAs is found to be the stacking fault energy (SFE, γ_{sf}) of the alloy [200], which is mainly affected by alloy composition and deformation conditions (e.g. temperature and strain rate). According to previous studies [135,140,373], dislocation passage and piling up dominate the plastic deformation when SFE exceeds 45 mJm^{-2}, while twinning will be more favourable with SFE in the range of 15~45 mJm^{-2}. If SFE lowers to less than 15 mJm^{-2}, the phase transformation from FCC-austenite to martensite with hexagonal close-packed (HCP) and/or body-centred-cubic (BCC) structure can be triggered.

Temperature is one of the dominant factors in deciding alloys' SFE- the lower the temperature, the lower the SFE- hence controlling the micro-mechanical behaviour. SFE of FeCoNiCr alloy at room temperature has been determined in the range of 23 to 31 mJ/m^2 by transmission electron microscopy [279], and 17.4 to 31.7 mJ/m^2 by X-ray diffraction and *ab initio* calculation [99]. Twinning and dislocation pilling up are the main deformation mechanism of a HEA from room temperature to 77 K [200]. However, some researches show that via tunning the alloy composition [374], phase transformation can also be induced during plastic deformation of HEAs at room temperature [370] and 77 K [375]. Mechanical performance and deformation mechanisms of HEAs at extremely low temperatures (≤ 77 K), however, have scarcely been reported. Lin et al [372]. recently reported FCC to HCP phase transformation when FeCoCrNi alloy was deformed at 4.5 K, in contrast to twinning reported at higher temperatures. Therefore, it is of great interest to perform mechanical testing at a

temperature below 77 K and to compare the micro-mechanical behaviour of the HEAs at different temperatures.

In this study, we have carried out *in situ* neutron diffraction on a $FeCoCrNiMo_{0.2}$ HEA at 77 and 15 K with the aim to probe its strengthening origins. This study provides a better understanding of the relationship among SFE, temperature, and mechanical properties of HEA and sheds a light on designing engineering alloys with a better combination of strength and ductility for cryogenic applications.

5.3 Materials and Methods

A HEA ($FeCoCrNiMo_{0.2}$) was prepared by powder metallurgy as detailed in Ref. [102]. The ENGIN-X diffractometer (ISIS spallation neutron source, the Rutherford Appleton Laboratory, UK) was utilized to perform the *in situ* time-of-flight neutron diffraction during the tensile tests. Dog-bone tensile samples with a gauge dimension of Φ 8 × 34.5 mm were machined. The tensile tests were carried out by a 100 kN Instron stress rig with a cryogenic chamber cooled by liquid helium [288]. The loading direction is orientated 45° relative to the incident neutron beam. The north and south detectors (correspond to the axial and radial detector, respectively) are capable of capturing diffraction signals parallel and perpendicular to the loading direction. The gauge volume for neutron diffraction measurements was $4 \times 4 \times 4$ mm^3 and each diffraction pattern collection took 20 mins.

5.4 Results

Representative true strain-stress curves of the alloy at 293 [102], 77, and 15 K are shown in Fig. 5-1a. The alloy showed high yield strength (YS) of 376 MPa, ultimate

tensile strength (UTS) of 767 MPa along with excellent total elongation of 52.5% at 293 K. At 77 K, the YS, UTS, and total elongation of the sample all enhanced to 637 MPa, 1212 MPa, and 71.2%, respectively. At 15 K, the YS further increased to 710 MPa, UTS to 1423 MPa, and the ductility dropped slightly to 41.8% (Table 5-1). As shown in Fig. 5-1a, the true stress-strain curves at 293 and 77 K show a very similar pattern, whereas the one at 15 K was different, which consisted of a plateau period within 0.02 to 0.12 true strain followed by an uptrend.

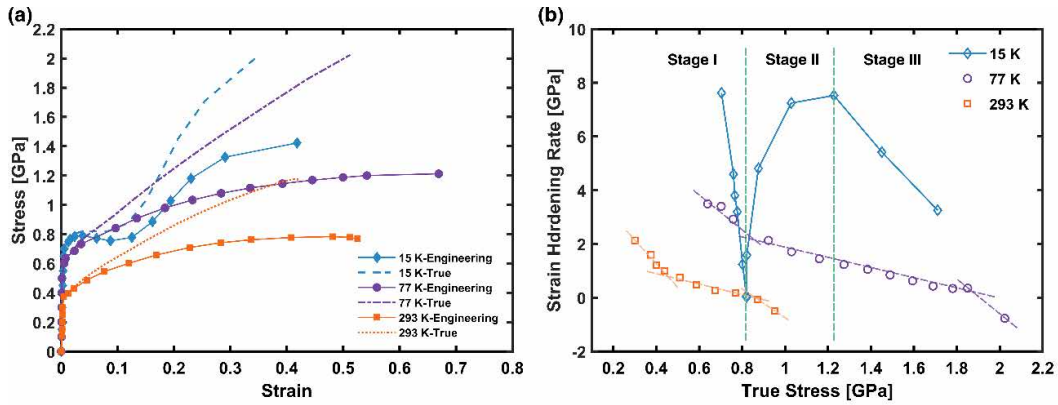

Fig. 5-1 (a) True strain-stress curve and (b) strain hardening rate curve at 293, 77, and 15 K.

Strain hardening rate (SHR) curves (shown in Fig. 5-1b) at 293 and 77 K shared a quite similar trend. They both experienced a rapid drop at the initial stage, then the decreasing rates slowed down until fracture. SHR at 77 K exhibited an overall higher value than that at 293 K. In contrast, SHR at 15 K changed more abruptly and showed an unusually large strain-hardening capability. Three pronounced stages can be observed as outlined in Fig. 5-1b: starting from a very large value of ~7.6 GPa, the SHR curve initially dropped dramatically to the bottom of ~0.06 GPa, corresponding to the plateau period in the stress-strain curve. It then soared to a peak of ~7.5 GPa with true stress of ~1270 MPa, characterizing stage II, after which it began dropping until facture (Stage III).

Table 5-1 Properties of the $FeCoCrNiMo_{0.2}$ alloy at three temperatures.

Temperature [K]	YS [MPa]	UTS [MPa]	Elongation [%]	Lattice Parameter [Å]	SFE [mJm^{-2}]	Measured [MPa]		Calculated [MPa]	
						τ_{tw}	b_p	τ_{tw}	b_p
293	376	767	52.5	3.595	28	245±10	750±30	251	767
173	637	1212	71.2	3.587	17	232±10	710±30	225	689
77	710	1423	41.8	3.585	11	219±10	670±30	210	642

The diffraction patterns collected at axial direction during tensile loading at 77 and 15 K are plotted in Fig. 5-2a and b, respectively. The sample at room temperature composes of a single FCC phase with a lattice parameter of 3.595 Å and no new phases appeared during cooling. The lattice parameter of FCC-phase decreased to 3.586 Å at 77 K and 3.584 Å at 15 K. During tensile testing at 77 K no new phase was observed (Fig. 5-2a). At 15 K (Fig. 5-2b), peaks belonging to FCC-phase were replaced progressively by newly formed peaks after yielding, which were identified as HCP/BCC- phases via TOPAS [376]. Fig. 5-2c shows the diffraction pattern between d spacing=2.125~1.75 Å, clearly demonstrating the occurrence of phase transformation. Formation of HCP/BCC- phases of the FCC HEA during tensile loading is similar to austenitic steels and transformation-induced-plasticity steels [75], so we simply use γ, ε, and α' to respectively symbolize FCC-, HCP-, and BCC- phases.

The change in lattice strain was measured with the following formula:

$$\varepsilon_{hkl} = \frac{d_{hkl} - d^0_{hkl}}{d^0_{hkl}} \qquad \text{Eq. 5-1}$$

, where ε_{hkl}, d_{hkl}, and d^0_{hkl} correspond to the lattice strain, inter-planar spacing under stress, the stress-free lattice spacing of $\{hkl\}$ crystallographic grain family, respectively. The *d* spacing was obtained by fitting a single reflection with the Pseudo-Voigt function using the GSAS program [377]. Fig. 5-3a and c show the evolution of elastic lattice strain from the axial and radial direction in different grain families during tensile deformation at 77 and 15 K, respectively. It is noted that the lattice strain at 15 K was depicted only at low strain conditions (≤ 0.15) because the occurrence of new peaks

overlapped with original peaks, leading to high uncertainty during single peak fitting of γ-phase peaks at larger strains. Different trends of lattice strain response against applied stress were observed at different temperatures. A linear relationship was kept before yielding at both temperatures, while the slope of the curves at 15 K was changed after yielding due to the phase transformation and the following stress partitioning.

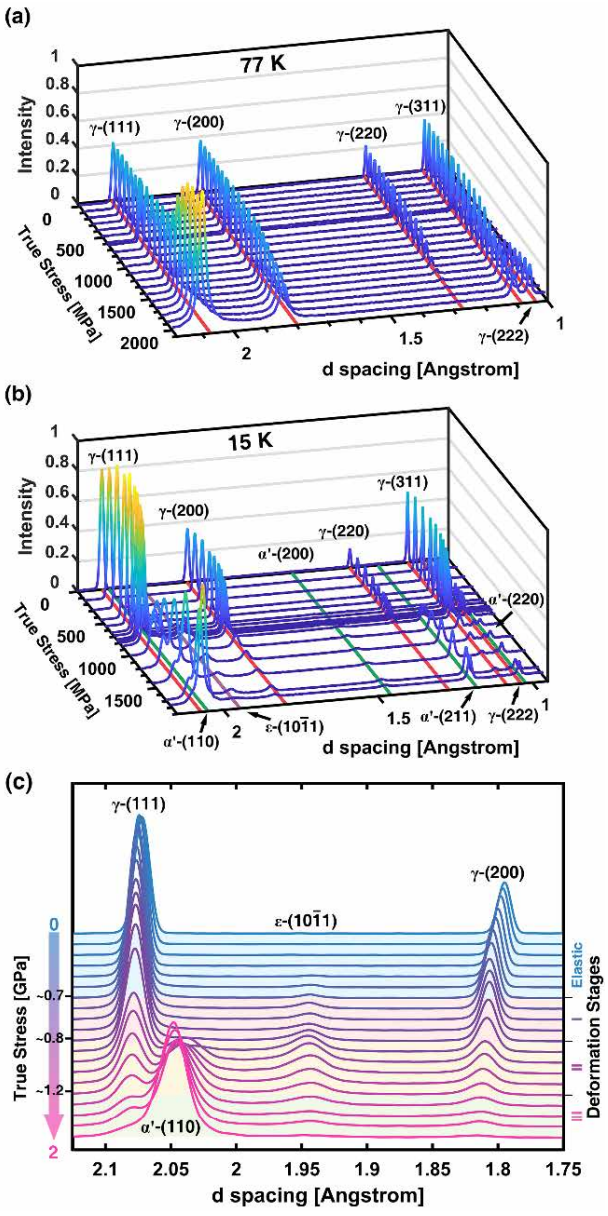

Fig. 5-2 Diffraction patterns during deformation at (a) 77 K, (b) 15 K, and (c) 15 K, with higher magnification.

Studies have shown that if stacking faults (SFs) formed during deformation, the shift of the peak positions for successive orders of reflections such as {111} and {222} will

be different due to the structure factor for SFs [378]. We present the lattice strain evolution of two successive grain planes of {111} and {222} at axial and radial directions at both temperatures (only strain ≤ 0.15 is illustrated at 15 K) in Fig. 5-3b and d, respectively. The lattice strain of {111} and {222} reflection deviated from each other when certain stress/strain was reached, confirming the formation of SFs.

The peak shifting can be ascribed to two main sources: macro-strain ($\varepsilon_{hkl}^{strain}$) and SFs (ε_{hkl}^{sf}), following a relationship [274,379] of:

$$\varepsilon_{hkl}^{exp} = \varepsilon_{hkl}^{strain} + \varepsilon_{hkl}^{sf} = \varepsilon_{hkl}^{strain} - \frac{\sqrt{3}}{4\pi} \frac{\sum b \pm (h+k+l)}{(u+b)(h^2+k^2+l^2)} SFP \qquad \text{Eq. 5-2}$$

, where the ε_{hkl}^{exp} is the measured lattice strain, SFP is the stacking fault probability, while *u* and *b* are the numbers of non-broadened and broadened components due to SFs [274].

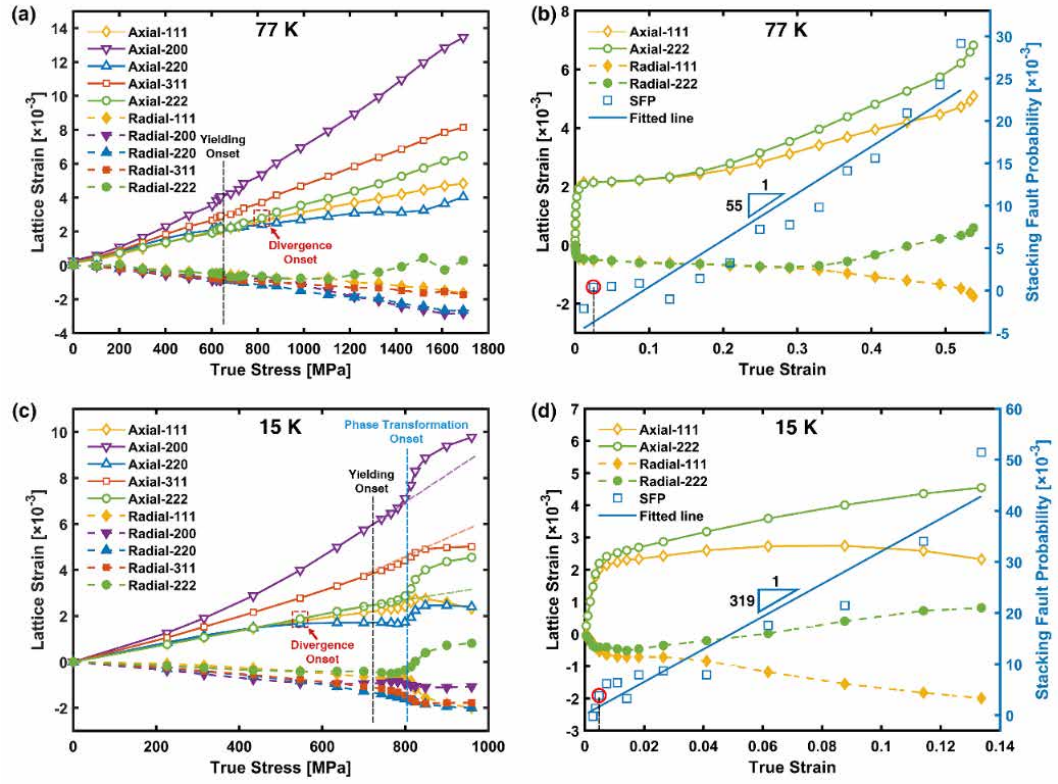

Fig. 5-3 Evolution of elastic lattice strain (a and c) and corresponding stacking fault probability (b and d) along with axial and radial directions in crystallographic planes of (222), (311), (220), (200), and (111) during tensile tests at (a)(b) 77 K, (c)(d) 15 K. "Divergence onset" indicates the start point of the observable separation of the two lattice strain curves belonging to (111) and (222) grain plane.

Accordingly, Fig. 5-3b and d illustrate the SFP change with respect to true strain at 77 and 15 K. After SFP surpassed 0, it increased almost linearly as a function of true strain. The fitted line representing the SFP at 77 K showed a gentle slope of ~55 (Fig. 5-3b), which boosted to ~319 when the temperature dropped to 15 K (Fig. 5-3d). SFP increased to 42 × 10^{-3} at 15 K at only 0.13 true strain, whereas it increased to only 24 × 10^{-3} at 77 K at 0.52 true strain. This indicated that at 15 K, the alloy has a much higher probability to form SFs than at 77 K.

SFE, which indicates the ease of dissociating perfect dislocations into partial dislocations and SFs, can be estimated according to Reed and Schramm [171]:

$$\gamma_{isf} = \frac{6.6a_0}{\pi\sqrt{3}} \frac{\langle \varepsilon^2 \rangle_{111}}{SFP} \left(\frac{2C_{44}}{C_{11} - C_{12}} \right)^{-0.37} \left(\frac{C_{44} + C_{11} - C_{12}}{3} \right) \quad \text{Eq. 5-3}$$

, where $\left\langle \varepsilon_{50}^2 \right\rangle_{111}$ represents mean square strain calculated by deconvoluting size and strain broadening effects with double-Voigt method [380]. Based on the *ab initio* simulation from [374], C_{11} =216 GPa, C_{12} =175 GPa, and C_{44} =189 GPa were used here for SFE calculation. The SFE evolution of the alloy at 293, 77, and 15 K was plotted as a function of true strain in Fig. 5-4a. All three fitted curves showed a similar trend that they continued to drop at lower strain until reaching the turning points and then kept at constant values, corresponding to the SFE of the alloy (Table 5-1). At low strain conditions, the calculated high SFE values are artefacts of Eq. 5-3 due to the fact that the formed SFs are not enough to be reflected in diffraction peaks, and uncertain inputs of small strain and SFP were used. The turning points indicate that the gathered SFs become significant enough and the SFE calculation tends to be stabilized and reliable. The value calculated here at room temperature is slightly higher than that in [200] because of the different methods used to calculate $\left\langle \varepsilon_{50}^2 \right\rangle_{111}$. It is noted that Mo

addition to this HEA might reduce the SFE significantly as demonstrated in Fe-Cr-Ni system. The dropping of SFE leads to the shifting of deformation mechanisms: deformation-induced twinning at 293 K with SFE of 28 mJm^{-2} [102], and at 77 K with SFE of 17 mJm^{-2}; whereas phase transformation (from γ-phase to ε-/α'- phase) occurred at 15 K with SFE of 11 mJm^{-2}.

Steinmetz's equation was used to calculate critical stress for twinning (σ_{tw}) [301]:

$$\sigma_{tw} = M\tau_{tw} = M\left(\frac{\gamma_{sf}}{3b_p} + \frac{3Gb_p}{L_0}\right) \quad \text{Eq. 5-4}$$

, where G is the shear modulus (85 GPa), τ_{tw} is the critical shear stress for twinning, b_p is the Burgers vector for partial dislocations ($a_0\langle 112\rangle/6$), M is the Taylor factor (3.06), and the L_0 is the width of the twin embryo (~200 nm) [200]. The calculated σ_{tw} decreases progressively from 767 MPa at 293 K to 642 MPa at 15 K. Experimentally, we used the stress at SFP = 0 (shown with red circles at Fig. 5-3 c and d) as the critical stress for twinning, which are 710±30 MPa/2.5% true strain at 77 K and 670±30 MPa/0.45% true strain at 15 K (Table 4-2). The values obtained by the two methods agree reasonably well. Although deformation-induced twinning and phase transformation are two exclusive strengthening mechanisms [381], the formation of twinning at low strain conditions may serve as nucleation sites for FCC-BCC/BCT phase transformation [45,323,382]. Hence the calculation of twinning stress at 15 K is relevant although the alloy tends to prompt phase transformation due to the reduced SFE at 15 K.

The phase transformation process during the tensile test at 15 K was depicted at Fig. 5-4b, where the weight fraction of the three phases (γ, ε and α') obtained by Rietveld refinement in TOPAS [376] was plotted with respect to true stress, along with the SHR

curve. During stage I (from 700 to 802 MPa), the SHR kept dropping whereas the phase fraction only changed slightly. The drop of SHR was due to dynamic recovery [383] and glide of partial dislocations in γ phase, serving as an incubation for the following phase transformation [108]. During stage II (from 802 MPa to 1270 MPa), the phase transformation occurred. At first, the phases transformed at an ultrafast speed within ~70 MPa, with α'-phase fraction soaring to ~42%, ε-phase to ~6% while γ-phase decreasing dramatically to ~52%. This mainly results from that the phase transformation originally occurred at favourable sites (i.e., grain boundaries and grains with preferred orientation). The phase transformation from FCC to BCC can trigger the TRIP effect, which can enhance the strain hardening over a wide deformation range and improve the ductility significantly [384]. The induced dense γ-/α'-/ε- phase interfaces, can also serve as barriers against the (partial-) dislocation motion and strengthen the alloy [385,386]. During the rest part of Stage II (from 870 to 1270 MPa), the phase transformation continued (α'-phase increased to ~81%, γ-phase decreased to ~16% and ε-phase disappeared gradually), however, with lower speed. This originates from that the phase transformation shifted to grain interior or not-so-good-orientated grains [53]. It also led to the slow-down of SHR growth. At stage III (>1270 MPa), the phase transformation reached a plateau (~87% for α'-phase and ~13% for γ-phase). Consequently, the SHR started to decrease since the supply of new phases was stopped.

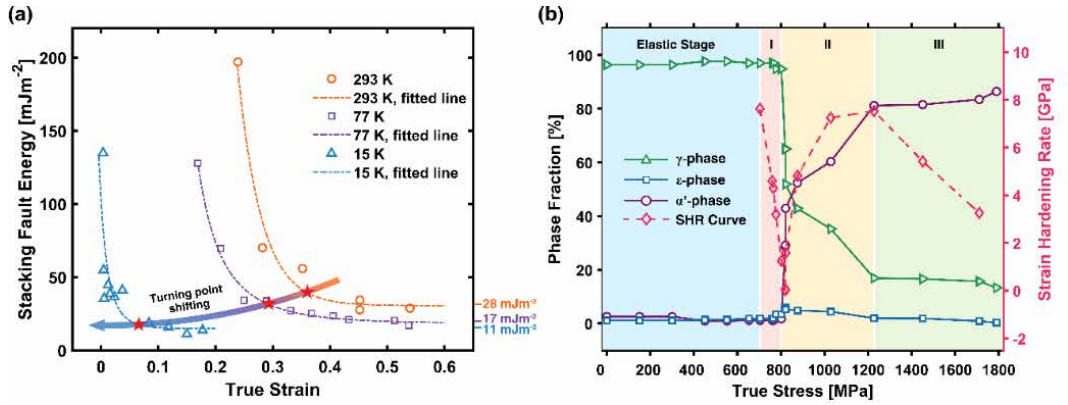

Fig. 5-4 (a) Stacking fault energy calculation curve at 293, 77 and 15 K and (b) fraction evolution of γ-, α′- and ε- phase and strain hardening rate curve as a function of true stress during deformation at 15 K.

5.5 Conclusion

In situ neutron diffraction measurements and tensile tests were applied to study the strengthening mechanisms of a high-performance HEA alloy ($FeCoCrNiMo_{0.2}$) at 77 and 15 K. The alloy prepared comprises a single FCC phase, which exhibited astonishing mechanical properties at both temperatures (YS of 637 MPa, UTS of 1212 MPa and elongation of 71.2% at 77 K, while YS of 710 MPa, UTS of 1423 MPa and elongation of 42% at 15 K). The strength and ductility enhancement at 77 K mainly benefit from the interaction between twinning boundaries and dislocations, while phase transformation plays a majority role in strengthening at 15 K. The transition of strengthening mechanism can be ascribed to the temperature-dependent SFE dropping, which was calculated to be 28, 17, and 11 mJ/m^2 at 298, 77, and 15 K, respectively. Hence, engineering SFE by tunning alloy composition and deformation temperature can induce desirable strengthening mechanisms (twinning and phase transformation), effectively improving the mechanical performance of alloys, which is a promising concept to exploit more advanced cryogenic HEAs.

Chapter 6. Cryogenic Deformation of a FeCrNi Medium Entropy Alloy

Published Article

Lei Tang[a], Fuqing Jiang[b], Jan S Wróbel[c], Bin Liu[d], Saurabh Kabra[e], Ranxi Duan[a], Junhua Luan[f], Zengbao Jiao[g], Moataz M Attallah[a], Duc Nguyen-Manh[h], Biao Cai[a], ***In Situ Neutron Diffraction Unravels Deformation Mechanisms of a Strong and Ductile FeCrNi Medium Entropy Alloy*****,** Journal of Materials Science and Technology, 116 (2022) 103–120.

https://doi.org/10.1016/j.jmst.2021.10.034.

Acknowledge of Collaborative Work

Lei Tang conceived and designed the experiment, performed the experiment, interpreted the data, and wrote the manuscript. Fuqing Jiang, Ranxi Duan, Zengbao Jiao, Junhua Luan, Saurabh Kabra, and Moztaz M. Attalah assisted in performing experiments. Jan S. Wróbel and Duc Nguyen-Manh performed the DFT theoretical modelling. Bin Liu assisted sample preparation. Biao Cai assisted with designing the experiments, revising the manuscript, and data analysis.

[a] School of Metallurgy and Materials, University of Birmingham, B15 2TT, United Kingdom
[b] Shenyang National Laboratory for Materials Science, Institute of Metal Research, Chinese Academy of Sciences, Shenyang 110016, China
[c] Faculty of Materials Science and Engineering, Warsaw University of Technology, ul. Woloska 141, 02-507 Warsaw, Poland
[d] State Key Laboratory for Powder Metallurgy, Central South University, 410083, PR China
[e] ISIS Facility, Rutherford Appleton Laboratory, Didcot OX11 0QX, United Kingdom
[f] Department of Materials Science and Engineering, City University of Hong Kong, Hong Kong, China
[g] Department of Mechanical Engineering, The Hong Kong Polytechnic University, Hong Kong, China
[h] CCFE, United Kingdom Atomic Energy Authority, Abingdon, Oxfordshire OX14 3DB, United Kingdom

6.1 Abstract

We investigated the mechanical and microstructural responses of a high-strength equal-molar medium entropy FeCrNi alloy at 293 and 15 K by *in situ* neutron diffraction testing. At 293 K, the alloy had a very high yield strength of 651±12 MPa, with total elongation of 48±5%. At 15 K, the yield strength increased to 1092±22 MPa, but the total elongation dropped to 18±1%. Via analysing the neutron diffraction data, we determined the lattice strain evolution, single-crystal elastic constants, stacking fault probability, and estimated stacking fault energy of the alloy at both temperatures, which are critical parameters to feed into and compare against our first-principles calculations and dislocation-based slip system modelling. The density functional theory calculations show that the alloy tends to form short-range order at room temperatures. However, atom probe tomography and atomic-resolution transmission electron microscopy did not identify the short-range order. Additionally, at 293 K, experimental measured single-crystal elastic constants do not agree with those determined by first-principles calculations with short-range order but agree well with the values from the calculation with the disordered configuration at 2000 K. This suggests that the alloy is at a metastable state related to the fabrication methods. In view of the high yield strength of the alloy, we calculated the strengthening contribution to the yield strength from grain boundaries, dislocations, and lattice distortion. The lattice distortion contribution was based on the Varenne-Luque-Curtine strengthening theory for multi-component alloys, which was found to be 316 MPa at 293 K and increased to 629 MPa at 15 K, making a marked contribution to the high yield strength. Regarding plastic deformation, dislocation movement and multiplication were found to be the dominant hardening mechanism at both temperatures, whereas twinning and phase transformation were not operative. This is mainly due to the high stacking fault energy of the alloy as estimated

to be 63 mJm^{-2} at 293 K and 47 mJm^{-2} at 15 K. This work highlights the significance of lattice distortion and dislocations played in this alloy, providing insights into the design of new multi-component alloys with superb mechanical performance for cryogenic applications.

6.2 Introduction

In the past decade, a revolutionary new metallurgy design strategy, multi-component alloys (MCAs), containing several equimolar or non-equimolar components (in the range of 5-35 at.%), has been developed [232], which include high entropy alloys (HEAs) and medium entropy alloys (MEAs). Among different groups of MCAs, the group based on 3*d* transition elements (Cr, Mn, Fe, Co, Ni, V, and Cu) can form a single face-centred cubic (FCC) structure, which shows great potential in achieving superior strength-ductility combinations [99,102,198,254,259,387–389]. The compositions include FeNiCo MEA [198], FeMnCoCr HEA [259], CrMnFeCoNi HEA [254], and other variations.

Recently, the intriguing mechanical performance of 3*d* element-metal MCAs under cryogenic temperatures has been demonstrated, such as high fracture tolerance [254], fatigue-crack growth resistance [390], and exceptional strength-ductility balance [282,348]. This makes them highly desirable in the rapid-growing cryogenic applications such as liquid gas storage, fusion reactors, and medical diagnosis. The application of MCAs at cryogenic temperatures, however, can be severely limited since the yield strength (YS) of those alloys is relatively low compared to conventional structural alloys. Many studies show the YS of these MCAs is generally lower than 400 MPa at room temperature and 500 MPa at cryogenic temperatures [198,200]. For

example, the YS of a single-phase FeCoCrNi HEA is only 260 MPa at 293 K and 480 MPa at 77 K [200]. Therefore, several conventional strengthening strategies (such as precipitating hardening and grain refinement) were applied to overcome this dilemma via introducing extensive dislocations and interfaces.

Based on the uniqueness of MCAs, two more promising strengthening strategies are emerging to resolve this dilemma: chemical short-range order (SRO) [117,391,392] and severe lattice distortion (i.e., a wide fluctuation of the atomic bond distances) [232]. SRO stems from the enthalpic interactions among constituent elements, and its formation is thermodynamically favoured in MCAs [117,391,392]. The densely distributed SROs can create strain fields; thus, an extra force is required to break the SROs when dislocations pass by. The cutting-through and the following de-trapping process during dislocation migration are expected to increase the opportunity for dislocation to interact and form entanglement [391]. However, the formation mechanism of SROs in MCAs has only been directly observed in two MEAs of VCoNi [117] and CrCoNi [391].

Severe lattice distortion originates from the randomly distributed constituent elements with varying atomic radii as no matrix or host element could be defined in MCAs [232]. Each individual atom in MCAs thus experiences different stress fields created by its interaction with a set of different neighbouring atoms. However, the role of the severe lattice distortion in strengthening the MCAs is under debate. Wu et al. [393] suggested that the large lattice distortion fluctuation can only provide weak Labusch-type pinning effects on dislocation motions. However, research has shown that enhancing the lattice distortion by adding extra vanadium can induce a significant YS improvement in both FCC and body-centred cubic (BCC) HEAs [387]. The critical role of lattice distortion in strengthening was also confirmed by theoretical studies, which successfully

predicted the YS of several MCAs using solute misfit volumes as the core parameter [250,394]. These theories also predicted the growing strengthening effect of lattice distortion with decreasing temperature [198].

Herein, we studied a new equimolar ternary MEA (FeCrNi alloy), which has been shown to achieve a high YS (644MPa) and good elongation (54%) at room temperature [395]. Several critical questions can be raised for this alloy: (i) Does SRO exist in the FeCrNi alloy, as observed in CrCoNi [391] and VCoNi MEAs [117]? Is SRO the main strengthening factor? (ii) To what degree the severe lattice distortion can strengthen the alloy and what is its strengthening contribution at cryogenic temperatures? In addition, the alloy should have high stacking fault energy >50 mJm^{-2} according to Ref. [396]. Twinning and phase transformation should not be operative, but the alloy still has very good ductility, so what are the underpinning mechanisms for the alloy to have a balanced combination of strength and ductility? This study intends to provide insights into these questions.

6.3 Materials and Methods

6.3.1 Materials

Powder metallurgy was used to produce the FeCrNi MEA with a nominal composition of $Fe_{33.3}Cr_{33.3}Ni_{33.3}$. Detailed procedures for the fabrication can be found in [395]. High purity (>99.99%) Fe, Cr, and Ni raw materials were melted in an induction vacuum furnace. The melted liquid was dropped through a ceramic cube and atomized by high purity Ar with a pressure of 4 MPa. The formed powder, with an average diameter of 50 μm, was then capsulated in a steel cylinder chamber (Φ50 × 150 mm). After degassing and preheating to 1200 ℃ for 1 h, the sample was subjected to hot extrusion

immediately with an extrusion ratio of 7:1 and a velocity of ~10 mm/s. The extruded bars were then cooled down to room temperature in the air. The actual chemical composition of the sample was measured to be $Fe_{33.7}Cr_{33.7}Ni_{32.5}$ (at. %) by inductively coupled plasma mass spectrometry (ICP-MS).

6.3.2 *In Situ* Neutron Diffraction

In situ time-of-flight neutron diffraction during tensile testing were carried out at the beamline of ENGIN-X at ISIS, spallation neutron and muon source, the Rutherford Appleton Laboratory, UK. The schematic illustration of the TOF neutron diffractometers and strain scanner can be seen in our previous work [327]. Originally, a pulsed beam of neutrons with a wide energy range (incident beam) travelled through a 100 K liquid methane moderator, and its horizontal and vertical angular divergence was then modified by two pairs of motorized slits (4×4 mm^2). A vacuum chamber and a 50 kN hydraulic stress rig with a horizontal loading direction (LD) were mounted 45° to the incident beam. Behind the collimators (4 mm wide), axial and radial diffraction detector bank (correspond to the north and south detector, respectively) were centred on a horizontal diffraction angle of ±90° to the incident beam to collect the diffraction signals from grain planes subjected to tensile and compressive load, respectively. Before the tests, instrument parameters (e.g., primary and secondary flight path distances) and instrumental peak broadening effects were determined by measuring a strain-free standard CeO_2 calibrant. Dog-bone tensile samples were mounted on the stress rig then the high vacuum and low-temperature conditions were stabilized for half an hour before the test. Diffraction patterns were collected for 20-min intervals between each loading step, iterating until fracture. Stress-control and displacement control were used at the elastic and plastic stages, respectively. The *in situ* neutron diffraction and

tensile testing were repeated on two specimens for both temperatures. The data collected at the same condition are very similar, and thus, the reproducibility was confirmed and only one of the data were analysed. Rietveld refinement and single peak fitting (with pseudo-Voigt function) were performed with the GSAS software, allowing the determination of lattice parameters, peak position, and full width at half maximum (FWHM) of the peaks. The lattice strain is defined as the change of inter-planar spacing with respect to its original inter-planar spacing. Its evolution can be calculated by [102]:

$$\varepsilon_{hkl} = \frac{d_{hkl} - d^0_{hkl}}{d^0_{hkl}} \qquad \text{Eq. 6-1}$$

where ε_{hkl} is the lattice strain of $\{hkl\}$ grain family, d_{hkl} and d^0_{hkl} is corresponding lattice spacing at the current stress state and stress-free state, respectively. Procedures for single crystal constant and dislocation density calculations were included in Section A.2.4 of the Appendices.

6.3.3 First Principal Calculation

Density Functional Theory (DFT) for elastic constant calculations were performed within the Vienna Ab-initio Simulation Package (VASP) using the Projector Augmented Wave (PAW) method and spin-polarized electronic structure scheme [397,398]. The electron exchange-correlation functional was in the Generalized Gradient Approximation (GGA) treated with Perdew-Burke-Ernzerhof parametrization [399]. All the calculations in this work were carried out within the PAW potentials for Cr, Fe, and Ni without semi-core electrons with the core configurations $[Ar]3d^4s^1$, $[Ar]3d^7s^{1,}$ and $[Ar]3d^9s^1$, respectively. The plane wave cut-off energy for the most of calculations was 400 eV. The total energy was converged to 10^{-6} eV/cell and the force components were relaxed to 10^{-3}eV/Å. Total energies used for elastic constant

calculations were performed using the Monkhorst-Pack meshes [400] with 4 × 4 × 4 k-point for both 3 × 3 × 3 FCC-supercell configurations with 108 atoms per unit cell configurations and additional calculations with the 6 × 6 × 6 k-point meshes were also performed for checking the convergence. A more detailed description of elastic constants from first-principles DFT calculations in different intermetallic phases can be found in Refs. [401–406].

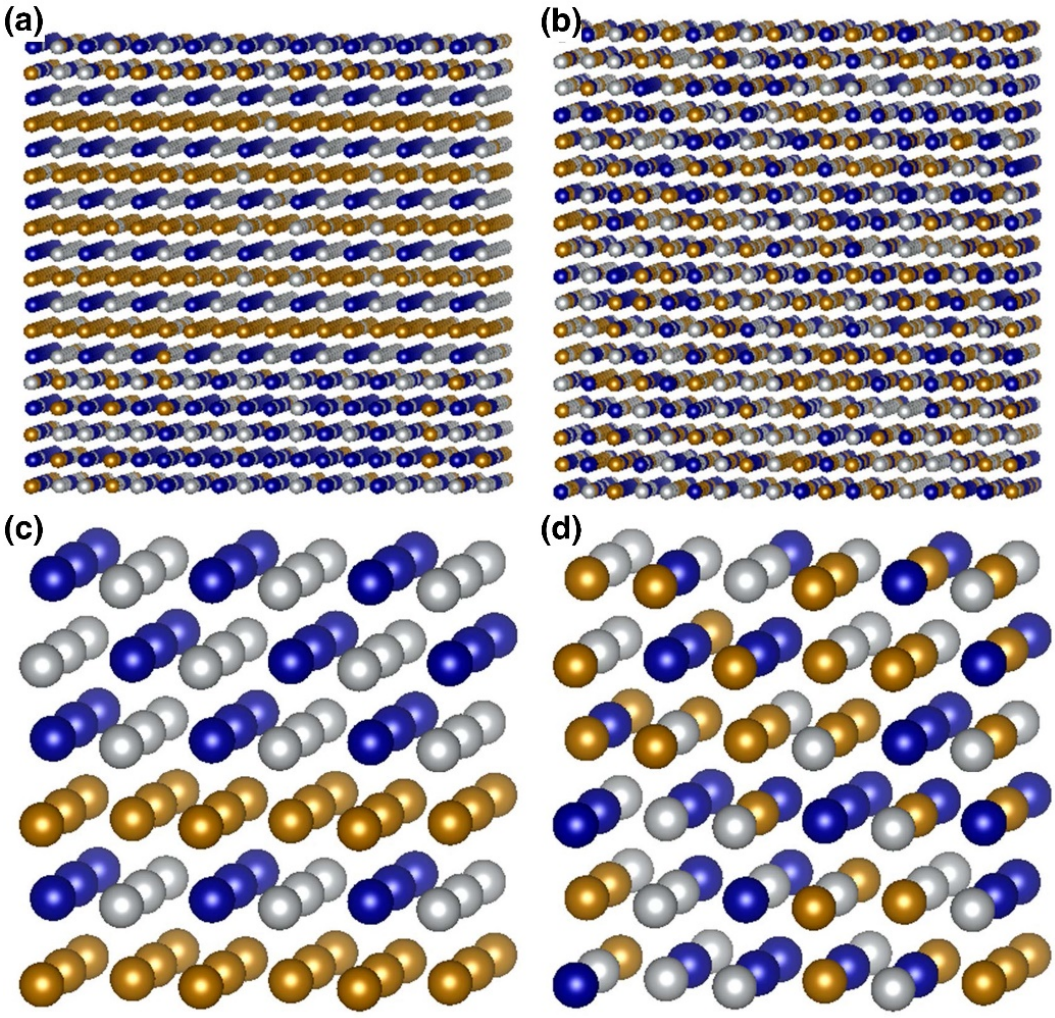

Fig. 6-1 Monte-Carlo simulations of FCC supercell configurations for equiatomic FeCrNi alloys with different sizes and temperatures using DFT based CE Hamiltonian: (a) 9 × 9 × 9, 300 K; (b) 9 × 9 × 9, 2000 K; (c) 3 × 3 × 3, 300 K; (d) 3 × 3 × 3, 2000 K. The colour code for Fe atoms is orange, Cr: blue and Ni: grey.

For disordered alloys, conventional approaches for evaluating elastic constants from DFT techniques are usually based on so-called Coherent Potential Approximation

(CPA) from which a single site mean field theory is applied to treat completely random configurations with different chemical compositions. The CPA method has been employed to investigate elastic property maps from DFT calculations for the case of concentrated random FCC Fe-Cr-Ni alloys which are the main base for austenitic stainless steels [407,408]. In the present study, an alternative DFT approach was employed to study the elastic properties of the FeCrNi medium-range entropy alloys. It was based on our recent and systematic work on the phase stability of both FCC and body-centred-cubic (BCC) Fe-Cr-Ni magnetic alloys using a combination of first-principles constructed Cluster Expansion (CE) Hamiltonian with exchange Monte-Carlo simulations at a finite temperature [409].

The new approach allows us to investigate not only the free energy but also the disorder-order transition of alloys as a function of composition and temperature in terms of Warren-Colley [379,410] SRO effects between different pairs of atoms. The theoretical expression of SRO parameters has recently been derived for MCAs in a matrix formulation [411–414]. The chemical SRO parameter $\alpha_n^{A,B}$ between two species A and B for the *n*-th nearest neighbour shell can be defined as follows:

$$\alpha_n^{A,B} = 1 - \frac{y_n^{A,B}}{x_A x_B} \qquad \text{Eq. 6-2}$$

, where $y_n^{A,B}$ denotes the pair probability, x_A and x_B are the concentration of A and B atoms, respectively. Segregation between A and B components gives rise to positive $\alpha_n^{A,B}$, whereas the negative value of $\alpha_n^{A,B}$ means that there is a chemical ordering between them. When $\alpha_n^{A,B}$=0, A and B atoms are found to be randomly distributed in alloys. Fig. 6-1a and b show the atomistic configurations of medium-range and equiatomic FeCrNi alloys obtained from the present Monte-Carlo simulations of the 9

× 9× 9 FCC supercell for the two temperatures: 300 K (Fig. 6-1a) and 2000 K (Fig. 6-1b), respectively.

For the practical study of elastic constants in the FeCrNi system from first-principles methods, it is more convenient to reduce the supercell size 9 × 9 × 9 (Fig. 6-1a and b) to 3 × 3 × 3 (Fig. 6-1c and d) in order to balance between computational time and accuracy of DFT calculations. Furthermore, for the high-temperature disordered configurations, the symmetry of the supercell is very low (space group *P1*) due to the random distribution of atoms in the supercell. Here, for obtaining the individual components of the elastic constants matrix, we applied the method based on the deformation of an unstrained structure and the analysis of the changes in the total energy, E_{tot}, computed using DFT as a function of strain [415–418]. The deformation leads to a change in the total energy of the crystal according to the following expressions:

$$U = \frac{E_{tot} - E_0}{V_0} = \frac{1}{2}\sum_{i=1}^{6}\sum_{j=1}^{6} c_{ij}\varepsilon_i\varepsilon_j \qquad \text{Eq. 6-3}$$

, where E_0 is the total energy of the unstrained lattice, V_0 is the volume of the undistorted cell and the C_{ij} are the elements of the elastic constant matrix with a notation that follows standard convention. Both *i* and *j* run from 1…6 in the sequence {*xx*, *yy*, *zz*, *yz*, *xz*, *xy*}. For each considered deformation, 8 magnitudes of strain (±0.2%, ±0.4%, ±0.6%, ±0.8%) were applied. The dependencies of the total energy on the deformation were then fitted to quadratic equations and the respective elastic constants were obtained.

To study the elastic properties of Fe-Cr-Ni alloys at high-temperature configuration (T=2000 K), strains were applied for 9 different deformation modes:

$$\varepsilon_1 = \{xx, 0, 0, 0, 0, 0\}$$

$$\varepsilon_2 = \{0, yy, 0, 0, 0, 0\}$$

$$\varepsilon_3 = \{0, 0, zz, 0, 0, 0\}$$

$$\varepsilon_4 = \{xx, yy, 0, 0, 0, 0\}$$

$$\varepsilon_5 = \{xx, 0, zz, 0, 0, 0\}$$

$$\varepsilon_6 = \{0, yy, zz, 0, 0, 0\}$$

$$\varepsilon_7 = \{0, 0, 0, yz, 0, 0\}$$

$$\varepsilon_8 = \{0, 0, 0, 0, xz, 0\}$$

$$\varepsilon_9 = \{0, 0, 0, 0, 0, xy\}$$

This allowed obtaining 9 elements of the elastic constant matrix:

$$(C_{ij}) = \begin{bmatrix} C_{11} & C_{12} & C_{13} & 0 & 0 & 0 \\ C_{12} & C_{22} & C_{23} & 0 & 0 & 0 \\ C_{13} & C_{23} & C_{33} & 0 & 0 & 0 \\ 0 & 0 & 0 & C_{44} & 0 & 0 \\ 0 & 0 & 0 & 0 & C_{55} & 0 \\ 0 & 0 & 0 & 0 & 0 & C_{66} \end{bmatrix} \quad \text{Eq. 6-4}$$

Note: In this study, we assumed that the elements of the elastic constant matrix other than C_{11}, C_{12}, C_{13}, C_{22}, C_{23}, C_{33}, C_{44}, C_{55}, C_{66} are equal to zero. Based on our previous study with structures with low symmetry [418], the values of those elements are usually much smaller than C_{11}, C_{12}, C_{13}, C_{22}, C_{23}, C_{33}, C_{44}, C_{55}, C_{66} and can therefore be neglected. Therefore, the lack of those constants should not significantly influence the predictions of the overall elastic properties of alloys. For the low-temperature configuration (T=300 K), the elastic tensor matrix elements (4) have been computed by direct diagonalization following the tetragonal symmetry as it will be discussed in the Modelling section.

Afterwards, we applied the calculation method of the anisotropy of Young's modulus and Poisson's ratio proposed by Wróbel et al. [406] to investigate the anisotropy of

elastic properties. In order to obtain the theoretical values of elastic moduli for polycrystalline materials, the Reuss-Voigt-Hill method has been employed [419]. The detailed procedure can be found in Section A.2.4 of the Appendices.

6.3.4 Microstructure Characterization

The microstructure characterizations were performed on the samples sectioned from the fractured tensile bars using electrical discharge machining. The samples were metallographically polished before electron backscatter diffraction (EBSD) test on an HKL EBSD detector based on a scanning electron microscope (SEM, TESCAN MIRA 3, Czech Republic). The SEM parameters for the EBSD were set to a voltage of 20 kV, a current of 25 nA, and a step size of 1.5 μm. The EBSD data analysis was carried out with HKL Channel 5 software. To avoid ambiguous grain boundaries, misorientation angles less than 2° were ignored during the analysis. The thin foils for scanning transmission electron microscope (STEM) observation were mechanically polished to a thickness of ~80 μm before the twin-jet electropolishing using a constant current of 150 mA in a solution of 5% perchloric acid and 95% methanol cooled to -30 ℃. The bright-field TEM observation was undertaken on a Tecnai G^2 F30 microscope operated at 300 kV. The atomic-resolution high-angle annular dark-field STEM (HAADF-STEM) images were performed on an aberration-corrected Titan 60-300 microscope at a voltage of 300 kV. The collection half-angle of the HAADF detector ranging from 60 to 290 mrad was used, with the convergence half-angle of 21.4 mrad, giving a probe size of ~1.2 Å. The dilatation field of the lattice was analysed with the geometric phase analysis (GPA) method on the software Strain++ [420], during which a dislocation-free region was chosen as a reference.

Needle-shaped samples for APT were prepared by lift-out and annular milled in an FEI Scios focused ion beam (FIB)/SEM. The APT characterization was performed in a local electrode atom probe (CAMEACA LEAP 5000 XR). The specimens were analysed at 70 K in voltage mode, at a pulse repetition rate of 200 kHz, a pulse fraction of 20%, and an evaporation detection rate of 0.3% atom per pulse. The 3D reconstructions and data analysis were performed on Imago Visualization and Analysis Software (IVAS) version 3.8.

6.4 Experimental Results

In this section, we first presented the microstructure and mechanical performance of the alloy at 293 and 15 K. We then presented the analysis of the *in situ* neutron diffraction spectra including the lattice strain, single-crystal elastic constants, the evolution of stacking fault probability (SFP) and dislocation density. Post-mortem TEM characterization was presented afterwards.

6.4.1 Initial Microstructure

Fig. 6-2 shows the micro to nanoscale microstructure of the virgin FeNiCr alloy characterized by SEM-based BSE, EDS, EBSD, HRTEM, and APT. According to the EBSD inverse pole figure (IPF) map on the plane perpendicular to the loading direction (Fig. 6-2a), the alloy is composed of large equiaxed grains with annealing twins. The average grain size of ~23.4 μm was determined by performing the line-intercept method on the EBSD maps excluding the annealing twin boundaries. In Fig. 6-2b, the band contrast map was overlapped with the boundaries map of Fig. 6-2a. The low-angle grain boundaries (LAGBs) were defined as misorientations with $15° \geqslant \theta \geqslant 2°$ (shown in red

lines) while the high-angle grain boundaries (HAGBs) comprise misorientations larger than 15° (shown in black lines). The annealing twin boundaries were defined as Σ3=60° {111} (shown in blue lines). The fraction of LAGBs is very low (less than 2%) and most of the boundaries were HAGBs. In addition to grain boundaries, a large fraction of annealing twinning boundaries was observed. SEM-BSE and corresponding EDS analysis results (Fig. 6-2c) show a small amount of Cr-rich phase located at grain boundaries. Typical bright-field TEM images of the annealing twin structure are shown in Fig. 6-2d. Two straight and parallel twin boundaries can be identified with a spacing distance of ~2.18 μm. The twin relationship is confirmed by the corresponding selected area diffraction (SAED) pattern inserted in Fig. 6-2d.

The chemical homogeneity of the alloy matrix was confirmed by APT analysis at the atomic scale. Fig. 6-2e displays the three-dimensional (3D) elemental maps of the three constituent elements, Fe, Cr, and Ni, from a reconstructed volume of 50 × 50 × 140 nm^3 containing ~12 million ions. There is no apparent elemental segregation in the tested volume. The tested region was found to have a composition of Fe 34.7, Ni 31.8, and Cr 33.5 (at.%), showing an acceptable match to the bulk composition obtained from the ICP-MS. Furthermore, the homogeneity of the atomic distribution of the alloy was also evaluated with the chi-squared statistics with a frequency distribution analysis (FDA) shown in Fig. 6-2f. The curves from the binomial simulation match well with the curves obtained from the experiments, indicating a randomly distributed solid solution. The parameters used for qualifying the fit are shown in the insert table in Fig. 6-2f. The normalized homogenization parameter, μ, for all three constituent elements are very close to 0, confirming their random distribution.

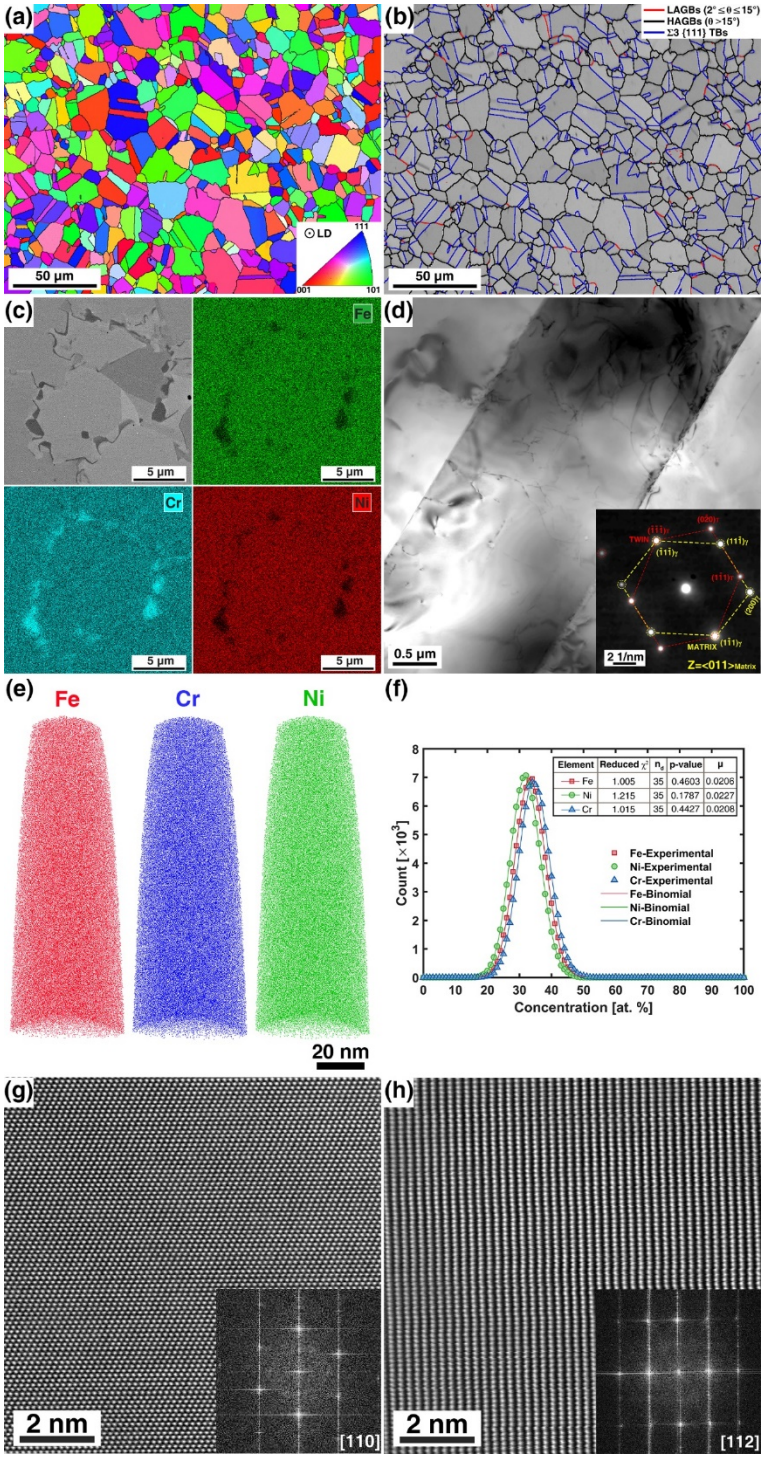

Fig. 6-2 Microstructure characterization of the virgin FeCrNi sample: (a) EBSD map (inverse pole figure) perpendicular to loading direction (LD); (b) Band contrast map overlapped with boundaries map of (a), the red, black, and green lines in the boundary map represents the low-angle grain boundaries (LAGBs), high-angle grain boundaries (HAGBs), and annealing twin boundaries (Σ3 {111}); (c) SEM-BSE images and corresponding elemental mapping of Fe, Cr, and Ni obtained from EDX analysis; (d) typical bright-field TEM image and SAED pattern taken along [110] zone axes; (e) Three-dimension APT tip reconstructions of Fe, Cr, and Ni atoms; (f) Frequency distribution analysis of the three constituent elements and corresponding parameters used for qualifying the fit; (g) and (h) HRSTEM images and the corresponding FFT images of the alloy taken from [110] and [112] zone axis, respectively.

As reported in Refs. [391,392], the existence of SROs can be confirmed by the diffuse superlattice features in the HRTEM images and the streaking intensity along the reciprocal lattice vectors in corresponding FFT images. Therefore, to determine if SROs exist in the present alloy, we took over 20 HRSTEM images along different zone axes on the undeformed sample. Two of them are shown in Fig. 6-2g and h, the inset images are the corresponding two-dimensional fast Fourier transforms (FFT) of the HRTEM images. Very vague diffusion disks were observed only in one of the HRTEM images (Fig. 6-2h), which may indicate the formation of a trace amount of SRO in the present alloy.

6.4.2 Tensile Properties

Fig. 6-3a shows the engineering and true stress-strain curves (up to the UTS points) of the FeCrNi alloy at 293 and 15 K. The alloy shows a high YS of 651±12 MPa and UTS of 1020±3 MPa, as well as a great elongation of 48±5% at 293 K. The mechanical properties of the alloy, were then compared with other high strength steels and single or multiphase MEAs/HEAs as shown in Fig. 6-3b, in which the YS was plotted with respect to uniform elongation [62,102,198,233,259,390,421–426]. The FeCrNi alloy shows an advantage in achieving high YS and a large elongation combination compared to other MCAs at 293 K.

At 15 K, the YS of the FeCrNi alloy increased to 1092±27 MPa, the UTS increased to 1451±2 MPa, while the total elongation decreased to 18±1%. Corresponding values of strength and ductility are listed in Table 6-1. We have also listed the mechanical properties of several HEA/MEA and FCC alloys at 15 K or lower in Table 6-1. The YS of FeCrNi alloy is highest among the listed alloys, although its elongation is much lower.

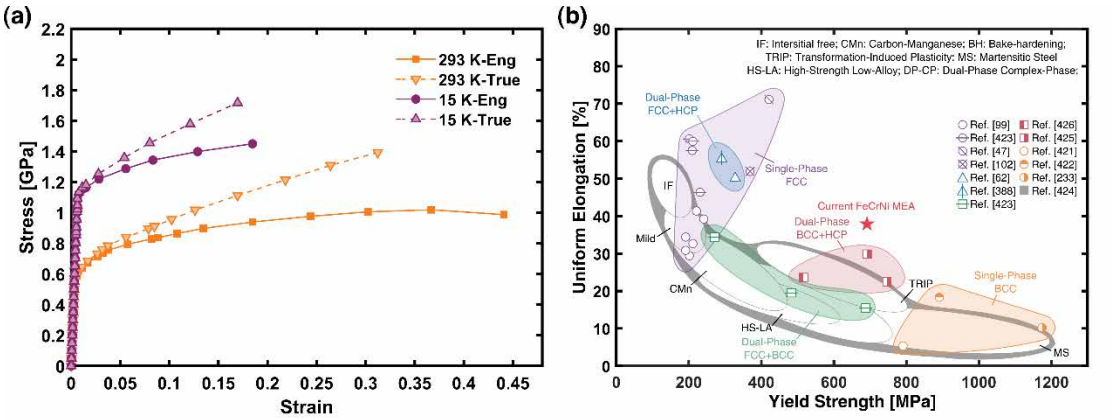

Fig. 6-3 (a) Engineering and true stress-strain curves of the alloy deformed at 293 and 15 K; (b) Yield strength-uniform elongation comparison among current FeCrNi MEA, several high-strength steels and single or multi-phase MEAs/HEAs [47,62,99,102,233,388,421–426].

Table 6-1 Uniaxial tensile properties of different alloys deformed at 293 K and cryogenic temperature.

Alloy	Temperature [K]	YS [MPa]	UTS [MPa]	Elongation [%]
FeCrNi	293	651±12	1020±3	48±5
FeCrNi	15	1092±22	1451±2	18±1
$FeCoCrNiMo_{0.2}$ [282]	15	710	1423	42
CrMnFeCoNi [348]	15	740	2500	62
CrCoNi [116]	15	670	2292	60
316LN stainless steel [427]	4.2	1045	1528	33

6.4.3 Neutron Diffraction Spectra

The *in situ* neutron diffraction patterns during tensile testing at 293 and 15 K plotted with respect to true stress were shown in Fig. 6-4a and b, respectively. Five reflections of {111}, {200}, {220}, {311}, and {222} from the single FCC phase can be observed at both 293 and 15 K before deformation. During and after the tensile testing at both temperatures, no new peaks appeared, indicating the FCC structure was stable and maintained as a single FCC phase solid solution under loading. The lattice parameter (a_0) was obtained by performing Rietveld refinement on neutron diffraction patterns. The lattice parameter decreased slightly from 3.602 to 3.594 Å as the temperature decreased from 293 to 15 K due to the shrinkage of atomic bands [327].

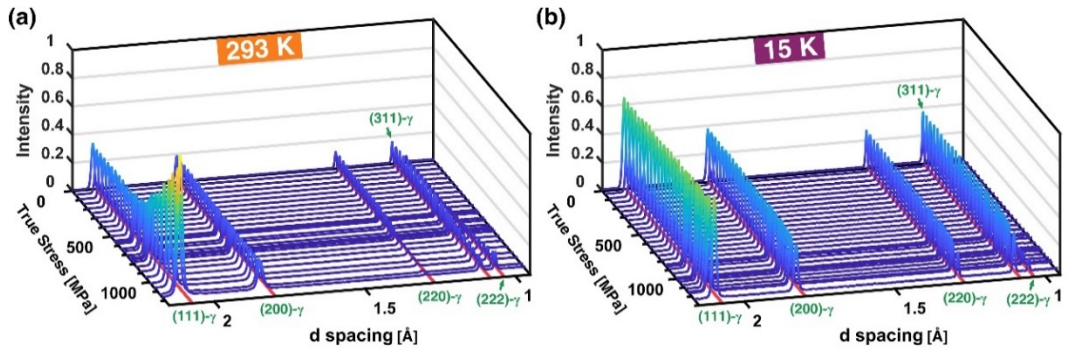

Fig. 6-4 *In situ* neutron diffraction spectra collected during deforming at (a) 293 K and (b) 15 K.

The measured lattice strain from five crystallographic planes of ({111}, {200}, {220}, {311}, and {222}) along axial and radial direction were plotted as a function of true stress in Fig. 6-5a (293 K) and b (15 K). The uncertainties in the measured internal strains were approximately 30 microstrain. The measured bulk elastic Young's modulus (E_M) at different temperatures were obtained by linear fitting the true stress and strain curves at the elastic stage. Similarly, the elastic constants of each orientation (E_{111}, E_{200}, E_{220}, and E_{311}) were then obtained by linear fitting the lattice strain and true stress before yielding (Table 6-2). After yielding, the orientation-dependent yielding behaviours were observed at both temperatures. As indicated in Fig. 6-5a and b, the {111} grain family has the highest stiffness (E_{111} of 248.1 GPa at 293 K and 260.4 GPa at 15 K). It, however, showed the earliest yielding behaviour (~550 MPa at 293 K and ~1000 MPa at 15 K). Meanwhile, among all 4 grain families, {200} showed the lowest stiffness (E_{200} of 148.6 GPa at 293 K and 162.3 GPa at 15 K) and a delayed yielding behaviour (~730 MPa at 293 K and ~1150 MPa at 15 K). The varied stiffness and yielding behaviours among different grain families can be ascribed to the elastic and plastic anisotropy of the crystals. After yielding of some stiff grain families (e.g. {111}), the external stress gradually transferred to other soft grain families (e.g. {200}).

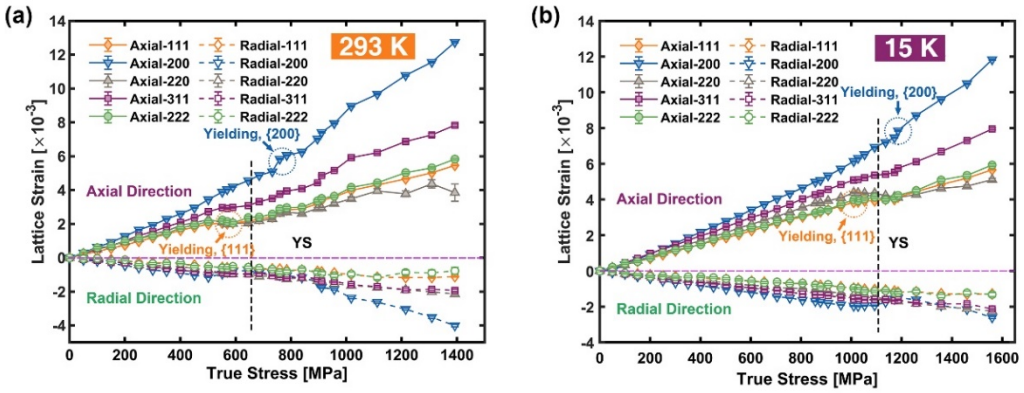

Fig. 6-5 Lattice strain evolution of crystallographic planes of {111}, {200}, {220}, {311}, and {222} from axial and radial directions during deforming at (a) 293 K and (b) 15 K.

Table 6-2 Experimentally measured elastic properties of the FeCrNi alloy at different temperatures.

Temp. [K]	E [GPa]	E_{111} [GPa]	E_{200} [GPa]	E_{220} [GPa]	E_{311} [GPa]	ν_{111}	ν_{200}	ν_{220}	ν_{311}	ν	G [GPa]
293	200.5	248.1	148.6	220.7	185.9	0.256	0.339	0.314	0.335	0.292	77.6
15	237.2	260.4	162.3	225.7	197.2	0.233	0.320	0.282	0.302	0.281	92.6

6.4.4 Single-crystal Elastic Constants Calculation

During elastic deformation, the lattice parameter obtained at axial and radial directions increased linearly with true stress. Their slopes at radial and axial directions were obtained by linear fitting and the ratio of the two slopes determines the Poisson's ratio (ν). Then the shear modulus (G) was obtained via $G = E/2(1+\nu)$. The drop of deformation temperature increased the stiffness of the alloy as the E_{hkl} at all four orientations increased to varying degrees.

To better understand the underlying elastic deformation behaviour of the alloy at different temperatures, several materials properties, including macroscopic elastic, shear, and bulk moduli (E_M, G_M, and K_M), were calculated from diffraction elastic moduli (E_{hkl}) and Poisson's ratio (ν_{hkl}) using the Voigt, Reuss, and Kroner models [347]. The detailed procedure can be found in Section A.2.1 of the Appendices. In Fig. 6-6a and b, the two reciprocal diffraction elastic constants ($1/E_{hkl}$ and ν_{hkl}/E_{hkl}) obtained from experimental elastic lattice strain and calculated with Voigt, Reuss, and

Kroner models are plotted with respect to the elastic anisotropy factor ($A_{hkl} = \frac{h^2k^2 + h^2l^2 + k^2l^2}{\left(h^2 + k^2 + l^2\right)^2}$) at 293 and 15 K, respectively. The fitting results indicate that among all three models, the Kroner model shows the best agreement with the experimental results at both 293 and 15 K. The Voigt model simply assumes that all grains were uniformly strained, but the force among grains cannot meet the equilibrium. In the Reuss model, homogeneous stress was assumed to be applied to all grains, but the distorted grains cannot fit together. Therefore, due to their simplicity, the Voigt and Reuss model are generally used to define the upper and lower bounds of the diffraction and isotropic macroscopic elastic constants. By contrast, the Kroner model provides a more accurate estimation of elastic properties after considering the orientation dependence of elastic parameters. The single-crystal elastic constants, elastic, polycrystalline moduli, and Poisson's ratio at 293 and 15 K calculated by this method are listed in Table 6-4. The values of C_{11} and C_{44} decreased slightly as the temperature decreased from 293 to 15 K, while C_{12} remains nearly constant.

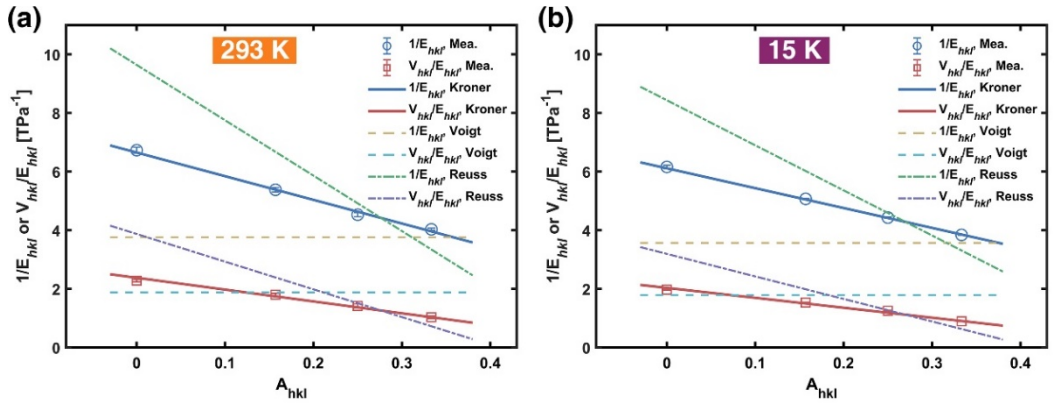

Fig. 6-6 The reciprocal diffraction elastic moduli ($1/E_{hkl}$ and v_{hkl}/E_{hkl}) plotted as a function of the elastic anisotropy factor, A_{hkl}, which were obtained from the experimental measured (Mea.) elastic lattice strain and fitted by Kroner, Voigt, and Reuss models at (a) 293 K and (b) 15 K, respectively.

The orientation-dependent elastic properties of the FeNiCr alloy at 293 K (determined from neutron diffraction and DFT simulation results) were illustrated in Fig. 6-7. To

calculate the elastic properties in any direction, the fourth-order elastic tensor was transformed in a new basis with Eq. A-36. The experimentally determined elastic properties of the alloy were illustrated with the three-dimensional (3D) surfaces (left column). The experimental results along directions at XY, XZ, and YZ planes were shown in the middle column by 2D contours. The Young's modulus is shown in Fig. 6-7a and e. The maximum and minimum values of 302 and 119 GPa were observed at $\langle 111 \rangle$ and $\langle 100 \rangle$ direction, respectively. The ratio of maximum-to-minimum elastic modulus of 2.5 indicates the high anisotropy property of the alloy. The 3D surfaces of shear modulus and Poisson's ratio were shown in Fig. 6-7b and f, respectively. The translucent outer surface represents the maximum value while the solid surface inside shows the minimum values. The maximum and minimum values were shown with dashed and solid lines in the corresponding 2D contours. The maximum value of the shear modulus (127 GPa) appeared at $\langle 100 \rangle$ direction whereas the minimum value of 55.3 GPa is in $\langle 110 \rangle$ direction, yielding the ratio of the maximum to the minimum shear modulus of 2.3 (Fig. 6-7c and g). For Poisson's ratio, the maximum value of 0.4 ($\langle 100 \rangle$ direction) while the minimum value is approaching 0 (Fig. 6-7c and g). In Fig. 6-7d and h, the linear compressibility (LC) has a value of 1.9 TPa^{-1}, showing negligible anisotropy in all directions.

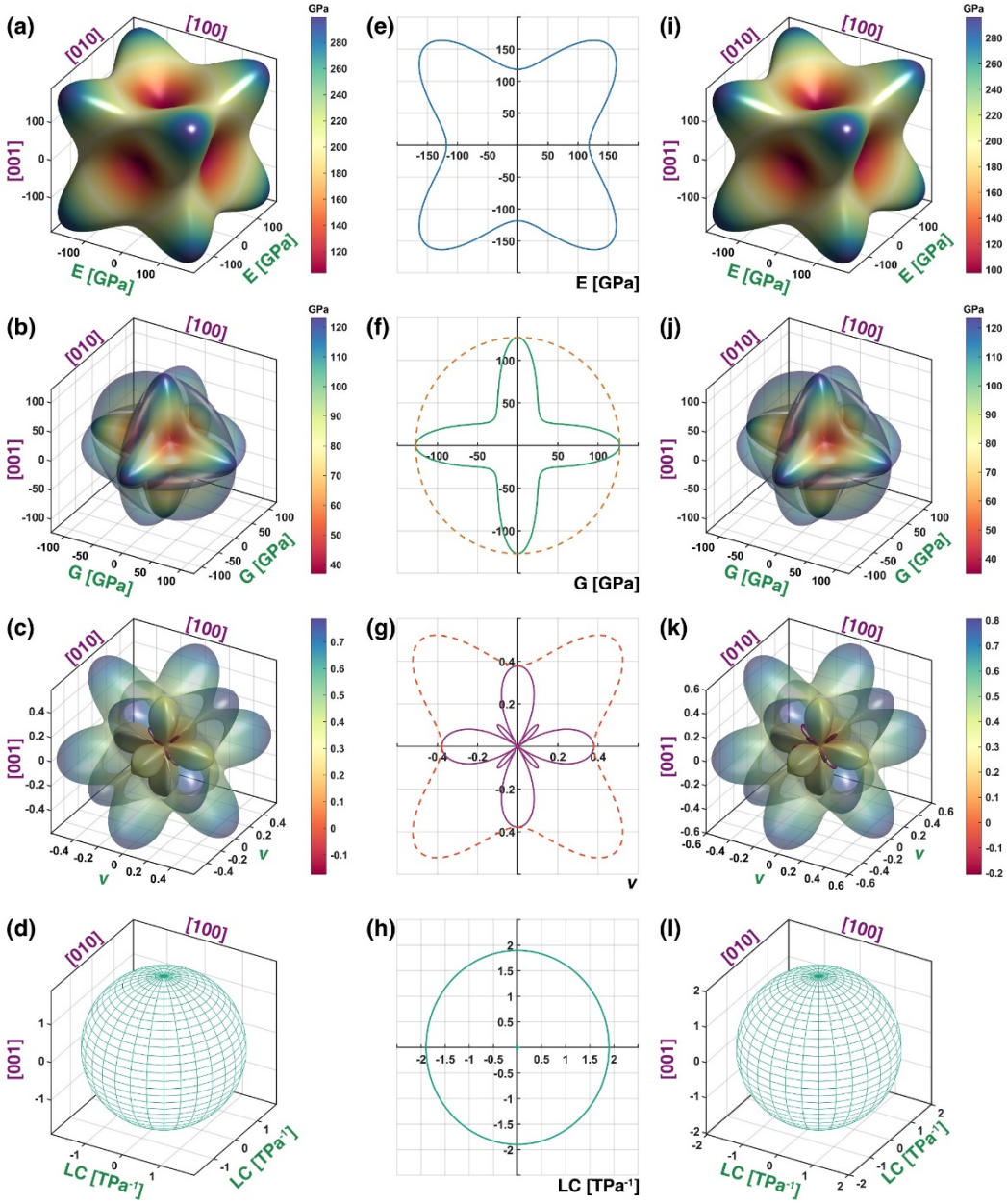

Fig. 6-7 Elastic properties of the FeNiCr alloy at 293 K determined via *in situ* neutron diffraction measurements (a-h) and DFT calculations (i-l). The magnitude with respect to the directions in three dimensions for: (a)(i) Young's modulus, (b)(j) shear modulus, (c)(k) Poisson's ratio, and (d)(l) linear compressibility, respectively. The maximum and minimum values of shear modulus and Poisson's ratio are represented by two surfaces. The magnitude with respect to directions of XY, XZ, and YZ plane for (e) Young's modulus, (f) shear modulus, (g) linear compressibility, and (h) Poisson's ratio, respectively. The maximum and minimum values of shear modulus and Poisson's ratio are represented by dashed and solid lines, respectively.

6.4.5 Stacking Fault Probability

The SFP measures the amount of stacking faults formed during deformation and allows the determination of the stacking fault energy (SFE) [200,282] of the alloy. The detailed

procedure of SFP and SFE calculations can be found in Section A.2.2 of the Appendices. The measured SFP evolution of the FeNiCr alloy at 293 K and 15 K is compared with another HEA ($FeCoCrNiMo_{0.2}$) (Fig. 6-8a) [102]. At high strain levels, the $FeCoCrNiMo_{0.2}$ showed a very high level of SFP. It can reach 2.9×10^{-2} at 77 K and even increase to 5.1×10^{-2} at 15 K. The alloy has a very low SFE of 17 mJm^{-2} and 11 mJm^{-2} at 77 and 15 K, respectively. By contrast, the SFP of FeNiCr alloy is very low (below 7×10^{-3}) at both temperatures. According to Eq. A-29, the SFE of the alloy was estimated to be 63±4 mJm^{-2} at 293 K and 47±3 mJm^{-2} at 15 K.

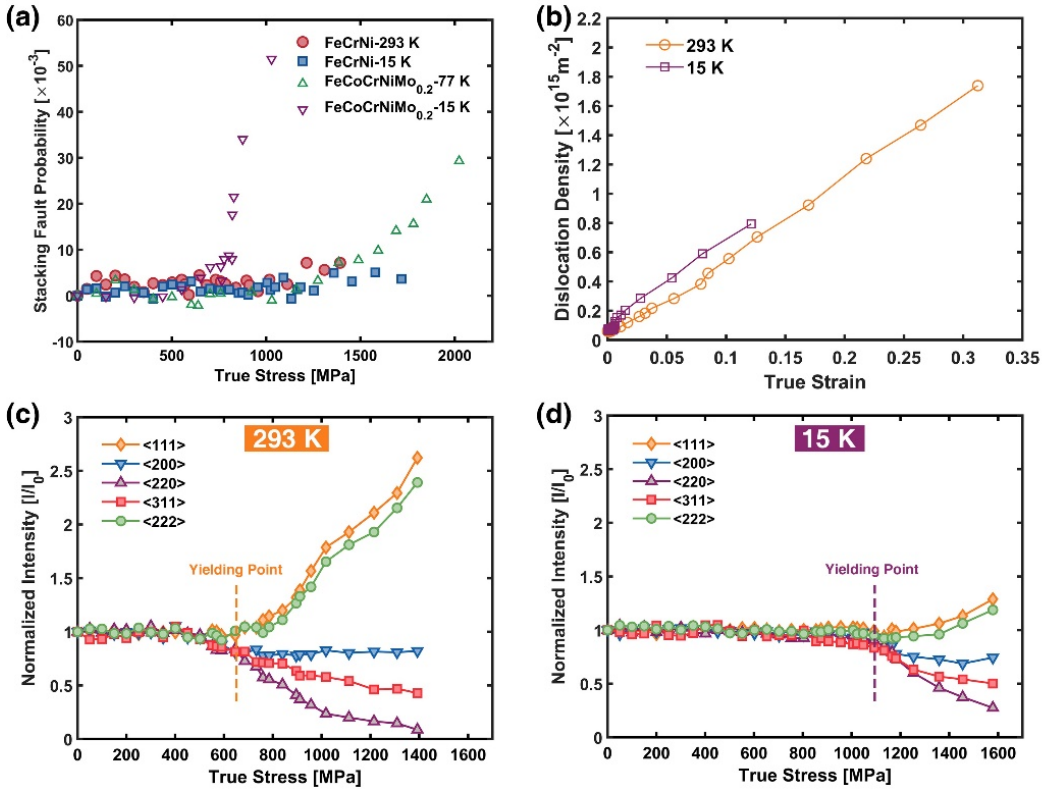

Fig. 6-8 Microstructure evolution during straining at 293 K and 15 K: (a) comparison of stacking fault probability (SFP) evolution between the FeNiCr alloy and $FeCoCrNiMo_{0.2}$ alloy at different temperatures; (b) dislocation density evolution of the FeNiCr alloy during deformation; The normalized peak intensity evolution of {111}, {200}, {220}, {311}, and {222} of the FeNiCr alloy during deforming at (c) 293 K and (d) 15 K.

Generally, the SFE of an alloy serves as one of the most crucial parameters determining the dominant deformation mechanisms. The strain hardening effects were mainly controlled by dislocation motion when the SFE exceeds 45 mJm^{-2}. As the SFE

decreased to the range of 18~45 mJm^{-2}, twinning is preferable to occur. The phase transformation, from the parent FCC to newborn phases with hexagonal close-packed (HCP) and/or body-centred tetragonal (BCT) structures, may occur if the SFE is further decreased to be lower than 18 mJm^{-2} [135,282,327]. The thermodynamic calculation results indicate that the SFE of the FeNiCr alloy is in the range of 50~60 mJm^{-2} [135]. This is also confirmed in Refs. [99,396], where the high SFE of the FeNiCr was predicted to be >50 mJm^{-2} by large-scale atomic simulations. These previous studies agree with our calculation based on the diffraction data analysis. The high SFE of the FeNiCr alloy (63±4 mJm^{-2} at 293 K and 47±3 mJm^{-2} 15 K) suggests that its deformation behaviour is mainly controlled by the dislocation motion, while the stacking fault, twins, and phase transformation are less likely to operate during deformation. This also means that the alloys are kept as non-magnetic during deformation at very low temperatures, which is favourable for applications in super-strong magnets.

The high SFE of the FeNiCr alloy can be attributed to two reasons: (1) the low configurational entropy and (2) the high concentration of Cr and Ni. Zaddach et al. [99] applied diffraction methods and first-principles calculations to investigate the SFE of a series of MCAs (FeCoNiCrMn) and the results indicated that the SFE decreases with the increase of element complexity, i.e., constituent number or configurational entropy. On the other hand, Ref. [428] indicates that the SFE of an alloy is the combined effect of each constituent element. The same element can influence the SFE differently in different alloy systems. For the FeCoNiCrMn alloy system, the SFE can be increased by increasing Ni contents due to the high intrinsic SFE of Ni (~125 mJm^{-2}) [429]. This also agrees with the study of Bonny et al.[396], which suggests that the SFE of FeNiCr alloy can be significantly increased by increasing Cr and Ni contents.

6.4.6 Dislocation Density Evolution

The dislocation density evolution of the alloy during deformation was calculated with the modified Williamson-Hall method [290]. The detailed procedure for dislocation density calculation can be seen in Section A.2.3 of the Appendices. The calculated dislocation density against true strain at both temperatures is shown in Fig. 6-8b. The evolution of dislocation density showed a very similar pattern at both temperatures. The dislocation density fluctuated slightly at around 6×10^{13} m^{-2} before yielding, after which both curves increase almost linearly upon further straining. At 293 K, the dislocation density of 1.74×10^{15} m^{-2} was achieved at true stress of 1392 MPa and a true strain of 0.31. At 15 K the dislocation density reached 7.93×10^{14} m^{-2} at true stress of 1576 MPa and a true strain of 0.12.

Meanwhile, the dislocation evolution is closely related to the texture development during tensile loading. The intensity of each reflection (<111>, <200>, <220>, <311>, and <222>) was normalized with that of the stress-free state and their evolution with true stress at 293 and 15 K are shown in Fig. 6-8c and d, respectively. At both temperatures, the peak intensity curves changed very little during the elastic stage while they started to vary after the yielding points. This originates from the difference in grain rotation in response to external loading. At 293 K, after yielding, (111)//LD and (222)//LD orientated grains gradually rotated towards the loading direction, making their peak intensity increase almost linearly with the increase of true stress during subsequent straining. By contrast, the intensity of (200) peak maintained at a similar level of ~0.8 after a slight dropping. The intensity of the other two peaks, (311) and (220), decreased to 0.43 and 0.09, respectively, as grains with these orientations gradually rotated away from LD. A similar phenomenon was also observed at 15 K (Fig.

8b) and reported in Refs. [102,200]. In the present study, the (111)//LD texture was used as a measure of the dislocation activity as the texture development is characteristic of dislocation slip during plastic deformation [348]. The highest (111) intensity reached 2.62 at 293 K, compared with a much lower value of 1.29 at 15 K. Meanwhile, at 293 K the texture developed at a faster pace (with a slope of ~2.35 × 10^{-3} MPa^{-1}) than that at 15 K (with a slope of ~0.67 × 10^{-3} MPa^{-1}). The slow texture change at 15 K also explains the lower strength enhancement after yielding and deterioration of the ductility observed at 15 K (Fig. 6-3). The inactive grain rotation and slow texture evolution limited the dislocation motions to well-orientated grains and led to the inability of catering to larger external strain [430]. Meanwhile, fewer slip systems can be activated in those "not-so-good-oriented" grains, leading to a much lower dislocation density achieved at 15 K. This result is in good agreement with the mechanical performance (Fig. 6-3a) and the dislocation density evolution (Fig. 6-8b).

6.4.7 TEM Characterization of Strained Samples

To further reveal the underlying deformation mechanisms, post-mortem TEM characterizations were performed on the fractured samples deformed at 293 and 15 K. The bright-field TEM images were taken at a two-beam condition while the SAED patterns of the corresponding area were collected along <110> zone axis and attached to the image. Fig. 6-9a shows the bright-field STEM micrograph of the alloy deformed to a low strain level of ~0.1 at 293 K. High density of parallel shear bands travelling through the whole grain interior were observed. The image on the inset of Fig. 6-9a is the SAED pattern taken from the area highlighted by the yellow circle, showing the matrix still maintained an FCC structure. The shear bands mainly consisted of closely arrayed dislocation walls whereas no SFs or twins were detected, indicating the alloy

deformed by typical planar dislocation glide on {111} planes. The shear bands were magnified in Fig. 6-9b, showing that the dislocation walls consisted of high density of parallel primary {111} slip traces. Fig. 6-9c is the bright-field TEM image taken from the sample sectioned near the fracture surface. Dense dislocation networks were produced between slip traces. Secondary {111} slip occurred and intersected with the primary slip traces, separating the matrix into small parallelogram blocks. No SFs or twins were formed according to the corresponding SAED patterns. The mean free path of mobile dislocations can be effectively reduced by the concentrated slip bands.

Similar dislocation motions were also observed at 15 K. Fig. 6-9d is the bright-field TEM image and corresponding SAED pattern showing the microstructure of the alloy deformed to a strain of ~0.1 at 15 K. Comparing with Fig. 6-9b, the secondary slip system is more easily activated at 15 K, and more dislocation tangling kinks were observed. Dislocations were preferably gathered around the crossing slip systems and formed parallelogram blocks. The interior of the nanosized dislocation substructure shows a relatively lower dislocation density than the block boundaries. The morphologies of dislocation networks deformed to a strain of ~0.1 and near the fracture surface were further revealed by STEM-HAADF images in Fig. 6-9e and f, respectively. The white lines were identified as dislocation traces according to the HRTEM image (Fig. 6-9f). In Fig. 6-9f, the density of intersecting active slip planes increased significantly as more slip systems were activated, refining the spacing between coplanar slip bands significantly. The concentrated slip bands can hinder dislocation slip on parallel slip bands by increasing the passing stresses. Furthermore, rapid dislocation multiplication occurred in both dislocation walls and the small dislocation-free zones (Fig. 6-9e), thickening the dislocation walls effectively and gradually expanding dislocations to the whole block interior (Fig. 6-9f). Fig. 6-9g displays the HAADF

image of a slip trace junction in Fig. 6-9f. Fig. 6-9h is the lattice dilatation resulting from the presence of a high strain field, obtained from the trace of the lattice distortion matrix via the GPA method [420]. This result identified the crossing slip traces, especially their junctions, mainly consisted of tangling dense dislocations accompanied by a high residual strain field. It is also worth noting that at both temperatures, very few short and isolated stacking faults were observed from our STEM observation, which is consistent with our neutron diffraction results in Fig. 6-8a.

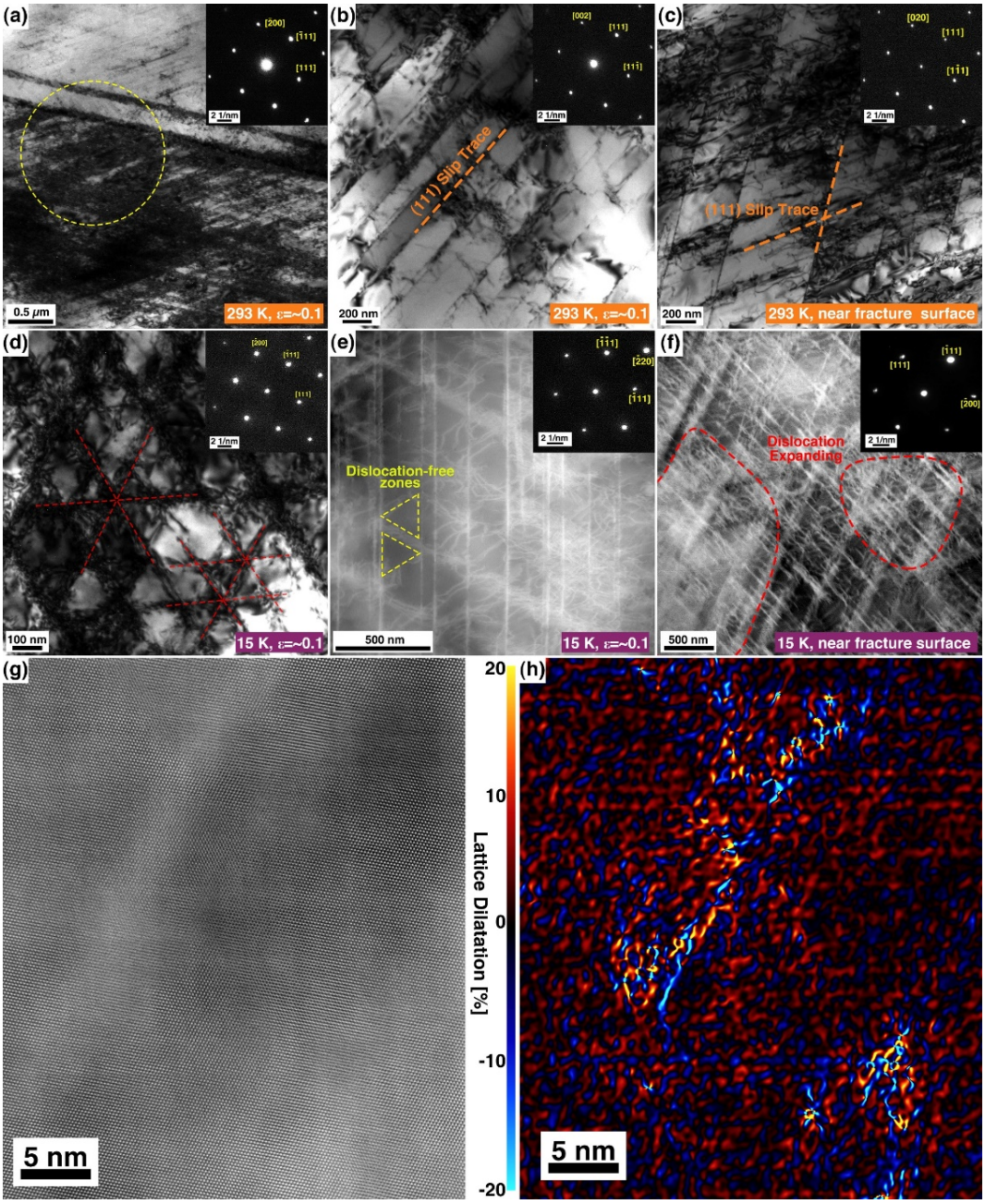

Fig. 6-9 Deformed microstructure of the alloy at different strain levels and different temperatures, 293 K and 15 K: (a) typical bright-field TEM image (at the strain of ~0.1, 293 K) and corresponding SAED pattern of the area marked by the yellow dashed circle; (b)(c) bright-field TEM images at the strain of ~0.1 and near the fracture surface at 293 K, respectively; (d) bright-field TEM image at the strain of ~0.1, 15 K; (e)(f) HAADF-STEM images of the deformed structure at the strain of ~0.1 and near the fracture surface at 15 K, respectively; (g) HRTEM image of the dislocation tangling zone in (e); (h) The geometric phase analysis (GPA) conducted on (g).

6.5 Modelling Results

In this section, we used density functional theory calculation to identify SRO and determine the single-crystal elastic constants, which were compared against experimental results. Via dislocation-based slip system modelling with key parameters taken from the neutron diffraction data, we were able to determine strengthening sources contributing to the yield strength, and the underlying factors controlling strain hardening during plastic deformation for the FeCrNi alloy.

6.5.1 Phase Formation Parameters

Several thermodynamic parameters related to phase formation including ΔS_{mix} (entropy of mixing), ΔH_{mix} (enthalpy of mixing), and T_m (melting point) were calculated (see Section A.2.5 of the Appendices). Besides, the parameter Ω, which can be applied to predict the solid-solution formation of random MCAs was calculated according to Ref. [223]:

$$\Omega = \frac{T_m \Delta S_{mix}}{|\Delta H_{mix}|} \qquad \text{Eq. 6-5}$$

When $\Omega > 1$, the MCAs are mainly composed of solid solutions while $\Omega \leqslant 1$, the formation of intermetallic compounds or segregations are favoured.

Another important parameter in predicting the solid-solution formation is the parameter δ [223], which describes the atomic size difference of the MCAs and can be expressed as follows:

$$\delta = \sqrt{\sum_{i=1}^{n} c_i \left(1 - \frac{r_i}{\bar{r}}\right)^2} \qquad \text{Eq. 6-6}$$

, where r_i is the atomic radius and $\bar{r} = \sum_{i=1}^{n} c_i r_i$ is the average atomic radius. According to Refs. [223,431], when $\Omega \geqslant 1.1$ and $\delta \leqslant 6.6\%$, stable solid-solution phases can be formed in MCAs.

Furthermore, Guo et al. [222] indicated that the valence electron concentration (VEC) serves as a criterion for determining the lattice structure of the MCAs as it correlated a structure's VEC with its FCC/BCC phase formation. It is defined by:

$$VEC = \sum_{i=1}^{n} c_i (VEC)_i \qquad \text{Eq. 6-7}$$

, where $(VEC)_i$ is the VEC for *i*th element and can be found at Ref. [222]. When VEC $\geqslant 8$, FCC structure is more stable while VEC $\leqslant 6.87$, BCC phases are more stable.

Therefore, multiple phase formation parameters can be calculated based on Eq. 6-5-Eq. 6-7and the results are shown in Table 6-3. As can be seen, the FeCrNi alloy has a very high ΔS_{mix} (9.132 J·K^{-1}mol^{-1}), T_m (1906.6 K), and relatively small ΔH_{mix} (-4.3972 KJ·mol^{-1}), yielding the high value of Ω (3.9596). Accompanied with a low δ value (only 0.002), the result indicates the alloy can favourably form stable solid-solution phases. Additionally, the VEC of the alloy is calculated to be 7.97, which is very close to the theoretical criterion of forming a single FCC structure [222]. According to the neutron diffraction spectra (Fig. 6-3) and TEM results (Fig. 6-2 and Fig. 6-9), a single FCC solid solution phase was observed, in good agreement with the theoretical prediction.

Table 6-3 Multiple phase formation parameters, δ, ΔH_{mix}, ΔS_{mix}, and Ω of the FeCrNi alloy.

Alloy	ΔS_{mix} [JK^{-1}mol^{-1}]	ΔH_{mix} [KJmol^{-1}]	T_m [K]	Ω	δ	*VEC*
FeCrNi	9.132	-4.3972	1906.6	3.9596	0.002	7.97

6.5.2 DFT Results

According to the DFT results, up to the melting point, the free energy calculations considering magnetic corrections demonstrate that the FCC phase is stable at the equiatomic composition of FeCrNi alloy, which is in excellent agreement with the available experimental data. The atomistic configurations of medium-range and equiatomic FeCrNi alloys obtained from the present Monte-Carlo (MC) simulations of the 9 × 9 × 9 FCC supercell for two temperatures: 300 and 2000 K are shown in Fig. 6-1a and b, respectively. At 2000 K, the configuration is more related to a disordered distribution of Fe, Cr, and Ni atoms over the simulation cell, whereas at 300 K, the configuration is more related to an ordering configuration. To understand this disorder-to-order transition, Fig. 6-10 shows the dependence of the first nearest-neighbour (1NN) SRO parameters of Fe-Cr, Fe-Ni, and C-Ni pairs as a function of temperature. At the high-temperature region, all the values of SRO trend to approach the zero values corresponding to random alloy configurations. For the region of temperature lower than 1000 K, it is found that the SRO parameters for Fe-Cr and Fe-Ni are negative expressing the chemical interactions between these pairs in the ternary FeCrNi alloy. Between them, the SRO parameters for Fe-Cr pairs are more negative than those of Fe-Ni demonstrating a stronger chemical ordering between Fe and Cr. The SRO parameters between Cr and Ni are positive in this temperature range demonstrating that these two atoms did not like each other within the 1NN shell of the FCC lattice.

Fig. 6-1c and d show the 3 × 3 × 3 supercell configurations used for DFT calculations of elastic constants in equiatomic FeCrNi alloys within the present work. They were generated by using combined first-principles CE Hamiltonian with exchange Monte Carlo simulations at 300 and 2000 K. Space group symmetry of these configurations

are found to be *P1* and *Pnnm*, respectively. The prediction of orthorhombic symmetry for the 300 K configuration demonstrates that the ordered structure obtained from the present theoretical study is strongly correlated with the SRO effects shown in Fig. 6-10 at low temperature for the medium-range FeCrNi alloy at equiatomic composition. It is worth noting that the point group symmetry of *Pnnm* crystal represents a subgroup of the tetragonal structure *P4/mmm* which has been previously predicted for intermetallic phase Fe_2CrNi from our DFT study in the FCC Fe-Cr-Ni system [409].

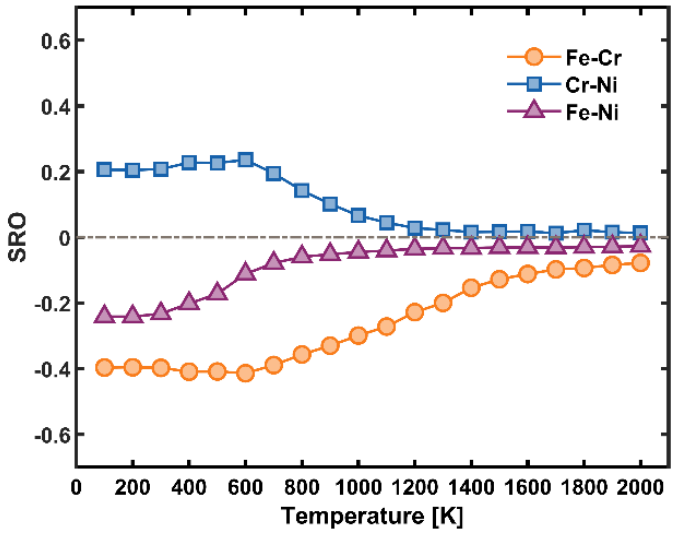

Fig. 6-10 Dependence of SRO parameters as a function of temperature between the three different pairs in equiatomic FeCrNi alloys.

The elastic constants calculated by DFT for configurations generated by MC simulations at 300 and 2000 K MC are shown in Table 6-4. Note that for the high-temperature (2000 K) configurations with *P1* symmetry, the elastic constant values were computed by the new method outlined from Eq. 6-3 and Eq. 6-4, where the 12 components from 21 independent elastic tensor components are negligible for the random alloy configuration. For the low-temperature configuration (300 K), DFT calculations provide 9 independent elastic constant values according to the orthorhombic group symmetry *Pnnm*. The optimized lattice constants from DFT

calculations for the low-temperature configurations are *a*=3.5549Å, *b*=3.5486Å, and *c*=3.6264Å which are slightly different from the ones for a cubic cell. The corresponding values for high-temperature configurations are *a*=3.5385Å, *b*=3.5459Å, and *c*=3.5722Å. A larger lattice constant value at low temperature can be explained by magneto-volume effects due to high values of predicted magnetic moments in the ordered FeCrNi alloys. According to our DFT calculations, the average ferromagnetic moments of Fe and Ni sites are 2.1 and 0.16 μ_B, respectively, whereas an average anti-ferromagnetic moment of ±2.2 μ_B was found from Cr sites within the orthorhombic structure *Pnnm*. Note that the magnetic moment value predicted for the Fe site in the Fe_2CrNi structure is also found to be close to 2.1 μ_B [409]. For the high-temperature configuration, magnetic moments at different atomic sites are found to be randomly distributed and their average values are smaller than those predicted above for the ordered structure as expected. As it can be seen from Table 6-4, the DFT calculations were performed within different options, either with the lattice and ionic relaxations (denoted as "Relaxed") or without ionic relaxations (denoted as "Unrelaxed").

From the DFT results, it is found that elastic constants at high temperatures are smaller than the ones under low-temperature configurations, demonstrating the strong effect of disorder with respect to chemical ordering for the latter one. From Table 6-4, the predicted DFT elastic properties for the disordered configuration generated by MC simulations at 2000 K are in very good agreement with the experimental values measured in this work. The elastic properties obtained by DFT are shown in Fig. 6-7i to l, which also closely resembles those measured experimentally. This strongly indicates that the prepared experimental FeCrNi alloy samples are more likely to be in a metastable state as a result of the fabrication (fast cooling after hot extrusion) without annealing treatment, which may prevent the formation of SROs and ordered

intermetallic phase predicted by DFT calculations at a low-temperature regime [391,392]. This means that the SRO effects shown in Fig. 6-10 from our modelling work are absent in the present experimental alloys. The absence of the SRO effect is checked by the neutron diffraction results (Fig. 6-4) and it is found that no other diffuse superlattice peaks can be identified experimentally. SRO formation preferably occurred after long-time annealing at high temperatures. For example, in CrCoNi alloy, SROs were observed after annealing at 1000 ℃ for 120 h [392].

Table 6-4 Elastic constants and moduli predicted by DFT calculations and compared with experimental data. (More detailed comparison can be found in Section A.2.4 of the Appendices)

	FeCrNi	DFT 2000 K	DFT 2000 K	DFT 300 K	DFT 300 K	*In situ* Exp. 293 K	*In situ* Exp. 15 K
	Symmetry	*P1*	*P1*	*Pnnm*	*Pnnm*		
	K-points	4 × 4 × 4	4 × 4 × 4	4 × 4 × 4	6 × 6 × 6		
		Relaxed	Unrelaxed	Relaxed	Relaxed		
Elastic Constant [GPa]	C_{11}	210.79	222.45	239.41	237.44	225	220
	C_{12}	141.19	134.8	117.01	116.4	151	134
	C_{13}	136.06	142.6	136.48	137.24	-	-
	C_{22}	200.47	213.16	231.37	229.99	-	-
	C_{23}	127.42	132.09	109.34	108.92	-	-
	C_{33}	206.05	218.31	257.46	259.19	-	-
	C_{44}	123.42	125.36	163.14	163.46	123	127
	C_{55}	122.36	138.84	143.22	142.18	-	-
	C_{66}	122.19	131.67	141.19	140.99	-	-
	C' (average)	35.4	40.7	60.9	60.7	37.0	43.0
Young's Modulus [GPa]	E_{av}	180.83	199.81	248.02	247.12	187.95	201.8
Poisson's Ratio	P_{av}	0.3093	0.2962	0.2429	0.2433	0.3216	0.2932
Polycrystalline Moduli [GPa]	$B_{(VRH)}$	158.33	163.53	161.09	160.77	175.65	162.67
	$G_{(VRH)}$	74.57	82.45	103.62	103.27	76.17	82.35
	$E_{(VRH)}$	192.64	211.12	255.64	254.82	199.06	210.9

6.5.3 Yield Strength Modelling

For the FeNiCr MEA, the YS can be the accumulative result of several strength contributors including frictional stress (σ_{fr}), initial dislocation density (σ_{dis}),

precipitate hardening (σ_{ppt}), grain boundary strengthening (σ_{gb}), and SRO strengthening (σ_{SRO}) [198]:

$$\sigma_{YS} = \sigma_{fr} + \sigma_{dis} + \sigma_{ppt} + \sigma_{gb} + \sigma_{SRO} \quad \text{Eq. 6-8}$$

First, the precipitation strengthening can be ignored in the present study. According to the neutron diffraction results shown in Fig. 6-4, during elastic deformation at both 293 and 15 K, the alloy keeps a single FCC phase, and no precipitates were detected except a small amount of Cr-rich phases at grain boundaries (Fig. 6-2c). The bright-field TEM images and corresponding SAED patterns (Fig. 6-2 and Fig. 6-9) did not reveal nano-precipitates. Next, we address the SRO hardening effects. On one hand, the HRTEM characterization in Fig. 6-2 indicated only a trace amount of SRO may be present. On the other hand, the strengthening effects of SRO can be very limited according to Ref. [432]. Therefore, the strengthening effects of trace SRO in the MEA can be neglected.

The strengthening contribution from forest dislocations can be evaluated by the classic Taylor hardening model [433]:

$$\sigma_{dis} = M\alpha Gb\sqrt{\rho} \quad \text{Eq. 6-9}$$

, where M is the Taylor factor and equals 3.06 for an FCC polycrystalline matrix, α is a constant of 0.35 [434] related to the interaction strength between dislocations, G is the shear modulus, b is the Burger's vector, and ρ is the dislocation density. The neutron diffraction results indicate that the dislocation density of the virgin sample is around 6×10^{13} m^{-2} at both 293 and 15 K (Fig. 6-8b). According to Eq. 6-9, the strengthening effects from initial dislocations are ~164 MPa at 293 K and ~196 MPa at 15 K.

The strengthening effect of grain boundaries (σ_{gb}) can be calculated via the Hall-Petch equation. The grain boundary strengthening effect keeps a linear relationship with the inverse square root of average grain size [67]:

$$\sigma_{gb} = \sqrt{\frac{G(T)}{G(RT)}} K_{gb} d^{-1/2} \quad \text{Eq. 6-10}$$

, where the Hall-Petch coefficient (K_{gb}) of 0.966 MPa·m$^{1/2}$ was used based on Ref. [388], $G(T)$ and $G(RT)$ are the shear modulus at a given temperature and room temperature, respectively. With the average grain size of ~23.4 μm, the grain boundaries contributed ~200 MPa (293 K) and ~218 MPa (15 K) to the yield stress.

Next, we address the lattice friction stress (σ_{fr}) of the alloy at the two temperatures. Note that the classical solid-solution strengthening mechanism is limited to the conventional ductile alloy systems where the dislocation movement can be inhibited by the strain field arising from the mismatch between discrete and solvent atoms [389]. The flexibility of dislocation lines enables them to bend to overcome the energy barriers and take on low-energy configurations. However, as the notion of "one principal element" was abandoned in MCAs, the constituent atoms with different sizes can be randomly distributed among the matrix, in which each elemental atom in the alloys can act as a solute. In this scenario, the traditional "solvent" lattice does not exist and the spacing distance between each energy barrier can be decreased significantly [250,387]. Thus, the traditional methods of depicting lattice friction stress and solution strengthening effects are no longer suitable for MCAs. According to Ref. [198], the MCAs can be treated as a stoichiometric compound with a fixed atomic ratio albeit disordered. Therefore, the traditional solid solution hardening contribution can be included in the lattice friction effect, which can be more representative of the averaged lattice resistance provided by all types of constituent elements.

Recently, Varvenne et al. [250] proposed a general mechanistic solute strengthening theory (here named as the Varvenne-Luque-Curtin theory) for arbitrary MCAs, showing great success in predicting the YS of multiple HEAs and MEAs by correlating composition, temperature, and strain rate [394]. Different from traditional solute strengthening effects, the Varvenne-Luque-Curtin theory assumes the MCA is an effective-medium matrix having all the average properties of the alloy. Each substitutional element is treated as a solute embedded in the matrix and serves as local fluctuation. The strengthening effect then originates from the rising fluctuating interaction energies between dislocations and dense local fluctuations. To reduce the total potential energy, the dislocation adopts a wavy configuration and is locally pinned in a low-energy region. The representative wavy configuration of dislocations was observed in the slightly deformed samples at 15 K (as shown in Fig. A-6 in Section A.2.6 of the Appendices), where the dislocation motion shows sluggish features, indicating high resistance originating from the pronounced lattice distortion in MCAs [392]. With the aid of stress-assisted thermal activation, the trapped dislocation can escape the adjacent energy well and reach the next low-energy region along the dislocation gliding plane. This theory calculated the zero-temperature flow stress (τ_{y0}) and fundamental zero-stress energy barrier (ΔE_b) at finite temperature (T) and finite strain-rate ($\dot{\varepsilon}$) [250]:

$$\tau_{y0} = A_\tau \alpha_\tau^{-\frac{1}{3}} G \left(\frac{1+\nu}{1-\nu} \right)^{\frac{4}{3}} \left[\frac{\sum_n c_n \Delta V_n^2}{b^6} \right]^{\frac{2}{3}} \quad \text{Eq. 6-11}$$

$$\Delta E_b = A_E \alpha_\tau^{\frac{1}{3}} G b^3 \left(\frac{1+\nu}{1-\nu} \right)^{\frac{2}{3}} \left[\frac{\sum_n c_n \Delta V_n^2}{b^6} \right]^{\frac{1}{3}} \quad \text{Eq. 6-12}$$

, where $A_\tau = 0.04865\left[1-\frac{A-1}{40}\right]$ and $A_E = 2.5785\left[1-\frac{A-1}{80}\right]$ are two constants related to the core structure of FCC dislocations consisting of two separated partial dislocations accompanied with a correction for elastic anisotropy with the Zener anisotropy factor $A=\frac{2C_{44}}{C_{11}-C_{12}}$. α_τ =0.125 is a dimensionless line tension parameter for FCC alloys [394]. ΔV_n is the misfit volume of a type-*n* element at composition (c_n) in the alloy [387]:

$$\Delta V_n = \frac{\partial V_{alloy}}{\partial c_m} - \sum_m^N c_m \frac{\partial V_{alloy}}{\partial c_m} \qquad \text{Eq. 6-13}$$

, where $V_{alloy} = V_{alloy}(c_1, c_2, c_3, ..., c_{N-1})$ is the atomic volume of the alloy and $\frac{\partial V_{alloy}}{\partial c_N} = 0$. The volume misfit can then be experimentally determined by measuring the lattice parameter evolution over a series of alloys [394]. It can also be computed precisely with the first-principles calculation, after replacing one type-*n* atom multiple times with a type-*m* atom at many different atomic environments [435]. In our case, we applied Vegard's law ($V_{alloy} = \sum_n c_n V_n$) to estimate the misfit volume [250,387]:

$$\Delta V_n = V_n - V_{alloy} \qquad \text{Eq. 6-14}$$

, where V_n is the apparent volume of the type-*n* element. Based on the experimental results on Ni, Ni-Cr, and Ni-Fe binary alloys from Ref. [250], the apparent atomic volumes of the three constituent elements Fe, Cr, and Ni were adapted to be 12.09, 12.27, and 10.94 Å^3, respectively.

At finite temperature *T* and finite strain-rate, Eq. 6-11 and Eq. 6-12 can be combined based on the standard thermal activation [436]:

$$\tau_y(T,\dot{\varepsilon}) = \tau_{y_0} \exp\left(-\frac{1}{0.51}\frac{kT}{\Delta E_b(T)}\ln\frac{\dot{\varepsilon}_0}{\dot{\varepsilon}}\right) \quad \text{Eq. 6-15}$$

where the strain rate ($\dot{\varepsilon}$) of 8×10^{-5} s^{-1} was used in the present study, $\dot{\varepsilon}_0$ is a reference strain rate and a value of 10^4 s^{-1} was adapted according to Refs. [250,394], and k is the Boltzmann constant. Therefore, the uniaxial friction stress can then be calculated by multiplying the shear stress by the Taylor factor:

$$\sigma_{fr}(T,\dot{\varepsilon}) = M\tau_y(T,\dot{\varepsilon}) \quad \text{Eq. 6-16}$$

Finally, with inputs obtained from the experiments (Table 6-4 and Table 6-5), the lattice friction stress of the FeCrNi alloy was determined to be 316 and 629 MPa at 293 and 15 K, respectively.

According to Eq. 6-8, the YS of the alloy at 293 and 15 K can be estimated to be 680 and 1043 MPa, respectively. As compared in Table 6-5, the modelled strength shows acceptable agreement with the measured results at both temperatures. The calculation of strengthening contribution from lattice distortion based on the Varvenne-Luque-Curtin theory of random MCAs plays a critical role in understanding the strengthening mechanisms and can serve as a guideline in designing and optimizing new MCAs.

Table 6-5 The modelled and measured strength of the alloy at different temperatures.

Temperature	293 K	15 K
σ_{dis} [MPa]	164	196
σ_{gb} [MPa]	200	218
σ_{fr} [MPa]	316	629
Modeled σ_{YS} [MPa]	680	1043
Measured σ_{YS} [MPa]	651±12	1092±22

6.5.4 Plastic Deformation

Generally, the large elongation of FCC alloys can be achieved via introducing extra strengthening mechanisms (such as TWIP and TRIP effects) [327]. The FeCrNi has

high SFE and no TWIP or TRIP effects were observed when deformed. The high SFE of the FeCrNi MEA means that the activation of multiple strengthening mechanisms is impeded. Hence, the dislocation activity becomes the main strain contributor during the plastic deformation [135,282,327]. Even with the only dislocation strengthening for the FeCrNi, a notably good combination of strength and ductility was obtained. This result further augments recent research [321] showing that TWIP and TRIP are not necessarily required for extra-large ductility. The large ductility (48%) at 293 K might be attributed to many slip systems activated and the high dislocation multiplication capacity of the alloy. According to the diffraction results (very low level of SFP, high SFE, and no twinning and phase transformation during deformation), together with the post-deformation TEM observations (Fig. 6-9), the dislocation motion and multiplication are the main strengthening resource and carrier of plasticity during plastic deformation.

Based on dislocation motions, the deformation procedure at 293 and 15 K was schematically compared in Fig. 6-11. At 15 K grain rotation from other orientations to (111)//LD developed much slower than that at 293 K (Fig. 6-8c and d). A similar phenomenon can also be observed in another MEA of CrCoNi during deforming at 15 K [116]. Grains orientated near (111)//LD were highly strained and dislocation entanglement forms more easily, leading to the deterioration of the ductility. Besides, the low temperature also impeded the dislocation motion, especially dislocation annihilation, contributing to the faster dislocation increment at 15 K (Fig. 6-8b) [327]. At 293 K, the rapid growing texture endowed not-so-good-orientated grains with the ability to activate more slip systems thus providing extra strain carriers. This process can sustainably support dislocation multiplication, providing a stronger dislocation strengthening effect and improved ductility.

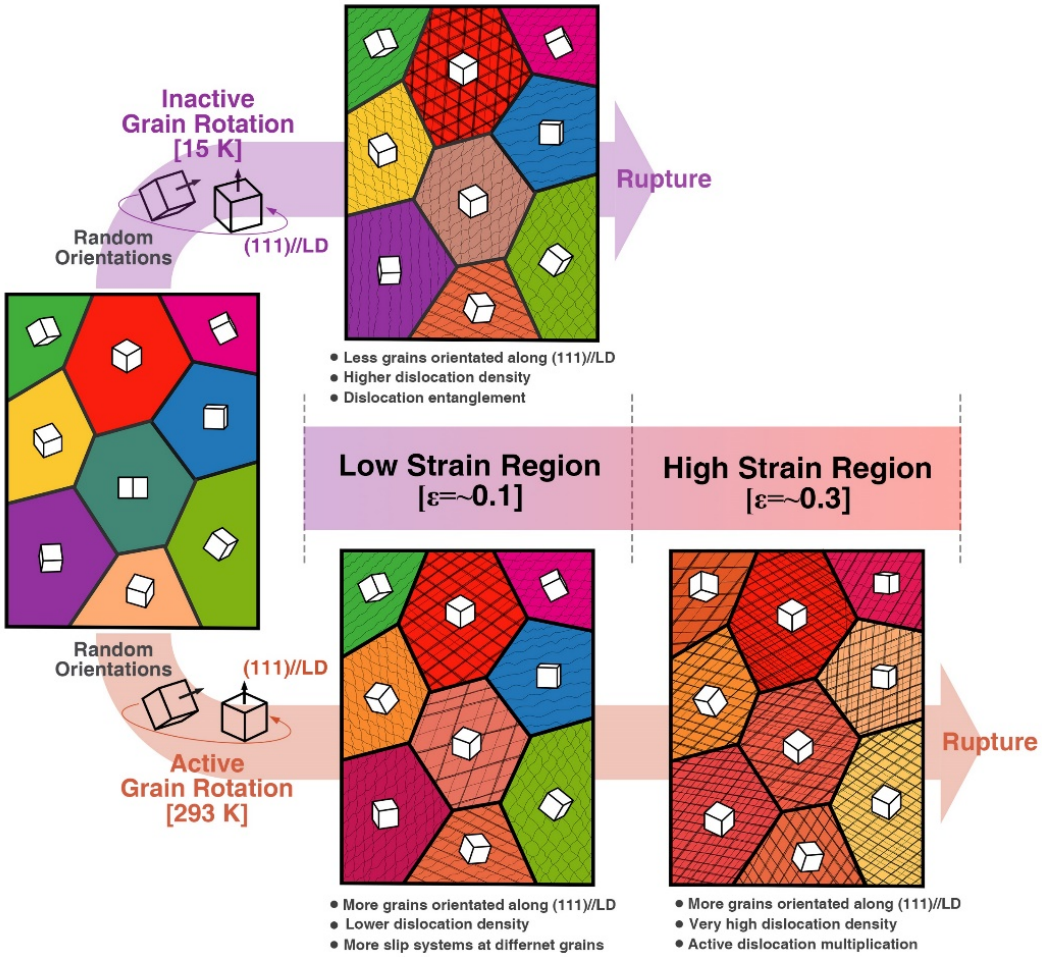

Fig. 6-11 Schematic illustrations of the deformation procedure at 293 and 15 K.

Based on the dislocation-dominated deformation mechanism, a constitutive model to depict the total flow stress (σ) of the alloy can be derived as follows:

$$\sigma = \sigma_{fr} + \sigma_{gb} + \sigma_{dis} \qquad \text{Eq. 6-17}$$

The strengthening effect from dislocation can be determined by Eq. 6-9 and the dislocation density evolution (Fig. 6-8b). After yielding, the dislocation density increased almost linearly with the true stress at both temperatures. When deforming at 293 K to a true strain of 0.31, strengthening contribution from dislocations can reach 854 MPa. At 15 K, dislocations contributed 697 MPa at a true strain of 0.12. The accumulated strengthening contributions from different resources at 293 and 15 K according to Eq. 6-17 are compared with the measured flow stress at 293 and 15 K as

shown in Fig. 6-12a and b, respectively. The model calculations agree very well with the experimental results.

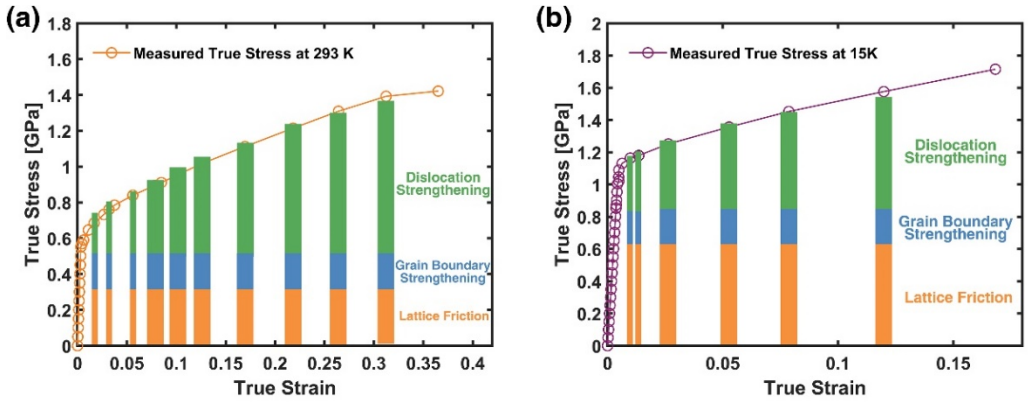

Fig. 6-12 The comparison between the calculated strength originating from different strengthening resources and the measured total flow stress at (a) 293 K and (b) 15 K.

6.6 Conclusion

In this study, we have investigated the deformation behaviours and strengthening mechanisms of an equiatomic ternary FeNiCr MEA at 293 K and 15 K. *In situ* neutron diffraction and theoretical simulations (DFT and dislocation slip system driven modelling) were synergistically employed to (i) map the microstructure evolution (e.g., lattice strain, SFP, and dislocation density); (ii) determine key mechanistic parameters (single-crystal elastic constants and SFE) and (iii) confirm the strengthening mechanisms. The investigation leads to the following conclusions:

1. The equiatomic ternary FeNiCr alloy showed excellent strength-ductility balance at 293 K with YS of 651±12 MPa, UTS of 1020±3 MPa, and total elongation of 48±5%. At 15 K, ultrahigh YS of 1092±22 MPa and UTS of 1451±2 MPa were achieved, while the elongation decreased to 18±1%.

2. MC simulation predicts the formation of short-range ordering and Fe_2CrNi intermetallic. However, no short-range orderings were observed according to the neutron diffraction spectra and APT. TEM analysis shows a very small amount of short-

range ordering. This indicates that the alloy was at a metastable state and the SRO effect was almost absent possibly due to the sample fabrication technique used.

3. Single-crystal elastic constants and bulk elastic moduli were calculated from the neutron diffraction data, which agree well with the DFT simulation for the disordered configuration generated by MC simulations at 2000 K, but less well with the ordered configuration generated by MC at 300 K. This again suggests that the alloy produced was in a metastable configuration.

4. At both 293 and 15 K, the FeNiCr MEA showed high phase stability and maintained as an FCC solid solution during deformation. Meanwhile, it showed a very low level of stacking fault probability during deformation and had high SFE (63±4 mJm^{-2} at 293 K and 47±3 mJm^{-2} at 15 K), indicating its inability of producing dense stacking faults and introducing TWIP and TRIP effects. The *in situ* neutron diffraction data and TEM analysis confirmed that no TWIP or TRIP effects occurred when the alloy was deformed at both temperatures.

5. The high solute misfit volumes of the FeNiCr can effectively introduce severe lattice distortion, which substantially improves the yield strength, especially at extremely low-temperature conditions. Based on the Varenne-Luque-Curtin theory, the strengthening contribution from the lattice distortion was calculated. At 293 K, the friction stress, resulting from the lattice distortion, can contribute 316 MPa to the YS, while it increased significantly to 629 MPa at 15 K. Strengthening contributions from dislocation and grain boundaries were also calculated. And the sum of the three contributions agreed well with the measured yield strength at both temperatures.

6. During plastic deformation, dislocation motion and multiplication serve as the dominant deformation mechanism and the main strain carrier at 293 and 15 K. The as-

fabricated samples had a low dislocation density of ~6 × 10^{13} m^{-2}. After yielding, dislocation density increased almost linearly with true stress.

Chapter 7. Cryogenic mechanical performance of a 3D-printed 316 L SS

Paper in Submission

Lei Tang[a], Fuqing Jiang[b], Bin Liu[c], Saurabh Kabra[d], Moataz M. Attallah[a], Biao Cai[a], ***Mechanical performance and deformation mechanisms of 316L stainless steel processed by laser powder bed fusion at cryogenic temperatures: in situ neutron diffraction***, to be submitted to Scripta Materialia.

Acknowledge of Collaborative Work

Lei Tang conceived and designed the experiment, performed the experiment, interpreted the data, and wrote the manuscript. Biao Cai assisted with designing the experiments, revising the manuscript, and data analysis. Fuqing Jiang, Bin Liu, and Moataz M. Attallah assisted in the preparation of the material. Saurabh Kabra assisted with performing experiments.

[a] School of Metallurgy and Materials, University of Birmingham, B15 2TT, United Kingdom
[b] Shenyang National Laboratory for Materials Science, Institute of Metal Research, Chinese Academy of Sciences, Shenyang 110016, China
[c] State Key Laboratory for Powder Metallurgy, Central South University, 410083, P.R. China
[d] ISIS Facility, Rutherford Appleton Laboratory, Didcot OX11 0QX, United Kingdom

7.1 Abstract

Manufacturing austenitic stainless steels (ASSs) using additive manufacturing (AM) is of great interest for cryogenic applications. Here, the mechanical and microstructural responses of a 316L ASS built by laser powder-bed-fusion (L-PBF) were revealed by performing *in situ* neutron diffraction tensile tests at the low-temperature range (from 373 to 10 K). The L-PBF procedure increased the stacking fault energy (SFE) level of the 316L ASS to 23.7±2.2 mJm^{-2} at room temperature. SFE almost linearly decreased from 29.2±3.1 mJm^{-2} at 373 K to 8.6±1.2 mJm^{-2} at 10 K, with a slope of 0.056 $mJm^{-2}\cdot K^{-1}$, leading to the transition of the dominant deformation mechanism from strain-induced twinning to martensite formation. As a result, excellent combinations of strength and ductility were achieved at the low-temperature range.

7.2 Introduction

With valuable combinations of excellent corrosion/oxidation resistance and strength-ductility balance, austenitic stainless steels (ASSs) serve as workhorse materials in various cryogenic applications such as liquified gas storage/transportation, superconductivity realization, and nuclear fusion devices [270,437]. Recently, ASSs have been gaining enormous research interests as a desirable material for additive manufacturing (AM), which fabricates 3-dimensional components layer-by-layer thus enabling complex geometrical design [438,439]. ASSs fabricated by laser powder-bed-fusion (L-PBF), one of the most promising AM methods, yields superior mechanical performance [95,440] originated from a variety of concurrent strengthening effects including dislocation slips, twinning, and strain-induced martensite transformation (SIMT), where the parent face-centred cubic (FCC) matrix (γ-austenite) can undergo

an athermal transition into martensite with hexagonal close-packed (ε) or body centred-tetragonal (α′) structures. It is well-accepted that these strengthening mechanisms are strongly dependent on the stacking fault energy (SFE), which is an inherent parameter measuring the energy barrier of dissociating perfect dislocations and can be influenced by chemical composition, strain rate, and temperature [68,200,327]. The decreasing of SFE can shift the dominant deformation mechanisms from dislocation motion (SFE > 45 mJm^{-2}) to twinning (45 mJm^{-2} > SFE > 18 mJm^{-2}) and to SIMT (SFE < 18 mJm^{-2}) [135,140,373].

The relationship among SFE, temperature, and the deformation mechanisms in the ASSs fabricated by AM, however, was still under debate. Pham et al. [441] reported very active twinning behaviour since the SFE of a 316L SS was reduced after L-PBF, This is attributed to the use of protective nitrogen atmosphere. Solute N atoms diffused into the faulted regions and reduced the SFE. Contrarily, Karthik [270] reported a much-delayed SIMT of a 316L ASS and the cellular dislocation structures produced by L-PBF has been attributed to the main contributor to the increased SFE. Similar phenomena were also reported in another L-PBF-built 316L ASS during cryogenic deformation [440], where SIMT was significantly postponed compared with the annealed counterparts. In addition, most of the previous investigations focused on the high or room-temperature performance of the AM-fabricated ASSs, the SFE-related mechanical responses and strengthening effects at ultralow temperatures, have rarely been investigated, which severely limited the application of L-PBF build ASSs for cryogenic environments.

Herein, *in situ* neutron diffraction and tensile tests were performed on an L-PBF-built 316L ASS at the low-temperature range (from 373 to 10 K), providing a better understanding of the relationship among SFE, temperature, and deformation

mechanisms of AM-built ASSs and thus paving a way to develop ASSs fabricated by L-PBF with superior cryogenic mechanical properties.

7.3 Materials and Methods

Near spherical-shaped 316L powder with a diameter of 32±5 μm was prepared by gas atomization. Specimens with a size of 100 × 40 × 40 mm^3 were manufactured in an L-PBF machine (FS271M, Farsoon, China) under the protection of nitrogen atmosphere and then annealed at 400 ℃ for 3 h, followed by air cooling. The printing parameters are listed in Table 7-1. The laser beam was rotated 67° after printing each layer. Dog-bone tensile samples (with gauge volume of Φ8 × 32 mm^3) were then machined along the building direction and used for the *in situ* tensile testing. The details of *in situ* neutron diffraction tensile testing and related data interpretation, such as the calculation of lattice strain, dislocation density, stacking fault probability (SFP), and SFE can be found at Refs. [102,200,282,327]. The phase volume fraction evolution was determined by Rietveld refinement performed with TOPAS (Coelho Software, Australia). The electron back scatter diffraction (EBSD) observation on the focal plane of the L-PBF was performed on a scanning electron microscope (SEM, Tescan Mira-3) with an accelerating voltage of 15 kV. The thin foils for transmission electron microscope (TEM) characterization were mechanically polished to a thickness of ~80 μm and then subjected to twin-jet electropolishing using a constant current of 150 mA in a solution of 5% perchloric acid and 95% methanol cooled to -30℃. The TEM observation was performed on a Tecnai G^2 F30 TEM operated at 300 kV.

Table 7-1 Parameters used in building 316L SS with L-PBF.

Scanning speed [$mm \cdot s^{-1}$]	Laser beam spot size [μm]	Laser power [W]	Layer thickness [μm]	Hatching space [μm]
1000	80	225	30	90

7.4 Results and Discussion

In Fig. 7-1 the heterogeneous distribution of grain shape/size and orientation gradient of the as-built 316L ASS were revealed with EBSD and bright-field TEM image. The inverse pole figure (IPF) shows multiple ripple patterns consisting of large elliptic grains, formed by the solidified molten pools, and slim grains distributing along the melt pool boundaries (Fig. 7-1a). The average grain size (d) of 19.5 μm was determined with the intercept length method. Unconventional orientation gradient across grains was observed and shown as a high-resolution kernel average misorientation map in Fig. 7-1b. The local misorientation within the large grain interior was in the range of 0.5°-1.5°, while the high local misorientation (>2°) was preferably located in slim grains or around (sub)grain boundaries. The misorientation distribution of the alloy was compared with random misorientation in Fig. 7-1c, showing a very high fraction of low angle grain boundaries (LAGBs, $2° < \theta < 15°$, 67.7% of the total grain boundaries). The bright-field TEM image in Fig. 7-1d reveals the densely arrayed dislocation cells (~200 nm in width and ~500 nm in length) within the grain interior, which can be the origin of the high fraction of LAGBs and high level of local misorientation. A high density of dislocations trapping within/along the fine dislocation cells are visible and induced dislocation entanglements (Fig. 7-1d).

Table 7-2 Mechanical properties of the 316L ASS at the low-temperature range (from 373 K to 10 K).

Temperature [K]	YS [MPa]	UTS [MPa]	Total elongation [%]
373	562	627	55
293	657	750	34
173	750	1017	55
77	849	1298	37
10	935	1364	34

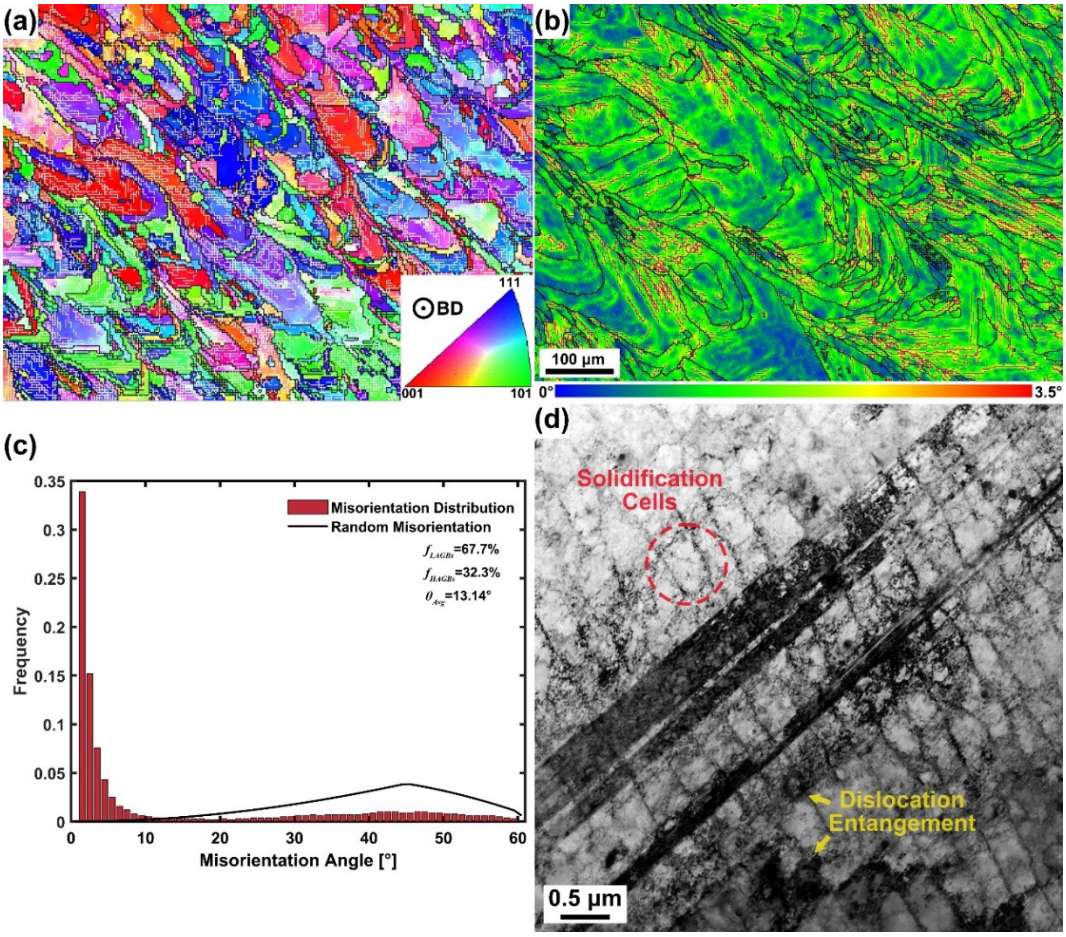

Fig. 7-1 Initial microstructure of the as-built 316L SS revealed by EBSD and TEM characterization: (a) inverse pole figure (IPF) map took at the plane perpendicular to the building direction, low angle grain boundaries (LAGBs, $2° < \theta < 10°$) and high angle grain boundaries (HAGBs, $\theta > 10°$) were shown with white and black lines, respectively; (b) high-resolution kernel average misorientation map showing the morphology of the ripple grains, (c) Misorientation distribution of the sample compared with theoretical random misorientation from Ref. [15], and (d) typical bright-field TEM image.

The temperature-dependent mechanical performance of the steel was presented in Fig. 7-2. Fig. 7-2a shows the representative true stress-strain curves, which shows typical parabolic patterns when the temperature is higher than 173 K and progressively evolves to sigmoidal/S-shaped type as temperature decreased to the ultra-low temperature range (< 173 K). The evolution of mechanical properties with temperature was summarized in Fig. 7-2b and listed in Table 7-2. With the decrease of temperature, the yield strength (YS) of the steel increased almost linearly from 562 MPa at 373 K, reaching its peak of 935 MPa at 10 K. The ultimate tensile strength (UTS) was also enhanced significantly from 627 MPa at 373 K to 1364 MPa at 10 K. The elongation was 55% at 373 K and

maintained at a high level of ~35% at cryogenic temperatures. The strain hardening rate (SHR, $d\sigma/d\varepsilon$) (Fig. 7-2c) can be roughly divided into three stages. At Stage I, SHR exhibited a steep decrease to a very low level (< 2 GPa) due to the elastic-plastic transition [442]. Afterwards, the SHR curves increased to a peak value at Stage II, indicating new sources contributing to strain hardening, followed by continuous decreasing until fracture (Stage III). The transition points from Stage I to Stage II were also marked with dash lines. The strain hardening effects mainly occurred at Stage II and can be significantly enhanced by decreasing the temperature. The peak value of SHR at Stage II was only 0.98 GPa at the strain of 0.17 at 373 K and boosted to 6.25 GPa at 0.29 strain level at 10 K.

Table 7-3 Lattice parameter and elastic properties of the 316L SS at the low-temperature range.

Temperature [K]	373	293	173	77	10
a_0 [Å]	3.582	3.578	3.572	3.568	3.565
E [GPa]	192	192	193	194	194
E_{111} [GPa]	257.2	263.2	267.1	270.8	277.6
E_{200} [GPa]	134.6	145.6	153.1	156.5	165.7
E_{220} [GPa]	221.2	218.8	236.2	239.9	243.2
E_{311} [GPa]	179.2	188	204.4	197.4	196.9
v	0.26	0.26	0.26	0.25	0.25
v_{111}	0.25	0.24	0.23	0.22	0.24
v_{200}	0.24	0.33	0.31	0.24	0.31
v_{220}	0.33	0.31	0.28	0.27	0.29
v_{311}	0.27	0.28	0.3	0.27	0.28
G [GPa]	75.7	76.9	77.3	77.6	77.7
C_{11} [GPa]	200	218	221	232	234
C_{12} [GPa]	132	136	127	144	148
C_{44} [GPa]	116	121	118	122	122

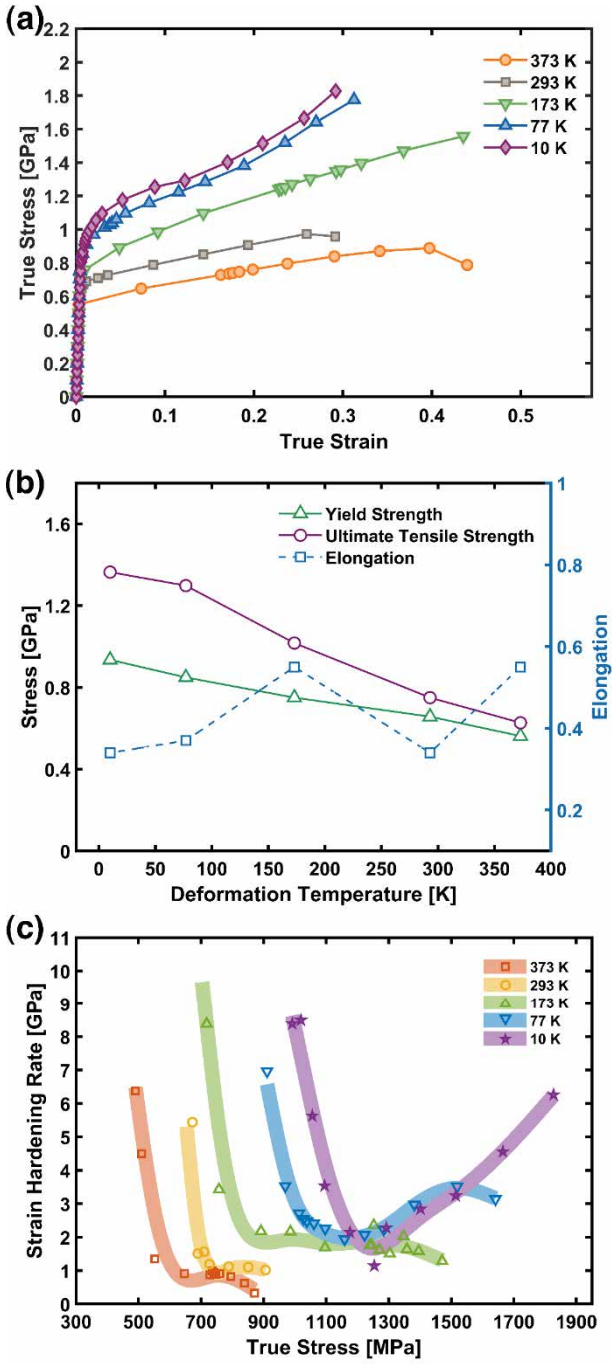

Fig. 7-2 Mechanical performance of the 316L SS at the low temperature range: (a) true stress-strain curves, (b) evolution of mechanical properties with respect to deformation temperature, and (c) strain hardening rate (SHR) plotted with true stress.

The diffraction spectra collected during deformation at different temperatures were plotted as a function of true stress in Fig. 7-3. The as-built steel exhibited an FCC structure during the temperature decreasing stage with decreasing lattice parameters (a_0, Table 7-3) as only five reflections of γ-phase can be identified. SIMT only occurred

during deforming at 173 K or lower (Fig. 7-3c-f), as three new diffraction peaks emerged and grew with strain, which can be identified as α′-(110), α′-(211), and ε-$(10\bar{1}1)$. The diffraction patterns at 10 K were magnified in Fig. 7-3f. The intensity of the α′-(111) increased progressively with straining, while the peak intensity of γ-(111) and γ-(200) decreased contrarily. Lattice strain evolution at axial and radial directions during deformation at different temperatures was shown in Fig. 7-4a-e. The lattice strain evolution at 77 and 10 K was plotted only at the low strains due to the overlap of diffraction peaks of γ and α′ phases, which can cause high ambiguity in determining lattice strain using the peak position.

The lattice strain evolution at radial and axial directions were applied to determine the macroscopic and *hkl*-specific moduli (See details at Ref. [327]) which are shown in Table 7-3. *E* is Young's modulus, *v* is the Poisson's ratio, and *G* is the shear modulus. The *hkl*-specific elastic moduli were then applied to determine the single-crystal elastic constants (C_{11}, C_{12}, and C_{44}) with the Kroner model [347] using the procedure detailed at the Section A.2.1 of the Appendices. The value of C_{11}, C_{12}, and C_{44} are consistent with literature data of 316L stainless steel [443]. They increase gradually as the temperature decreases.

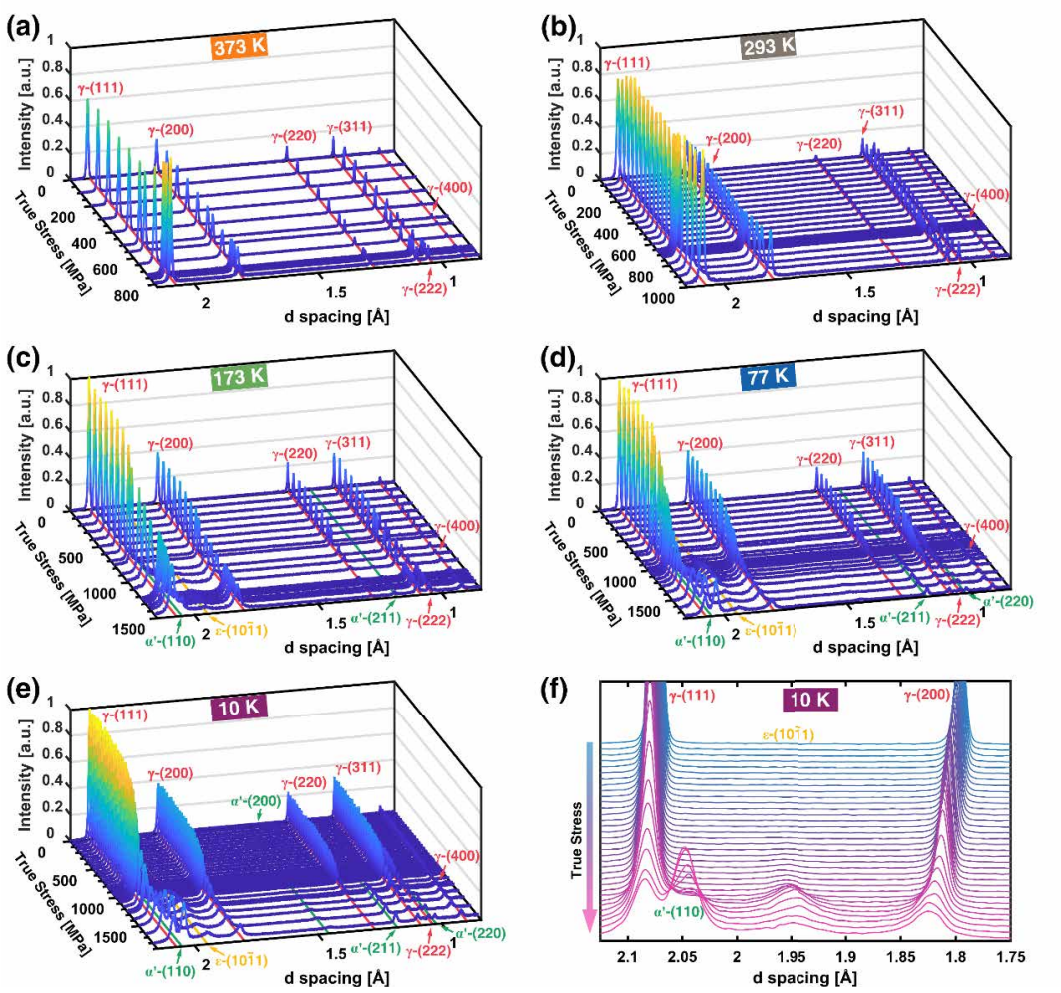

Fig. 7-3 The *in situ* neutron diffraction patterns collected during deformation at different temperatures: (a) 373 K, (b) 293 K, (c) 173 K, (d) 77 K, (e) 10 K, and (f) 10 K, with a narrow d-spacing range.

The SFP, which measures the amount of SFs, can be determined by the separation distance of lattice strain of two consecutive grain planes (See details in Refs. [282,327]). The lattice strain of {111} and {222} grain planes and SFP at different temperatures were plotted in Fig. 7-4f. SFP showed a nearly linear increase with true strain, whereas the slope of the fitted line ($\partial SFP/\partial \varepsilon$) depicts the speed of SFs formation. At 373 K SFs gathered with a very slow pace with $\partial SFP/\partial \varepsilon$ of 23.2×10^{-3}, which boosted to 336.8×10^{-3} at 10 K. The evolution of $\partial SFP/\partial \varepsilon$ and SFE (calculated according to Refs. [282,327]) were plotted as a function of temperature in Fig. 7-5a, showing that the low temperature significantly reduced the SFE thus accelerated the formation of SFs. The

SFE of the 316L SS decreased almost linearly from 29.2±3.1 mJm^{-2} at 373 K to a very low value of 8.6 mJm^{-2} at 10 K, with a slope of 0.056 $mJm^{-2}\cdot K^{-1}$. This result agrees well with the SFE-temperature relationship for typical ASSs predicted in [145]: $SFE^{T} = SFE^{RT} + 0.05(T - 293)$, where SFE^{T} and SFE^{RT} are the SFE of the alloy at a designated temperature (T) and room temperature, respectively. It is worth noting that the L-PBF-fabricated 316L ASS showed a higher SFE level (23.7±2.2 mJm^{-2} at 293 K) than the annealed 316L ASS, which was only 14.2 mJm^{-2} measured by TEM [150,151] and 10 mJm^{-2} predicted by the *ab initio* calculation [444]. The increased SFE can be ascribed to the inhomogeneous distribution of grain size/shape and misorientation gradient produced during L-PBF. The formation of faulted structures (i.e., SFs and following twins), is not favourable in refined grains [445]. Chen et al. [446] reported the SFE of a high Mn steel increased from 26.0 mJm^{-2} to 34.0 mJm^{-2} as the grain size decreased from ~47 to ~11 μm. According to the thermodynamics simulation [447], the reduced grain size (d) can increase the excess of free energy (ΔG_{ex}) required to create SFs: $\Delta G_{ex} = 170.06\exp\left(-d/18.55\right)$. SFE can be increased exponentially when d decreased to be below 35 μm [448]. The work here demonstrated that SFE of 316L ASS can be tuned by L-PBF via modulating the grain structure. A possible future work would be to investigate the effect of L-PBF processing parameters on the SFE of austenitic steels.

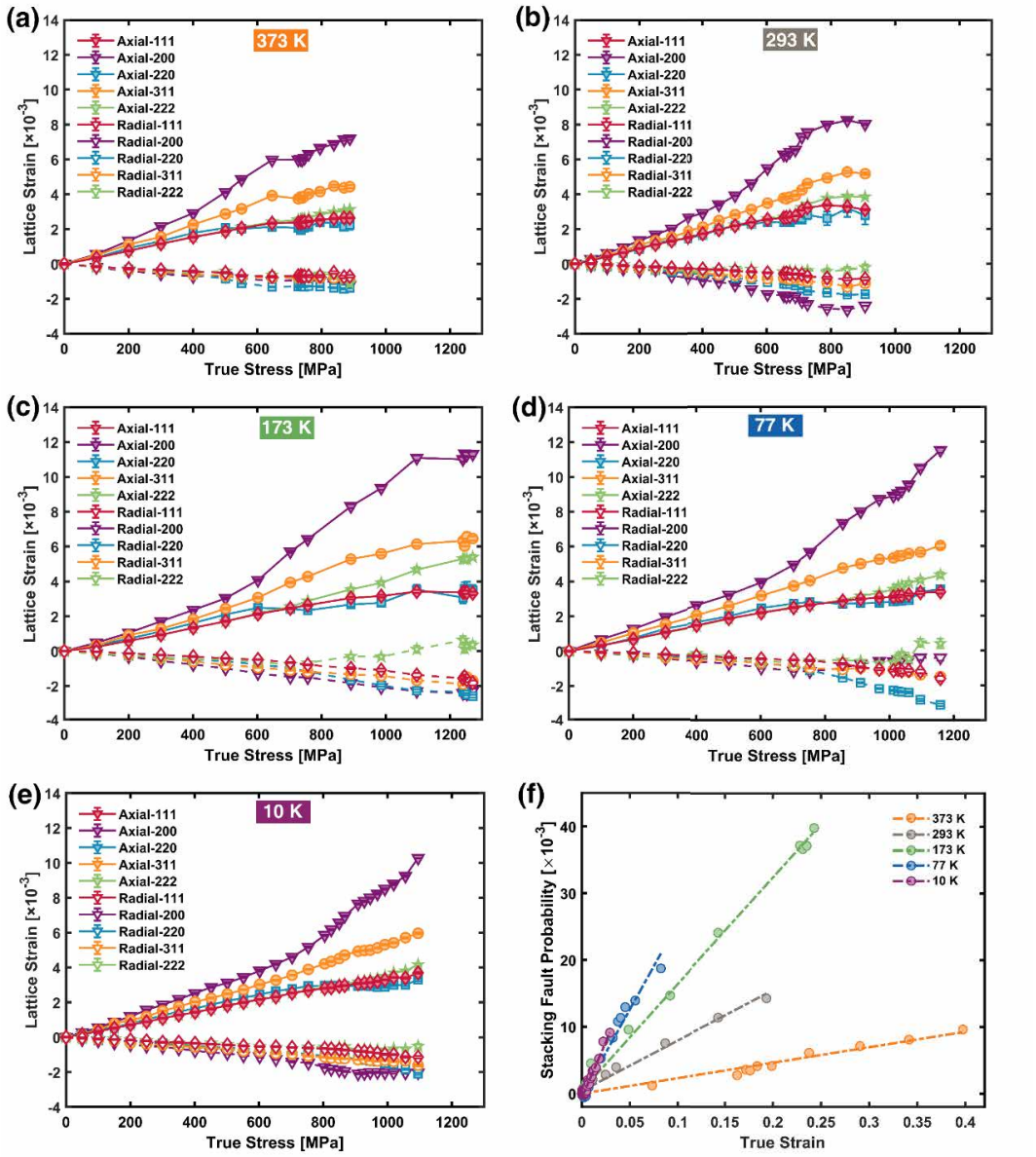

Fig. 7-4 The lattice strain evolution of crystallographic planes {111}, {200}, {220}, {311}, and {222} along the axial/radial direction and the stacking fault probability evolution at 373 K, 293 K, 173 K, 77 K, and 10 K.

Meanwhile, the measured SFE matches well with the SFE-deformation mechanism map (Fig. 7-5a). According to the diffraction results (Fig. 7-3), the strain-induced phase transformation occurred only when temperature decreased to 173 K or lower and SIMT can be significantly promoted by decreasing temperature due to the reduced SFE. The larger dissociation width between partial dislocations provided a higher probability of nucleating martensite. The strain-induced phase transformation occurred only when the

temperature decreased to be 173 K or lower, as the SFE lowered to 15.8±1.6 mJm^{-2} at 173 K. SIMT was significantly promoted (Fig. 7-3) as the temperature decreased further.

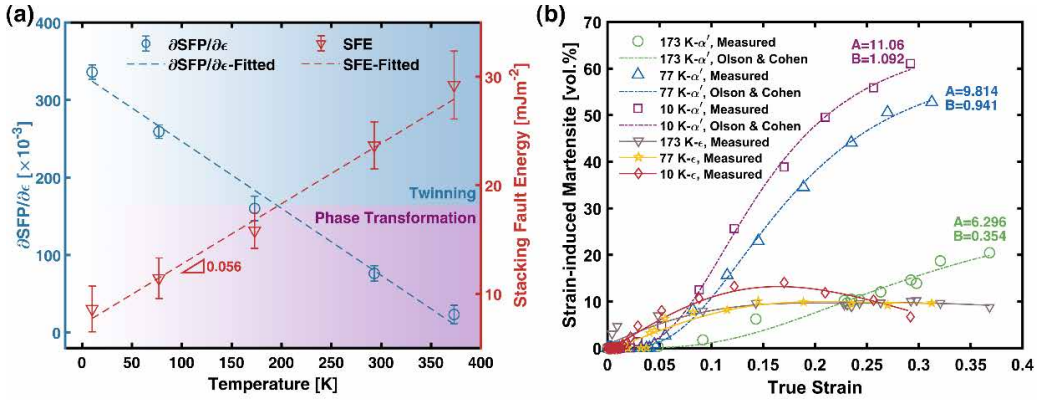

Fig. 7-5 (a) The temperature dependency of the stacking fault probability (SFP) increase rate and stacking fault energy (SFE) overlapped with SFE-deformation mechanism map; (b) The measured volume fraction of strain-induced ε- and α′-martensite and the fitted curves with Olson & Cohen model at different deformation temperatures: 173, 77, and 10 K.

The volume fraction evolution of the strain-induced ε- and α′-martensite was plotted as a function of true strain in Fig. 7-5b. The transition of ε-martensite initialized at very low strain levels (< 5%), after which its volume fraction was maintained at a level of ~10% and decreased slightly at high strains. The formation of α′-martensite, following ε-martensite, started at higher strains (>5%). The volume fraction of α′-martensite increased monotonically with strain at the three temperatures, 173, 77 and 10 K (Fig. 7-5b). Initially, they increased with an accelerated rate after nucleation, gradually saturated until reaching their maximum values (20.46% at 173 K to 52.78% at 77 K and to 61.09% at 10 K) before fracture. This indicates that two sequences of phase transformation, $\gamma \rightarrow \varepsilon \rightarrow \alpha'$ and $\gamma \rightarrow \alpha'$, were both involved during plastic straining. The ε-martensite was first produced and served as an intermediate phase for the following α′-martensite formation. As indicated in Refs. [75,207], the ε/ε interface, including intersection/non-intersection of ε laths, serves as preferable nucleation sites of α′-martensite, which can grow into the interior of the ε-domain and γ matrix at high

strain levels, consuming the ε-martensite and triggering the direct transition from γ to α′ [125].

The volume fraction of α′-martensite ($f_{\alpha'}$) was fitted based using the sigmoidal Olson-Cohen model [449]:

$$f_{\alpha'} = 1 - \exp\left\{-B\left[1 - \exp\left(-A\varepsilon_T\right)\right]^n\right\} \quad \text{Eq. 7-1}$$

, where ε_T is the true strain, A is the parameter that defines the course of the deformation bands formation and is related to SFE. Parameter B corresponds to the probability of the deformation bands intersection forming α′-martensite embryo. An n value of 4.5 was set according to Refs. [207,266,449]. The fitted lines were compared with the measured results in Fig. 7-5b, indicating that the kinetic of SIMT can be well predicted by the Olson-Cohen model.

The strengthening behaviour during plastic straining is closely related to dislocation multiplication, twinning, and most importantly, SIMT. According to Fig. 7-2c, new strengthening resources appeared at the SHR transition points (from SHR Stage I to Stage II), where the decreasing trend of SHR curves at Stage I were reversed to be an increasing trend at Stage II. At 173 K, the transition point located at a true strain of 0.05, where no α′-martensite was produced, and the volume fraction of ε-martensite reached 8%. This indicates the ε-martensite dominated the strengthening effects at low strains. The ε-martensite can exist as thin laths/plates, which creates extensive matrix/phase interfaces to continuous segregate gains and thus reduce the mean free path of dislocations [359,360]. At 77 and 10 K, the transition points were observed at strains of 0.08 and 0.09, respectively. The volume fraction of both ε-martensite and α′-martensite reached ~10%, indicating their strengthening effects originate from the synergistic hardening effects of the two martensites. Refs. [65,66] indicated that α′-

martensite can serve as an elastic reinforcing phase, which withstands higher stress and co-deforms with the soft austenite. Refs. [112,113] indicated SIMT can refine the structure continuously and create stress partitioning, thus enabling composite-like strengthening effects. Additionally, the strengthening effects of the multiphase structure can be interpreted based on dislocation activities [115], where γ and ε phases withstand the plastic strain while SIMT creates multiple impenetrable obstacles and promotes dislocation multiplication.

7.5 Conclusion

In situ neutron diffraction and tensile tests were utilized to explore the SFE-deformation mechanisms of an L-PBF-built 316L ASS at the low-temperature range. The 316L ASS showed excellent strength-ductility combinations at the low-temperature range. At 373 K, the alloy showed a high YS of 562 MPa, UTS of 627 MPa, and large elongation of 55%. The ultralow temperature of 10 K boosted YS to 935 MPa and UTS to 1364 MPa while maintaining a large elongation of 34 %. SFE of the L-PBF-built 316L ASS is higher than that of the fully annealed counterparts due to its inhomogeneous distribution of grain size/shape and misorientation gradient. The SFE showed strong temperature dependency, decreasing from 29.2±3.1 mJm^{-2} at 373 K to 8.6±1.2 mJm^{-2} at 10 K, with a slope of 0.056 $mJm^{-2}\cdot K^{-1}$. The decrease of SFE shifted the dominant deformation mechanism from dislocation and twinning (373 and 293 K) to SIMT (173, 77, and 10 K), significantly enhancing the strain hardening effects. The work shows that ASSs fabricated by L-PBF is very promising in achieving desirable strengthening mechanisms and thus premier mechanical performance for cryogenic applications.

Chapter 8. Conclusions and Future Work

8.1 Conclusions

In situ neutron diffraction and tensile tests were combined with post-mortem microscopic characterization to explore the mechanical behaviours (e.g., strength, ductility, elastic moduli, and single-crystal elastic constants) and microstructural responses (dislocation multiplication, strain-induced twinning, and phase transformation). The superior strength-ductility combinations and strengthening mechanisms of several types of face-centred cubic alloys (high Mn steel, multi-component alloy, and additively manufactured austenitic stainless steel) were revealed from 373 K to an ultralow temperature of 10 K. The investigation leads to the following conclusions:

(1) Excellent combinations of high strength and large ductility at cryogenic conditions were achieved in the three FCC alloys, high Mn steels, multi-component alloys, and additively manufactured austenitic stainless steel. The YS, UTS, and elongation of the alloys at different deformation temperatures are shown in Table 8-1.

Table 8-1 Mechanical properties of the high Mn steels, multi-component alloys, and 316L stainless steel at different temperatures.

Alloys		Temperature [K]	YS [MPa]	UTS [MPa]	Total Elongation [%]
High Mn Steels	Fe-24Mn-4Cr-0.5C	293	336	930	104
		173	539	1159	79
		77	700	1361	68
	Fe-24Mn-4Cr-0.5Cu-0.5C	293	442	918	72
		173	625	1107	54
		77	760	1312	56
	Fe-24Mn-4Cr-1Cu-0.5C	293	457	876	78
		173	643	1115	94
		77	793	1323	86
Multi-component Alloys	$FeCoCrNiMo_{0.2}$	293	376	767	52.5
		77	637	1212	71.2
		15	710	1423	41.8
	FeNiCr	293	651	1020	48
		15	1092	1451	18
Austenitic Stainless Steels	316 L	373	562	627	55
		293	657	750	34
		173	750	1017	55
		77	849	1298	37
		10	935	1364	34

(2) SFE of the three alloys at cryogenic temperatures was measured via *in situ* neutron diffraction method, allowing the validation of the SFE-deformation map in the three FCC alloys at the cryogenic conditions: the decrease of SFE can lead to the shifting of dominant deformation mechanisms from dislocation motion (SFE>45 mJm^{-2}) to TWIP (45 mJm^{-2}> SFE > 18 mJm^{-2}) and strain-induced martensite phase transformation (SFE < 18 mJm^{-2}). Adjusting SFE is a very promising method in tailoring deformation mechanisms and achieving superior strength-ductility combinations. The effect of temperature, chemical composition, and microstructure on tailoring SFE were investigated in the present study: (i) The decrease of deformation temperature can effectively promote the formation of stacking faults. The stacking fault probability increased almost linearly with the strain and its increase rate became higher at lower temperatures. As shown in Fig. 8-1, the SFE of the alloys can be decreased almost linearly with the temperature decreasing with a similar slope of ~0.05 $mJm^{-2}\cdot K^{-1}$. (ii)

Micro alloying with Cu serves as a promising method in tailoring SFE of high Mn steels, adjusting strengthening mechanisms, and thus enhancing mechanical properties of high Mn steels. It cannot only enhance the YS (~100 MPa with 1 wt.% of Cu addition) but also enhance the SFE (~5 mJm^{-2} with 1 wt.% of Cu addition). (iii) L-PBF enhanced the SFE of the 316L ASS, which might be due to the process-induced inhomogeneous grain structure and orientation gradient.

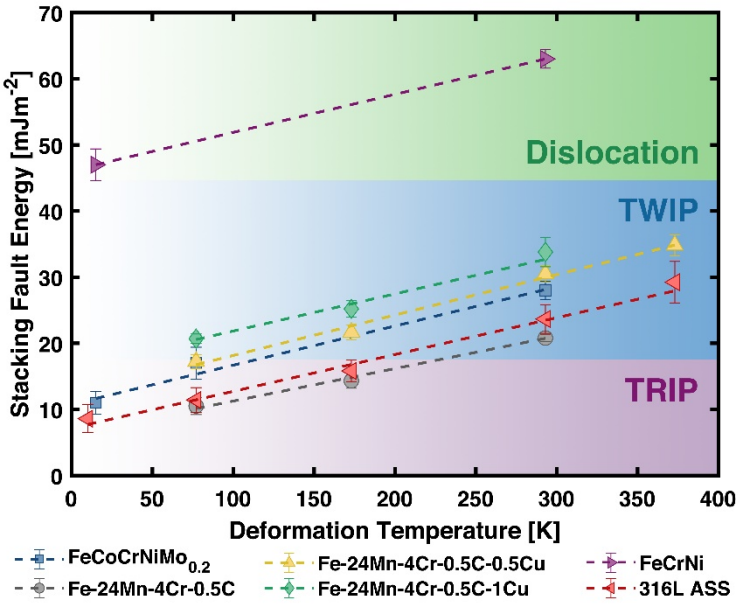

Fig. 8-1 The temperature dependence of several FCC alloys: $FeCoCrNiMo_{0.2}$, FeCrNi, Fe-24Mn-4Cr-0.5C, Fe-24Mn-4Cr-0.5C-0.5Cu, Fe-24Mn-4Cr-0.5C-1Cu, and 316L ASS, overlapped with SFE-deformation map.

(3) The decrease of deformation temperature can effectively increase the yield strength of the alloys by activating multiple strengthening effects working synergistically. At the elastic stage, a variety of hardening effects from initial dislocations, grain boundaries, precipitates, and lattice friction stress can contribute to the yield strength. The lattice friction stress can be improved by solid solution strengthening in conventional alloys and severe lattice distortion in multi-component alloys. The lattice friction stress can also be improved almost linearly with the temperature decreasing. The lattice friction stress contributed 316 MPa to the YS of the FeCrNi MEA at 293 K

and 629 MPa at 15 K; At a high Mn steel (Fe-24Mn-4Cr-1Cu-0.5C wt.%), the lattice friction stress contributed 214 MPa at 293 K and the contribution increased to 596 MPa at 77 K.

(4) During plastic deformation, a variety of concurrent strengthening mechanisms not only contributed to the high strain hardening rate but also guaranteed large elongations. (i) Dislocation serves as an important strength contributor, the dislocation density increases with strain after yielding, the decrease of deformation temperature and SFE can promote the dislocation multiplication by accelerating the formation and reducing dynamic recovery. (ii) The strain-induced twinning can effectively segregate the original large FCC matrix by introducing dense hierarchical twin structures, which serve as dislocation barriers, significantly reduce the mean free path of dislocation motion, and thus provide high strain hardening effects. (iii) During plastic deformation, the hardening effects of dislocation and twinning can work synergistically and increase almost linearly with strain. Their hardening rates in three high Mn steels with different SFE can be linearly increased by decreasing deformation temperature with a slope of ~2.0 $MPa \cdot K^{-1}$ for dislocation and ~1.1 $MPa \cdot K^{-1}$ for twinning. (iv) As the SFE approaches the SFE boundary separating TWIP and TRIP effect (18 mJm^{-2}), the phase transformation from γ to ε can be triggered. The newborn ε-martensite exists in the form of thin laths/plates and preferably distribute distantly or along twin boundaries. The ε laths serve as an additional source of introducing dense phase/matrix interfaces, refining grain structure, reducing mean free path of dislocations, and thus providing strain hardening effects. Its strengthening effects at high Mn steels can be very limited with a low volume fraction (< 5.2%) due to the thin thickness and far distributing distance. (v) During plastic deformation of ASS (316L, with SFE of 8.6±1.2 mJm^{-2} at 10 K) and HEA ($FeCoCrNiMo_{0.2}$, with SFE of 11 mJm^{-2} at 15 K), two sequences of

strain-induced phase transformation, $\gamma \rightarrow \varepsilon \rightarrow \alpha'$ and $\gamma \rightarrow \alpha'$, were involved. The ε-martensite transition initializes at low strain levels (< 5%) and serves as an intermediate phase for the following α′-martensite formation. The volume fraction of ε-martensite was maintained at a low level (< ~10%) and strengthening the alloy at low strains. The α′-martensite formation serves as the dominant strengthening resource and strain carrier at high strains. The volume fraction evolution of α′-martensite can be well described with the sigmoidal Olson-Cohen model. The decrease of deformation temperature can significantly motivate the α′-martensite transition, the highest volume fraction for the 316L ASS is only 20.5% at a true strain of 0.37 with SFE of 15.8±1.6 mJm^{-2}, which increased to 61.1% at a true strain of 0.29 with SFE of 8.6±1.2 mJm^{-2}.

(5) The merits of these three alloys at cryogenic conditions can be summarized as: (i) With very low production cost and suitable SFE, high Mn steels have shown great value in cryogenic applications since it has great potential in activating multiple strengthening effects and achieving premier strength-ductility combinations. (ii) The multi-component alloys, due to their inherent high flexibility in adjusting chemical composition, show the huge potential of reducing production cost, enhancing YS, tailoring SFE, and thus improving strain hardening behaviour. (iii) The ASSs can be more attractive for cryogenic applications, not only because of the valuable combinations of excellent corrosion/oxidation resistance, but also because it is easily printable by L-PBF and very promising to tailor microstructure, SFE, and enhance mechanical performance via adjusting parameters of L-PBF.

8.2 Future Work

The excellent mechanical properties of three types of FCC alloys were revealed by *in situ* neutron diffraction and tensile tests at cryogenic temperatures. However, there are still a lot of problems that remain unsolved.

First, other mechanical properties (such as fatigue, cyclic loading, and fracture toughness), and corresponding microstructural evolution (such as de-twinning) are very interesting and important in various working conditions. But these aspects remain rarely explored. To deal with the complex deformation conditions, it can be very helpful to combine other *in situ* methods, such as *in situ* TEM and X-ray diffraction, to capture some phenomena fast-occurring and understand the microstructural responses at the atomic level.

Second, considering the low speed of experimental validation, especially for the large number of multi-component alloys, it is hoped that the data collection efficiency of experiments can be improved, such as developing and using high-speed neutron diffraction. On the other hand, it is of great interest and importance to combine theoretical calculation methods (e.g., first principal calculation and molecular simulation) and experiments to establish a well-rounded system concerning strengthening mechanisms, temperature, chemical composition, SFE, and microstructure. With very high efficiency, it might provide valuable guidance in developing more economical alloys not only just for cryogenic conditions but also various serving conditions, such as high temperature and high strain rate.

Furthermore, the potential of FCC alloys in achieving improved mechanical performance has not been fully explored and investigated. Since the FCC matrix is relative soft than other phases, it is very promising to introduce other strengthening

mechanisms, e.g., fine grain strengthening and precipitation strengthening, to enhance the mechanical performance, especially the yield strength. The interaction among multiple strengthening effects and their influence on their mechanical performance at cryogenic conditions are very interesting and should be further explored.

Appendices

A.1 Appendices of Chapter 3 (a high Mn steel)

A.1.1 Calculation of Dislocation Density

This method was also used in dislocation density determination of high Mn steels (Chapter 4).

The instrumental broadening was determined by measuring a reference CeO_2 specimen. The instrumental broadening effects (ΔK_{inst}^2) were removed through [450,451]:

$$\Delta K_{sample}^2 = \Delta K_{meas}^2 - \Delta K_{inst}^2 \qquad \text{Eq. A-1}$$

, where ΔK_{sample}^2 and ΔK_{meas}^2 is the broadening of each peak of the steel specimens, and the measured broadening, respectively.

According to the Williamson-Hall model [452], the diffraction peak broadening can be described with the following equation:

$$\Delta K \cong \frac{a_s}{D} + Nb\sqrt{\rho}K \qquad \text{Eq. A-2}$$

, where $\frac{a_s}{D}$ and $Nb\sqrt{\rho}K$ correspond to the peak broadening caused by size effect and strain effect, respectively. ΔK is the full width at half maximum (FWHM) of each diffraction peak after removing the instrumental broadening via Eq. A-1, a_s is the shape factor for cubic-symmetric spherical crystals and equals 0.9 [453]. D is the crystalline size, N is a constant (0.263), ρ is the dislocation density, b is the magnitude of the Burger's vector and K is defined to be $1/d$ for TOF neutron diffraction spectra, wherein d is the planar spacing. After considering the effect of strain anisotropy, the

modified Williamson-Hall model developed by Ungár et al. [289] used in this study can be written as follows:

$$\Delta K - \beta' W(g) \cong \frac{a_s}{D} + bM_d \sqrt{\frac{\pi}{2}\rho}(K\overline{C}_{hkl}^{1/2}) + O\left(K^2\overline{C}\right) \qquad \text{Eq. A-3}$$

, in which M_d depicts the shape of the tail of a profile and is defined with the outer cut-off radius of dislocation [454]. $\beta' W(g)$ depicts the influence of stacking faults and twin-boundaries. $\beta' = (1.5\alpha + \beta)/a$, where α and β denote the density of stacking fault and twin boundary. $W(g)$ is a scaling factor of the faulting-induced peak broadening and varies with *hkl* indices [290]. The derivation related to dislocation correction is represented with $O\left(K^2\overline{C}\right)$ and was ignored for simplicity as suggested by [453]. $\overline{C}_{hkl}$ is the average dislocation contrast factor for each *hkl* reflection [349]:

$$\overline{C}_{hkl} = \overline{C}_{h00}\left(1 - qH^2\right) \qquad \text{Eq. A-4}$$

, where the q is a parameter that depends on the edge or screw character of the dislocation, which can be determined experimentally. H^2 is the fourth-order invariant of *hkl* indices: $\frac{h^2k^2 + h^2l^2 + k^2l^2}{\left(h^2 + k^2 + l^2\right)^2}$ [455]. $\overline{C}_{h00}$ is the average contrast factor for $\{h00\}$ peak and is determined by the screw/edge dislocation ratio and their contrast factors for $\{h00\}$ reflections. C_{h00} for pure screw and edge dislocations can be calculated with [349]:

$$C_{h00i} = a_i^{c_{h00}}\left[1 - \exp\left(\frac{-A_i}{b_i^{c_{h00}}}\right)\right] + c_i^{c_{h00}}A_i + d_i^{c_{h00}} \qquad \text{Eq. A-5}$$

, in which $A_i = \frac{2C_{44}}{C_{11} - C_{12}}$ is the elastic anisotropy parameter. The coefficients $a_i^{c_{h00}}$, $b_i^{c_{h00}}$, $c_i^{c_{h00}}$, and $d_i^{c_{h00}}$ (i means edge or screw dislocation) are determined by the elastic

constants of the alloy [349]. According to Ref. [290], the stacking faults and twinning can introduce order dependence broadening effects. As shown in Fig. A-1, we used the $\beta' W(g)$ as a fitting parameter and ρ was carefully determined to obtain the best fitting results between $\Delta K - \beta' W(g)$ and $K\overline{C}_{hkl}^{1/2}$ of five reflections of (111), (200), (220), (311), and (222). β' can reach ~0.04 at high strain stages (~0.4).

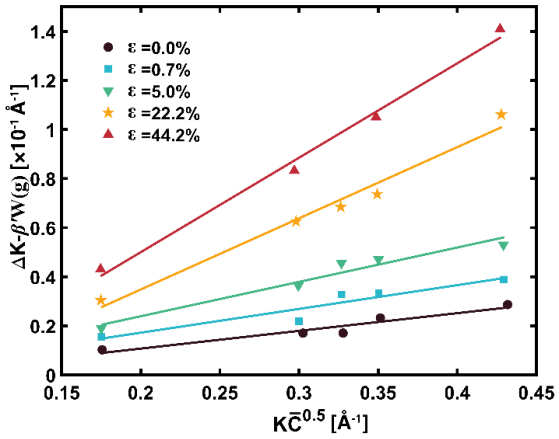

Fig. A-1 The modified Williamson-Hall plots of the Fe-24Mn-4Cr-0.5Cu-0.5C steel deformed to different strains at 77 K.

A.1.2 Mean-square Strain Calculation

This method was also used for the mean-square strain determination of high Mn steels (Chapter 4), FeCoCrNiMo$_{0.2}$ high entropy alloy (Chapter 5), FeCrNi medium entropy alloy (Chapter 6), and the 316L ASS (Chapter 7).

Warren-Averbach (W-A) [456] and integral breadth method [457] were widely used to separate the size and strain component of the intrinsic sample broadening profile. In W-A approach the broadened profile was formulated as Fourier transform coefficients (A), consisting of size (A_S) and distortion (A_D) components. A_S and A_D contribute the broadening effect separately and a simple Voigt function was developed in Ref. [294]:

$$A_D(L) \cong \exp\left(-2\pi^2 s^2 L^2 \left\langle \varepsilon^2(L) \right\rangle\right) = \exp(-2L\beta_{LD} - \pi L^2 \beta_{GD}^2) \qquad \text{Eq. A-6}$$

in which L is the distance between diffraction planes in real space, $s = 1/d$ is the diffraction vector. β_{LD} and β_{GD}^2 is the Lorentzian (L) and Gaussian (G) integral breadth strain breadth, respectively. According to Ref. [93], $\langle \varepsilon^2 \rangle_{111}$ (mean-square strain), defined as averaged strain component normal to reflecting planes, can be measured with [456]:

$$\langle \varepsilon^2 \rangle_{111} = \left(\frac{\beta_{LD,hkl}}{\pi^2 L} + \frac{\beta_{GD,hkl}^2}{2\pi} \right) \frac{1}{s_{hkl}^2} \qquad \text{Eq. A-7}$$

The measured diffraction profile (β_{Lh} and β_{Gh}) is the mathematical convolution of the instrumental effects (β_{Lg} and β_{Gg}) and intrinsic specimen effects (β_L and β_G). In the present study, the double-Voigt method was applied to perform the deconvolution and subtraction of instrumental broadening. We developed a Matlab code using modified Thomson–Cox–Hasting (TCH) pseudo-Voigt function [458] for peak fitting and the Gaussian (δ^2) and Lorentzian (H) width of the peak profile were obtained. After measuring a standard reference sample under the same condition of the sample, the peak position (d, Å) was calibrated with TOF by $TOF = C_0 + C_1 d + C_2 d^2$, in which C is the instrumental parameter. Then the instrumental broadening effect was fitting with:

$$H_{ins} = \gamma_0 + \gamma_1 d + \gamma_2 d^2 \qquad \text{Eq. A-8}$$

$$\delta_{ins}^2 = \delta_0 + \delta_1^2 d^2 + \delta_2^2 d^4 \qquad \text{Eq. A-9}$$

, in which the γ and δ are the instrumental width parameters. Then the instrumental broadening effect was subtracted according to Ref. [450,457]:

$$Lorentzian: \beta_L = \beta_{Lh} - \beta_{Lg} \qquad \text{Eq. A-10}$$

$$Gaussian: \beta_G^2 = \beta_{Gh}^2 - \beta_{Gg}^2 \qquad \text{Eq. A-11}$$

The intrinsic broadening effects ($\beta_L = H\pi/2$ and $\beta_G^2 = 2\pi\sigma^2$) from the sample can be obtained and used as input parameters in following double-Voigt size-strain analysis [380], in which the size and distortion broadening effects of Lorentzian (β_{LS} and β_{LD}) and Gaussian (β_{GS}^2 and β_{GD}^2) components can be obtained by plotting β_L and β_G^2 via [380]:

$$\beta_L = \beta_{LS} + \beta_{LD}\frac{s^2}{s_0^2} \qquad \text{Eq. A-12}$$

$$\beta_G^2 = \beta_{GS}^2 + \beta_{GD}^2\frac{s^2}{s_0^2} \qquad \text{Eq. A-13}$$

, where $s_0 = 1/d_0$ is the position of peak maximum. The real-space integral breadths were then converted into reciprocal space by $\beta_L^* = \frac{\beta_L}{C_1 d^2}$ and $\beta_G^{*2} = \frac{\beta_G^2}{C_1^2 d^4}$ considering $C_1 \gg C_0, C_2$. According to Ref. [294], the size broadening components are constant for the pattern while the strain broadening components dependent differently on the diffraction vector. Then the unknown β_{LD}, β_{GD}^2 (slopes) and β_{LS}, β_{GS}^2 (intercepts) can be obtained by plotting both β_L and β_G^2 as functions of *s* for different orders of reflections. Here we used the peak of (111) and (222), thus Eq. A-12 and Eq. A-13 became:

$$\frac{\beta_{LD}^*}{s_0^2} = \left[(\beta_L^*)_{222} - (\beta_L^*)_{111}\right] \Big/ (1/d_{222}^2 - 1/d_{111}^2) \qquad \text{Eq. A-14}$$

$$\frac{\beta_{GD}^*}{s_0^2} = \left[(\beta_G^{*2})_{222} - (\beta_G^{*2})_{111}\right] \Big/ (1/d_{222}^2 - 1/d_{111}^2) \qquad \text{Eq. A-15}$$

The mean-squared strain in SFE calculation, defined as the inhomogeneous strain quantity resulting from the faulting components averaged over a Fourier length *L*=50 Å along [111] direction, can be calculated with:

$$\langle \varepsilon_{50}^2 \rangle_{111} = (\beta_{LD}^* / s_0)/50\pi^2 + (\beta_{GD}^{*2} / s_0^2)/2\pi \qquad \text{Eq. A-16}$$

The mean-square strain evolution during deforming at different temperatures is illustrated in Fig. A-2.

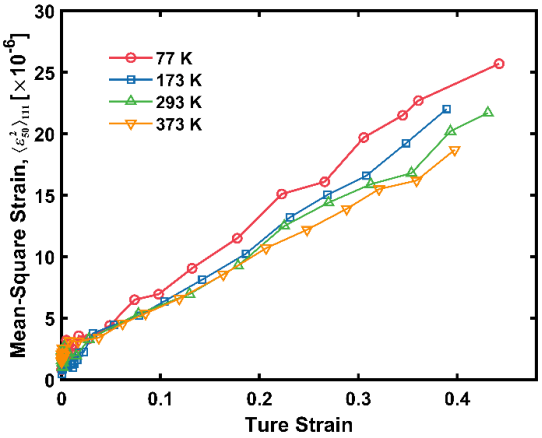

Fig. A-2 Mean-square strain of the Fe-24Mn-4Cr-0.5Cu-0.5C steel during deforming at 373, 293, 173, and 77 K.

A.1.3 The Influence of Temperature on Elastic-constants-related Parameters

Single-crystal elastic constants play an important role in dislocation density and SFE calculation, since C_{11}/C_{44}, $A_i = \dfrac{2C_{44}}{C_{11}-C_{12}}$ can influence the contrast factor in dislocation density calculation [289] while $\left(\dfrac{2C_{44}}{C_{11}-C_{12}}\right)^{-0.37}\left(\dfrac{C_{44}+C_{11}-C_{12}}{3}\right)$ serves as a coefficient in SFE calculation [171]. According to Ref. [296–298], at the low-temperature range (< 400 K), elastic constants can monotonously increase with temperature decreasing. We investigated the influence of temperature on the three parameters, C_{11}/C_{44}, A_i, and $\left(\dfrac{2C_{44}}{C_{11}-C_{12}}\right)^{-0.37}\left(\dfrac{C_{44}+C_{11}-C_{12}}{3}\right)$ based on single-crystal

elastic constants of Fe [296], CrCoNi medium entropy alloy [298] and Cr-Mn-Fe-Co-Ni high-entropy alloy [299].

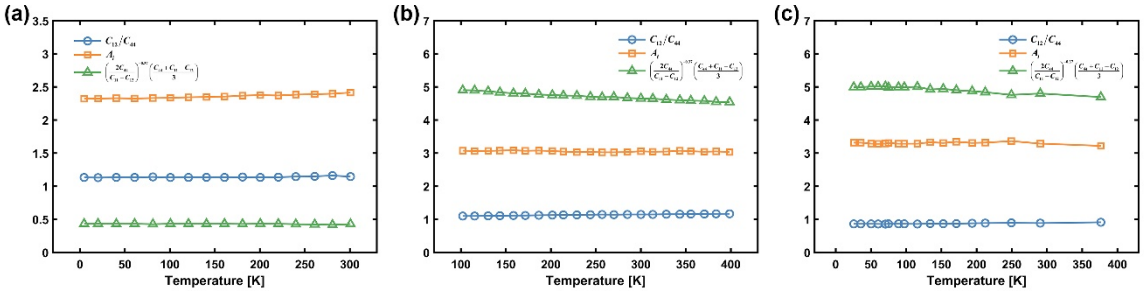

Fig. A-3 Temperature dependence of C_{11}/C_{44}, A_i, and $\left(\frac{2C_{44}}{C_{11}-C_{12}}\right)^{-0.37}\left(\frac{C_{44}+C_{11}-C_{12}}{3}\right)$ of (a) Fe [296], (b) CrCoNi medium entropy alloy [298], and Cr-Mn-Fe-Co-Ni high-entropy alloy [299].

Even though the three elastic constants can be increased during temperature dropping, the three parameters, C_{11}/C_{44}, A_i, and $\left(\frac{2C_{44}}{C_{11}-C_{12}}\right)^{-0.37}\left(\frac{C_{44}+C_{11}-C_{12}}{3}\right)$ is not sensitive to temperature change (Fig. A-3). Considering the narrow temperature range (from 77 K to 373 K) in our case, we used the elastic constants at room temperature in dislocation density and SFE calculation.

A.1.4 TEM Observation

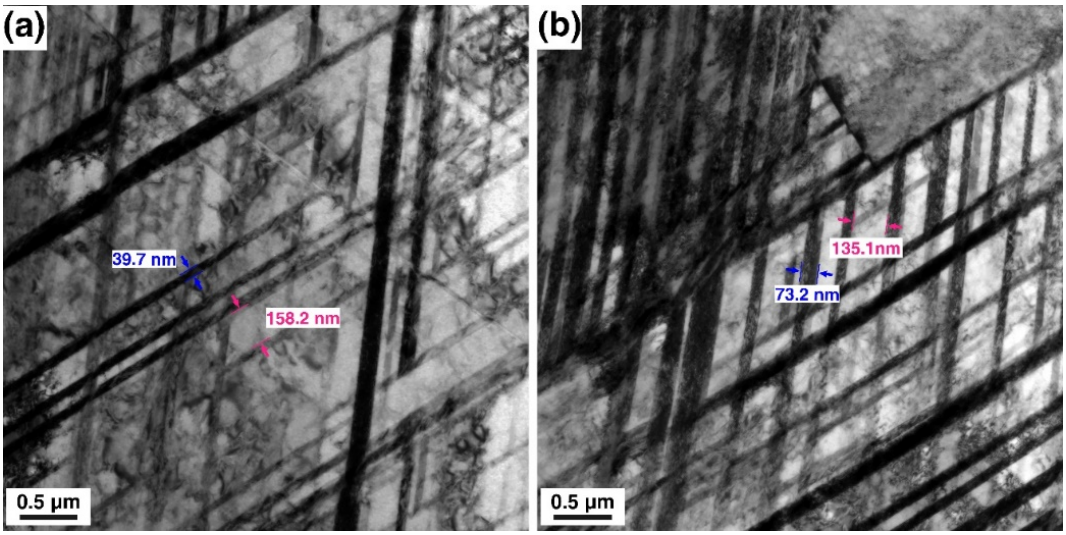

Fig. A-4 Typical bright-field TEM images of the Fe-24Mn-4Cr-0.5Cu-0.5C alloy deformed to a true strain of (a) ~0.2 and (b) ~0.3 at 77 K.

A.2 Appendices for Chapter 6 (FeCrNi MEA)

A.2.1 Single-crystal Elastic Constants Calculation

This method was also used in the single-crystal calculation for the high Mn steels (Chapter 4) and the 316L ASS (Chapter 7).

The diffraction shear moduli based on the Voigt [459], Reuss [460], and Kroner [461] model can be defined with three independent elastic constants, C_{11}, C_{12}, and C_{44}:

$$G_V = \frac{1}{5}(2\mu + 3\eta) \qquad \text{Eq. A-17}$$

$$G_R = \frac{\mu\eta}{(\eta + 3(\mu - \eta)A_{hkl})} \qquad \text{Eq. A-18}$$

, in which $A_{hkl} = \frac{h^2k^2 + h^2l^2 + k^2l^2}{\left(h^2 + k^2 + l^2\right)^2}$ is the elastic anisotropy factor, $\mu = (C_{11} - C_{12})/2$ and $\eta = C_{44}$ are the shear moduli, while the diffraction shear moduli in the Kroner model can be written with:

$$G_K^3 - \alpha G_K^2 - \beta G_K - \gamma = 0 \qquad \text{Eq. A-19}$$

, in which G_K is the shear modulus in Kroner model and the coefficients, α, β, and γ are given by:

$$\alpha = \frac{1}{5}(2\mu + 3\eta) - \frac{3}{8}\left\{3K + 4\left[\eta + 3\left(\mu - \eta\right)A_{hkl}\right]\right\} \qquad \text{Eq. A-20}$$

$$\beta = \frac{3}{40}(6K\mu + 9K\eta + 20\mu\eta) - \frac{3}{4}K\left[\eta + 3\left(\mu - \eta\right)A_{hkl}\right] \qquad \text{Eq. A-21}$$

$$\gamma = \frac{3}{4}K\mu\eta \qquad \text{Eq. A-22}$$

, where $K = (C_{11} + 2C_{12})/3$ is the bulk modulus. Then the reciprocal diffraction elastic moduli ($1/E_{hkl}$ and v_{hkl}/E_{hkl}) can be calculated with:

$$\frac{1}{6G_{hkl}} - \frac{1}{9K} = \frac{v_{hkl}}{E_{hkl}} \qquad \text{Eq. A-23}$$

$$\frac{1}{G_{hkl}} = 2\left(\frac{1}{E_{hkl}} + \frac{v_{hkl}}{E_{hkl}}\right) \qquad \text{Eq. A-24}$$

Then least squares estimation was applied to obtain the optimized combination of the three single-crystal elastic constants to minimize the value of a cost function:

$$\chi^2 = \sum_{i=1}^{n}\left(\left(1/E_{hkl}\right)_{mea,i} - \left(1/E_{hkl}\right)_{mod,i}\right)^2 \Big/ e_{1,i}^2 + \left(\left(v_{hkl}/E_{hkl}\right)_{mea,i} - \left(v_{hkl}/E_{hkl}\right)_{mod,} \right. \qquad \text{Eq. A-25}$$

, where n is the number of the reflections, the subscript of "*mea*" and "*mod*" represents the values obtained from the experimental measurement and theoretical calculation with Kroner models, respectively. The e_1 and e_2 are the corresponding experimental errors.

The diffraction shear moduli (G_K) in Eq. A-19 can become the isotropic macroscopic shear modulus (G_M) when A_{hkl} equals 0.2. The isotropic macroscopic Young's modulus (E_M) can be obtained via:

$$E_M = \frac{9G_M K}{G_M + 3K} \qquad \text{Eq. A-26}$$

The best-fitted single-crystal elastic constants, macroscopic moduli (E_M, G_M, and K_M), and corresponding Poisson's ratio (v_c) at 293 and 15 K are listed in Table. A-1.

Table. A-1 The macroscopic moduli of the FeCrNi MEA fitted with neutron diffraction.

Temperature [K]	E_M [GPa]	G_M [GPa]	K_M [GPa]
293	202.3	77.6	175.7
15	213.3	83.7	162.7

A.2.2 SFP and SFE Calculation

This method was also used in SFE and SFP determination of high Mn steels (Chapter 4), 316L ASS (Chapter 7).

According to Ref. [462], the shifting of Bragg's diffraction peaks can be influenced by both orientation-dependent macro-strain and stacking faults. Therefore, the experimentally measured lattice strain (ε_{hkl}^{exp}) can be concurrent effects of the macro-strain ($\varepsilon_{hkl}^{strain}$) and stacking-fault-induced strain (ε_{hkl}^{sf}). To determine the influence from stacking faults, a deconvolution procedure was proposed in Ref. [379]:

$$\varepsilon_{hkl}^{exp} = \varepsilon_{hkl}^{strain} + \varepsilon_{hkl}^{sf} = \varepsilon_{hkl}^{strain} - \frac{\sqrt{3}}{4\pi} \frac{\sum_b \pm(h+k+l)}{(u+b)(h^2+k^2+l^2)} SFP \qquad \text{Eq. A-27}$$

, in which u and b are the number of un-broadened and broadened components due to stacking faults [463]. Considering the successive grain families are equivalent in crystallographic directions and their lattice strain evolution should be consistent without the disturbance from stacking faults. This allows us to calculate the SFP via subtracting ε_{111}^{exp} from ε_{222}^{exp}:

$$SFP = \frac{32\pi}{3\sqrt{3}} \left(\varepsilon_{222}^{exp} - \varepsilon_{111}^{exp} \right) \qquad \text{Eq. A-28}$$

The stacking fault energy (SFE) of the alloy can then be calculated with the Reed and Schramm equation [171]:

$$SFE = \frac{6.6a_0}{\pi\sqrt{3}} \frac{\left\langle \varepsilon^2 \right\rangle_{111}}{SFP} \left(\frac{2C_{44}}{C_{11} - C_{12}} \right)^{-0.37} \left(\frac{C_{44} + C_{11} - C_{12}}{3} \right) \qquad \text{Eq. A-29}$$

, in which $\left\langle \varepsilon^2 \right\rangle_{111}$ is the mean square microstrain, which is obtained by deconvoluting size and strain broadening effects with the double-Voigt method [294].

A.2.3 Dislocation Density Calculation

The peak broadening effect analysis was carried out to obtain the dislocation density via the modified Williamson-Hall method. The sample and instrumental factors can both contribute to the broadening of diffraction peaks. It is critical to remove instrumental broadening effects (K_{inst}) before further characterization of the microstructure of the samples. The instrument contribution to peak broadening was determined with the stress-free calibrant of CeO_2 and was then subtracted from the measured FWHM (K_{mea}) to obtain the broadening effects of samples (K_{sample}) via [327]:

$$\Delta K^2_{sample} = \Delta K^2_{meas} - \Delta K^2_{inst} \qquad \text{Eq. A-30}$$

, as a result of deconvolution considering the line profile is very close to Gaussian function as the Gaussian fraction in pseudo-Voigt function is higher than 0.8 for most peaks. Then the dislocation density of the sample was calculated with the modified Williamson-Hall method (W-H), which considers the anisotropy in strain broadening due to the orientation-dependent geometric factors thus a good linear relationship between strain broadening and diffraction vector length can be obtained. In the modified W-H model, sample broadening effect can be ascribed to several factors:

average crystalline size (D), stacking faults/twinning probability (β'), and dislocation density (ρ) [290]:

$$\Delta K - \beta' W(g) \cong \frac{a_s}{D} + bM_d\sqrt{\frac{\pi}{2}\rho}(K\overline{C}_{hkl}^{1/2}) + O\left(K^2\overline{C}\right) \qquad \text{Eq. A-31}$$

, where ΔK is the FWHM of each diffraction peak after subtracting instrumental broadening with Eq. A-30. $\beta' = (1.5\alpha + \beta)/a$, where α and β denote the density of stacking fault and twin boundary. *W(g)* is a scaling factor to obtain the broadening effects of the faults at different peaks [290]. a_s =0.9 is the shape factor for cubic-symmetric spherical crystals, *b* is the magnitude of the Burger's vector, and M_d is a coefficient depicting the shape of the tail of a profile and was decided by the effective outer cut-off radius of dislocations. *K=1/d* is the diffraction vector length in TOF neutron diffraction and *d* is the d-spacing of each reflection. $\overline{C}_{hkl}$ is the averaged contrast factor for each *hkl* reflection and can be calculated with:

$$\overline{C}_{hkl} = \overline{C}_{h00}\left(1 - q\left[\frac{h^2k^2 + h^2l^2 + k^2l^2}{\left(h^2 + k^2 + l^2\right)^2}\right]\right) \qquad \text{Eq. A-32}$$

, in which *q* is a parameter related to the characteristic of edge of screw dislocation and can be determined experimentally. Three elastic constants (C_{11}, C_{12}, and C_{44}) of the alloy obtained at 293 and 15 K were applied in the calculation of $\overline{C}_{h00}$, the average contrast factor of {*h00*} reflection, which is also dependent on the ratio of screw/edge dislocation and their contrast factors of {*h00*} reflections ($C_{h00,i}$, the subscript *i* means the dislocation type). The C_{h00} of pure screw/edge dislocations can be determined with:

$$C_{h00i} = a_i^{c_{h00}}\left[1 - \exp\left(\frac{-A_i}{b_i^{c_{h00}}}\right)\right] + c_i^{c_{h00}}A_i + d_i^{c_{h00}} \qquad \text{Eq. A-33}$$

, where $A_i = 2C_{44}/(C_{11}-C_{12})$ is the elastic anisotropy parameter. According to Ref. [349], the four coefficients of $a_i^{c_{h00}}$, $b_i^{c_{h00}}$, $c_i^{c_{h00}}$, and $d_i^{c_{h00}}$ are dependent with two parameters (C_{11}/C_{44} and A_i) strongly related to the elastic constants. The low SFP results shown in Fig. 6-6c and d indicate that the very low density of stacking faults/twinning were introduced at both temperatures, hence we do not consider the faults-induced broadening effects ($\beta' W(g)$) in the peak broadening analysis. Then the screw/edge ratio ranging from 0 to 1 was used in Eq. A-31 to fit the modified W-H plots and the C_{hkl} gives the highest R-square value was chosen to evaluate the dislocation density [464]. ΔK and K of five reflections of (111), (200), (220), (311), and (222) were used for fitting the modified W-H plots at 293 and 15 K (a and b) with very high R-square values (above 0.9).

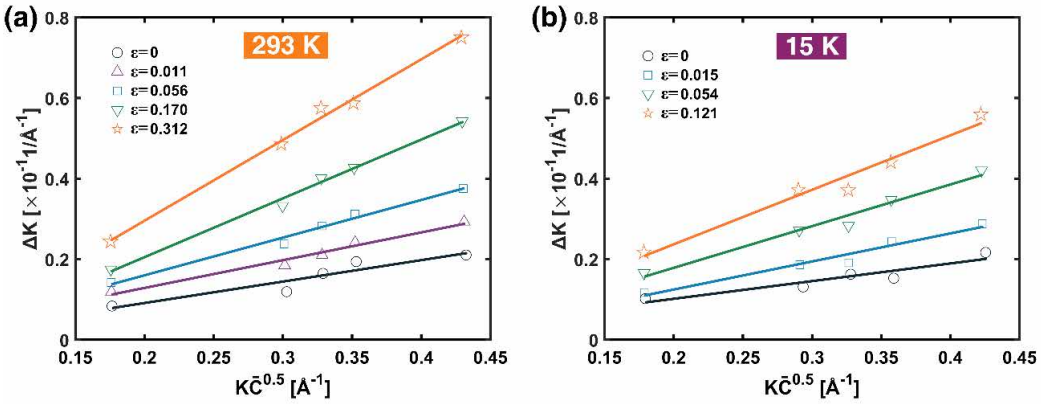

Fig. A-5 Modified Williamson Hall plots of the FeCrNi medium entropy alloy alloy during deforming at (a) 293 K and (b) 15 K.

A.2.4 Elastic Modulus Calculation from DFT

In this study, we applied the method of calculation of the anisotropy of Young's modulus and Poisson's ratio proposed by Wróbel et al. [406] in order to investigate the anisotropy of elastic properties. The variation of Young's modulus and Poisson's ratio as a function of the orientation with respect to the crystal lattice required the calculation of the fourth-order elastic compliance tensor, S_{ijkl}, which was determined via inversion

of the second-order elasticity tensor, C_{ij}. The Young's modulus, $E_{(hkl)}$, and the average Poisson ratio, $\upsilon_{(hkl)}$, along a direction normal to the lattice plane system described with Miller indices (hkl) (in amorphous structure these Miller indices describe spatial coordinates) are given as:

$$E_{(hkl)} = \frac{1}{s'_{3333}} \qquad \text{Eq. A-34}$$

$$v_{(hkl)} = -\frac{s'_{1133} + s'_{2233}}{2s'_{3333}} \qquad \text{Eq. A-35}$$

Here, s'_{ijkl} are components of the compliance tensor in the new reference system (the new lattice plane system rotated from the original one and described with Miller indices (hkl)) written in fourth-order tensor notation and transformed from the compliances of the crystal, s_{mnop}, in the original cubic crystal axes. Hence

$$s'_{ijkl} = a_{im}a_{jn}a_{ko}a_{lp}s_{mnop} \qquad \text{Eq. A-36}$$

, where a_{im}, a_{jn}, a_{ko}, and a_{lp} are the transformation matrices [465]. The transformation matrix, a_{rt}, from the original cubic crystal axes to the new lattice plane system described with Miller indices (hkl) can be expressed explicitly in terms of Miller indices of this plane [466].

$$(a_{rt}) = \begin{bmatrix} \frac{hl}{\sqrt{h^2+k^2}\sqrt{h^2+k^2+l^2}} & \frac{kl}{\sqrt{h^2+k^2}\sqrt{h^2+k^2+l^2}} & -\frac{\sqrt{h^2+k^2}}{\sqrt{h^2+k^2+l^2}} \\ -\frac{k}{\sqrt{h^2+k^2}} & \frac{h}{\sqrt{h^2+k^2}} & 0 \\ \frac{h}{\sqrt{h^2+k^2+l^2}} & \frac{k}{\sqrt{h^2+k^2+l^2}} & \frac{l}{\sqrt{h^2+k^2+l^2}} \end{bmatrix} \qquad \text{Eq. A-37}$$

, where h, k, l are the direction cosines.

In the method presented here, the transformation matrix, a_{rt}, is calculated for each orientation (chosen from a uniformly distributed set of directions) and $E_{(hkl)}$ and $\upsilon_{(hkl)}$ are obtained from Eq. A-34-Eq. A-36. A convenient representation of anisotropy is a plot of Young's modulus and Poisson's ratio surfaces. Each point on a given surface

represents the magnitude of Young's modulus in the direction of a vector from the origin to a given point on the surface. In this way, the surfaces map out how Young's modulus varies with direction.

In order to obtain the theoretical values of elastic moduli for polycrystalline materials, the Reuss-Voigt-Hill method has been employed with the following equations [419]:

$$B_{Voigt} = \frac{1}{9}[c_{11} + c_{22} + c_{33} + 2(c_{12} + c_{23} + c_{13})] \quad \text{Eq. A-38}$$

$$G_{Voigt} = \frac{1}{15}[c_{11} + c_{22} + c_{33} - c_{12} - c_{23} - c_{13} + 3(c_{44} + c_{55} + c_{66})] \quad \text{Eq. A-39}$$

$$E_{Voigt} = \frac{9B_{Voigt}G_{Voigt}}{3B_{Voigt} + G_{Voigt}} \quad \text{Eq. A-40}$$

$$B_{Reuss} = [s_{11} + s_{22} + s_{33} + 2(s_{12} + s_{23} + s_{13})]^{-1} \quad \text{Eq. A-41}$$

$$G_{Reuss} = 15[4(s_{11} + s_{22} + s_{33} - s_{12} - s_{23} - s_{13}) + (s_{44} + s_{55} + s_{66})]^{-1} \quad \text{Eq. A-42}$$

$$E_{Reuss} = \frac{9B_{Reuss}G_{Reuss}}{3B_{Reuss} + G_{Reuss}} \quad \text{Eq. A-43}$$

Table. A-2 Elastic constants and moduli of the FeCrNi MEA predicted by DFT calculations and compared with experimental data.

	FeCrNi	DFT 2000 K	DFT 2000 K	DFT 300 K	DFT 300 K	*in situ* Exp. 293 K	*in situ* Exp. 15 K
	Symmetry K-points	*P1* 4×4×4 Relaxed	*P1* 4×4×4 Unrelaxed	*Pnnm* 4×4×4 Relaxed	*Pnnm* 6×6×6 Relaxed		
Elastic Constant [GPa]	C_{11}	210.79	222.45	239.41	237.44	225	220
	C_{12}	141.19	134.8	117.01	116.4	151	134
	C_{13}	136.06	142.6	136.48	137.24	-	-
	C_{22}	200.47	213.16	231.37	229.99	-	-
	C_{23}	127.42	132.09	109.34	108.92	-	-
	C_{33}	206.05	218.31	257.46	259.19	-	-
	C_{44}	123.42	125.36	163.14	163.46	123	127
	C_{55}	122.36	138.84	143.22	142.18	-	-
	C_{66}	122.19	131.67	141.19	140.99	-	-
	$(C_{11}+C_{22}+C_{33})/3$	205.8	218.0	242.7	242.2	-	-
	$(C_{12}+C_{13}+C_{23})/3$	134.9	136.5	120.9	120.9	-	-
	$(C_{44}+C_{55}+C_{66})/3$	122.7	132.0	149.2	148.9	-	-
	C' (average)	35.4	40.7	60.9	60.7	37.0	43.0
Young's Modulus [GPa]	E_{min}	94.2	111.02	148.21	146.05	103.71	118.55
	E_{max}	292.52	311.98	341.52	340.82	299.1	302.27
	E_{av}	180.83	199.81	248.02	247.12	187.95	201.8
	E_{max}/E_{min}	3.105	2.81	2.304	2.334	2.884	2.55
	SD	50.77	52.26	48.63	48.78	50.93	48.31
	SD/E_{av} (%)	28.08	26.15	19.61	19.74	27.09	23.94
Poisson's Ratio	P_{min}	0.1914	0.1823	0.1449	0.1447	0.2162	0.1903
	P_{max}	0.4196	0.3985	0.3569	0.3572	0.4016	0.3785
	P_{av}	0.3093	0.2962	0.2429	0.2433	0.3216	0.2932
	P_{max}/P_{min}	2.192	2.186	2.463	2.468	1.856	1.989
	SD	0.055	0.0539	0.0534	0.0539	0.04016	0.0496
	SD/P_{av} (%)	17.78	18.21	21.97	22.14	15.08	16.93
Polycrystalline Moduli [GPa]	$B_{(VRH)}$	158.33	163.53	161.09	160.77	175.65	162.67
	$G_{(VRH)}$	74.57	82.45	103.62	103.27	76.17	82.35
	$E_{(VRH)}$	192.64	211.12	255.64	254.82	199.06	210.9

A.2.5 Calculation of Phase Formation Parameters

Solid-solution phases are the more desirable in multi-component alloys as their promising mechanical properties. There are several criteria in predicting the constituent

phases of the multi-component alloys. According to Ref. [467], the Gibbs free energy difference between solid- and liquid-state (ΔG_{mix}) can be expressed with:

$$\Delta G_{mix} = \Delta H_{mix} - T\Delta S_{mix} \qquad \text{Eq. A-44}$$

, in which T is the absolute temperature, ΔS_{mix} and ΔH_{mix} are the entropy of mixing and the enthalpy of mixing, respectively. For a random multi-component alloy with n elements, they can be calculated with [245,468]:

$$\Delta S_{mix} = -R\sum_{i}^{n} c_i \ln c_i \qquad \text{Eq. A-45}$$

$$\Delta H_{mix} = \sum_{i=1, i\neq j}^{n} \Omega_{ij} c_i c_j \qquad \text{Eq. A-46}$$

, in which R=8.314 JK^{-1}mol^{-1} is the gas constant, c_i is the mole percent of component i. $\Omega_{ij} = 4\Delta H_{AB}^{mix}$ is the regular solution interaction parameter between two elements (ith and jth). ΔH_{AB}^{mix} is the mixing enthalpy ΔH_{mix} of binary alloys, its values can be calculated with the Miedema macroscopic model in Ref. [431]. The multi-component alloys preferably form solid-solution phases if their ΔG_{mix} drops to the lowest level compared with other possible phases. According to Ref. [468], the large absolute value of ΔH_{mix} can impede the solid-solution formation. When ΔH_{mix} approaches zero, the different elements can randomly distribute among the matrix and form a solid-solution phase. On the other hand, increasing ΔS_{mix} can effectively lower ΔG_{mix} and lower the tendency of ordering and segregation of alloy elements.

A.2.6 TEM Characterization

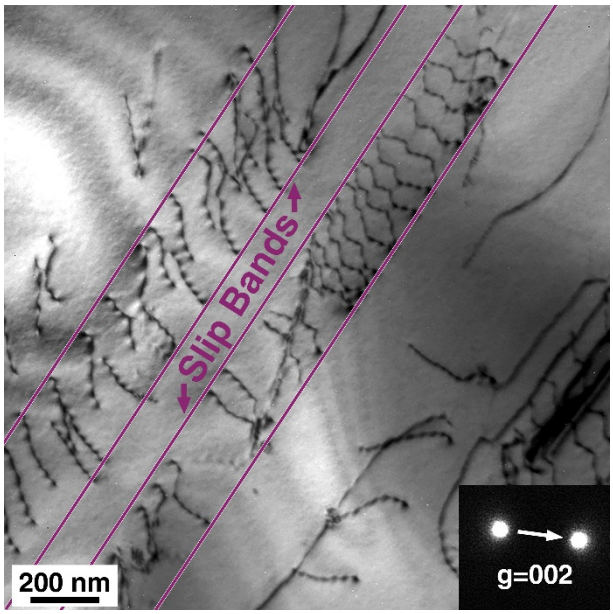

Fig. A-6 Two-beam bright-field TEM image shows the representative wavy configuration of dislocation in the FeCrNi medium entropy alloy.

References

[1] J. Moon, E. Tabachnikova, S. Shumilin, T. Hryhorova, Y. Estrin, J. Brechtl, P.K. Liaw, W. Wang, K.A. Dahmen, A. Zargaran, J.W. Bae, H.-S. Do, B.-J. Lee, H.S. Kim, Deformation behavior of a Co-Cr-Fe-Ni-Mo medium-entropy alloy at extremely low temperatures, Mater. Today. (2021). https://doi.org/10.1016/j.mattod.2021.08.001.

[2] A.R. Jha, Cryogenic Technology and Applications, 2006. https://doi.org/10.1016/B978-0-7506-7887-2.X5000-X.

[3] M. Bhattacharya, J.N. Inekwe, P. Sadorsky, Consumption-based and territory-based carbon emissions intensity: Determinants and forecasting using club convergence across countries, Energy Econ. 86 (2020) 104632. https://doi.org/10.1016/j.eneco.2019.104632.

[4] J.W. Morris, Steels: for low temperature applications, Lawrence Berkeley Natl. Lab. (1993).

[5] J.G. Kaufman, Properties of Aluminum Alloys: Tensile, Creep and Fatigue Data at High and Low Temperatures, ASM International, 1999.

[6] A. Association, Aluminum: properties and physical metallurgy, ASM international, 1984.

[7] S.A.F. Oleg N. Senkov, Daniel B. Miracle, Metallic Materials with High Structural Efficiency, Springer Netherlands. (2004) 444.

[8] F.R. Schwartzberg, S.H. Osgood, R.D. Keys, Cryogenic materials data handbook, Martin Co denver Co, 1963.

[9] S. Kalia, Cryogenic processing: A study of materials at low temperatures, J. Low Temp. Phys. 158 (2010) 934–945. https://doi.org/10.1007/s10909-009-0058-x.

[10] P. Mallick, N.K. Tewary, S.K. Ghosh, P.P. Chattopadhyay, Effect of cryogenic deformation on microstructure and mechanical properties of 304 austenitic stainless steel, Mater. Charact. 133 (2017) 77–86. https://doi.org/10.1016/J.MATCHAR.2017.09.027.

[11] A. Sharafian, O.E. Herrera, W. Mérida, Performance analysis of liquefied natural gas storage tanks in refueling stations, J. Nat. Gas Sci. Eng. 36 (2016) 496–509. https://doi.org/10.1016/j.jngse.2016.10.062.

[12] J. kuan Ren, Q. yuan Chen, J. Chen, Z. yu Liu, Enhancing strength and cryogenic toughness of high manganese TWIP steel plate by double strengthened structure design, Mater. Sci. Eng. A. 786 (2020) 139397. https://doi.org/10.1016/j.msea.2020.139397.

[13] S. Hany, M. Milochova, K. Littrell, R. Lorange, J.-B. Vogt, E. Abi-Aad, E. Bychkov, Advanced characterization of cryogenic 9Ni steel using synchrotron radiation, neutron scattering and 57Fe Mössbauer spectroscopy, Mater. Des. 146 (2018) 219–227. https://doi.org/10.1016/j.matdes.2018.03.024.

[14] D. Kuhl, J. Riccius, O.J. Haidn, Thermomechanical Analysis and Optimization

of Cryogenic Liquid Rocket Engines, J. Propuls. Power. 18 (2002) 835–846. https://doi.org/10.2514/2.6007.

[15] S. Kumar, H.T. Kwon, K.H. Choi, W. Lim, J.H. Cho, K. Tak, I. Moon, LNG: An eco-friendly cryogenic fuel for sustainable development, Appl. Energy. 88 (2011) 4264–4273. https://doi.org/10.1016/J.APENERGY.2011.06.035.

[16] Statistical Review of World Energy | Energy economics | Home, (n.d.). https://www.bp.com/en/global/corporate/energy-economics/statistical-review-of-world-energy.html (accessed November 16, 2021).

[17] H. Jiang, X. Dong, Q. Jiang, K. Dong, What drives China's natural gas consumption? Analysis of national and regional estimates, Energy Econ. 87 (2020) 104744. https://doi.org/10.1016/j.eneco.2020.104744.

[18] S.W. Van Sciver, Cryogenic systems for superconducting devices, Phys. C Supercond. 354 (2001) 129–135. https://doi.org/10.1016/S0921-4534(01)00013-2.

[19] Y. Lvovsky, P. Jarvis, Superconducting systems for MRI-present solutions and new trends, IEEE Trans. Appl. Supercond. 15 (2005) 1317–1325. https://doi.org/10.1109/TASC.2005.849580.

[20] M. Ono, S. Koga, H. Ohtsuki, Japan's superconducting Maglev train, IEEE Instrum. Meas. Mag. 5 (2002) 9–15. https://doi.org/10.1109/5289.988732.

[21] H. Yaghoubi, The Most Important Maglev Applications, J. Eng. 2013 (n.d.). https://doi.org/10.1155/2013/537986.

[22] Y. Yoshino, A. Iwabuchi, R. Onodera, A. Chiba, K. Katagiri, T. Shimizu, Vickers hardness properties of structural materials for superconducting magnet at cryogenic temperatures, Cryogenics (Guildf). 41 (2001) 505–511. https://doi.org/10.1016/S0011-2275(01)00118-7.

[23] P.K. Liaw, W.A. Logsdon, Fatigue crack growth threshold at cryogenic temperatures: A review, Eng. Fract. Mech. 22 (1985) 585–594. https://doi.org/10.1016/0013-7944(85)90122-5.

[24] V.M. Chernov, B.K. Kardashev, K.A. Moroz, Low-temperature embrittlement and fracture of metals with different crystal lattices – Dislocation mechanisms, Nucl. Mater. Energy. 9 (2016) 496–501. https://doi.org/10.1016/J.NME.2016.02.002.

[25] N. Koga, T. Nameki, O. Umezawa, V. Tschan, K.P. Weiss, Tensile properties and deformation behavior of ferrite and austenite duplex stainless steel at cryogenic temperatures, Mater. Sci. Eng. A. 801 (2021) 140442. https://doi.org/10.1016/J.MSEA.2020.140442.

[26] Q. An, R. An, C. Wang, H. Wang, Ductile-to-brittle transition in fracture behaviors of common solder alloys over a temperature range down to −150 °C, Mater. Today Commun. 29 (2021) 102962. https://doi.org/10.1016/J.MTCOMM.2021.102962.

[27] N. Saini, C. Pandey, M.M. Mahapatra, H.K. Narang, R.S. Mulik, P. Kumar, A comparative study of ductile-brittle transition behavior and fractography of P91 and P92 steel, Eng. Fail. Anal. 81 (2017) 245–253. https://doi.org/10.1016/j.engfailanal.2017.06.044.

[28] E.D. Marquardt, J.P. Le, R. Radebaugh, Cryogenic Material Properties Database, in: Cryocoolers 11, Springer US, Boston, MA, 2002: pp. 681–687. https://doi.org/10.1007/0-306-47112-4_84.

[29] J.A. Turner, A Realizable Renewable Energy Future, Science (80-.). 285 (1999) 687–689. https://doi.org/10.1126/science.285.5428.687.

[30] J.S. Kim, J.B. Jeon, J.E. Jung, K.K. Um, Y.W. Chang, Effect of deformation induced transformation of ε-martensite on ductility enhancement in a Fe-12 Mn steel at cryogenic temperatures, Met. Mater. Int. 20 (2014) 41–47. https://doi.org/10.1007/s12540-014-1010-4.

[31] Fracture toughness properties of aerospace materials, in: Introd. to Aerosp. Mater., Elsevier, 2012: pp. 454–468. https://doi.org/10.1533/9780857095152.454.

[32] M.R. Gilbert, S. Queyreau, J. Marian, Stress and temperature dependence of screw dislocation mobility in α-Fe by molecular dynamics, Phys. Rev. B - Condens. Matter Mater. Phys. 84 (2011) 174103. https://doi.org/10.1103/PHYSREVB.84.174103/FIGURES/11/MEDIUM.

[33] Y. Lu, Y. Zhang, E. Ma, W. Han, Relative mobility of screw versus edge dislocations controls the ductile-to-brittle transition in metals, Proc. Natl. Acad. Sci. 118 (2021) e2110596118. https://doi.org/10.1073/pnas.2110596118.

[34] A.W. Magnusson, W.M. Baldwin, Low temperature brittleness, J. Mech. Phys. Solids. 5 (1957) 172–181. https://doi.org/10.1016/0022-5096(57)90003-0.

[35] V.E. Panin, L.S. Derevyagina, N.M. Lemeshev, A. V. Korznikov, A. V. Panin, M.S. Kazachenok, On the nature of low-temperature brittleness of BCC steels, Phys. Mesomech. 17 (2014) 89–96. https://doi.org/10.1134/S1029959914020015.

[36] V.I. Trefilov, Y. V Mil'man, S.A. Firstov, Physical Fundamentals of the Strength of Refractory Metals, Nuakova Dumka, Ukr. (1975).

[37] K.T. Kashyap, A. Bhat, P.G. Koppad, K.B. Puneeth, On Peierls Nabarro stress in Iron, Comput. Mater. Sci. 56 (2012) 172–173. https://doi.org/10.1016/j.commatsci.2011.12.033.

[38] S.C. Liu, T. Hashida, H. Takahashi, H. Kuwano, Y. Hamaguchi, Study on fractography in the low-temperature brittle fracture of an 18Cr-18Mn-0.7N austenitic steel, Metall. Mater. Trans. A Phys. Metall. Mater. Sci. 29 A (1998) 791–798. https://doi.org/10.1007/s11661-998-0270-3.

[39] Liberty Ship Failures | Metallurgy & Materials Engineering, (n.d.). https://metallurgyandmaterials.wordpress.com/2015/12/25/liberty-ship-failures/ (accessed November 16, 2021).

[40] At least six dead after liquid nitrogen leak | News | gasworld, (n.d.). https://www.gasworld.com/at-least-six-dead-after-liquid-nitrogen-leak/2020445.article (accessed November 16, 2021).

[41] Safety alert - Restricted pipe movement in cryogenic tanks, (n.d.). https://www.hse.gov.uk/chemicals/cryogenicalert.htm#footnote1 (accessed November 16, 2021).

[42] L. Zhang, X. Du, L. Zhang, W. Li, Y. Liang, J. Yu, N. Zou, G. Wan, Y. Tang,

G. Duan, B. Wu, Achieving ultra-high strength in a precipitation-hardened CoCrNi-based medium-entropy alloy with partially recrystallized microstructure and heterogeneous grains, Vacuum. 188 (2021) 110169. https://doi.org/10.1016/j.vacuum.2021.110169.

[43] Z.B. Jiao, J.H. Luan, Z.W. Zhang, M.K. Miller, W.B. Ma, C.T. Liu, Synergistic effects of Cu and Ni on nanoscale precipitation and mechanical properties of high-strength steels, Acta Mater. 61 (2013) 5996–6005. https://doi.org/10.1016/j.actamat.2013.06.040.

[44] R.O. Ritchie, The conflicts between strength and toughness, Nat. Mater. 10 (2011) 817–822. https://doi.org/10.1038/NMAT3115.

[45] S.S. Sohn, S. Hong, J. Lee, B.C. Suh, S.K. Kim, B.J. Lee, N.J. Kim, S. Lee, Effects of Mn and Al contents on cryogenic-temperature tensile and Charpy impact properties in four austenitic high-Mn steels, Acta Mater. 100 (2015) 39–52. https://doi.org/10.1016/j.actamat.2015.08.027.

[46] H. Kim, J. Park, Y. Ha, W. Kim, S.S. Sohn, H.S. Kim, B.J. Lee, N.J. Kim, S. Lee, Dynamic tension-compression asymmetry of martensitic transformation in austenitic Fe-(0.4, 1.0)C-18Mn steels for cryogenic applications, Acta Mater. 96 (2015) 37–46. https://doi.org/10.1016/j.actamat.2015.06.021.

[47] B. Gludovatz, A. Hohenwarter, K.V.S.S. Thurston, H. Bei, Z. Wu, E.P. George, R.O. Ritchie, Exceptional damage-tolerance of a medium-entropy alloy CrCoNi at cryogenic temperatures, Nat. Commun. 7 (2016) 10602. https://doi.org/10.1038/ncomms10602.

[48] T. Yang, Y.L. Zhao, J.H. Luan, B. Han, J. Wei, J.J. Kai, C.T. Liu, Nanoparticles-strengthened high-entropy alloys for cryogenic applications showing an exceptional strength-ductility synergy, Scr. Mater. 164 (2019) 30–35. https://doi.org/10.1016/j.scriptamat.2019.01.034.

[49] H. Choo, S.C. Vogel, H. Li, K. Tao, D.W. Brown, J.J. Wall, In situ neutron diffraction study of grain-orientation-dependent phase transformation in 304L stainless steel at a cryogenic temperature , J. Appl. Phys. 100 (2006) 123515. https://doi.org/10.1063/1.2402474.

[50] D. Huang, Y. Zhuang, C. Wang, Advanced mechanical properties obtained via accurately tailoring stacking fault energy in Co-rich and Ni-depleted CoxCr33Ni67-x medium-entropy alloys, Scr. Mater. 207 (2022) 114269. https://doi.org/10.1016/j.scriptamat.2021.114269.

[51] M. Gao, H. Kang, Z. Chen, E. Guo, Y. Fu, Y. Xu, T. Wang, Enhanced strength-ductility synergy in a boron carbide reinforced aluminum matrix composite at 77 K, J. Alloys Compd. 818 (2020) 153310. https://doi.org/10.1016/J.JALLCOM.2019.153310.

[52] S. Esmaeili, L.M. Cheng, A. Deschamps, D.J. Lloyd, W.J. Poole, The deformation behaviour of AA6111 as a function of temperature and precipitation state, Mater. Sci. Eng. A. 319–321 (2001) 461–465. https://doi.org/10.1016/S0921-5093(01)01113-3.

[53] J.W. Bae, J.B. Seol, J. Moon, S.S. Sohn, M.J. Jang, H.Y. Um, B.-J. Lee, H.S. Kim, Exceptional phase-transformation strengthening of ferrous medium-entropy alloys at cryogenic temperatures, Acta Mater. 161 (2018) 388–399.

https://doi.org/10.1016/j.actamat.2018.09.057.

[54] Z. Lyu, X. Fan, C. Lee, S.Y. Wang, R. Feng, P.K. Liaw, Fundamental understanding of mechanical behavior of high-entropy alloys at low temperatures: A review, J. Mater. Res. 33 (2018) 2998–3010. https://doi.org/10.1557/jmr.2018.273.

[55] Y. Chen, Y.J. Luo, Y.F. Shen, Y. Liu, R.D.K. Misra, Cumulative contribution of grain structure and twin boundaries on cyclic deformation behavior of a 20Mn-0.6C- TWIP steel: Experimental and theoretical analysis, Mater. Sci. Eng. A. 767 (2019) 138415. https://doi.org/10.1016/j.msea.2019.138415.

[56] Z. Chen, Z. Sun, B. Panicaud, Constitutive modeling of TWIP/TRIP steels and numerical simulation of single impact during Surface Mechanical Attrition Treatment, Mech. Mater. 122 (2018) 69–75. https://doi.org/10.1016/j.mechmat.2018.04.005.

[57] X. Gao, Y. Lu, J. Liu, J. Wang, T. Wang, Y. Zhao, Extraordinary ductility and strain hardening of Cr26Mn20Fe20Co20Ni14 TWIP high-entropy alloy by cooperative planar slipping and twinning, Materialia. 8 (2019) 100485. https://doi.org/10.1016/j.mtla.2019.100485.

[58] Z.Y. Tang, R.D.K. Misra, M. Ma, N. Zan, Z.Q. Wu, H. Ding, Deformation twinning and martensitic transformation and dynamic mechanical properties in Fe-0.07C-23Mn-3.1Si-2.8Al TRIP/TWIP steel, Mater. Sci. Eng. A. 624 (2015) 186–192. https://doi.org/10.1016/j.msea.2014.11.078.

[59] L. a Dobrzański, W. Borek, Mechanical Properties and Microstructure of High-Manganese TWIP, TRIP and TRIPLEX Type Steels, J. Achiev. Mater. Manuf. Eng. 55 (2012) 230–238.

[60] I.C. Jung, B.C. De Cooman, Temperature dependence of the flow stress of Fe-18Mn-0.6C-xAl twinning-induced plasticity steel, Acta Mater. 61 (2013) 6724–6735. https://doi.org/10.1016/j.actamat.2013.07.042.

[61] J. Gil Sevillano, An alternative model for the strain hardening of FCC alloys that twin, validated for twinning-induced plasticity steel, Scr. Mater. 60 (2009) 336–339. https://doi.org/10.1016/j.scriptamat.2008.10.035.

[62] Z. Li, C.C. Tasan, K.G. Pradeep, D. Raabe, A TRIP-assisted dual-phase high-entropy alloy: Grain size and phase fraction effects on deformation behavior, Acta Mater. 131 (2017) 323–335. https://doi.org/10.1016/j.actamat.2017.03.069.

[63] X.D. Wang, B.X. Huang, Y.H. Rong, L. Wang, Microstructures and stability of retained austenite in TRIP steels, Mater. Sci. Eng. A. 438–440 (2006) 300–305. https://doi.org/10.1016/J.MSEA.2006.02.149.

[64] M. Soleimani, A. Kalhor, H. Mirzadeh, Transformation-induced plasticity (TRIP) in advanced steels: A review, Mater. Sci. Eng. A. 795 (2020) 140023. https://doi.org/10.1016/j.msea.2020.140023.

[65] K. Spencer, J.D. Embury, K.T. Conlon, M. Véron, Y. Bréchet, Strengthening via the formation of strain-induced martensite in stainless steels, Mater. Sci. Eng. A. 387–389 (2004) 873–881. https://doi.org/10.1016/j.msea.2003.11.084.

[66] D. Maréchal, C.W. Sinclair, P. Dufour, P.J. Jacques, J.D. Mithieux, In-situ measurements of load partitioning in a metastable austenitic stainless steel:

Neutron and magnetomechanical measurements, Metall. Mater. Trans. A Phys. Metall. Mater. Sci. 43 (2012) 4601–4609. https://doi.org/10.1007/s11661-012-1258-6.

[67] J.P. Hirth, J. Lothe, T. Mura, Theory of dislocations, J. Appl. Mech. 50 (1983) 476.

[68] S. Curtze, V.-T.T. Kuokkala, Dependence of tensile deformation behavior of TWIP steels on stacking fault energy, temperature and strain rate, Acta Mater. 58 (2010) 5129–5141. https://doi.org/https://doi.org/10.1016/j.actamat.2010.05.049.

[69] J.H. Choi, M.C. Jo, H. Lee, A. Zargaran, T. Song, S.S. Sohn, N.J. Kim, S. Lee, Cu addition effects on TRIP to TWIP transition and tensile property improvement of ultra-high-strength austenitic high-Mn steels, Acta Mater. 166 (2019) 246–260. https://doi.org/10.1016/j.actamat.2018.12.044.

[70] I. Gutierrez-Urrutia, D. Raabe, Dislocation and twin substructure evolution during strain hardening of an Fe-22 wt.% Mn-0.6 wt.% C TWIP steel observed by electron channeling contrast imaging, Acta Mater. 59 (2011) 6449–6462. https://doi.org/10.1016/j.actamat.2011.07.009.

[71] B.C. De Cooman, O. Kwon, K.G. Chin, State-of-the-knowledge on TWIP steel, Mater. Sci. Technol. 28 (2012) 513–527. https://doi.org/10.1179/1743284711Y.0000000095.

[72] Z.Y. Liang, Y.Z. Li, M.X. Huang, The respective hardening contributions of dislocations and twins to the flow stress of a twinning-induced plasticity steel, Scr. Mater. 112 (2016) 28–31. https://doi.org/10.1016/j.scriptamat.2015.09.003.

[73] M. Zhang, L. Li, J. Ding, Q. Wu, Y.D. Wang, J. Almer, F. Guo, Y. Ren, Temperature-dependent micromechanical behavior of medium-Mn transformation-induced-plasticity steel studied by in situ synchrotron X-ray diffraction, Acta Mater. 141 (2017) 294–303. https://doi.org/10.1016/j.actamat.2017.09.030.

[74] P. Kusakin, A. Belyakov, C. Haase, R. Kaibyshev, D.A. Molodov, Microstructure evolution and strengthening mechanisms of Fe-23Mn-0.3C-1.5Al TWIP steel during cold rolling, Mater. Sci. Eng. A. 617 (2014) 52–60. https://doi.org/10.1016/j.msea.2014.08.051.

[75] X.S. Yang, S. Sun, H.H. Ruan, S.Q. Shi, T.Y. Zhang, Shear and shuffling accomplishing polymorphic fcc $\gamma \rightarrow$ hcp $\varepsilon \rightarrow$ bct α martensitic phase transformation, Acta Mater. 136 (2017) 347–354. https://doi.org/10.1016/j.actamat.2017.07.016.

[76] J. Kim, Y. Estrin, B.C. De Cooman, Application of a dislocation density-based constitutive model to Al-alloyed TWIP steel, Metall. Mater. Trans. A Phys. Metall. Mater. Sci. 44 (2013) 4168–4182. https://doi.org/10.1007/s11661-013-1771-2.

[77] W.Z. Han, Z.F. Zhang, S.D. Wu, S.X. Li, Combined effects of crystallographic orientation, stacking fault energy and grain size on deformation twinning in fcc crystals, Philos. Mag. 88 (2008) 3011–3029. https://doi.org/10.1080/14786430802438168.

[78] T.S. Byun, On the stress dependence of partial dislocation separation and

deformation microstructure in austenitic stainless steels, Acta Mater. 51 (2003) 3063–3071. https://doi.org/10.1016/S1359-6454(03)00117-4.

[79] B.C. De Cooman, Y. Estrin, S.K. Kim, Twinning-induced plasticity (TWIP) steels, Acta Mater. 142 (2018) 283–362. https://doi.org/10.1016/j.actamat.2017.06.046.

[80] V. Tsakiris, D. V. Edmonds, Martensite and deformation twinning in austenitic steels, Mater. Sci. Eng. A. 273–275 (1999) 430–436. https://doi.org/10.1016/s0921-5093(99)00322-6.

[81] O. Grässel, G. Frommeyer, C. Derder, H. Hofmann, Phase transformations and mechanical properties of Fe-Mn-Si-Al TRIP-steels, J. Phys. IV JP. 7 (1997) 1–6. https://doi.org/10.1051/jp4:1997560.

[82] O. Grässel, G. Frommeyer, Effect of martensitic phase transformation and deformation twinning on mechanical properties of Fe-Mn-Si-Al steels, Mater. Sci. Technol. 14 (1998) 1213–1217. https://doi.org/10.1179/mst.1998.14.12.1213.

[83] G. Frommeyer, U. Brüx, P. Neumann, Supra-ductile and high-strength manganese-TRIP/TWIP steels for high energy absorption purposes, ISIJ Int. 43 (2003) 438–446. https://doi.org/10.2355/isijinternational.43.438.

[84] B. Gwalani, S. Gorsse, D. Choudhuri, Y. Zheng, R.S. Mishra, R. Banerjee, Tensile yield strength of a single bulk Al 0.3 CoCrFeNi high entropy alloy can be tuned from 160 MPa to 1800 MPa, Scr. Mater. 162 (2019) 18–23. https://doi.org/10.1016/j.scriptamat.2018.10.023.

[85] K. Marthinsen, E. Nes, Modelling strain hardening and steady state deformation of Al-Mg alloys, Mater. Sci. Technol. 17 (2001) 376–388. https://doi.org/10.1179/026708301101510096.

[86] P. Leo, E. Cerri, P.P. De Marco, H.J. Roven, Properties and deformation behaviour of severe plastic deformed aluminium alloys, J. Mater. Process. Technol. 182 (2007) 207–214. https://doi.org/10.1016/j.jmatprotec.2006.07.038.

[87] K. Jeong, J.E. Jin, Y.S. Jung, S. Kang, Y.K. Lee, The effects of Si on the mechanical twinning and strain hardening of Fe-18Mn-0.6C twinning-induced plasticity steel, Acta Mater. 61 (2013) 3399–3410. https://doi.org/10.1016/j.actamat.2013.02.031.

[88] J. Chen, F. Dong, Z. Liu, G. Wang, Grain size dependence of twinning behaviors and resultant cryogenic impact toughness in high manganese austenitic steel, J. Mater. Res. Technol. 10 (2021) 175–187. https://doi.org/10.1016/j.jmrt.2020.12.030.

[89] R. Liu, Z. Liang, L. Lin, M. Huang, Dislocation Source and Pile-up in a Twinning-induced Plasticity Steel at High-Cycle Fatigue, Acta Metall. Sin. (English Lett. 34 (2021) 169–173. https://doi.org/10.1007/s40195-020-01176-z.

[90] H. Idrissi, K. Renard, L. Ryelandt, D. Schryvers, P.J. Jacques, On the mechanism of twin formation in Fe–Mn–C TWIP steels, Acta Mater. 58 (2010) 2464–2476. https://doi.org/10.1016/J.ACTAMAT.2009.12.032.

[91] P. Zhou, Z.Y. Liang, R.D. Liu, M.X. Huang, Evolution of dislocations and twins in a strong and ductile nanotwinned steel, Acta Mater. 111 (2016) 96–107.

https://doi.org/10.1016/j.actamat.2016.03.057.

[92] P. Zhou, Z.Y. Liang, M.X. Huang, Microstructural evolution of a nanotwinned steel under extremely high-strain-rate deformation, Acta Mater. 149 (2018) 407–415. https://doi.org/10.1016/j.actamat.2018.02.062.

[93] W. Woo, J.S. Jeong, D.K. Kim, C.M. Lee, S.H. Choi, J.Y. Suh, S.Y. Lee, S. Harjo, T. Kawasaki, Stacking Fault Energy Analyses of Additively Manufactured Stainless Steel 316L and CrCoNi Medium Entropy Alloy Using In Situ Neutron Diffraction, Sci. Rep. 10 (2020) 2–4. https://doi.org/10.1038/s41598-020-58273-3.

[94] I. Gutierrez-Urrutia, D. Raabe, Grain size effect on strain hardening in twinning-induced plasticity steels, Scr. Mater. 66 (2012) 992–996. https://doi.org/10.1016/j.scriptamat.2012.01.037.

[95] Y.M. Wang, T. Voisin, J.T. McKeown, J. Ye, N.P. Calta, Z. Li, Z. Zeng, Y. Zhang, W. Chen, T.T. Roehling, R.T. Ott, M.K. Santala, P.J. Depond, M.J. Matthews, A. V. Hamza, T. Zhu, Additively manufactured hierarchical stainless steels with high strength and ductility, Nat. Mater. 17 (2018) 63–70. https://doi.org/10.1038/NMAT5021.

[96] J. Li, M. Yi, H. Wu, Q. Fang, Y. Liu, B. Liu, K. Zhou, P.K. Liaw, Fine-grain-embedded dislocation-cell structures for high strength and ductility in additively manufactured steels, Mater. Sci. Eng. A. 790 (2020) 139736. https://doi.org/10.1016/j.msea.2020.139736.

[97] K. Yamanaka, M. Mori, S. Sato, A. Chiba, Stacking-fault strengthening of biomedical Co-Cr-Mo alloy via multipass thermomechanical processing, Sci. Rep. 7 (2017) 1–13. https://doi.org/10.1038/s41598-017-10305-1.

[98] W. Lu, X. Luo, Y. Yang, W. Le, B. Huang, P. Li, Co-free non-equilibrium medium-entropy alloy with outstanding tensile properties, J. Alloys Compd. 833 (2020) 155074. https://doi.org/10.1016/j.jallcom.2020.155074.

[99] A.J. Zaddach, C. Niu, C.C. Koch, D.L. Irving, Mechanical properties and stacking fault energies of NiFeCrCoMn high-entropy alloy, Jom. 65 (2013) 1780–1789. https://doi.org/10.1007/s11837-013-0771-4.

[100] X.D. Xu, P. Liu, Z. Tang, A. Hirata, S.X. Song, T.G. Nieh, P.K. Liaw, C.T. Liu, M.W. Chen, Transmission electron microscopy characterization of dislocation structure in the face-centered cubic high-entropy alloy Al0.1CoCrFeNi, Acta Mater. 144 (2017) 107–115. https://doi.org/10.1016/j.actamat.2017.10.050.

[101] Y. Deng, C.C. Tasan, K.G. Pradeep, H. Springer, A. Kostka, D. Raabe, Design of a twinning-induced plasticity high entropy alloy, Acta Mater. 94 (2015) 124–133. https://doi.org/10.1016/j.actamat.2015.04.014.

[102] B. Cai, B. Liu, S. Kabra, Y. Wang, K. Yan, P.D. Lee, Y. Liu, Deformation mechanisms of Mo alloyed FeCoCrNi high entropy alloy: In situ neutron diffraction, Acta Mater. 127 (2017) 471–480. https://doi.org/10.1016/j.actamat.2017.01.034.

[103] C.E. Slone, S. Chakraborty, J. Miao, E.P. George, M.J. Mills, S.R. Niezgoda, Influence of deformation induced nanoscale twinning and FCC-HCP transformation on hardening and texture development in medium-entropy CrCoNi alloy, Acta Mater. 158 (2018) 38–52.

https://doi.org/10.1016/j.actamat.2018.07.028.

[104] J. Miao, C.E. Slone, T.M. Smith, C. Niu, H. Bei, M. Ghazisaeidi, G.M. Pharr, M.J. Mills, The evolution of the deformation substructure in a Ni-Co-Cr equiatomic solid solution alloy, Acta Mater. 132 (2017) 35–48. https://doi.org/10.1016/j.actamat.2017.04.033.

[105] M. Calcagnotto, Y. Adachi, D. Ponge, D. Raabe, Deformation and fracture mechanisms in fine- and ultrafine-grained ferrite/martensite dual-phase steels and the effect of aging, Acta Mater. 59 (2011) 658–670. https://doi.org/10.1016/j.actamat.2010.10.002.

[106] M.M. Wang, C.C. Tasan, D. Ponge, A.C. Dippel, D. Raabe, Nanolaminate transformation-induced plasticity-twinning-induced plasticity steel with dynamic strain partitioning and enhanced damage resistance, Acta Mater. 85 (2015) 216–228. https://doi.org/10.1016/j.actamat.2014.11.010.

[107] M.M. Wang, C.C. Tasan, D. Ponge, A. Kostka, D. Raabe, Smaller is less stable: Size effects on twinning vs. transformation of reverted austenite in TRIP-maraging steels, Acta Mater. 79 (2014) 268–281. https://doi.org/10.1016/j.actamat.2014.07.020.

[108] A.K. De, J.G. Speer, D.K. Matlock, D.C. Murdock, M.C. Mataya, R.J. Comstock, Deformation-induced phase transformation and strain hardening in type 304 austenitic stainless steel, Metall. Mater. Trans. A Phys. Metall. Mater. Sci. 37 (2006) 1875–1886. https://doi.org/10.1007/s11661-006-0130-y.

[109] L. Morales-Rivas, H.W. Yen, B.M. Huang, M. Kuntz, F.G. Caballero, J.R. Yang, C. Garcia-Mateo, Tensile Response of Two Nanoscale Bainite Composite-Like Structures, JOM. 67 (2015) 2223–2235. https://doi.org/10.1007/s11837-015-1562-x.

[110] G. Cios, T. Tokarski, A. Żywczak, R. Dziurka, M. Stępień, Ł. Gondek, M. Marciszko, B. Pawłowski, K. Wieczerzak, P. Bała, The Investigation of Strain-Induced Martensite Reverse Transformation in AISI 304 Austenitic Stainless Steel, Metall. Mater. Trans. A 2017 4810. 48 (2017) 4999–5008. https://doi.org/10.1007/S11661-017-4228-1.

[111] A. Sato, K. Soma, T. Mori, Hardening due to pre-existing ϵ-Martensite in an Fe-30Mn-1Si alloy single crystal, Acta Metall. 30 (1982) 1901–1907. https://doi.org/10.1016/0001-6160(82)90030-X.

[112] L. Chen, Q. Jia, S. Hao, Y. Wang, C. Peng, X. Ma, Z. Zou, M. Jin, The effect of strain-induced martensite transformation on strain partitioning and damage evolution in a duplex stainless steel with metastable austenite, Mater. Sci. Eng. A. 814 (2021) 141173. https://doi.org/10.1016/J.MSEA.2021.141173.

[113] G.L. Huang, D.K. Matlock, G. Krauss, Martensite formation, strain rate sensitivity, and deformation behavior of type 304 stainless steel sheet, Metall. Trans. A, Phys. Metall. Mater. Sci. 20 A (1989) 1239–1246. https://doi.org/10.1007/BF02647406.

[114] T. Shintani, Y. Murata, Evaluation of the dislocation density and dislocation character in cold rolled Type 304 steel determined by profile analysis of X-ray diffraction, Acta Mater. 59 (2011) 4314–4322. https://doi.org/10.1016/j.actamat.2011.03.055.

[115] E.I. Galindo-Nava, P.E.J. Rivera-Díaz-del-Castillo, Understanding martensite and twin formation in austenitic steels: A model describing TRIP and TWIP effects, Acta Mater. 128 (2017) 120–134. https://doi.org/10.1016/j.actamat.2017.02.004.

[116] H. He, M. Naeem, F. Zhang, Y. Zhao, S. Harjo, T. Kawasaki, B. Wang, X. Wu, S. Lan, Z. Wu, W. Yin, Y. Wu, Z. Lu, J.J. Kai, C.T. Liu, X.L. Wang, Stacking Fault Driven Phase Transformation in CrCoNi Medium Entropy Alloy, Nano Lett. 21 (2021) 1419–1426. https://doi.org/10.1021/acs.nanolett.0c04244.

[117] J. Ding, Q. Yu, M. Asta, R.O. Ritchie, Tunable stacking fault energies by tailoring local chemical order in CrCoNi medium-entropy alloys, Proc. Natl. Acad. Sci. U. S. A. 115 (2018) 8919–8924. https://doi.org/10.1073/pnas.1808660115.

[118] S. Mahajan, G.Y. Chin, Formation of deformation twins in f.c.c. crystals, Acta Metall. 21 (1973) 1353–1363. https://doi.org/10.1016/0001-6160(73)90085-0.

[119] J.A. Venables, Deformation twinning in face-centred cubic metals, Philos. Mag. 6 (1961) 379–396. https://doi.org/10.1080/14786436108235892.

[120] J.B. Cohen, J. Weertman, A dislocation model for twinning in f.c.c. metals, Acta Metall. 11 (1963) 996–998. https://doi.org/10.1016/0001-6160(63)90074-9.

[121] H. Fujita, T. Mori, A formation mechanism of mechanical twins in F.C.C. Metals, Scr. Metall. 9 (1975) 631–636. https://doi.org/10.1016/0036-9748(75)90476-7.

[122] S. Miura, J.-I. Takamura, N. Narita, Orientation dependence of flow stress for twinning in silver crystals, in: Trans. Japan Inst. Met., JAPAN INST METALS AOBA ARAMAKI, SENDAI 980, JAPAN, 1968: p. 555.

[123] H. Fujita, S. Ueda, Stacking faults and f.c.c. (γ) → h.c.p. (ϵ) transformation in 188-type stainless steel, Acta Metall. 20 (1972) 759–767. https://doi.org/10.1016/0001-6160(72)90104-6.

[124] S. Mahajan, M.L. Green, D. Brasen, A model for the FCC→HCP transformation, its applications, and experimental evidence, Metall. Trans. A. 8 (1977) 283–293. https://doi.org/10.1007/BF02661642.

[125] X.S. Yang, S. Sun, T.Y. Zhang, The mechanism of bcc α′ nucleation in single hcp ε laths in the fcc γ → hcp ε → bcc α′ martensitic phase transformation, Acta Mater. 95 (2015) 264–273. https://doi.org/10.1016/j.actamat.2015.05.034.

[126] A.J. Bogers, W.G. Burgers, Partial dislocations on the {110} planes in the B.C.C. lattice and the transition of the F.C.C. into the B.C.C. lattice, Acta Metall. 12 (1964) 255–261. https://doi.org/10.1016/0001-6160(64)90194-4.

[127] G.B. Olson, M. Cohen, A mechanism for the strain-induced martensitic transformations, J. Less-Common Met. 28 (1972) 107–118.

[128] L. BRACKE, L. KESTENS, J. PENNING, Transformation mechanism of α′-martensite in an austenitic Fe–Mn–C–N alloy, Scr. Mater. 57 (2007) 385–388. https://doi.org/10.1016/j.scriptamat.2007.05.003.

[129] X.S. Yang, S. Sun, X.L. Wu, E. Ma, T.Y. Zhang, Dissecting the mechanism of martensitic transformation via atomic-scale observations, Sci. Rep. 4 (2014) 1–7. https://doi.org/10.1038/srep06141.

[130] J. Liu, C. Chen, Y. Xu, S. Wu, G. Wang, H. Wang, Y. Fang, L. Meng,

Deformation twinning behaviors of the low stacking fault energy high-entropy alloy : An in-situ TEM study, Scr. Mater. 137 (2017) 9–12. https://doi.org/10.1016/j.scriptamat.2017.05.001.

[131] M. Muzyk, Z. Pakiela, K.J. Kurzydlowski, Ab initio calculations of the generalized stacking fault energy in aluminium alloys, Scr. Mater. 64 (2011) 916–918. https://doi.org/10.1016/j.scriptamat.2011.01.034.

[132] D. Geissler, J. Freudenberger, A. Kauffmann, S. Martin, D. Rafaja, Assessment of the thermodynamic dimension of the stacking fault energy, Philos. Mag. 94 (2014) 2967–2979. https://doi.org/10.1080/14786435.2014.944606.

[133] S. Crampin, K. Hampel, D.D. Vvedensky, J.M. MacLaren, The Calculation of Stacking Fault Energies in Close-Packed Metals, J. Mater. Res. 5 (1990) 2107–2119. https://doi.org/10.1557/JMR.1990.2107.

[134] T.L. Achmad, W. Fu, H. Chen, C. Zhang, Z.G. Yang, Effects of alloying elements concentrations and temperatures on the stacking fault energies of Co-based alloys by computational thermodynamic approach and first-principles calculations, J. Alloys Compd. 694 (2017) 1265–1279. https://doi.org/10.1016/J.JALLCOM.2016.10.113.

[135] S. Curtze, V.-T.T. Kuokkala, Dependence of tensile deformation behavior of TWIP steels on stacking fault energy, temperature and strain rate, Acta Mater. 58 (2010) 5129–5141. https://doi.org/10.1016/j.actamat.2010.05.049.

[136] G.B. Olson, M. Cohen, A general mechanism of martensitic nucleation: Part II. FCC→BCC and other martensitic transformations, Metall. Trans. A. 7 (1976) 1905–1914. https://doi.org/10.1007/BF02654988.

[137] N.R. Tao, X.L. Wu, M.L. Sui, J. Lu, K. Lu, Grain refinement at the nanoscale via mechanical twinning and dislocation interaction in a nickel-based alloy, J. Mater. Res. 19 (2004) 1623–1629. https://doi.org/10.1557/JMR.2004.0227.

[138] Y. Lü, B. Hutchinson, D.A. Molodov, G. Gottstein, Effect of deformation and annealing on the formation and reversion of ε-martensite in an Fe-Mn-C alloy, Acta Mater. 58 (2010) 3079–3090. https://doi.org/10.1016/j.actamat.2010.01.045.

[139] Z. Li, K.G. Pradeep, Y. Deng, D. Raabe, C.C. Tasan, Metastable high-entropy dual-phase alloys overcome the strength–ductility trade-off, Nature. 534 (2016) 1–8. https://doi.org/10.1038/nature17981.

[140] S. Huang, H. Huang, W. Li, D. Kim, S. Lu, X. Li, E. Holmström, S.K. Kwon, L. Vitos, Twinning in metastable high-entropy alloys, Nat. Commun. 9 (2018) 2381. https://doi.org/10.1038/s41467-018-04780-x.

[141] O.A. Zambrano, Stacking Fault Energy Maps of Fe–Mn–Al–C–Si Steels: Effect of Temperature, Grain Size, and Variations in Compositions, J. Eng. Mater. Technol. 138 (2016) 041010. https://doi.org/10.1115/1.4033632.

[142] Q. Luo, H.H. Wang, G.Q. Li, C. Sun, D.H. Li, X.L. Wan, On mechanical properties of novel high-Mn cryogenic steel in terms of SFE and microstructural evolution, Mater. Sci. Eng. A. 753 (2019) 91–98. https://doi.org/10.1016/j.msea.2019.02.093.

[143] L.M. Roncery, S. Weber, W. Theisen, Development of Mn-Cr-(C-N) corrosion

resistant twinning induced plasticity steels: Thermodynamic and diffusion calculations, production, and characterization, Metall. Mater. Trans. A Phys. Metall. Mater. Sci. 41 (2010) 2471–2479. https://doi.org/10.1007/s11661-010-0334-z.

[144] B. Cantor, Multicomponent high-entropy Cantor alloys, Prog. Mater. Sci. (2020) 100754. https://doi.org/10.1016/j.pmatsci.2020.100754.

[145] A.P. Miodownik, The calculation of stacking fault energies in Fe-Ni-Cr alloys, Calphad. 2 (1978) 207–226. https://doi.org/10.1016/0364-5916(78)90010-X.

[146] P.J. Ferreira, P. Müllner, A thermodynamic model for the stacking-fault energy, Acta Mater. 46 (1998) 4479–4484. https://doi.org/10.1016/S1359-6454(98)00155-4.

[147] L. Li, T.Y. Hsu, X. Zuyao, GIBBS FREE ENERGY EVALUATION OF THE FCC(y) AND HCP(&) PHASES IN FE-MN-S1 ALLOYS, Pergamon Calphad. 21 (1997) 443–448.

[148] G. Kresse, J. Hafner, Ab initio molecular dynamics for liquid metals, Phys. Rev. B. 47 (1993) 558–561. https://doi.org/10.1103/PhysRevB.47.558.

[149] M. Chandran, S.K. Sondhi, First-principle calculation of stacking fault energies in Ni and Ni-Co alloy, J. Appl. Phys. 109 (2011). https://doi.org/10.1063/1.3585786.

[150] M. Ojima, Y. Adachi, Y. Tomota, Y. Katada, Y. Kaneko, K. Kuroda, H. Saka, Weak beam TEM study on stacking fault energy of high nitrogen steels, Steel Res. Int. 80 (2009) 477–481. https://doi.org/10.2374/SRI09SP038.

[151] S. Lu, Q.M. Hu, B. Johansson, L. Vitos, Stacking fault energies of Mn, Co and Nb alloyed austenitic stainless steels, Acta Mater. 59 (2011) 5728–5734. https://doi.org/10.1016/J.ACTAMAT.2011.05.049.

[152] X. Peng, D. Zhu, Z. Hu, M. Wang, L. Liu, H. Liu, Effect of Carbon Content on Stacking Fault Energy of Fe-20Mn-3Cu TWIP Steel, J. Iron Steel Res. Int. 21 (2014) 116–120. https://doi.org/10.1016/S1006-706X(14)60018-2.

[153] C. Zheng, Q. Zhen, Y. Wang, N. Li, Low temperature macro- and micro-mechanical behavior of an ultrafine-grained metastable 304 austenitic stainless steel investigated by in situ high-energy X-ray diffraction, Mater. Sci. Eng. A. 817 (2021) 141295. https://doi.org/10.1016/j.msea.2021.141295.

[154] G.B. Olson, M. Cohen, A general mechanism of martensitic nucleation: Part I. General concepts and the FCC → HCP transformation, Metall. Trans. A. 7 (1976) 1897–1904. https://doi.org/10.1007/BF02659822.

[155] S. Curtze, V.-T. Kuokkala, A. Oikari, J. Talonen, H. Hänninen, Thermodynamic modeling of the stacking fault energy of austenitic steels, Acta Mater. 59 (2011) 1068–1076. https://doi.org/10.1016/j.actamat.2010.10.037.

[156] S. Cotes, M. Sade, A.F. Guillermet, Fcc/Hcp martensitic transformation in the Fe-Mn system: Experimental study and thermodynamic analysis of phase stability, Metall. Mater. Trans. A. 26 (1995) 1957–1969. https://doi.org/10.1007/BF02670667.

[157] O. Redlich, A.T. Kister, Algebraic Representation of Thermodynamic Properties and the Classification of Solutions, Ind. Eng. Chem. 40 (1948) 345–348.

https://doi.org/10.1021/ie50458a036.

[158] D. Joubert, From ultrasoft pseudopotentials to the projector augmented-wave method, Phys. Rev. B - Condens. Matter Mater. Phys. 59 (1999) 1758–1775. https://doi.org/10.1103/PhysRevB.59.1758.

[159] T.L. Achmad, W. Fu, H. Chen, C. Zhang, Z.-G. Yang, Computational thermodynamic and first-principles calculation of stacking fault energy on ternary Co-based alloys, Comput. Mater. Sci. 143 (2018) 112–117. https://doi.org/10.1016/j.commatsci.2017.11.004.

[160] D. Wei, X. Li, J. Jiang, W. Heng, Y. Koizumi, W.-M. Choi, B.-J. Lee, H.S. Kim, H. Kato, A. Chiba, Novel Co-rich high performance twinning-induced plasticity (TWIP) and transformation-induced plasticity (TRIP) high-entropy alloys, Scr. Mater. 165 (2019) 39–43. https://doi.org/10.1016/j.scriptamat.2019.02.018.

[161] R. Mohammadzadeh, M. Mohammadzadeh, Correlation between stacking fault energy and lattice parameter in nanocrystalline Fe–Cr–Ni austenitic stainless steels by atomistic simulation study, Int. J. Model. Simul. 37 (2017) 227–233. https://doi.org/10.1080/02286203.2017.1331109.

[162] X. Wang, W. Xiong, Stacking fault energy prediction for austenitic steels: thermodynamic modeling vs. machine learning, Sci. Technol. Adv. Mater. 21 (2020) 626–634. https://doi.org/10.1080/14686996.2020.1808433.

[163] H. Van Swygenhoven, P.M. Derlet, A.G. Frøseth, Stacking fault energies and slip in nanocrystalline metals, Nat. Mater. 3 (2004) 399–403. https://doi.org/10.1038/nmat1136.

[164] T.L. Achmad, W. Fu, H. Chen, C. Zhang, Z.G. Yang, First-principles calculations of generalized-stacking-fault-energy of Co-based alloys, Comput. Mater. Sci. 121 (2016) 86–96. https://doi.org/10.1016/j.commatsci.2016.04.031.

[165] L. Mosecker, A. Saeed-Akbari, Nitrogen in chromium-manganese stainless steels: A review on the evaluation of stacking fault energy by computational thermodynamics, Sci. Technol. Adv. Mater. 14 (2013). https://doi.org/10.1088/1468-6996/14/3/033001.

[166] S.J. Lee, Y. Sun, H. Fujii, Stacking-fault energy, mechanical twinning and strain hardening of Fe-18Mn-0.6C-(0, 1.5)Al twinning-induced plasticity steels during friction stir welding, Acta Mater. 148 (2018) 235–248. https://doi.org/10.1016/j.actamat.2018.02.004.

[167] S. Kibey, J.B. Liu, M.J. Curtis, D.D. Johnson, H. Sehitoglu, Effect of nitrogen on generalized stacking fault energy and stacking fault widths in high nitrogen steels, Acta Mater. 54 (2006) 2991–3001. https://doi.org/10.1016/j.actamat.2006.02.048.

[168] A.W. Ruff, Measurement of stacking fault energy from dislocation interactions, Metall. Trans. 1 (1970) 2391–2413. https://doi.org/10.1007/BF03038368.

[169] S.F. Liu, Y. Wu, H.T. Wang, J.Y. He, J.B. Liu, C.X. Chen, X.J. Liu, H. Wang, Z.P. Lu, Stacking fault energy of face-centered-cubic high entropy alloys, Intermetallics. 93 (2018) 269–273. https://doi.org/10.1016/J.INTERMET.2017.10.004.

[170] S.J. Lee, Y.S. Jung, S. Il Baik, Y.W. Kim, M. Kang, W. Woo, Y.K. Lee, The

effect of nitrogen on the stacking fault energy in Fe–15Mn–2Cr–0.6C–xN twinning-induced plasticity steels, Scr. Mater. 92 (2014) 23–26. https://doi.org/10.1016/J.SCRIPTAMAT.2014.08.004.

[171] R.P. Reed, R.E. Schramm, Relationship between stacking-fault energy and x-ray measurements of stacking-fault probability and microstrain, J. Appl. Phys. 45 (1974) 4705–4711. https://doi.org/10.1063/1.1663122.

[172] G. Laplanche, A. Kostka, C. Reinhart, J. Hunfeld, G. Eggeler, E.P. George, Reasons for the superior mechanical properties of medium-entropy CrCoNi compared to high-entropy CrMnFeCoNi, Acta Mater. 128 (2017) 292–303. https://doi.org/10.1016/J.ACTAMAT.2017.02.036.

[173] J. Liu, C. Chen, Y. Xu, S. Wu, G. Wang, H. Wang, Y. Fang, L. Meng, Deformation twinning behaviors of the low stacking fault energy high-entropy alloy: An in-situ TEM study, Scr. Mater. 137 (2017) 9–12. https://doi.org/10.1016/J.SCRIPTAMAT.2017.05.001.

[174] J.H. Lee, T.B. Holland, A.K. Mukherjee, X. Zhang, H. Wang, Direct observation of Lomer-Cottrell Locks during strain hardening in nanocrystalline nickel by in situ TEM, Sci. Rep. 3 (2013) 1–6. https://doi.org/10.1038/srep01061.

[175] Q. Ding, Y. Zhang, X. Chen, X. Fu, D. Chen, S. Chen, L. Gu, F. Wei, H. Bei, Y. Gao, M. Wen, J. Li, Z. Zhang, T. Zhu, R.O. Ritchie, Q. Yu, Tuning element distribution, structure and properties by composition in high-entropy alloys, Nature. 574 (2019) 223–227. https://doi.org/10.1038/s41586-019-1617-1.

[176] C. Ullrich, S. Martin, C. Schimpf, A. Stark, N. Schell, D. Rafaja, Deformation Mechanisms in Metastable Austenitic TRIP/TWIP Steels under Compressive Load Studied by in situ Synchrotron Radiation Diffraction, Adv. Eng. Mater. 21 (2019) 1801101. https://doi.org/10.1002/ADEM.201801101.

[177] M. Frank, Y. Chen, S.S. Nene, S. Sinha, K. Liu, K. An, R.S. Mishra, Investigating the deformation mechanisms of a highly metastable high entropy alloy using in-situ neutron diffraction, Mater. Today Commun. 23 (2020) 100858. https://doi.org/10.1016/J.MTCOMM.2019.100858.

[178] M. Frank, S.S. Nene, Y. Chen, B. Gwalani, E.J. Kautz, A. Devaraj, K. An, R.S. Mishra, Correlating work hardening with co-activation of stacking fault strengthening and transformation in a high entropy alloy using in-situ neutron diffraction, Sci. Rep. 10 (2020) 1–10. https://doi.org/10.1038/s41598-020-79492-8.

[179] S.-M. Bak, Z. Shadike, R. Lin, X. Yu, X.-Q. Yang, In situ/operando synchrotron-based X-ray techniques for lithium-ion battery research, NPG Asia Mater. 2018 107. 10 (2018) 563–580. https://doi.org/10.1038/s41427-018-0056-z.

[180] M. Drakopoulos, T. Connolley, C. Reinhard, R. Atwood, O. Magdysyuk, N. Vo, M. Hart, L. Connor, B. Humphreys, G. Howell, S. Davies, T. Hill, G. Wilkin, U. Pedersen, A. Foster, N. De Maio, M. Basham, F. Yuan, K. Wanelik, I12: The Joint Engineering, Environment and Processing (JEEP) beamline at Diamond Light Source, J. Synchrotron Radiat. 22 (2015) 828–838. https://doi.org/10.1107/S1600577515003513.

[181] S. Sharma, R. Haigh, L. Edwards, M.E. Fitzpatrick, M. Turski, S77 Neutron Diffraction Study of Intergranular Stress Development in Austenitic Stainless

Steel Weld Metal, Powder Diffr. 23 (2008) 185–185. https://doi.org/10.1154/1.2951791.

[182] R.N. Shaikh, M. Anis, A.B. Gambhire, M.D. Shirsat, S.S. Hussaini, Growth, optical and dielectric studies of glycine doped ammonium dihydrogen phosphate NLO crystal: Potential material for optoelectronics applications, Mater. Res. Express. 1 (2014). https://doi.org/10.1088/2053-1591/1/1/015016.

[183] R.D. Haigh, M.T. Hutchings, J.A. James, S. Ganguly, R. Mizuno, K. Ogawa, S. Okido, A.M. Paradowska, M.E. Fitzpatrick, Neutron diffraction residual stress measurements on girth-welded 304 stainless steel pipes with weld metal deposited up to half and full pipe wall thickness, Int. J. Press. Vessel. Pip. 101 (2013) 1–11. https://doi.org/10.1016/J.IJPVP.2012.08.003.

[184] M. Dutta, G. Bruno, L. Edwards, M.E. Fitzpatrick, Neutron diffraction measurement of the internal stresses following heat treatment of a plastically deformed Al/SiC particulate metal–matrix composite, Acta Mater. 52 (2004) 3881–3888. https://doi.org/10.1016/J.ACTAMAT.2004.05.002.

[185] J.R. Santisteban, M.R. Daymond, J.A. James, L. Edwards, ENGIN-X: a third-generation neutron strain scanner, J. Appl. Crystallogr. 39 (2006) 812–825. https://doi.org/10.1107/S0021889806042245.

[186] C.K. Syn, S. Jin, J.W. Morris, Cryogenic fracture toughness of 9Ni Steel enhanced through grain refinement, Metall. Trans. A. 7 (1976) 1827–1832. https://doi.org/10.1007/BF02654977.

[187] Z. Zhu, S. Yan, H. Chen, G. Gou, Unprecedented combination of strength and ductility in laser welded NiCoCr medium entropy alloy joints, Mater. Sci. Eng. A. (2020) 140501. https://doi.org/10.1016/j.msea.2020.140501.

[188] J.B. Seol, J.W. Bae, J.G. Kim, H. Sung, Z. Li, H.H. Lee, S.H. Shim, J.H. Jang, W.-S.S. Ko, S.I. Hong, H.S. Kim, Short-range order strengthening in boron-doped high-entropy alloys for cryogenic applications, Acta Mater. 194 (2020) 366–377. https://doi.org/10.1016/j.actamat.2020.04.052.

[189] J.W. Bae, J. Lee, A. Zargaran, H.S. Kim, Enhanced cryogenic tensile properties with multi-stage strain hardening through partial recrystallization in a ferrous medium-entropy alloy, Scr. Mater. 194 (2021) 113653. https://doi.org/10.1016/j.scriptamat.2020.113653.

[190] H. Nam, C. Park, J. Moon, Y. Na, H. Kim, N. Kang, Laser weldability of cast and rolled high-entropy alloys for cryogenic applications, Mater. Sci. Eng. A. 742 (2019) 224–230. https://doi.org/10.1016/j.msea.2018.11.009.

[191] L.B. Chen, R. Wei, K. Tang, J. Zhang, F. Jiang, J. Sun, Ductile-brittle transition of carbon alloyed Fe40Mn40Co10Cr10 high entropy alloys, Mater. Lett. 236 (2019) 416–419. https://doi.org/10.1016/j.matlet.2018.10.144.

[192] G. Laplanche, A. Kostka, O.M. Horst, G. Eggeler, E.P. George, Microstructure evolution and critical stress for twinning in the CrMnFeCoNi high-entropy alloy, Acta Mater. 118 (2016) 152–163. https://doi.org/10.1016/j.actamat.2016.07.038.

[193] G. Laplanche, A. Kostka, C. Reinhart, J. Hunfeld, G. Eggeler, E.P. George, Reasons for the superior mechanical properties of medium-entropy CrCoNi compared to high-entropy CrMnFeCoNi, Acta Mater. 128 (2017) 292–303. https://doi.org/10.1016/j.actamat.2017.02.036.

[194] A.S. Tirunilai, T. Hanemann, C. Reinhart, V. Tschan, K.P. Weiss, G. Laplanche, J. Freudenberger, M. Heilmaier, A. Kauffmann, Comparison of cryogenic deformation of the concentrated solid solutions CoCrFeMnNi, CoCrNi and CoNi, Mater. Sci. Eng. A. 783 (2020) 139290. https://doi.org/10.1016/j.msea.2020.139290.

[195] D. Li, C. Li, T. Feng, Y. Zhang, G. Sha, J.J. Lewandowski, P.K. Liaw, Y. Zhang, High-entropy Al0.3CoCrFeNi alloy fibers with high tensile strength and ductility at ambient and cryogenic temperatures, Acta Mater. 123 (2017) 285–294. https://doi.org/10.1016/j.actamat.2016.10.038.

[196] Z. He, N. Jia, H. Wang, H. Yan, Y. Shen, Synergy effect of multi-strengthening mechanisms in FeMnCoCrN HEA at cryogenic temperature, J. Mater. Sci. Technol. 86 (2021) 158–170. https://doi.org/10.1016/j.jmst.2020.12.079.

[197] B.B. Bian, N. Guo, H.J. Yang, R.P. Guo, L. Yang, Y.C. Wu, J.W. Qiao, A novel cobalt-free FeMnCrNi medium-entropy alloy with exceptional yield strength and ductility at cryogenic temperature, J. Alloys Compd. 827 (2020) 153981. https://doi.org/10.1016/j.jallcom.2020.153981.

[198] Z. Wu, H. Bei, G.M. Pharr, E.P. George, Temperature dependence of the mechanical properties of equiatomic solid solution alloys with face-centered cubic crystal structures, Acta Mater. 81 (2014) 428–441. https://doi.org/10.1016/j.actamat.2014.08.026.

[199] Q. Luo, H.H. Wang, G.Q. Li, C. Sun, D.H. Li, X.L. Wan, On mechanical properties of novel high-Mn cryogenic steel in terms of SFE and microstructural evolution, Mater. Sci. Eng. A. 753 (2019) 91–98. https://doi.org/10.1016/J.MSEA.2019.02.093.

[200] Y. Wang, B. Liu, K. Yan, M. Wang, S. Kabra, Y.L. Chiu, D. Dye, P.D. Lee, Y. Liu, B. Cai, Probing deformation mechanisms of a FeCoCrNi high-entropy alloy at 293 and 77 K using in situ neutron diffraction, Acta Mater. 154 (2018) 79–89. https://doi.org/10.1016/j.actamat.2018.05.013.

[201] Z. Han, C. Ding, G. Liu, J. Yang, Y. Du, R. Wei, Y. Chen, G. Zhang, Analysis of deformation behavior of VCoNi medium-entropy alloy at temperatures ranging from 77 K to 573 K, Intermetallics. 132 (2021) 107126. https://doi.org/10.1016/j.intermet.2021.107126.

[202] Z. Han, W. Ren, J. Yang, Y. Du, R. Wei, C. Zhang, Y. Chen, G. Zhang, The deformation behavior and strain rate sensitivity of ultra-fine grained CoNiFeCrMn high-entropy alloys at temperatures ranging from 77 K to 573 K, J. Alloys Compd. 791 (2019) 962–970. https://doi.org/10.1016/j.jallcom.2019.03.373.

[203] H. Steel, Hadfield's manganese steel, Science (80-.). ns-12 (1882) 284–287. https://doi.org/10.1126/science.ns-12.306.284-a.

[204] M. Sabzi, M. Farzam, Hadfield manganese austenitic steel: a review of manufacturing processes and properties, Mater. Res. Express. 6 (2019) 1065c2. https://doi.org/10.1088/2053-1591/AB3EE3.

[205] D. Pérez Escobar, S. Silva Ferreira De Dafé, D. Brandão Santos, Martensite reversion and texture formation in 17Mn-0.06C TRIP/TWIP steel after hot cold rolling and annealing, J. Mater. Res. Technol. 4 (2015) 162–170.

https://doi.org/10.1016/j.jmrt.2014.10.004.

[206] Z. Yanushkevich, A. Belyakov, R. Kaibyshev, C. Haase, D.A. Molodov, Effect of cold rolling on recrystallization and tensile behavior of a high-Mn steel, Mater. Charact. 112 (2016) 180–187. https://doi.org/10.1016/j.matchar.2015.12.021.

[207] I.R. Souza Filho, A. Dutta, D.R. Almeida Junior, W. Lu, M.J.R. Sandim, D. Ponge, H.R.Z. Sandim, D. Raabe, The impact of grain-scale strain localization on strain hardening of a high-Mn steel: Real-time tracking of the transition from the $\gamma \rightarrow \varepsilon \rightarrow \alpha'$ transformation to twinning, Acta Mater. 197 (2020) 123–136. https://doi.org/10.1016/j.actamat.2020.07.038.

[208] M. Ghiasabadi Farahani, A. Zarei-Hanzaki, H.R. Abedi, J.H. Kim, M. Jaskari, P. Sahu, L.P. Karjalainen, On the activation of alternated stacking fault pair twinning mechanism in a very large-grained Fe–29Mn–2.4Al steel, Scr. Mater. 178 (2020) 301–306. https://doi.org/10.1016/j.scriptamat.2019.11.035.

[209] W. Tofaute, K. Linden, Transformations in solid state of manganese steels containing to 1.2% C and 17% Mn, Arch Eisenhuttenwes. 10 (1936) 515–519.

[210] T. Xing, Z. Yansheng, Nonequilibrium phase diagram of Fe-Mn-Al system, Scr. Metall. Mater. 28 (1993) 1219–1222. https://doi.org/10.1016/0956-716X(93)90457-4.

[211] O. Grässel, L. Krüger, G. Frommeyer, L.W. Meyer, High strength Fe-Mn-(Al, Si) TRIP/TWIP steels development - properties - application, Int. J. Plast. 16 (2000) 1391–1409. https://doi.org/10.1016/S0749-6419(00)00015-2.

[212] D. Li, Y. Feng, S. Song, Q. Liu, Q. Bai, F. Ren, F. Shangguan, Influences of silicon on the work hardening behavior and hot deformation behavior of Fe-25 wt%Mn-(Si, Al) TWIP steel, J. Alloys Compd. 618 (2015) 768–775. https://doi.org/10.1016/j.jallcom.2014.08.239.

[213] R. Kalsar, P. Khandal, S. Suwas, Effects of Stacking Fault Energy on Deformation Mechanisms in Al-Added Medium Mn TWIP Steel, Metall. Mater. Trans. A Phys. Metall. Mater. Sci. 50 (2019) 3683–3696. https://doi.org/10.1007/s11661-019-05274-1.

[214] F. de las Cuevas, M. Reis, A. Ferraiuolo, G. Pratolongo, L.P. Karjalainen, J. Alkorta, J. Gil Sevillano, Hall-Petch Relationship of a TWIP Steel, Key Eng. Mater. 423 (2010) 147–152. https://doi.org/10.4028/www.scientific.net/KEM.423.147.

[215] K. Renard, H. Idrissi, D. Schryvers, P.J. Jacques, On the stress state dependence of the twinning rate and work hardening in twinning-induced plasticity steels, Scr. Mater. 66 (2012) 966–971. https://doi.org/10.1016/j.scriptamat.2012.01.063.

[216] A. Soulami, K.S. Choi, Y.F. Shen, W.N. Liu, X. Sun, M.A. Khaleel, On deformation twinning in a 17.5% Mn-TWIP steel: A physically based phenomenological model, Mater. Sci. Eng. A. 528 (2011) 1402–1408. https://doi.org/10.1016/j.msea.2010.10.031.

[217] A.A. Saleh, E. V. Pereloma, B. Clausen, D.W. Brown, C.N. Tomé, A.A. Gazder, On the evolution and modelling of lattice strains during the cyclic loading of TWIP steel, Acta Mater. 61 (2013) 5247–5262. https://doi.org/10.1016/j.actamat.2013.05.017.

[218] I.R. Souza Filho, D.R. Almeida Junior, C. Gauss, M.J.R. Sandim, P.A. Suzuki, H.R.Z. Sandim, Austenite reversion in AISI 201 austenitic stainless steel evaluated via in situ synchrotron X-ray diffraction during slow continuous annealing, Mater. Sci. Eng. A. 755 (2019) 267–277. https://doi.org/10.1016/j.msea.2019.04.014.

[219] W. Chuaiphan, L. Srijaroenpramong, Optimization of TIG welding parameter in dissimilar joints of low nickel stainless steel AISI 205 and AISI 216, J. Manuf. Process. 58 (2020) 163–178. https://doi.org/10.1016/j.jmapro.2020.07.052.

[220] L. Remy, A. Pineau, Twinning and strain-induced F.C.C. → H.C.P. transformation in the FeMnCrC system, Mater. Sci. Eng. 28 (1977) 99–107. https://doi.org/10.1016/0025-5416(77)90093-3.

[221] M. Koyama, T. Lee, C.S. Lee, K. Tsuzaki, Grain refinement effect on cryogenic tensile ductility in a Fe-Mn-C twinning-induced plasticity steel, Mater. Des. 49 (2013) 234–241. https://doi.org/10.1016/j.matdes.2013.01.061.

[222] S. Guo, C.T. Liu, Phase stability in high entropy alloys: Formation of solid-solution phase or amorphous phase, Prog. Nat. Sci. Mater. Int. 21 (2011) 433–446. https://doi.org/10.1016/S1002-0071(12)60080-X.

[223] X. Yang, Y. Zhang, Prediction of high-entropy stabilized solid-solution in multi-component alloys, Mater. Chem. Phys. 132 (2012) 233–238. https://doi.org/10.1016/j.matchemphys.2011.11.021.

[224] A. V. Ceguerra, M.P. Moody, R.C. Powles, T.C. Petersen, R.K.W. Marceau, S.P. Ringer, Short-range order in multicomponent materials, Acta Crystallogr. Sect. A Found. Crystallogr. 68 (2012) 547–560. https://doi.org/10.1107/S0108767312025706.

[225] C. Lee, F. Maresca, R. Feng, Y. Chou, T. Ungar, M. Widom, K. An, J.D. Poplawsky, Y.C. Chou, P.K. Liaw, W.A. Curtin, Strength can be controlled by edge dislocations in refractory high-entropy alloys, Nat. Commun. 12 (2021) 6–13. https://doi.org/10.1038/s41467-021-25807-w.

[226] J.W. Yeh, S.Y. Chang, Y. Der Hong, S.K. Chen, S.J. Lin, Anomalous decrease in X-ray diffraction intensities of Cu-Ni-Al-Co-Cr-Fe-Si alloy systems with multi-principal elements, Mater. Chem. Phys. 103 (2007) 41–46. https://doi.org/10.1016/j.matchemphys.2007.01.003.

[227] C.W. Tsai, Y.L. Chen, M.H. Tsai, J.W. Yeh, T.T. Shun, S.K. Chen, Deformation and annealing behaviors of high-entropy alloy Al0.5CoCrCuFeNi, J. Alloys Compd. 486 (2009) 427–435. https://doi.org/10.1016/J.JALLCOM.2009.06.182.

[228] B. Cantor, I.T.H. Chang, P. Knight, A.J.B. Vincent, Microstructural development in equiatomic multicomponent alloys, Mater. Sci. Eng. A. 375–377 (2004) 213–218. https://doi.org/10.1016/J.MSEA.2003.10.257.

[229] M.-H.H. Tsai, J.-W.W. Yeh, High-Entropy Alloys: A Critical Review, Mater. Res. Lett. 2 (2014) 107–123. https://doi.org/10.1080/21663831.2014.912690.

[230] B. Cantor, Stable and metastable multicomponent alloys, in: Ann. Chim. (Paris. 1914), 2007: pp. 245–256.

[231] T.B. Massalski, Phase diagrams in materials science, Metall. Trans. B. 20 (1989) 445–473.

[232] J.W. Yeh, S.K. Chen, S.J. Lin, J.Y. Gan, T.S. Chin, T.T. Shun, C.H. Tsau, S.Y. Chang, Nanostructured high-entropy alloys with multiple principal elements: Novel alloy design concepts and outcomes, Adv. Eng. Mater. 6 (2004) 299–303. https://doi.org/10.1002/adem.200300567.

[233] O.N. Senkov, S.L. Semiatin, Microstructure and properties of a refractory high-entropy alloy after cold working, J. Alloys Compd. 649 (2015) 1110–1123. https://doi.org/10.1016/j.jallcom.2015.07.209.

[234] Z. Wu, H. Bei, Microstructures and mechanical properties of compositionally complex Co-free FeNiMnCr18 FCC solid solution alloy, Mater. Sci. Eng. A. 640 (2015) 217–224. https://doi.org/10.1016/j.msea.2015.05.097.

[235] Z. Wu, C.M. Parish, H. Bei, Nano-twin mediated plasticity in carbon-containing FeNiCoCrMn high entropy alloys, J. Alloys Compd. 647 (2015) 815–822. https://doi.org/10.1016/j.jallcom.2015.05.224.

[236] Y. Zhang, T.T. Zuo, Z. Tang, M.C. Gao, K.A. Dahmen, P.K. Liaw, Z.P. Lu, Microstructures and properties of high-entropy alloys, Prog. Mater. Sci. 61 (2014) 1–93. https://doi.org/10.1016/j.pmatsci.2013.10.001.

[237] M. Hillert, Phase Equilibria, Phase Diagrams and Phase Transformations, 2nd ed., Cambridge University Press, Cambridge, 2007. https://doi.org/10.1017/CBO9780511812781.

[238] J.W. Yeh, S.K. Chen, S.J. Lin, J.Y. Gan, T.S. Chin, T.T. Shun, C.H. Tsau, S.Y. Chang, Nanostructured high-entropy alloys with multiple principal elements: Novel alloy design concepts and outcomes, Adv. Eng. Mater. (2004). https://doi.org/10.1002/adem.200300567.

[239] N. Ikenoue, A. Wakatsuki, Y. Okatani, Small low-density lipoprotein particles in women with natural or surgically induced menopause, 1999. https://doi.org/10.1097/00006250-199904000-00018.

[240] Y.E.H. Jien-Wei, Recent progress in high entropy alloys, Ann. Chim. Sci. Mat. 31 (2006) 633–648.

[241] D.B. Miracle, O.N. Senkov, A critical review of high entropy alloys and related concepts, Acta Mater. 122 (2017) 448–511. https://doi.org/10.1016/j.actamat.2016.08.081.

[242] D.B. Miracle, J.D. Miller, O.N. Senkov, C. Woodward, M.D. Uchic, J. Tiley, Exploration and development of high entropy alloys for structural applications, Entropy. 16 (2014) 494–525. https://doi.org/10.3390/e16010494.

[243] C.-J. Tong, M.-R. Chen, J.-W. Yeh, S.-J. Lin, S.-K. Chen, T.-T. Shun, S.-Y. Chang, Mechanical performance of the AlxCoCrCuFeNi high-entropy alloy system with multiprincipal elements, Metall. Mater. Trans. A. 36 (2005) 1263–1271. https://doi.org/10.1007/s11661-005-0218-9.

[244] J.M. Zhu, H.M. Fu, H.F. Zhang, A.M. Wang, H. Li, Z.Q. Hu, Microstructures and compressive properties of multicomponent AlCoCrFeNiMox alloys, Mater. Sci. Eng. A. 527 (2010) 6975–6979. https://doi.org/https://doi.org/10.1016/j.msea.2010.07.028.

[245] J.-W. Yeh, Alloy Design Strategies and Future Trends in High-Entropy Alloys, JOM. 65 (2013) 1759–1771. https://doi.org/10.1007/s11837-013-0761-6.

[246] E. Antillon, C. Woodward, S.I. Rao, B. Akdim, T.A. Parthasarathy, Chemical short range order strengthening in a model FCC high entropy alloy, Acta Mater. 190 (2020) 29–42. https://doi.org/10.1016/j.actamat.2020.02.041.

[247] Y. Chen, Y. Fang, X. Fu, Y. Lu, S. Chen, H. Bei, Q. Yu, Origin of strong solid solution strengthening in the CrCoNi-W medium entropy alloy, J. Mater. Sci. Technol. 73 (2021) 101–107. https://doi.org/10.1016/j.jmst.2020.08.058.

[248] S.S. Sohn, D.G. Kim, Y.H. Jo, A.K. da Silva, W. Lu, A.J. Breen, B. Gault, D. Ponge, High-rate superplasticity in an equiatomic medium-entropy VCoNi alloy enabled through dynamic recrystallization of a duplex microstructure of ordered phases, Acta Mater. 194 (2020) 106–117. https://doi.org/10.1016/j.actamat.2020.03.048.

[249] W.R. Jian, Z. Xie, S. Xu, Y. Su, X. Yao, I.J. Beyerlein, Effects of lattice distortion and chemical short-range order on the mechanisms of deformation in medium entropy alloy CoCrNi, Acta Mater. 199 (2020) 352–369. https://doi.org/10.1016/j.actamat.2020.08.044.

[250] C. Varvenne, A. Luque, W.A. Curtin, Theory of strengthening in fcc high entropy alloys, Acta Mater. 118 (2016) 164–176. https://doi.org/10.1016/j.actamat.2016.07.040.

[251] M. Komarasamy, N. Kumar, Z. Tang, R.S. Mishra, P.K. Liaw, Effect of microstructure on the deformation mechanism of friction stir-processed Al0.1CoCrFeNi high entropy alloy, Mater. Res. Lett. 3 (2014) 30–34. https://doi.org/10.1080/21663831.2014.958586.

[252] Y. Zhang, Q. Zhu, X. Lin, Z. Xu, J. Liu, Z. Wang, J. Zhou, K. Cen, A novel thermochemical cycle for the dissociation of CO2 and H2O using sustainable energy sources, Appl. Energy. 108 (2013) 1–7. https://doi.org/https://doi.org/10.1016/j.apenergy.2013.03.019.

[253] O.N. Senkov, J.M. Scott, S. V Senkova, D.B. Miracle, C.F. Woodward, Microstructure and room temperature properties of a high-entropy TaNbHfZrTi alloy, J. Alloys Compd. 509 (2011) 6043–6048. https://doi.org/10.1016/j.jallcom.2011.02.171.

[254] B. Gludovatz, A. Hohenwarter, D. Catoor, E.H. Chang, E.P. George, R.O. Ritchie, A fracture-resistant high-entropy alloy for cryogenic applications, Science (80-.). 345 (2014) 1153–1159. https://doi.org/10.1126/science.1254581.

[255] E.P. George, W.A. Curtin, C.C. Tasan, High entropy alloys: A focused review of mechanical properties and deformation mechanisms, Acta Mater. 188 (2020) 435–474. https://doi.org/10.1016/j.actamat.2019.12.015.

[256] C.-Y. Hsu, W.-R. Wang, W.-Y. Tang, S.-K. Chen, J.-W. Yeh, Microstructure and Mechanical Properties of New AlCoxCrFeMo0.5Ni High-Entropy Alloys, Adv. Eng. Mater. 12 (2010) 44–49. https://doi.org/10.1002/adem.200900171.

[257] S.W. Wu, G. Wang, Q. Wang, Y.D. Jia, J. Yi, Q.J. Zhai, J.B. Liu, B.A. Sun, H.J. Chu, J. Shen, P.K. Liaw, C.T. Liu, T.Y. Zhang, Enhancement of strength-ductility trade-off in a high-entropy alloy through a heterogeneous structure, Acta Mater. 165 (2019) 444–458. https://doi.org/10.1016/j.actamat.2018.12.012.

[258] Z. Zhang, H. Sheng, Z. Wang, B. Gludovatz, Z. Zhang, E.P. George, Q. Yu, S.X. Mao, R.O. Ritchie, Dislocation mechanisms and 3D twin architectures generate

exceptional strength-ductility-toughness combination in CrCoNi medium-entropy alloy, Nat. Commun. 8 (2017) 14390. https://doi.org/10.1038/ncomms14390.

[259] Z. Li, K.G. Pradeep, Y. Deng, D. Raabe, C.C. Tasan, Metastable high-entropy dual-phase alloys overcome the strength-ductility trade-off, Nature. 534 (2016) 227–230. https://doi.org/10.1038/nature17981.

[260] W. Woo, J.S. Jeong, D.K. Kim, C.M. Lee, S.H. Choi, J.Y. Suh, S.Y. Lee, S. Harjo, T. Kawasaki, Stacking Fault Energy Analyses of Additively Manufactured Stainless Steel 316L and CrCoNi Medium Entropy Alloy Using In Situ Neutron Diffraction, Sci. Rep. 10 (2020) 1–15. https://doi.org/10.1038/s41598-020-58273-3.

[261] M.S.F. De Lima, S. Sankaré, Microstructure and mechanical behavior of laser additive manufactured AISI 316 stainless steel stringers, Mater. Des. 55 (2014) 526–532. https://doi.org/10.1016/J.MATDES.2013.10.016.

[262] Y. Huang, J.M.K. Wiezorek, F.A. Garner, P.D. Freyer, T. Okita, M. Sagisaka, Y. Isobe, T.R. Allen, Microstructural characterization and density change of 304 stainless steel reflector blocks after long-term irradiation in EBR-II, J. Nucl. Mater. 465 (2015) 516–530. https://doi.org/10.1016/J.JNUCMAT.2015.06.031.

[263] K.H. Lo, C.H. Shek, J.K.L. Lai, Recent developments in stainless steels, Mater. Sci. Eng. R Reports. 65 (2009) 39–104. https://doi.org/10.1016/j.mser.2009.03.001.

[264] Y.F. Shen, X.X. Li, X. Sun, Y.D. Wang, L. Zuo, Twinning and martensite in a 304 austenitic stainless steel, Mater. Sci. Eng. A. 552 (2012) 514–522. https://doi.org/10.1016/j.msea.2012.05.080.

[265] N. Li, Y.D. Wang, W.J. Liu, Z.N. An, J.P. Liu, R. Su, J. Li, P.K. Liaw, In situ X-ray microdiffraction study of deformation-induced phase transformation in 304 austenitic stainless steel, Acta Mater. 64 (2014) 12–23. https://doi.org/10.1016/j.actamat.2013.11.001.

[266] S. Alsultan, C. Quitzke, Z. Cheng, L. Krüger, O. Volkova, M. Wendler, Strain-Induced Martensite Formation and Mechanical Properties of Fe–19Cr–4Ni–3Mn–0.15N–0.15C Austenitic Stainless Steel at Cryogenic Temperature, Steel Res. Int. 92 (2021) 2000611. https://doi.org/10.1002/srin.202000611.

[267] H.K.D.H. Bhadeshia, TRIP-assisted steels?, ISIJ Int. 42 (2002) 1059–1060. https://doi.org/10.2355/isijinternational.42.1059.

[268] A. Kovalev, A. Jahn, A. Weiß, S. Wolf, P.R. Scheller, Stress-Temperature-Transformation and Deformation-Temperature-Transformation Diagrams for an Austenitic CrMnNi as-cast Steel, Steel Res. Int. 82 (2011) 1101–1107. https://doi.org/10.1002/srin.201100065.

[269] Z. Sun, X. Tan, S.B. Tor, C.K. Chua, Simultaneously enhanced strength and ductility for 3D-printed stainless steel 316L by selective laser melting, NPG Asia Mater. 10 (2018) 127–136. https://doi.org/10.1038/s41427-018-0018-5.

[270] G.M. Karthik, E.S. Kim, P. Sathiyamoorthi, A. Zargaran, S.G. Jeong, R. Xiong, S.H. Kang, J.W. Cho, H.S. Kim, Delayed deformation-induced martensite transformation and enhanced cryogenic tensile properties in laser additive manufactured 316L austenitic stainless steel, Addit. Manuf. 47 (2021) 102314.

https://doi.org/10.1016/j.addma.2021.102314.

[271] Z. Wang, A.M. Beese, Effect of chemistry on martensitic phase transformation kinetics and resulting properties of additively manufactured stainless steel, Acta Mater. 131 (2017) 410–422. https://doi.org/10.1016/j.actamat.2017.04.022.

[272] J.G. Kim, N.A. Enikeev, J.B. Seol, M.M. Abramova, M. V Karavaeva, R.Z. Valiev, C.G. Park, H.S. Kim, Superior Strength and Multiple Strengthening Mechanisms in Nanocrystalline TWIP Steel, Sci. Rep. 8 (2018). https://doi.org/10.1038/s41598-018-29632-y.

[273] Y.F. Shen, Y.D. Wang, X.P. Liu, X. Sun, R. Lin Peng, S.Y. Zhang, L. Zuo, P.K. Liaw, Deformation mechanisms of a 20Mn TWIP steel investigated by in situ neutron diffraction and TEM, Acta Mater. 61 (2013) 6093–6106. https://doi.org/10.1016/j.actamat.2013.06.051.

[274] J.S. Jeong, W. Woo, K.H. Oh, S.K. Kwon, Y.M. Koo, In situ neutron diffraction study of the microstructure and tensile deformation behavior in Al-added high manganese austenitic steels, Acta Mater. 60 (2012) 2290–2299. https://doi.org/https://doi.org/10.1016/j.actamat.2011.12.043.

[275] L. Zhang, M. Wen, M. Imade, S. Fukuyama, K. Yokogawa, Effect of nickel equivalent on hydrogen gas embrittlement of austenitic stainless steels based on type 316 at low temperatures, Acta Mater. 56 (2008) 3414–3421. https://doi.org/10.1016/j.actamat.2008.03.022.

[276] D.G. Kim, Y.H. Jo, J. Yang, W.M. Choi, H.S. Kim, B.J. Lee, S.S. Sohn, S. Lee, Ultrastrong duplex high-entropy alloy with 2 GPa cryogenic strength enabled by an accelerated martensitic transformation, Scr. Mater. 171 (2019) 67–72. https://doi.org/10.1016/j.scriptamat.2019.06.026.

[277] J. Yoo, K. Choi, A. Zargaran, N.J. Kim, Effect of stacking faults on the ductility of Fe-18Mn-1.5Al-0.6C twinning-induced plasticity steel at low temperatures, Scr. Mater. 137 (2017) 18–21. https://doi.org/10.1016/j.scriptamat.2017.04.037.

[278] S. Huang, W. Li, S. Lu, F. Tian, J. Shen, E. Holmström, L. Vitos, Temperature dependent stacking fault energy of FeCrCoNiMn high entropy alloy, Scr. Mater. 108 (2015) 44–47. https://doi.org/10.1016/j.scriptamat.2015.05.041.

[279] S.F. Liu, Y. Wu, H.T. Wang, J.Y. He, J.B. Liu, C.X. Chen, X.J. Liu, H. Wang, Z.P. Lu, Stacking fault energy of face-centered-cubic high entropy alloys, Intermetallics. 93 (2018) 269–273. https://doi.org/10.1016/j.intermet.2017.10.004.

[280] N.L. Okamoto, S. Fujimoto, Y. Kambara, M. Kawamura, Z.M.T. Chen, H. Matsunoshita, K. Tanaka, H. Inui, E.P. George, Size effect, critical resolved shear stress, stacking fault energy, and solid solution strengthening in the CrMnFeCoNi high-entropy alloy, Sci. Rep. 6 (2016) 1–10. https://doi.org/10.1038/srep35863.

[281] Q. Ding, X. Fu, D. Chen, H. Bei, B. Gludovatz, J. Li, Z. Zhang, E.P. George, Q. Yu, T. Zhu, R.O. Ritchie, Real-time nanoscale observation of deformation mechanisms in CrCoNi-based medium- to high-entropy alloys at cryogenic temperatures, Mater. Today. 25 (2019) 21–27. https://doi.org/10.1016/j.mattod.2019.03.001.

[282] L. Tang, K. Yan, B. Cai, Y. Wang, B. Liu, S. Kabra, M.M. Attallah, Y. Liu,

Deformation mechanisms of FeCoCrNiMo0.2 high entropy alloy at 77 and 15 K, Scr. Mater. 178 (2020) 166–170. https://doi.org/10.1016/j.scriptamat.2019.11.026.

[283] J. Liu, D. Kaoumi, Use of in-situ TEM to characterize the deformation-induced martensitic transformation in 304 stainless steel at cryogenic temperature, Mater. Charact. 136 (2018) 331–336. https://doi.org/https://doi.org/10.1016/j.matchar.2017.12.005.

[284] J.G. Kim, J.W. Bae, J.M. Park, W. Woo, S. Harjo, K.-G. Chin, S. Lee, H.S. Kim, Synergetic strengthening of layered steel sheet investigated using an in situ neutron diffraction tensile test, Sci. Rep. 9 (2019) 6829. https://doi.org/10.1038/s41598-019-43369-2.

[285] J.S. Jeong, W. Woo, K.H. Oh, S.K. Kwon, Y.M. Koo, In situ neutron diffraction study of the microstructure and tensile deformation behavior in Al-added high manganese austenitic steels, Acta Mater. 60 (2012) 2290–2299. https://doi.org/https://doi.org/10.1016/j.actamat.2011.12.043.

[286] K.S. Raghavan, A.S. Sastri, M.J. Marcinkowski, Nature of the Work-hardening Behavior in Hadfields Manganese steel, Trans Met Soc AIME. 245 (1969) 1569–1575.

[287] H. Beladi, I.B. Timokhina, Y. Estrin, J. Kim, B.C. De Cooman, S.K. Kim, Orientation dependence of twinning and strain hardening behaviour of a high manganese twinning induced plasticity steel with polycrystalline structure, Acta Mater. 59 (2011) 7787–7799. https://doi.org/10.1016/j.actamat.2011.08.031.

[288] O. Kirichek, J.D. Timms, J.F. Kelleher, R.B.E.E. Down, C.D. Offer, S. Kabra, S.Y. Zhang, Sample environment for neutron scattering measurements of internal stresses in engineering materials in the temperature range of 6 K to 300 K, Rev. Sci. Instrum. 88 (2017) 25103. https://doi.org/10.1063/1.4974815.

[289] T. Ungár, A. Borbély, The effect of dislocation contrast on x-ray line broadening: A new approach to line profile analysis, Appl. Phys. Lett. 69 (1996) 3173–3175. https://doi.org/10.1063/1.117951.

[290] T. Ungár, S. Ott, P.G. Sanders, A. Borbély, J.R. Weertman, Dislocations, grain size and planar faults in nanostructured copper determined by high resolution X-ray diffraction and a new procedure of peak profile analysis, Acta Mater. 46 (1998) 3693–3699. https://doi.org/10.1016/S1359-6454(98)00001-9.

[291] R. Hielscher, C.B. Silbermann, E. Schmidl, J. Ihlemann, Denoising of crystal orientation maps, J. Appl. Crystallogr. 52 (2019) 984–996. https://doi.org/10.1107/S1600576719009075.

[292] Y.Q. Wang, S. Hossain, S. Kabra, S.Y. Zhang, D.J. Smith, C.E. Truman, Effect of boundary conditions on the evolution of lattice strains in a polycrystalline austenitic stainless steel, J. Mater. Sci. 52 (2017) 7929–7936. https://doi.org/10.1007/s10853-017-0997-6.

[293] A. Argon, Strengthening mechanisms in crystal plasticity, OUP Oxford, 2008.

[294] D. Balzar, Voigt-function model in diffraction line-broadening analysis, Microstruct. Anal. from Diffr. (1999) 44. https://doi.org/10.1.1.30.7311.

[295] V.I. Razumovskiy, C. Hahn, M. Lukas, L. Romaner, Ab initio study of elastic

and mechanical properties in FeCrMn alloys, Materials (Basel). 12 (2019) 1129. https://doi.org/10.3390/ma12071129.

[296] J.A. Rayne, B.S. Chandrasekhar, Elastic constants of iron from 4.2 to 300°K, Phys. Rev. 122 (1961) 1714–1716. https://doi.org/10.1103/PhysRev.122.1714.

[297] S.M. Foiles, Temperature dependence of grain boundary free energy and elastic constants, Scr. Mater. 62 (2010) 231–234. https://doi.org/10.1016/j.scriptamat.2009.11.003.

[298] G. Laplanche, M. Schneider, F. Scholz, J. Frenzel, G. Eggeler, J. Schreuer, Processing of a single-crystalline CrCoNi medium-entropy alloy and evolution of its thermal expansion and elastic stiffness coefficients with temperature, Scr. Mater. 177 (2020) 44–48. https://doi.org/10.1016/j.scriptamat.2019.09.020.

[299] T. Teramoto, K. Yamada, R. Ito, K. Tanaka, Monocrystalline elastic constants and their temperature dependences for equi-atomic Cr-Mn-Fe-Co-Ni high-entropy alloy with the face-centered cubic structure, J. Alloys Compd. 777 (2019) 1313–1318. https://doi.org/10.1016/j.jallcom.2018.11.052.

[300] I. Gutierrez-Urrutia, S. Zaefferer, D. Raabe, The effect of grain size and grain orientation on deformation twinning in a Fe–22wt.% Mn–0.6wt.% C TWIP steel, Mater. Sci. Eng. A. 527 (2010) 3552–3560. https://doi.org/https://doi.org/10.1016/j.msea.2010.02.041.

[301] D.R. Steinmetz, T. Jäpel, B. Wietbrock, P. Eisenlohr, I. Gutierrez-Urrutia, A. Saeed-Akbari, T. Hickel, F. Roters, D. Raabe, Revealing the strain-hardening behavior of twinning-induced plasticity steels: Theory, simulations, experiments, Acta Mater. 61 (2013) 494–510. https://doi.org/10.1016/j.actamat.2012.09.064.

[302] D. Hull, D.J. Bacon, Introduction to dislocations, Elsevier, 2011.

[303] M. Eskandari, A. Zarei-Hanzaki, M.A. Mohtadi-Bonab, Y. Onuki, R. Basu, A. Asghari, J.A. Szpunar, Grain-orientation-dependent of γ–ε–α′ transformation and twinning in a super-high-strength, high ductility austenitic Mn-steel, Mater. Sci. Eng. A. 674 (2016) 514–528. https://doi.org/10.1016/j.msea.2016.08.024.

[304] O. Bouaziz, N. Guelton, Modelling of TWIP effect on work-hardening, Mater. Sci. Eng. A. 319–321 (2001) 246–249. https://doi.org/10.1016/S0921-5093(00)02019-0.

[305] G. Dini, R. Ueji, A. Najafizadeh, S.M. Monir-Vaghefi, Flow stress analysis of TWIP steel via the XRD measurement of dislocation density, Mater. Sci. Eng. A. 527 (2010) 2759–2763. https://doi.org/10.1016/j.msea.2010.01.033.

[306] Z. Chen, Z. Sun, B. Panicaud, Investigation of ductile damage during surface mechanical attrition treatment for TWIP steels using a dislocation density based viscoplasticity and damage models, Mech. Mater. 129 (2019) 279–289. https://doi.org/10.1016/j.mechmat.2018.12.009.

[307] H. Zhi, C. Zhang, S. Antonov, H. Yu, T. Guo, Y. Su, Investigations of dislocation-type evolution and strain hardening during mechanical twinning in Fe-22Mn-0.6C twinning-induced plasticity steel, Acta Mater. 195 (2020) 371–382. https://doi.org/10.1016/j.actamat.2020.05.062.

[308] H. Conrad, G. Schoeck, Cottrell locking and the flow stress in iron, Acta Metall. 8 (1960) 791–796. https://doi.org/10.1016/0001-6160(60)90175-9.

[309] R.J. Arsenault, Solid solution strengthening and weakening of b.c.c. solid solutions, Acta Metall. 17 (1969) 1291–1297. https://doi.org/10.1016/0001-6160(69)90144-8.

[310] S. Allain, O. Bouaziz, J.P. Chateau, Thermally activated dislocation dynamics in austenitic FeMnC steels at low homologous temperature, Scr. Mater. 62 (2010) 500–503. https://doi.org/10.1016/j.scriptamat.2009.12.026.

[311] U.F. Kocks, Realistic constitutive relations for metal plasticity, Mater. Sci. Eng. A. 317 (2001) 181–187. https://doi.org/https://doi.org/10.1016/S0921-5093(01)01174-1.

[312] N. Tsuchida, Application of the Kocks–Mecking model to tensile deformation of an austenitic 25Cr–19Ni steel, Acta Mater. 49 (2001) 3029–3038. https://doi.org/10.1016/S1359-6454(01)00197-5.

[313] Y.P. Varshni, Temperature dependence of the elastic constants, Phys. Rev. B. 2 (1970) 3952–3958. https://doi.org/10.1103/PhysRevB.2.3952.

[314] P.S. Follansbee, U.F. Kocks, A constitutive description of the deformation of copper based on the use of the mechanical threshold stress as an internal state variable, Acta Metall. 36 (1988) 81–93. https://doi.org/https://doi.org/10.1016/0001-6160(88)90030-2.

[315] R.S. Ganji, P. Sai Karthik, K. Bhanu Sankara Rao, K. V. Rajulapati, Strengthening mechanisms in equiatomic ultrafine grained AlCoCrCuFeNi high-entropy alloy studied by micro- and nanoindentation methods, Acta Mater. 125 (2017) 58–68. https://doi.org/10.1016/j.actamat.2016.11.046.

[316] I. Gutierrez-Urrutia, S. Zaefferer, D. Raabe, The effect of grain size and grain orientation on deformation twinning in a Fe-22wt.% Mn-0.6wt.% C TWIP steel, Mater. Sci. Eng. A. 527 (2010) 3552–3560. https://doi.org/10.1016/j.msea.2010.02.041.

[317] I. Gutierrez-Urrutia, D. Raabe, Study of Deformation Twinning and Planar Slip in a TWIP Steel by Electron Channeling Contrast Imaging in a SEM, Mater. Sci. Forum. 702–703 (2011) 523–529. https://doi.org/10.4028/www.scientific.net/msf.702-703.523.

[318] J. Gil Sevillano, F. De Las Cuevas, Internal stresses and the mechanism of work hardening in twinning-induced plasticity steels, Scr. Mater. 66 (2012) 978–981. https://doi.org/10.1016/j.scriptamat.2012.02.019.

[319] I. Shakhova, V. Dudko, A. Belyakov, K. Tsuzaki, R. Kaibyshev, Effect of large strain cold rolling and subsequent annealing on microstructure and mechanical properties of an austenitic stainless steel, Mater. Sci. Eng. A. 545 (2012) 176–186. https://doi.org/10.1016/j.msea.2012.02.101.

[320] R.L. Fullman, Measurement of Particle Sizes in Opaque Bodies, JOM. 5 (1953) 447–452. https://doi.org/10.1007/bf03398971.

[321] Z.C. Luo, M.X. Huang, Revisit the role of deformation twins on the work-hardening behaviour of twinning-induced plasticity steels, Scr. Mater. 142 (2018) 28–31. https://doi.org/10.1016/j.scriptamat.2017.08.017.

[322] Z.-H. Jin, P. Gumbsch, E. Ma, K. Albe, K. Lu, H. Hahn, H. Gleiter, The interaction mechanism of screw dislocations with coherent twin boundaries in

different face-centred cubic metals, Scr. Mater. 54 (2006) 1163–1168. https://doi.org/https://doi.org/10.1016/j.scriptamat.2005.11.072.

[323] T.S. Byun, N. Hashimoto, K. Farrell, Temperature dependence of strain hardening and plastic instability behaviors in austenitic stainless steels, Acta Mater. 52 (2004) 3889–3899. https://doi.org/10.1016/j.actamat.2004.05.003.

[324] J. Chen, J.J. Wang, G. Yuan, C.M. Liu, Twin boundary bending during tensile deformation and its temperature dependence, Mater. Sci. Eng. A. 759 (2019) 47–54. https://doi.org/10.1016/j.msea.2019.04.097.

[325] Y.G. Kim, J.M. Han, J.S. Lee, Composition and temperature dependence of tensile properties of austenitic FeMnAlC alloys, Mater. Sci. Eng. A. 114 (1989) 51–59. https://doi.org/10.1016/0921-5093(89)90844-7.

[326] Y.F. Shen, N. Jia, R.D.K. Misra, L. Zuo, Softening behavior by excessive twinning and adiabatic heating at high strain rate in a Fe-20Mn-0.6C TWIP steel, Acta Mater. 103 (2016) 229–242. https://doi.org/10.1016/j.actamat.2015.09.061.

[327] L. Tang, L. Wang, M. Wang, H. Liu, S. Kabra, Y. Chiu, B. Cai, Synergistic deformation pathways in a TWIP steel at cryogenic temperatures: In situ neutron diffraction, Acta Mater. 200 (2020) 943–958. https://doi.org/10.1016/j.actamat.2020.09.075.

[328] E. El-Danaf, S.R. Kalidindi, R.D. Doherty, Influence of grain size and stacking fault energy on deformation twinning in fcc metals, Metall. Mater. Trans. A. 30 (1999) 1223–1999. https://doi.org/10.1007/s11661-001-0109-7.

[329] S. Lee, J. Kim, S.J. Lee, B.C. De Cooman, Effect of Cu addition on the mechanical behavior of austenitic twinning-induced plasticity steel, Scr. Mater. 65 (2011) 1073–1076. https://doi.org/10.1016/J.SCRIPTAMAT.2011.09.019.

[330] X. Peng, D. Zhu, Z. Hu, W. Yi, H. Liu, M. Wang, Stacking fault energy and tensile deformation behavior of high-carbon twinning-induced plasticity steels: Effect of Cu addition, Mater. Des. 45 (2013) 518–523. https://doi.org/10.1016/J.MATDES.2012.09.014.

[331] A. Saeed-Akbari, A. Schwedt, W. Bleck, Low stacking fault energy steels in the context of manganese-rich iron-based alloys, Scr. Mater. 66 (2012) 1024–1029. https://doi.org/10.1016/j.scriptamat.2011.12.041.

[332] X. Rao, Y. Wu, X. Pei, Y. Jing, L. Luo, Y. Liu, J. Lu, Influence of rolling temperature on microstructural evolution and mechanical behavior of AZ31 alloy with accumulative roll bonding, Mater. Sci. Eng. A. 754 (2019) 112–120. https://doi.org/10.1016/j.msea.2019.03.047.

[333] S.J. Kim, C.G. Lee, T.H. Lee, C.S. Oh, Effect of Cu, Cr and Ni on mechanical properties of 0.15 wt.% C TRIP-aided cold rolled steels, Scr. Mater. 48 (2003) 539–544. https://doi.org/10.1016/S1359-6462(02)00477-3.

[334] A. Dumay, J.-P.P. Chateau, S. Allain, S. Migot, O. Bouaziz, Influence of addition elements on the stacking-fault energy and mechanical properties of an austenitic Fe-Mn-C steel, Mater. Sci. Eng. A. 483–484 (2008) 184–187. https://doi.org/10.1016/j.msea.2006.12.170.

[335] B.M. Gonzalez, C.S.B. Castro, V.T.L. Buono, J.M.C. Vilela, M.S. Andrade, J.M.D. Moraes, M.J. Mantel, The influence of copper addition on the formability

of AISI 304 stainless steel, Mater. Sci. Eng. A. 343 (2003) 51–56. https://doi.org/10.1016/S0921-5093(02)00362-3.

[336] G.B. Olson, M. Cohen, Stress-assisted isothermal martensitic transformation: Application to TRIP steels, Metall. Trans. A. 13 (1982) 1907–1914. https://doi.org/10.1007/BF02645934.

[337] Y.K. Lee, C.S. Choi, Driving force for γ → ε martensitic transformation and stacking fault energy of γ in Fe-Mn binary system, Metall. Mater. Trans. A Phys. Metall. Mater. Sci. 31 (2000) 355–360. https://doi.org/10.1007/s11661-000-0271-3.

[338] S. Allain, J.P. Chateau, O. Bouaziz, S. Migot, N. Guelton, Correlations between the calculated stacking fault energy and the plasticity mechanisms in Fe-Mn-C alloys, Mater. Sci. Eng. A. 387–389 (2004) 158–162. https://doi.org/10.1016/j.msea.2004.01.059.

[339] P.H. Adler, G.B. Olson, W.S. Owen, Strain Hardening of Hadfield Manganese Steel, Metall. Mater. Trans. A. 17 (1986) 1725–1737. https://doi.org/10.1007/BF02817271.

[340] M. Hillert, M. Jarl, A model for alloying in ferromagnetic metals, Calphad. 2 (1978) 227–238. https://doi.org/10.1016/0364-5916(78)90011-1.

[341] W. Huang, An assessment of the Fe-Mn system, Calphad. 13 (1989) 243–252. https://doi.org/10.1016/0364-5916(89)90004-7.

[342] G. Inden, The role of magnetism in the calculation of phase diagrams, Phys. B+C. 103 (1981) 82–100. https://doi.org/10.1016/0378-4363(81)91004-4.

[343] K. Ishida, Direct estimation of stacking fault energy by thermodynamic analysis, Phys. Status Solidi. 36 (1976) 717–728. https://doi.org/10.1002/pssa.2210360233.

[344] W.S. Yang, C.M. Wan, The influence of aluminium content to the stacking fault energy in Fe-Mn-Al-C alloy system, J. Mater. Sci. 25 (1990) 1821–1823. https://doi.org/10.1007/BF01045392.

[345] I.A. Yakubtsov, A. Ariapour, D.D. Perovic, Effect of nitrogen on stacking fault energy of f.c.c. iron-based alloys, Acta Mater. 47 (1999) 1271–1279. https://doi.org/10.1016/S1359-6454(98)00419-4.

[346] Z. Wang, A.D. Stoica, D. Ma, A.M. Beese, Diffraction and single-crystal elastic constants of Inconel 625 at room and elevated temperatures determined by neutron diffraction, Mater. Sci. Eng. A. 674 (2016). https://doi.org/http://dx.doi.org/10.1016/j.msea.2016.08.010.

[347] C. Lee, G. Kim, Y. Chou, B.L. Musicó, M.C. Gao, K. An, G. Song, Y.C. Chou, V. Keppens, W. Chen, P.K. Liaw, Temperature dependence of elastic and plastic deformation behavior of a refractory high-entropy alloy, Sci. Adv. 6 (2020) eaaz4748. https://doi.org/10.1126/sciadv.aaz4748.

[348] M. Naeem, H. He, F. Zhang, H. Huang, S. Harjo, T. Kawasaki, B. Wang, S. Lan, Z. Wu, F. Wang, Y. Wu, Z. Lu, Z. Zhang, C.T. Liu, X.L. Wang, Cooperative deformation in high-entropy alloys at ultralow temperatures, Sci. Adv. 6 (2020). https://doi.org/10.1126/sciadv.aax4002.

[349] T. Ungár, I. Dragomir, Á. Révész, A. Borbély, The contrast factors of

dislocations in cubic crystals: the dislocation model of strain anisotropy in practice, J. Appl. Crystallogr. 32 (1999) 992–1002. https://doi.org/10.1107/S0021889899009334.

[350] E.I. Galindo-Nava, P.E.J. Rivera-Díaz-del-Castillo, Modelling plastic deformation in BCC metals: Dynamic recovery and cell formation effects, Mater. Sci. Eng. A. 558 (2012) 641–648. https://doi.org/10.1016/J.MSEA.2012.08.068.

[351] J. Yoo, K. Choi, A. Zargaran, N.J. Kim, Effect of stacking faults on the ductility of Fe-18Mn-1.5Al-0.6C twinning-induced plasticity steel at low temperatures, Scr. Mater. 137 (2017) 18–21. https://doi.org/10.1016/J.SCRIPTAMAT.2017.04.037.

[352] X.L. Wu, Y.T. Zhu, Y.G. Wei, Q. Wei, Strong Strain Hardening in Nanocrystalline Nickel, Phys. Rev. Lett. 103 (2009) 1–4. https://doi.org/10.1103/PhysRevLett.103.205504.

[353] V. Yamakov, D. Wolf, S.R. Phillpot, A.K. Mukherjee, H. Gleiter, Deformation-mechanism map for nanocrystalline metals by molecular-dynamics simulation, Nat. Mater. 2003 31. 3 (2003) 43–47. https://doi.org/10.1038/nmat1035.

[354] L. Dupuy, M.C. Fivel, A study of dislocation junctions in FCC metals by an orientation dependent line tension model, Acta Mater. 50 (2002) 4873–4885. https://doi.org/10.1016/S1359-6454(02)00356-7.

[355] J.W. Brooks, M.H. Loretto, R.E. Smallman, Direct observations of martensite nuclei in stainless steel, Acta Metall. 27 (1979) 1839–1847. https://doi.org/10.1016/0001-6160(79)90074-9.

[356] M. Wang, Z. Li, D. Raabe, In-situ SEM observation of phase transformation and twinning mechanisms in an interstitial high-entropy alloy, Acta Mater. 147 (2018) 236–246. https://doi.org/10.1016/j.actamat.2018.01.036.

[357] W.S. Choi, B.C. De Cooman, S. Sandlöbes, D. Raabe, Size and orientation effects in partial dislocation-mediated deformation of twinning-induced plasticity steel micro-pillars, Acta Mater. 98 (2015) 391–404. https://doi.org/10.1016/J.ACTAMAT.2015.06.065.

[358] B. Chen, L. Zhu, Y. Xin, J. Lei, Grain Rotation in Plastic Deformation, Quantum Beam Sci. 3 (2019) 17. https://doi.org/10.3390/qubs3030017.

[359] R. Xiong, H. Peng, T. Zhang, J.W. Bae, H.S. Kim, Y. Wen, Superior strain-hardening by deformation-induced nano-HCP martensite in Fe–Mn–Si–C high-manganese steel, Mater. Sci. Eng. A. 824 (2021) 141864. https://doi.org/10.1016/J.MSEA.2021.141864.

[360] S.L. Wong, M. Madivala, U. Prahl, F. Roters, D. Raabe, A crystal plasticity model for twinning- and transformation-induced plasticity, Acta Mater. 118 (2016) 140–151. https://doi.org/10.1016/j.actamat.2016.07.032.

[361] L. Zhu, H. Kou, J. Lu, On the role of hierarchical twins for achieving maximum yield strength in nanotwinned metals, Appl. Phys. Lett. 101 (2012) 081906. https://doi.org/10.1063/1.4747333.

[362] O. Bouaziz, S. Allain, C.P. Scott, P. Cugy, D. Barbier, High manganese austenitic twinning induced plasticity steels: A review of the microstructure properties relationships, Curr. Opin. Solid State Mater. Sci. 15 (2011) 141–168.

https://doi.org/10.1016/j.cossms.2011.04.002.

[363] Y. Ma, F. Yuan, M. Yang, P. Jiang, E. Ma, X. Wu, Dynamic shear deformation of a CrCoNi medium-entropy alloy with heterogeneous grain structures, Acta Mater. 148 (2018) 407–418. https://doi.org/10.1016/j.actamat.2018.02.016.

[364] K.Y. Tsai, M.H. Tsai, J.W. Yeh, Sluggish diffusion in Co-Cr-Fe-Mn-Ni high-entropy alloys, Acta Mater. 61 (2013) 4887–4897. https://doi.org/10.1016/j.actamat.2013.04.058.

[365] Z.P. Lu, H. Wang, M.W. Chen, I. Baker, J.W. Yeh, C.T. Liu, T.G. Nieh, An assessment on the future development of high-entropy alloys: Summary from a recent workshop, Intermetallics. 66 (2015) 67–76. https://doi.org/10.1016/j.intermet.2015.06.021.

[366] B. Cantor, I.T.H.H. Chang, P. Knight, A.J.B.B. Vincent, Microstructural development in equiatomic multicomponent alloys, Mater. Sci. Eng. A. 375–377 (2004) 213–218. https://doi.org/https://doi.org/10.1016/j.msea.2003.10.257.

[367] K. Liu, M. Komarasamy, B. Gwalani, S. Shukla, R.S. Mishra, Fatigue behavior of ultrafine grained triplex Al0.3CoCrFeNi high entropy alloy, Scr. Mater. 158 (2019) 116–120. https://doi.org/10.1016/J.SCRIPTAMAT.2018.08.048.

[368] Z. Tang, T. Yuan, C.W. Tsai, J.W. Yeh, C.D. Lundin, P.K. Liaw, Fatigue behavior of a wrought Al0.5CoCrCuFeNi two-phase high-entropy alloy, Acta Mater. 99 (2015) 247–258. https://doi.org/10.1016/j.actamat.2015.07.004.

[369] M. Bönisch, Y. Wu, H. Sehitoglu, Hardening by slip-twin and twin-twin interactions in FeMnNiCoCr, Acta Mater. 153 (2018) 391–403. https://doi.org/10.1016/j.actamat.2018.04.054.

[370] D. Wei, X. Li, W. Heng, Y. Koizumi, F. He, W.-M. Choi, B.-J. Lee, H.S. Kim, H. Kato, A. Chiba, Novel Co-rich high entropy alloys with superior tensile properties, Mater. Res. Lett. 7 (2018) 82–88. https://doi.org/10.1080/21663831.2018.1553803.

[371] B. Gwalani, S. Gorsse, D. Choudhuri, Y. Zheng, R.S. Mishra, R. Banerjee, Tensile yield strength of a single bulk Al0.3CoCrFeNi high entropy alloy can be tuned from 160 MPa to 1800 MPa, Scr. Mater. 162 (2019) 18–23. https://doi.org/10.1016/J.SCRIPTAMAT.2018.10.023.

[372] Q. Lin, J. Liu, X. An, H. Wang, Y. Zhang, X. Liao, Cryogenic-deformation-induced phase transformation in an FeCoCrNi high-entropy alloy, Mater. Res. Lett. 6 (2018) 236–243. https://doi.org/10.1080/21663831.2018.1434250.

[373] J. Lu, L. Hultman, E. Holmström, K.H. Antonsson, M. Grehk, W. Li, L. Vitos, A. Golpayegani, Stacking fault energies in austenitic stainless steels, Acta Mater. 111 (2016) 39–46. https://doi.org/10.1016/j.actamat.2016.03.042.

[374] F. Tian, L.K. Varga, N. Chen, L. Delczeg, L. Vitos, Ab initio investigation of high-entropy alloys of 3 d elements, Phys. Rev. B. 87 (2013) 75144. https://doi.org/10.1103/PhysRevB.87.075144.

[375] Z.F. He, N. Jia, D. Ma, H.L. Yan, Z.M. Li, D. Raabe, Joint contribution of transformation and twinning to the high strength-ductility combination of a FeMnCoCr high entropy alloy at cryogenic temperatures, Mater. Sci. Eng. A. 759 (2019) 437–447. https://doi.org/10.1016/j.msea.2019.05.057.

[376] K. Yan, K.-D.D. Liss, I.B. Timokhina, E. V. Pereloma, In Situ Synchrotron X-ray Diffraction Studies of the Effect of Microstructure on Tensile Behavior and Retained Austenite Stability of Thermo-mechanically Processed Transformation Induced Plasticity Steel, Mater. Sci. Eng. A. 662 (2016) 185–197. https://doi.org/10.1016/j.msea.2016.03.048.

[377] F. Sánchez-Bajo, F.L. Cumbrera, The use of the pseudo-voigt function in the variance method of X-ray line-broadening analysis. Erratum, J. Appl. Crystallogr. 30 (1997) 550. https://doi.org/10.1107/S0021889897098956.

[378] S. Kibey, J.B. Liu, D.D. Johnson, H. Sehitoglu, Predicting twinning stress in fcc metals: Linking twin-energy pathways to twin nucleation, Acta Mater. 55 (2007) 6843–6851. https://doi.org/10.1016/j.actamat.2007.08.042.

[379] B.E. Warren, X-ray Diffraction, Courier Corporation, 1990.

[380] D. Balzar, H. Ledbetter, Voigt-function modeling in Fourier analysis of size- and strain-broadened X-ray diffraction peaks, J. Appl. Crystallogr. 26 (1993) 97–103. https://doi.org/10.1107/S0021889892008987.

[381] M. Jo, Y.M. Koo, B.-J. Lee, B. Johansson, L. Vitos, S.K. Kwon, Theory for plasticity of face-centered cubic metals, Proc. Natl. Acad. Sci. 111 (2014) 6560–6565. https://doi.org/10.1073/pnas.1400786111.

[382] Y.H. Jo, W.M. Choi, D.G. Kim, A. Zargaran, S.S. Sohn, H.S. Kim, B.J. Lee, N.J. Kim, S. Lee, FCC to BCC transformation-induced plasticity based on thermodynamic phase stability in novel V10Cr10Fe45CoxNi35−x medium-entropy alloys, Sci. Rep. 9 (2019) 2948. https://doi.org/10.1038/s41598-019-39570-y.

[383] A. Rohatgi, K.S. Vecchio, G.T. Gray, The influence of stacking fault energy on the mechanical behavior of Cu and Cu-Al alloys: Deformation twinning, work hardening, and dynamic recovery, Metall. Mater. Trans. A. 32 (2001) 135–145. https://doi.org/10.1007/s11661-001-0109-7.

[384] C. Herrera, D. Ponge, D. Raabe, Design of a novel Mn-based 1GPa duplex stainless TRIP steel with 60% ductility by a reduction of austenite stability, Acta Mater. 59 (2011) 4653–4664. https://doi.org/https://doi.org/10.1016/j.actamat.2011.04.011.

[385] S. Martin, C. Ullrich, D. Rafaja, Deformation of Austenitic CrMnNi TRIP/TWIP Steels: Nature and Role of the ε−martensite, Mater. Today Proc. 2 (2015) S643–S646. https://doi.org/10.1016/J.MATPR.2015.07.366.

[386] G. Sha, N. Liang, J. Liu, X. Gao, Y. Lu, B. Zhang, G. Wu, Y. Zhao, Microstructural origins of high strength and high ductility in an AlCoCrFeNi2.1 eutectic high-entropy alloy, Acta Mater. 141 (2017) 59–66. https://doi.org/10.1016/j.actamat.2017.07.041.

[387] B. Yin, F. Maresca, W.A. Curtin, Vanadium is an optimal element for strengthening in both fcc and bcc high-entropy alloys, Acta Mater. 188 (2020) 486–491. https://doi.org/10.1016/j.actamat.2020.01.062.

[388] M. Schneider, G. Laplanche, Effects of temperature on mechanical properties and deformation mechanisms of the equiatomic CrFeNi medium-entropy alloy, Acta Mater. 204 (2020) 116470. https://doi.org/10.1016/j.actamat.2020.11.012.

[389] S.S. Sohn, A. Kwiatkowski da Silva, Y. Ikeda, F. Körmann, W. Lu, W.S. Choi, B. Gault, D. Ponge, J. Neugebauer, D. Raabe, Ultrastrong Medium-Entropy Single-Phase Alloys Designed via Severe Lattice Distortion, Adv. Mater. 31 (2019) 1–8. https://doi.org/10.1002/adma.201807142.

[390] B. Gludovatz, A. Hohenwarter, K.V.S.S. Thurston, H. Bei, Z. Wu, E.P. George, R.O. Ritchie, Exceptional damage-tolerance of a medium-entropy alloy CrCoNi at cryogenic temperatures, Nat. Commun. 7 (2016) 10602. https://doi.org/10.1038/ncomms10602.

[391] X. Chen, Q. Wang, Z. Cheng, M. Zhu, H. Zhou, P. Jiang, L. Zhou, Q. Xue, F. Yuan, J. Zhu, X. Wu, E. Ma, Direct observation of chemical short-range order in a medium-entropy alloy, Nature. 592 (2021) 712–716. https://doi.org/10.1038/s41586-021-03428-z.

[392] R. Zhang, S. Zhao, J. Ding, Y. Chong, T. Jia, C. Ophus, M. Asta, R.O. Ritchie, A.M. Minor, Short-range order and its impact on the CrCoNi medium-entropy alloy, Nature. 581 (2020) 283–287. https://doi.org/10.1038/s41586-020-2275-z.

[393] Z. Wu, Y. Gao, H. Bei, Thermal activation mechanisms and Labusch-type strengthening analysis for a family of high-entropy and equiatomic solid-solution alloys, Acta Mater. 120 (2016) 108–119. https://doi.org/10.1016/j.actamat.2016.08.047.

[394] B. Yin, S. Yoshida, N. Tsuji, W.A. Curtin, Yield strength and misfit volumes of NiCoCr and implications for short-range-order, Nat. Commun. 11 (2020) 2507. https://doi.org/10.1038/s41467-020-16083-1.

[395] A. Fu, B. Liu, W. Lu, B. Liu, J. Li, Q. Fang, Z. Li, Y. Liu, A novel supersaturated medium entropy alloy with superior tensile properties and corrosion resistance, Scr. Mater. 186 (2020) 381–386. https://doi.org/10.1016/j.scriptamat.2020.05.023.

[396] G. Bonny, D. Terentyev, R.C. Pasianot, S. Poncé, A. Bakaev, Interatomic potential to study plasticity in stainless steels: The FeNiCr model alloy, Model. Simul. Mater. Sci. Eng. 19 (2011). https://doi.org/10.1088/0965-0393/19/8/085008.

[397] G. Kresse, J. Furthmüller, Efficient iterative schemes for ab initio total-energy calculations using a plane-wave basis set, Phys. Rev. B. 54 (1996) 11169–11186. https://doi.org/10.1103/PhysRevB.54.11169.

[398] G. Kresse, J. Furthmüller, Efficiency of ab-initio total energy calculations for metals and semiconductors using a plane-wave basis set, Comput. Mater. Sci. 6 (1996) 15–50. https://doi.org/10.1016/0927-0256(96)00008-0.

[399] J.P. Perdew, K. Burke, M. Ernzerhof, Generalized gradient approximation made simple, Phys. Rev. Lett. 77 (1996) 3865–3868. https://doi.org/10.1103/PhysRevLett.77.3865.

[400] H.J. Monkhorst, J.D. Pack, Special points for Brillouin-zone integrations, Phys. Rev. B. 13 (1976) 5188–5192. https://doi.org/10.1103/PhysRevB.13.5188.

[401] D. Nguyen-Manh, D.G. Pettifor, G. Shao, A.P. Miodownik, A. Pasturel, Metastability of the ω-phase in transition-metal aluminides: First-principles structural predictions, Philos. Mag. A Phys. Condens. Matter, Struct. Defects Mech. Prop. 74 (1996) 1385–1397.

https://doi.org/10.1080/01418619608240730.

[402] D. Nguyen-Manh, D.G. Pettifor, Electronic structure, phase stability and elastic moduli of AB transition metal aluminides, Intermetallics. 7 (1999) 1095–1106. https://doi.org/10.1016/S0966-9795(99)00040-0.

[403] D. Nguyen-Manh, D.G. Pettifor, D. Kim, M.H. Loretto, Origin of O-phase and pseudo-twinning in Ti-Al-Nb alloys: a first-principles study, Gamma Titan. Alum. Kim, Y.-W., Dimiduk, DM, Loretto, MH, Eds. (1999) 175–182.

[404] D. Nguyen-Manh, V. Vitek, A.P. Horsfield, Environmental dependence of bonding: A challenge for modelling of intermetallics and fusion materials, Prog. Mater. Sci. 52 (2007) 255–298. https://doi.org/10.1016/j.pmatsci.2006.10.010.

[405] M. Muzyk, D. Nguyen-Manh, K.J. Kurzydłowski, N.L. Baluc, S.L. Dudarev, Phase stability, point defects, and elastic properties of W-V and W-Ta alloys, Phys. Rev. B - Condens. Matter Mater. Phys. 84 (2011) 104115. https://doi.org/10.1103/PhysRevB.84.104115.

[406] J. Wróbel, L.G. Hector, W. Wolf, S.L. Shang, Z.K. Liu, K.J. Kurzydłowski, Thermodynamic and mechanical properties of lanthanum-magnesium phases from density functional theory, J. Alloys Compd. 512 (2012) 296–310. https://doi.org/10.1016/j.jallcom.2011.09.085.

[407] L. Vitos, P.A. Korzhavyi, B. Johansson, Elastic Property Maps of Austenitic Stainless Steels, Phys. Rev. Lett. 88 (2002) 4. https://doi.org/10.1103/PhysRevLett.88.155501.

[408] N. Al-Zoubi, Elastic parameters of paramagnetic fe–20cr–20ni-based alloys: A first-principles study, Metals (Basel). 9 (2019) 792. https://doi.org/10.3390/met9070792.

[409] J.S. Wróbel, D. Nguyen-Manh, M.Y. Lavrentiev, M. Muzyk, S.L. Dudarev, Phase stability of ternary fcc and bcc Fe-Cr-Ni alloys, Phys. Rev. B - Condens. Matter Mater. Phys. 91 (2015) 024108. https://doi.org/10.1103/PhysRevB.91.024108.

[410] J.M. Cowley, An Approximate Theory of Order in Alloys, Phys. Rev. 77 (1950) 669–675. https://doi.org/10.1103/PhysRev.77.669.

[411] A. Fernández-Caballero, J.S. Wróbel, P.M. Mummery, D. Nguyen-Manh, Short-Range Order in High Entropy Alloys: Theoretical Formulation and Application to Mo-Nb-Ta-V-W System, J. Phase Equilibria Diffus. 38 (2017) 391–403. https://doi.org/10.1007/s11669-017-0582-3.

[412] A. Fernández-Caballero, M. Fedorov, J. Wróbel, P. Mummery, D. Nguyen-Manh, Configurational Entropy in Multicomponent Alloys: Matrix Formulation from Ab Initio Based Hamiltonian and Application to the FCC Cr-Fe-Mn-Ni System, Entropy. 21 (2019) 68. https://doi.org/10.3390/e21010068.

[413] M. Fedorov, J.S. Wróbel, A. Fernández-Caballero, K.J. Kurzydłowski, D. Nguyen-Manh, Phase stability and magnetic properties in fcc Fe-Cr-Mn-Ni alloys from first-principles modeling, Phys. Rev. B. 101 (2020) 174416. https://doi.org/10.1103/PhysRevB.101.174416.

[414] D. Sobieraj, J.S. Wróbel, T. Rygier, K.J. Kurzydłowski, O. El Atwani, A. Devaraj, E. Martinez Saez, D. Nguyen-Manh, Chemical short-range order in

derivative Cr-Ta-Ti-V-W high entropy alloys from the first-principles thermodynamic study, Phys. Chem. Chem. Phys. 22 (2020) 23929–23951. https://doi.org/10.1039/d0cp03764h.

[415] M. Łopuszyński, J.A. Majewski, Ab initio calculations of third-order elastic constants and related properties for selected semiconductors, Phys. Rev. B - Condens. Matter Mater. Phys. 76 (2007) 045202. https://doi.org/10.1103/PhysRevB.76.045202.

[416] D. Holec, M. Friák, J. Neugebauer, P.H. Mayrhofer, Trends in the elastic response of binary early transition metal nitrides, Phys. Rev. B. 85 (2012) 64101. https://doi.org/10.1103/PhysRevB.85.064101.

[417] M.A. Caro, S. Schulz, E.P. O'Reilly, Comparison of stress and total energy methods for calculation of elastic properties of semiconductors, J. Phys. Condens. Matter. 25 (2013) 025803. https://doi.org/10.1088/0953-8984/25/2/025803.

[418] J.S. Wróbel, M.R. Zemła, D. Nguyen-Manh, P. Olsson, L. Messina, C. Domain, T. Wejrzanowski, S.L. Dudarev, Elastic dipole tensors and relaxation volumes of point defects in concentrated random magnetic Fe-Cr alloys, Comput. Mater. Sci. 194 (2021) 110435. https://doi.org/https://doi.org/10.1016/j.commatsci.2021.110435.

[419] R. Hill, The elastic behaviour of a crystalline aggregate, Proc. Phys. Soc. Sect. A. 65 (1952) 349–354. https://doi.org/10.1088/0370-1298/65/5/307.

[420] M.J. Hÿtch, E. Snoeck, R. Kilaas, Quantitative measurement of displacement and strain fields from HREM micrographs, Ultramicroscopy. 74 (1998) 131–146. https://doi.org/10.1016/S0304-3991(98)00035-7.

[421] G. Dirras, L. Lilensten, P. Djemia, M. Laurent-Brocq, D. Tingaud, J.P. Couzinié, L. Perrière, T. Chauveau, I. Guillot, Elastic and plastic properties of as-cast equimolar TiHfZrTaNb high-entropy alloy, Mater. Sci. Eng. A. 654 (2016) 30–38. https://doi.org/10.1016/j.msea.2015.12.017.

[422] S. Sheikh, S. Shafeie, Q. Hu, J. Ahlström, C. Persson, J. Veselý, J. Zýka, U. Klement, S. Guo, Alloy design for intrinsically ductile refractory high-entropy alloys, J. Appl. Phys. 120 (2016). https://doi.org/10.1063/1.4966659.

[423] J.Y. He, W.H. Liu, H. Wang, Y. Wu, X.J. Liu, T.G. Nieh, Z.P. Lu, Effects of Al addition on structural evolution and tensile properties of the FeCoNiCrMn high-entropy alloy system, Acta Mater. 62 (2014) 105–113. https://doi.org/10.1016/j.actamat.2013.09.037.

[424] J. Liu, Y. Jin, X. Fang, C. Chen, Q. Feng, X. Liu, Y. Chen, T. Suo, F. Zhao, T. Huang, H. Wang, X. Wang, Y. Fang, Y. Wei, L. Meng, J. Lu, W. Yang, Dislocation Strengthening without Ductility Trade-off in Metastable Austenitic Steels, Sci. Rep. 6 (2016) 1–9. https://doi.org/10.1038/srep35345.

[425] H. Huang, Y. Wu, J. He, H. Wang, X. Liu, K. An, W. Wu, Z. Lu, Phase-Transformation Ductilization of Brittle High-Entropy Alloys via Metastability Engineering, Adv. Mater. 29 (2017) 1–7. https://doi.org/10.1002/adma.201701678.

[426] L. Lilensten, J.P. Couzinié, J. Bourgon, L. Perrière, G. Dirras, F. Prima, I. Guillot, Design and tensile properties of a bcc Ti-rich high-entropy alloy with transformation-induced plasticity, Mater. Res. Lett. 5 (2017) 110–116.

https://doi.org/10.1080/21663831.2016.1221861.

[427] J. Sas, K.P. Weiss, A. Jung, The Mechanical and material properties of 316LN austenitic stainless steel for the fusion application in cryogenic temperatures, IOP Conf. Ser. Mater. Sci. Eng. 102 (2015). https://doi.org/10.1088/1757-899X/102/1/012003.

[428] L. Vitos, J.O. Nilsson, B. Johansson, Alloying effects on the stacking fault energy in austenitic stainless steels from first-principles theory, Acta Mater. 54 (2006) 3821–3826. https://doi.org/10.1016/j.actamat.2006.04.013.

[429] C.B. Carter, S.M. Holmes, The stacking-fault energy of nickel, Philos. Mag. A J. Theor. Exp. Appl. Phys. 35 (1977) 1161–1172. https://doi.org/10.1080/14786437708232942.

[430] W.F. Hosford, Mechanical Behavior of Materials, Cambridge University Press, Cambridge, 2005. https://doi.org/DOI: 10.1017/CBO9780511810930.

[431] M. Zhang, L.G. Hector, Y. Guo, M. Liu, L. Qi, First-principles search for alloying elements that increase corrosion resistance of Mg with second-phase particles of transition metal impurities, Comput. Mater. Sci. 165 (2019) 154–166. https://doi.org/10.1016/j.commatsci.2019.04.018.

[432] R. Zhang, S. Zhao, C. Ophus, Y. Deng, S.J. Vachhani, B. Ozdol, R. Traylor, K.C. Bustillo, J.W. Morris, D.C. Chrzan, Direct imaging of short-range order and its impact on deformation in Ti-6Al, Sci. Adv. 5 (2019) eaax2799.

[433] O. Bouaziz, S. Allain, C. Scott, Effect of grain and twin boundaries on the hardening mechanisms of twinning-induced plasticity steels, Scr. Mater. 58 (2008) 484–487. https://doi.org/10.1016/j.scriptamat.2007.10.050.

[434] R. Madec, B. Devincre, L.P. Kubin, From Dislocation Junctions to Forest Hardening, Phys. Rev. Lett. 89 (2002) 1–4. https://doi.org/10.1103/PhysRevLett.89.255508.

[435] B. Yin, W.A. Curtin, First-principles-based prediction of yield strength in the RhIrPdPtNiCu high-entropy alloy, Npj Comput. Mater. 5 (2019) 1–7. https://doi.org/10.1038/s41524-019-0151-x.

[436] G.P.M. Leyson, L.G. Hector, W.A. Curtin, Solute strengthening from first principles and application to aluminum alloys, Acta Mater. 60 (2012) 3873–3884. https://doi.org/10.1016/j.actamat.2012.03.037.

[437] Y. Wang, Y. Zhang, A. Godfrey, J. Kang, Y. Peng, T. Wang, N. Hansen, X. Huang, Cryogenic toughness in a low-cost austenitic steel, Commun. Mater. 2 (2021) 1–10. https://doi.org/10.1038/s43246-021-00149-8.

[438] D. Herzog, V. Seyda, E. Wycisk, C. Emmelmann, Additive manufacturing of metals, Acta Mater. 117 (2016) 371–392. https://doi.org/10.1016/J.ACTAMAT.2016.07.019.

[439] M.K. Thompson, G. Moroni, T. Vaneker, G. Fadel, R.I. Campbell, I. Gibson, A. Bernard, J. Schulz, P. Graf, B. Ahuja, F. Martina, Design for Additive Manufacturing: Trends, opportunities, considerations, and constraints, CIRP Ann. 65 (2016) 737–760. https://doi.org/10.1016/J.CIRP.2016.05.004.

[440] Y. Hong, C. Zhou, Y. Zheng, L. Zhang, J. Zheng, X. Chen, B. An, Formation of strain-induced martensite in selective laser melting austenitic stainless steel,

Mater. Sci. Eng. A. 740–741 (2019) 420–426. https://doi.org/10.1016/j.msea.2018.10.121.

[441] M.S. Pham, B. Dovgyy, P.A. Hooper, Twinning induced plasticity in austenitic stainless steel 316L made by additive manufacturing, Mater. Sci. Eng. A. 704 (2017) 102–111. https://doi.org/10.1016/J.MSEA.2017.07.082.

[442] H.T. Wang, N.R. Tao, K. Lu, Strengthening an austenitic Fe-Mn steel using nanotwinned austenitic grains, Acta Mater. 60 (2012) 4027–4040. https://doi.org/10.1016/j.actamat.2012.03.035.

[443] J.C. Stinville, C. Tromas, P. Villechaise, C. Templier, Anisotropy changes in hardness and indentation modulus induced by plasma nitriding of 316L polycrystalline stainless steel, Scr. Mater. 64 (2011) 37–40. https://doi.org/10.1016/j.scriptamat.2010.08.058.

[444] Z. Dong, W. Li, G. Chai, L. Vitos, Strong temperature – Dependence of Ni - alloying influence on the stacking fault energy in austenitic stainless steel, Scr. Mater. 178 (2020) 438–441. https://doi.org/10.1016/j.scriptamat.2019.12.013.

[445] R. Ueji, N. Tsuchida, D. Terada, N. Tsuji, Y. Tanaka, A. Takemura, K. Kunishige, Tensile properties and twinning behavior of high manganese austenitic steel with fine-grained structure, Scr. Mater. 59 (2008) 963–966. https://doi.org/10.1016/J.SCRIPTAMAT.2008.06.050.

[446] J. Chen, F.T. Dong, Z.Y. Liu, G.D. Wang, Grain size dependence of twinning behaviors and resultant cryogenic impact toughness in high manganese austenitic steel, J. Mater. Res. Technol. 10 (2021) 175–187. https://doi.org/10.1016/j.jmrt.2020.12.030.

[447] Y. Lee, C. Choi, Driving force for γ→ε martensitic transformation and stacking fault energy of γ in Fe-Mn binary system, Metall. Mater. Trans. A. 31 (2000) 355–360. https://doi.org/10.1007/s11661-000-0271-3.

[448] J.H. Jun, C.S. Choi, Variation of stacking fault energy with austenite grain size and its effect on the MS temperature of γ → ε martensitic transformation in Fe-Mn alloy, Mater. Sci. Eng. A. 257 (1998) 353–356. https://doi.org/10.1016/S0921-5093(98)00994-0.

[449] G.B. Olson, M. Cohen, Kinetics of strain-induced martensitic nucleation, Metall. Trans. A. 6 (1975) 791–795. https://doi.org/10.1007/BF02672301.

[450] T.-H. Lee, E. Shin, C.-S. Oh, H.-Y. Ha, S.-J. Kim, Correlation between stacking fault energy and deformation microstructure in high-interstitial-alloyed austenitic steels, Acta Mater. 58 (2010) 3173–3186. https://doi.org/10.1016/j.actamat.2010.01.056.

[451] M. Connolly, M. Martin, P. Bradley, D. Lauria, A. Slifka, R. Amaro, C. Looney, J.S. Park, In situ high energy X-ray diffraction measurement of strain and dislocation density ahead of crack tips grown in hydrogen, Acta Mater. 180 (2019) 272–286. https://doi.org/10.1016/j.actamat.2019.09.020.

[452] G.. Williamson, W.. Hall, X-ray line broadening from filed aluminium and wolfram, Acta Metall. 1 (1953) 22–31. https://doi.org/10.1016/0001-6160(53)90006-6.

[453] T.H. Simm, P.J. Withers, J. Quinta da Fonseca, An evaluation of diffraction peak

profile analysis (DPPA) methods to study plastically deformed metals, Mater. Des. 111 (2016) 331–343. https://doi.org/10.1016/j.matdes.2016.08.091.

[454] M. Wilkens, The determination of density and distribution of dislocations in deformed single crystals from broadened X-ray diffraction profiles, Phys. Status Solidi. 2 (1970) 359–370. https://doi.org/10.1002/pssa.19700020224.

[455] M. Wilkens, X-ray line broadening and mean square strains of straight dislocations in elastically anisotropic crystals of cubic symmetry, Phys. Status Solidi. 104 (1987) K1–K6. https://doi.org/10.1002/pssa.2211040137.

[456] B.E. Warren, B.L. Averbach, The Separation of Cold-Work Distortion and Particle Size Broadening in X-Ray Patterns, J. Appl. Phys. 23 (1952) 497–497. https://doi.org/10.1063/1.1702234.

[457] R.A. Young, The rietveld method, Oxford university press, 1993.

[458] P. Thompson, D.E. Cox, J.B. Hastings, Rietveld refinement of Debye–Scherrer synchrotron X-ray data from Al2O3, J. Appl. Crystallogr. 20 (1987) 79–83. https://doi.org/10.1107/S0021889887087090.

[459] W. Voigt, Lehrbuch der kristallphysik, Teubner Leipzig, 1928.

[460] A. Reuss, Berechnung der Fließgrenze von Mischkristallen auf Grund der Plastizitätsbedingung für Einkristalle ., ZAMM - Zeitschrift Für Angew. Math. Und Mech. 9 (1929) 49–58. https://doi.org/10.1002/zamm.19290090104.

[461] A. Morawiec, Calculation of Polycrystal Elastic Constants from Single-Crystal Data, Phys. Status Solidi. 154 (1989) 535–541. https://doi.org/10.1002/pssb.2221540213.

[462] J.S. Jeong, Y.M. Koo, I.K. Jeong, S.K. Kim, S.K. Kwon, Micro-structural study of high-Mn TWIP steels using diffraction profile analysis, Mater. Sci. Eng. A. 530 (2011) 128–134. https://doi.org/10.1016/j.msea.2011.09.060.

[463] G. Caglioti, A. t Paoletti, F.P. Ricci, Choice of collimators for a crystal spectrometer for neutron diffraction, Nucl. Instruments. 3 (1958) 223–228. https://doi.org/10.1016/0369-643X(58)90029-X.

[464] X. Zhang, M. Li, J.S. Park, P. Kenesei, J. Almer, C. Xu, J.F. Stubbins, In situ high-energy X-ray diffraction study of tensile deformation of neutron-irradiated polycrystalline Fe-9%Cr alloy, Acta Mater. 126 (2017) 67–76. https://doi.org/10.1016/j.actamat.2016.12.038.

[465] J.F. Nye, Physical properties of crystals: their representation by tensors and matrices, Oxford university press, 1985.

[466] J. Wróbel, L.G. Hector, W. Wolf, S.L. Shang, Z.K. Liu, K.J. Kurzydłowski, Thermodynamic and mechanical properties of lanthanum–magnesium phases from density functional theory, J. Alloys Compd. 512 (2012) 296–310. https://doi.org/10.1016/j.jallcom.2011.09.085.

[467] A. Takeuchi, A. Inoue, Quantitative evaluation of critical cooling rate for metallic glasses, Mater. Sci. Eng. A. 304–306 (2001) 446–451. https://doi.org/10.1016/S0921-5093(00)01446-5.

[468] A.R. Miedema, P.F. de Châtel, F.R. de Boer, Cohesion in alloys — fundamentals of a semi-empirical model, Phys. B+C. 100 (1980) 1–28. https://doi.org/https://doi.org/10.1016/0378-4363(80)90054-6.